Clinical applications of the kT-points method to homogenise spin excitation in 3T MRI

Raphaël Tomi-Tricot

NNT : 2018SACLS260

Clinical Applications of the K_T-Points Method to Homogenise Spin Excitation in 3T MRI

Thèse de doctorat de l'Université Paris-Saclay
préparée à l'Université Paris-Sud
et au sein de NeuroSpin, CEA Paris-Saclay

École doctorale n°575 Physique et ingénierie: électrons, photons et sciences du vivant (EOBE)
Spécialité de doctorat: Imagerie et Physique Médicale

Thèse présentée et soutenue à Gif-sur-Yvette, le 26 septembre 2018, par

Raphaël Tomi-Tricot

Composition du Jury :

Shaihan Malik Senior Lecturer King's College London	Président, Rapporteur
Benedikt Poser Assistant Professor Maastricht University	Rapporteur
Robin Heidemann Senior Scientist Siemens Healthcare GmbH	Examinateur
Alexandre Vignaud Chargé de Recherche CEA NeuroSpin, Université Paris-Saclay	Examinateur
Alexis Amadon Directeur de Recherche CEA NeuroSpin, Université Paris-Saclay	Directeur de thèse
Alain Luciani Professeur des Universités – Praticien Hospitalier INSERM, Hôpital Henri Mondor	Co-Directeur de thèse

Thèse de doctorat

Fata viam invenient

Virgil

Acknowledgements

As Bertie Wooster once said, under P.G. Wodehouse's pen, 'I've found, as a general rule of life, that the things you think are going to be the scaliest nearly always turn out not so bad after all.' Today it seems to me that it conveys my feeling about the past three years pretty well. Surely I cannot say that I had always seen myself completing a PhD.

During my internship as support for the Application Service at Siemens Healthineers France, I encountered the hospital world and clinical applications of MRI for the first time. After this experience, I knew that I wanted to keep working in healthcare at least for a while, in particular in MRI, and to be as much as possible at the interface between physics and medicine, so as to have a direct impact on patient outcome. Around that time, I received a message from Franck Mauconduit, the on-site Siemens clinical scientist based at NeuroSpin, about an opening for a research engineer position with Alexis Amadon, in the UNIRS/METRIC team led by Alexandre Vignaud. This offer had everything I was looking for: MR physics, clinical applications, research-oriented work with a strong engineering touch, ... and rather short – two years. This was perfect for me, since for some reason research intimidated me, not to mention a PhD: I could not possibly picture myself working three years on the very same topic. Still, this did not save me from a copious dose of hesitation before I signed!

A year later, the question of whether I wanted to extend my mission to three years and turn it into a thesis was raised. My answer was quick to come: 'Yes!' This, in contrast to all my previous doubts, should give you an idea of the quality of the environment and the people I had met in the meantime, as well as at AIM and Henri Mondor Hospital. This is why there are so many people I want to thank today.

First, I would like to thank my advisors. Alexis Amadon, whose unfailing optimism and composure helped me keep a cool head and focus on my objectives in times of uncertainty. Alain Luciani, whose humanity and passion for both healthcare and research have comforted me in my choice to stay in that line of work. And Alexandre Vignaud, whose impressive knowledge of clinical aspects of MRI was of course priceless, and who

was always ready to share some precious advice on my mission in NeuroSpin, but also, more often than not, on life in general. Their combined guidance was essential to me in conducting my thesis, and in forming my projects for the future.

Having the luxury to discover research before diving into it is a rare thing, and I realise today how lucky I am to have been offered this opportunity. For that I want to thank Denis Le Bihan for letting me into NeuroSpin in the first place, as well as Cyril Poupon for welcoming me into the UNIRS unit. I would like to acknowledge CEA's *Programme Transverse, Technologies pour la Santé* (Transverse Programme for Health Technologies) for funding the first part of my project. Then, I cannot say how grateful I am to Alexandre Vignaud, Nicolas Boulant and Alexis Amadon, who strove to manage to keep me for a third year, so I could complete this PhD.

I am confident I could not have achieved half of what is described in the present document without the tremendous work of Alexis Amadon, Martijn A. Cloos, Nicolas Boulant, Aurélien Massire, Andrés Hoyos-Idrobo, Laura Dupas and Vincent Gras over the last eight years or so, on k_T-points, parallel transmission, and high-field inhomogeneity issues in general. Special thanks go to Vincent, my deskmate, who would always answer my many questions calmly and thoroughly and would never decline a discussion on any subject.

Also, thank you Franck, not only for sending me this job offer in the first place, but also for all the good times we have had later. I will not forget our long discussions and our endless hours of code analysis and debugging, which seemed like mere minutes thanks to you.

I am thankful to Bertrand Thirion and Hamza Cherkaoui, who spared no effort to help me launch my final project and guide my first steps into the world of machine learning. Here I would also like to stress that without the support and trust of Alexandre and Alexis, this project would never have come into existence.

During these three years, I have spent many hours at Henri Mondor Hospital, first to test and fine-tune sequences and algorithms on phantoms, but most importantly to perform large-scale acquisitions on patients which were at the core of my thesis. This is what made our projects alive, and gave a true meaning to our efforts. I want to thank Alain Luciani for welcoming me there and making me feel at home on so many early Wednesdays for liver imaging sessions. Thank you also to Thu-Ha Dao, who opened the door for me on Thursdays for our study in breast imaging, and to François Legou and Antoine Perrot for their contribution to the different projects. Of course this experience would not have been the same without Pierre Zerbib and his team of MR technicians who stood alongside me throughout these long days: Jimmy, both Camilles, Manon, Sophie, Fabrice, and many others.

In several occasions, I had the opportunity to have valuable discussions with Berthold

Kiefer and Matthias Gebhardt from Siemens Healthineers in Erlangen, and I thank them for that today, along with Dieter Ritter for his advice on safety calculations on clinical scanners. Thank you also, of course, to Iulius Dragonu from Siemens Healthineers UK for his enthusiastic look on *Composite SeqLoops* and for tremendously helping me find my way towards a future job.

I am grateful to Pierre Carlier who let me perform my first in-vivo experiments on thighs at AIM, and I want to also thank the people with whom I have worked there during our collaboration: in particular Benjamin Marty, Alfredo Lopez Kolkovsky and Teresa Gerhalter.

In addition to the people directly involved in my project, I would like to thank many colleagues at NeuroSpin, who contributed in making my years there memorable. Thank you to Cécile Lerman, Benoît Larrat, Fawzi Boumezbeur, Michel Luong, Philippe Ciuciu, Fabrice Poupon and Pierre Brugières for our many exchanges.

Many thanks also to Chantal Ginisty, Séverine Becuwe, Séverine Roger, Lionel Allirol, Nathalie Blancho, Christine Doublé, Denis Fournier and Joël Cotton, not forgetting Maryline Hévin-Delamare who saved me on multiple occasions – especially the day I called her from North Carolina, asking her to find a last minute return flight that would avoid the East Coast 'Snowzilla' of January 2016!

And of course my experience would never have been the same if not for the many PhD students, post-docs and interns whose paths I have crossed. Lisa Leroi, always cheerful, and the best assistant film director one could wish for. Arthur Coste, a true example of passion and righteousness. Gaël Saïb, partner of many a late evening at NeuroSpin. Zo Raolison, a ray of sunshine in his own special way. Loubna El Gueddari (and M. Patate) and Hamza Cherkaoui who were always there to laugh to (and not only at) my most questionable puns, and also provided their share of terrible jokes. Caroline Le Ster, who can now extend her desk territory. Bruno Pinho Meneses, thanks to whom I can now say '*muito obrigado pela física das partículas e pelas lições de português*'. Carole Lazarus and Amicie de Pierrefeu, with whom I have had the pleasure to share the *Ma thèse en 180 secondes* adventure. Emilie Poirion, who worked most of the time at another institution, but whose presence at NeuroSpin never went unnoticed. Sylvain Lannuzel, for his good taste and advice in typesetting and plotting. Kévin Ginsburger, with whom I have spent an unforgettable week in Kauai. Jacques Stout, with whom I went for an unforgettable hike in Kauai. Not forgetting Justine Beaujoin, Arnaud Gloagen, Achille Teillac, Yann Le Guen, Benoît Sarthou, Hanaé Carrié, Morgane Le Garrec, Cédric de Bras De Fer, Véra Feldman, David Gay, Nicole Labra Avila, Solenne Vaillant, Pauline Agou and many others.

There are also former colleagues, from my time at Siemens France, that I would like to thank for their participation in my professional education, each in their own way: Pascal Laumain, Cécile Laffaye, Agnès Malgouyres, Serge Ripart, Aurélien Monnet, Matthieu Lepetit-Coiffé, Benjamin Robert and Isabelle Ginja.

I could not end these acknowledgements without deeply thanking my friends and family for supporting me even at my worst. Thank you Anthony N, Nathan V, Nicolas B, Valentin V, Charles CL, Romain B, and all my friends from the B2. I also want to acknowledge all the encouragements I received from Bernadette, Josette, Eugène, Françoise and René.

I send my regards to my siblings Etienne, Agnès, Séverine, and especially Marie-Zélie who had to put up with my bad temper during the last few months of my thesis.

A very warm thank you to my parents Marie-Ange and François, and my step-parents Monique and François, who all brought me here today. This thesis is the result of the many sacrifices you have made and the guidance with which you have provided me for all these years. I also think of my late grandfather, Jean-Ange, whose values, hard work and dedication have been a source of inspiration for so many years.

And of course thank you, Coline, for always believing in me.

Looking back at this three-year adventure among all these great people, it seems that it was not simply 'not so bad after all': it was grand!

Finally, I would like to pay homage to Professor Alain Rahmouni, who passed away suddenly this year. His commitment to research at Henri Mondor Hospital was exceptional, and so was his contribution to radiology. This project is one of the many he supported, and it would never have been without him. I will remember his profound humanity and selflessness, and the way he inspired people around him to strive for better healthcare, always in the best interest of patients. Thank you, Professor.

* * *
* *
*

Contents

List of Figures

List of Tables

Symbols Used

Symbol	Constant name	Value
c	Speed of light in a vacuum	$299\,792\,458\,\mathrm{m}\cdot\mathrm{s}^{-1}$ (exact)
$\hbar$	Planck constant (reduced)	$1.055\times10^{-34}\,\mathrm{J}\cdot\mathrm{s}$
k_B	Boltzmann constant	$1.381\times10^{-23}\,\mathrm{J}\cdot\mathrm{K}^{-1}$
γ_{H}	^{1}H gyromagnetic ratio	$267.5\times10^{6}\,\mathrm{rad}\cdot\mathrm{s}^{-1}\cdot\mathrm{T}^{-1}$
$\frac{1}{2\pi}\gamma_{\mathrm{H}}$	^{1}H gyromagnetic ratio (reduced)	$42.57\times10^{6}\,\mathrm{Hz}\cdot\mathrm{T}^{-1}$

Symbol	Description	Unit
B_0	static main field	$\mathrm{kg}\cdot\mathrm{s}^{-2}\cdot\mathrm{A}^{-1}$ (T)
B_1^+	coil transmission field	T
B_1^-	coil reception field	T
BW	radiofrequency bandwidth	s^{-1} (Hz)
E	electric field	$\mathrm{V}\cdot\mathrm{m}^{-1}$
$\mathcal{E}$	energy	$\mathrm{kg}\cdot\mathrm{m}^2\cdot\mathrm{s}^{-2}$ (J)
f	temporal frequency	s^{-1} (Hz)
f_0	Larmor temporal frequency	s^{-1} (Hz)
G	spatial static field gradients	$\mathrm{T}\cdot\mathrm{m}^{-1}$
k	spatial frequency	m^{-1}
M	macroscopic magnetisation	$\mathrm{A}\cdot\mathrm{m}^{-1}$
M_o	macroscopic equilibrium magnetisation	$\mathrm{A}\cdot\mathrm{m}^{-1}$
$\mathcal{P}$	power	$\mathrm{J}\cdot\mathrm{s}^{-1}$ (W)
S^+	coil transmit sensitivity profile	$\mathrm{T}\cdot\mathrm{V}^{-1}$
T	temperature	K
T_1	spin-lattice relaxation time	s
T_2	spin-spin relaxation time	s
T_2^*	effective spin-spin relaxation time	s
α	magnetisation nutation angle (flip angle)	degree (°), rad
$\hat{\alpha}$	complex nutation angle: $\alpha = \lvert\hat{\alpha}\rvert$	degree (°), rad

α_E	Ernst flip angle	degree (°), rad
γ	gyromagnetic ratio	$\mathrm{rad} \cdot \mathrm{s}^{-1} \cdot \mathrm{T}^{-1}$
$\Delta \mathrm{B}_0$	static field inhomogeneity	T
Δf_0	offset from carrier frequency	s^{-1} (Hz)
$\Delta\omega$	offset from carrier angular frequency	$\mathrm{rad} \cdot \mathrm{s}^{-1}$
ε_r	relative permittivity	—
ω_0	Larmor angular frequency	$\mathrm{rad} \cdot \mathrm{s}^{-1}$
ρ	volumetric mass density	$\mathrm{kg} \cdot \mathrm{m}^{-3}$
σ	electrical conductivity	$\mathrm{kg}^{-1} \cdot \mathrm{m}^{-2} \cdot \mathrm{s}^3 \cdot \mathrm{A}^2$ ($\mathrm{S} \cdot \mathrm{m}^{-1}$)
φ	radiofrequency phase	degree (°), rad
χ	magnetic susceptibility	—

Mathematical notations

The imaginary unit is expressed by $\imath$, such that $\imath^2 = -1$.
The real and imaginary parts of a complex number z are respectively $\Re(z)$ and $\Im(z)$.
Complex conjugation is conveyed by an exponent asterisk (*).
Lower-case bold letters denote vectors, *e.g.* $\mathbf{v}$.
Upper-case bold letters denote matrices, *e.g.* $\mathbf{M}$.
Vector or matrix transpose is represented by an exponent T following the object, *e.g.* $\mathbf{v}^{\mathrm{T}}$.
Conjugate transpose is denoted by an exponent H following the object, *e.g.* $\mathbf{M}^{\mathrm{H}} = (\mathbf{M}^*)^{\mathrm{T}}$.
Vector dot product and cross product are denoted by $\cdot$ and $\times$, respectively.

General Introduction

Science Finds, Industry Applies, Man Adapts
— The Chicago World's Fair, 1933

Such was the motto welcoming visitors to one of the largest events celebrating industrial progress. At the time, the world was in the midst of the Great Depression, and people saw in science and technology a crumb of hope for a brighter future. Nearly a century later, tremendous progress has indeed been made in every domain: energy, transportation, construction, environment to name a few. And of course healthcare.

In particular, medical imaging was still in its early days in 1933: X-ray radiography was then the only non-invasive way to explore the human body, allowing to visualise bones and a few organs such as the lungs in two-dimensional projections. It was complemented in the 1960s by ultrasound imaging, a great tool for inspecting soft tissues such as tendons, muscles or blood vessels, and extensively used in obstetrics. Some years later, computed tomography, the 'big brother' of projectional radiography, allowed to obtain three-dimensional images of extended volumes in the body. All these techniques are widely used today as each is relevant for many applications. However, both X-ray-based methods involve ionising radiations, which can harm or even destroy biological tissues. As far as ultrasound imaging is concerned, it has a limited range of use and its result is highly operator-dependant.

In the early 1980s, the first magnetic resonance imaging (MRI) devices were introduced in hospitals. With no ionising radiations nor known long-term effects on health, and thanks to the wide range of applications in medical diagnosis brought by more than thirty years of research, MRI now stands out as the most powerful and versatile medical imaging tool available. An MRI scanner is organised around a strong magnet, and is characterised by the magnetic field it produces. Stronger magnetic fields allow for higher signal-to-noise ratios in acquisitions. This gives a number of advantages, including faster examinations, higher resolution images, or both. With that in mind, human-sized MRI scanners have seen their magnetic field increase, from a mere 0.04 T in the beginning to 10.5 T today.

Science Finds. NeuroSpin, part of the CEA (French Alternative Energies and Atomic Energy Commission) Saclay centre near Paris, is a department committed to understand-

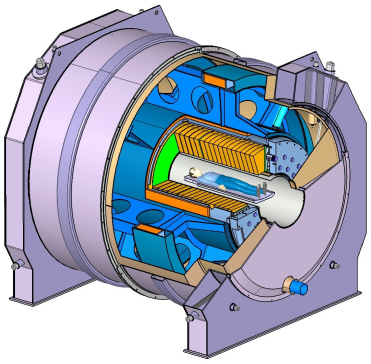

(a) Stripped-down representation.

(b) Magnet delivery in July 2017.

Figure GI.1: ISEULT project: 11.7 T MRI scanner being built in NeuroSpin.

ing brain structure, connectivity and function, with applications in neuroscience, cognitive science and research into neurodegenerative diseases. In order to further explore these areas, powerful MRI scanners are needed. In NeuroSpin, a team of MR physicists is dedicated to improving hardware and acquisitions, to exploit the possibilities of those scanners to their fullest extent. At the moment, the department is equipped with two human-sized imagers: one 3 T and one 7 T. In 2007, along with the Institute of research into the fundamental laws of the Universe (Irfu), NeuroSpin launched the ISEULT project, consisting in the conception and exploitation of a 11.7 T MRI scanner – the largest in the world – to obtain images of the human brain of unrivalled precision. The magnet itself was delivered in July 2017 (fig. GI.1), and the imager will soon be assembled. The first images are expected by the end of 2020. But as we will see, increasing the magnetic field comes with a number of challenges, and the ISEULT project is accompanied with funding to answer those problems and to ensure that the obtained images will be of the highest possible quality. One of the main pitfalls of high-field MRI is the inhomogeneous distribution of the radiofrequency field involved in the process of making an image. As a result, zones of shade and loss of contrast are observed in brain acquisitions at 7 T, and are expected to be even worse at 11.7 T; they are referred to as B_1 artefacts. In 2011, Alexis Amadon and Martijn A. Cloos developed and patented a technique to overcome this problem in the context of 3D imaging: the k_T-points™, now well-known in the ultra-high field community.

Industry Applies. The next step is to bring out the k_T-points method, by attracting the attention of industrial MRI manufacturers, and eventually turning k_T-points into a product useful for everyday clinical practice, with a direct positive impact on patient outcome. This was made possible thanks to the Life Sciences Division (DSV) of the CEA (now part of the Fundamental Research Division): they organised a competition to provide funding to develop applications from patents associated with the ISEULT project. The k_T-points project was selected, which set off this thesis. The hospital world is dominated by 1.5 T scanners, and the highest field available as of today is 3 T. Note that 7 T clinical scanners have been recently introduced by Siemens Healthineers, but currently concern a handful of hospitals with a strong interest in neurological research. At 1.5 T, there are no

radiofrequency inhomogeneity issues. However at 3 T, B_1 artefacts are still a challenge in large human organs and regions such as the abdomen, breasts or thighs. With the firm belief that those artefacts are one of the main obstacles to the adoption of 3 T MRI as an indisputable gold standard in clinical routine, this thesis aims at showing the potential of the k_T-points technique for applications in those organs. This involved collaborating with clinical practitioners to define targeted applications and to assess the efficacy of our method.

Man Adapts? So far, the motto of the 1933 World's Fair perfectly fits with the objectives of this thesis. Nevertheless, the last statement is a bit outdated. At the time, technological progress appeared as an unstoppable wheel that defined the future of mankind. Today the situation is somewhat reversed. Part of what makes an innovation successful is its capacity to be as transparent as can be to the end user: '*Man Benefits*' from progress. It is with this belief in mind that we tackled our project; in particular, it gave rise to the last chapter of this dissertation, whose goal is to hide the use of k_T-points from practitioners and operators.

Thesis Overview

This manuscript is organised in two parts progressively leading the reader from general MRI considerations to the latest results of this three-year adventure.

The first part will describe the context of this work: starting from an overview of MRI and its applications in clinical practice (chapter 1), we will then elaborate on the specificities of high- and ultrahigh-field imaging (chapter 2). In particular, in order to counteract RF inhomogeneity, recent 3 T scanners usually come with a two-RF-channel parallel transmission (pTx) setup. In clinical practice, only static RF shimming is implemented: a single waveform is used, with adjusted amplitude and phase on each channel, to counteract transmission inhomogeneities in the patient. This technique works best when many channels are available, but shows its limits when good homogeneity is expected over a large field of view. Going a step further, dynamic RF shimming exploits the possibility to transmit different waveforms on each channel. At that point, the keystone of this project will be described: the k_T-points method relies on a succession of short rectangular RF pulses interleaved with static gradient 'blips' to modulate magnetisation at will, thus producing homogeneous excitation in spite of an imperfect RF field. Those composite pulses are even more effective as they can take advantage of pTx. They are generally tailored for each patient based on the initial mapping of the RF fields stemming from each channel (calibration process). Patient safety matters will also be discussed. In MRI, it is essential to ensure the energy deposited in the patient by RF pulses (SAR, for specific absorption rate) is below a certain level: k_T-points pulses that we design must respect those limitations, or else they are rejected by the scanner.

The second part of the manuscript gathers the original contributions of this thesis. We will first detail a modification of the k_T-points technique. In the original algorithm, the amplitude and phase on each transmit channel for each short RF 'sub-pulse' is optimised

jointly with the amplitude of the gradient 'blips'. Here, we will allow the duration of each sub-pulse and that of the overall k_T-points pulse to be adjusted as well to improve the robustness of the pulse design (chapter 3). Then we will describe three studies led in a clinical environment, at Henri Mondor University Hospital (Créteil), to investigate the applicability and impact of k_T-points. Chapter 4 will recount a study in breast MRI without pTx, while chapter 5 will focus on liver imaging with dual transmission. Finally, in chapter 6, we will go a step further in the integration of our technique into routine workflows by eliminating the hassle generally associated with radiofrequency inhomogeneity reduction, *i.e.* the calibration process and subsequent in-line RF pulse design.

I hope this manuscript will cater to physicists interested in clinical applications of MRI, and to physicians keen on technology alike, united towards a common goal: to improve healthcare and to provide the best diagnosis possible to every patient.

* * *
* *
*

Part I

Context and State of the Art

Chapter 1

Magnetic Resonance Imaging in Clinical Practice

Chapter Outline

This chapter is an overview of several physical principles behind magnetic resonance imaging (MRI), as well as some techniques that allow to obtain different sorts of images and contrasts that are used along this thesis. It also includes a description of clinical applications in breast and abdominal imaging. Further details about MRI physics can be found in many works, including [McRobbie 2006,Haacke 1999,Bernstein 2004]. For more information on clinical practice MRI, one can refer to [Liney 2007], or [Luciani 2017] (in French) for an extensive review.

1.1 Formation of an Image

The history of magnetic resonance imaging is punctuated with Nobel Prizes. MRI is based on the nuclear magnetic resonance (NMR) phenomenon, that was first described in 1938 by Isidor Isaac Rabi [Rabi 1938], who won the Nobel Prize in Physics in 1944. Applications to molecular structure exploration quickly followed with the independent works of Felix Bloch [Bloch 1946] and Edward Mills Purcell [Purcell 1946], for which they were jointly awarded the Nobel Prize in Physics in 1952. The principles described by these scientists are briefly explained in sections 1.1.1 and 1.1.2.

It is only three decades later that the works of Paul Lauterbur [Lauterbur 1973] and Sir Peter Mansfield [Mansfield 1977b] allowed to encode the NMR signal spatially, thus enabling NMR imaging, or MRI. For this, they shared the Nobel Prize in Medicine and Physiology in 2003. Spatial encoding is the subject of section 1.1.4.

The NMR phenomenon can be observed in any atom that has a non-zero *spin*, a quantum-mechanical property conveying an intrinsic form of angular momentum. Atoms composed of an odd number of nucleons all have a non-zero spin. This is the case, for instance, for the naturally abundant isotopes of hydrogen, fluorine, sodium and phosphorus (^{1}H, ^{19}F, ^{23}Na and ^{31}P, respectively) as well as for rarer isotopes of carbon (^{13}C), sodium (^{15}N) or oxygen (^{17}0).

As body tissues are mostly made of water and fat compounds, it is extremely rich in hydrogen atoms ^{1}H, whose nucleus consists in a unique proton, with a $\frac{1}{2}$-spin. For this reason, most clinical applications focus on proton imaging. Non-proton – or 'exotic' – nuclei spectroscopy is a wide and rich area of research, and their imaging is a dynamic and rising field with a promising future for clinical research [Coste 2017]. This is, however, beyond the scope of this thesis, which focuses solely on ^{1}H imaging.

1.1.1 Magnetisation

The non-zero spin of protons confers them a magnetic moment that makes them behave like microscopic magnets. When a spin is exposed to an external static magnetic field $\mathbf{B_0}$, its magnetic moment aligns to it and follows a precession movement about the field axis at the Larmor angular frequency ω_0, defined as:

$$\omega_0 = \gamma \mathrm{B}_0 \tag{1.1}$$

where γ is the gyromagnetic ratio specific to a given nucleus. For the proton ^{1}H, the gyromagnetic ratio is equal to $267.5 \times 10^{6}\,\mathrm{rad\,s^{-1}\,T^{-1}}$ (often used as $\frac{1}{2\pi}\gamma_{\mathrm{H}} = 42.57\,\mathrm{MHz\,T^{-1}}$). As ordinary frequencies are often preferred, the Larmor frequency is defined as $f_0 = \frac{1}{2\pi}\omega_0$. At 3 T, $f_0 \approx 128\,\mathrm{MHz}$ for proton.

In addition, from a quantum physics point of view, a $\frac{1}{2}$-spin exists in one of two states: *spin-up* or *spin-down*.[1] Consequently, a proton's magnetic moment can be either parallel or anti-parallel to $\mathbf{B_0}$, which corresponds to a low energy or high energy level, respectively.

[1] One should rather say: *in a combination of two principal states.*

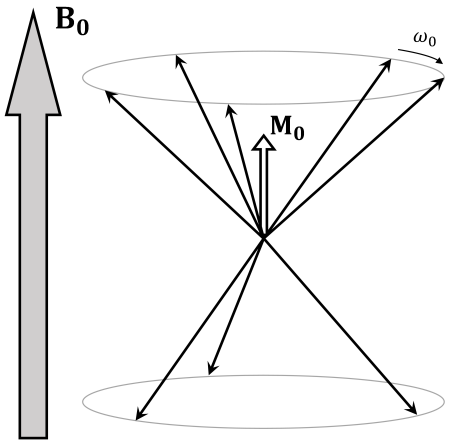

Figure 1.1: Classical representation of macroscopic net magnetisation $\mathbf{M_0}$ (hollow vector) in an isochromat consisting of several adjacent spins immersed in an external static magnetic field ($\mathbf{B_0}$, grey vector). It is induced by the slight excess of magnetic moments (black vectors) parallel to $\mathbf{B_0}$, compared to anti-parallel ones. ω_0 is the Larmor angular frequency at which each spin precesses about $\mathbf{B_0}$. Adapted from [Luciani 2017, ch. 1].

NMR is by nature a quantum phenomenon. However, for the sake of simplicity and because NMR experiments regard not one but millions to billions of protons, it is possible to describe the behaviour of an aggregate of adjacent spins: an *isochromat*. As pictured in fig. 1.1, one can then consider the average of magnetic moments taken over the isochromat, called the net magnetisation vector $\mathbf{M}$, with $\mathbf{M} = \mathbf{M_0}$ at equilibrium in a static field $\mathbf{B_0}$. This is particularly convenient, as this net magnetisation operates under the laws of classical physics.

At thermal equilibrium, the repartition of low and high energy spins within the isochromat follows a Maxwell-Boltzmann distribution. If we denote by N the number of spins considered, T the temperature, $\hbar$ the reduced Planck constant and k_B the Boltzmann constant (see 'Symbols Used' on page xv), and if we consider that the energy difference is negligible compared to k_BT, then the macroscopic magnetisation at equilibrium pictured in fig. 1.1 can be written:

$$\mathbf{M_0} \approx N\frac{\gamma^2\hbar^2}{4k_BT}\,\mathbf{B_0} \tag{1.2}$$

This magnetisation has the potential to create NMR signal when correctly manipulated as explained below. One can already notice that the available magnetisation depends on B_0; this is the reason for the development of magnets of stronger and stronger fields, as detailed in chapter 2.

1.1.2 Excitation and Relaxation

No NMR signal can be observed when the system is at equilibrium and macroscopic magnetisation is aligned with $\mathbf{B_0}$. In order to obtain signal, one must excite the system with the help of a RF magnetic field B_1^+ of frequency ω_{rf}, transmitted through a RF coil disposed such that the oscillating $\mathbf{B_1^+}$ field be orthogonal to $\mathbf{B_0}$.

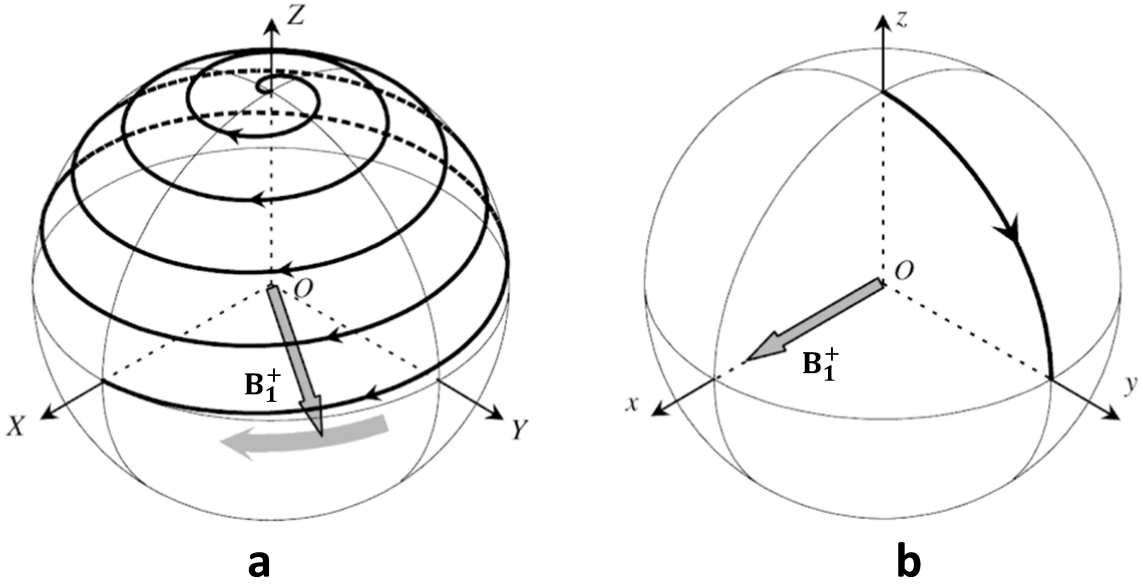

Figure 1.2: Effect on macroscopic magnetisation of a $\mathbf{B_1^+}$ field rotating at the Larmor frequency ω_0 viewed (a) from laboratory frame (XYZ) where $\mathbf{B_0}$ is aligned with the Z axis. (b) It is generally convenient to represent it in a rotating frame of reference (xyz) of frequency ω_{rf}, where $\mathbf{B_1^+}$ lies along with the x axis. The z axis is aligned with Z. Adapted from [Décorps 2012].

The RF field must oscillate at the Larmor frequency, *i.e.* $\omega_{rf} = \omega_0$, in order to resonate with the spins. At a microscopic level, it has two effects:

- It provides energy to the system, allowing some low energy spins to transfer to a high energy level.
- It forces the spins to precess in phase.

At a macroscopic scale, its effect is to tilt the net magnetisation vector $\mathbf{M}$ towards the transverse plane, as shown on fig. 1.2. Let us decompose magnetisation as:

$$\mathbf{M} = \begin{bmatrix} M_x \\ M_y \\ M_z \end{bmatrix} \quad \text{and} \quad \mathbf{M_{xy}} = \begin{bmatrix} M_x \\ M_y \\ 0 \end{bmatrix} \tag{1.3}$$

where $\mathbf{M_{xy}}$ is the transverse magnetisation, and M_z is called longitudinal magnetisation.

Once the magnetisation has been tilted, the B_1^+ field is stopped and the system starts returning to its initial equilibrium state. This is called relaxation, and it can be explained by two distinct phenomena:

- The longitudinal – or *spin-lattice* – relaxation accounts for the loss of magnetic moment of spins in collisions with their environment. At a macroscopic scale, it corresponds to the regrowth of longitudinal magnetisation M_z. It is associated with a relaxation parameter T_1, which can take different values depending on field strength and tissue type [Stanisz 2005] and is the time needed for M_z to retrieve 63 % of its initial value M_0 (see fig. 1.3). It is sometimes referred to as T_1 recovery.
- The transverse – or *spin-spin* – relaxation emanates microscopically from the loss of phase coherence between spins due to subtle local changes in magnetic field.

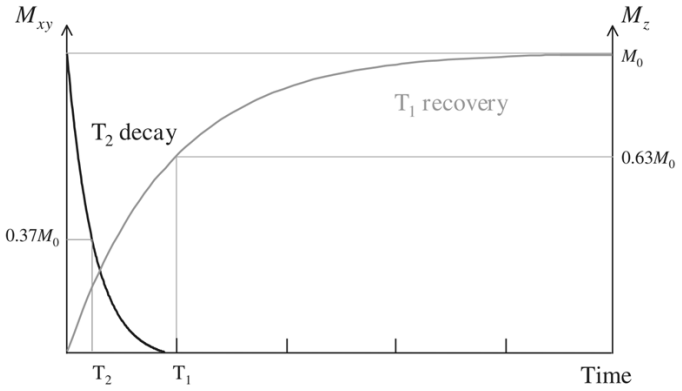

Figure 1.3: Longitudinal (grey) and transversal (black) relaxation of magnetisation for a given T_1 and T_2. From [McRobbie 2006].

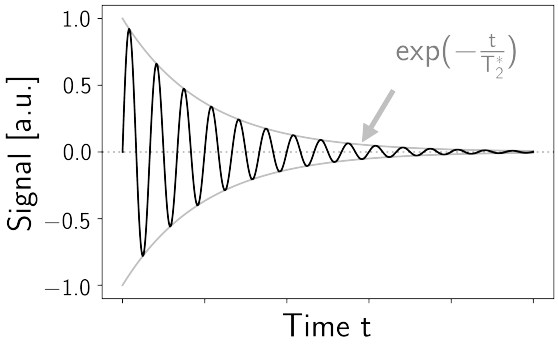

Figure 1.4: Free induction decay signal representation, showing the signal oscillating at the carrier frequency (128 MHz at 3 T), weighted by a decreasing exponential caused by T_2^* decay. No values are shown on the time axis, as in this simple representation, for the sake of readability, the frequency is orders of magnitude lower than in reality.

Macroscopically, this phenomenon is characterized by the T_2 relaxation parameter (see fig. 1.3), whose value also differs depending on tissue type. It can be referred to as T_2 decay. In practice, because B_0 is not perfectly uniform macroscopically (*e.g.* small magnet defects), this decay is faster than expected, and transverse relaxation is characterized by the parameter T_2^*, such that $T_2^* < T_2$. The effects of those 'static' B_0 changes can be recovered as explained in section 1.2.2 'Fast Spin-Echo Sequences'.

While magnetisation relaxes to its equilibrium state, it is possible to measure the evolution of its transverse component, using either the same coil that was used for transmission of B_1^+, or a dedicated receive coil. Indeed, the rotation of $\mathbf{M_{xy}}$ in the transverse plane induces a measurable voltage in the coil [Hoult 1997]. This signal is called free induction decay (FID) [Hahn 1950a]; as shown in fig. 1.4, it oscillates at ω_0, with an exponential attenuation corresponding to T_2^*. Note that the amplitude of the FID depends on the initial longitudinal magnetisation M_0, that is tipped into the transverse plane: it is therefore related to eq. (1.2).

The behaviour of magnetisation exposed to a magnetic field $\mathbf{B}$ was formalised by Felix

Bloch [Bloch 1946] and is written in the laboratory frame (XYZ) as:

$$\left(\frac{\mathrm{d}\mathbf{M}}{\mathrm{d}t}\right)_{\mathrm{lab}} = \gamma\mathbf{M}\times\mathbf{B} - \begin{bmatrix} M_X/\mathrm{T}_2 \\ M_Y/\mathrm{T}_2 \\ (M_Z - M_0)/\mathrm{T}_1 \end{bmatrix} \tag{1.4}$$

As pictured in fig. 1.2, it is convenient to describe the evolution of magnetisation in a frame (xyz) rotating according to the rotation vector $\mathbf{\Omega}$:

$$\mathbf{\Omega} = \begin{bmatrix} 0 & 0 & \omega \end{bmatrix}^{\mathrm{T}} \tag{1.5}$$

Equation (1.4) then becomes:

$$\left(\frac{\mathrm{d}\mathbf{M}}{\mathrm{d}t}\right)_{\mathrm{rot}} = \gamma\mathbf{M}\times\left(\mathbf{B} - \frac{\mathbf{\Omega}}{\gamma}\right) - \begin{bmatrix} M_x/\mathrm{T}_2 \\ M_y/\mathrm{T}_2 \\ (M_z - M_0)/\mathrm{T}_1 \end{bmatrix} \tag{1.6}$$

For instance, fig. 1.2b is obtained, ignoring relaxation, with $\mathbf{B} = \mathbf{B_0} + \mathbf{B_1^+}$ and $\omega = \omega_0 = \omega_{\mathrm{rf}}$: in ($xyz$), $\mathbf{B_0}$ disappears from eq. (1.6), and $\mathbf{B_1^+}$ is fixed. In all that follows, we will consider a rotating frame matching the RF angular frequency: $\omega = \omega_{\mathrm{rf}}$.

1.1.3 Excitation: Selective and Non-Selective

Let us delve into more detail on RF excitation, as it is a central aspect of this thesis. The effect of the B_1^+ field is to tip magnetisation into the transverse plane. The nutation angle α, generally referred to as flip angle (FA), is defined as:

$$\begin{aligned} \alpha &= \arccos\left(\frac{M_z}{\|\mathbf{M}\|}\right) \quad \text{for} \quad 0 \leq \alpha \leq 180° \\ \alpha &= \arcsin\left(\frac{\|\mathbf{M_{xy}}\|}{\|\mathbf{M}\|}\right) \quad \text{if} \quad \alpha \leq 90° \end{aligned} \tag{1.7}$$

The relation between a RF excitation duration T and of temporal envelope $\mathrm{B}_1^+(t)$ and the accumulated FA is generally non-linear, as it follows Bloch's equation. However, for flip angles small enough, a good approximation can be made for $\alpha < 30°$, which severely breaks down only for $\alpha > 90°$ [Pauly 1989, Bernstein 2004]. Consider eq. (1.6) for a rotating frame chosen to match the RF frequency ($\omega = \omega_{\mathrm{rf}}$), with $\mathbf{B_1^+}$ along the x axis, and neglecting relaxation as it is generally done when studying (short) RF pulses:

$$\left(\frac{\mathrm{d}\mathbf{M}}{\mathrm{d}t}\right)_{\mathrm{rot}} = \gamma\mathbf{M}\times\begin{bmatrix} \mathrm{B}_1^+(t) \\ 0 \\ \mathrm{B}_0 - \omega_{\mathrm{rf}}/\gamma \end{bmatrix} \tag{1.8}$$

One may wonder why at this point we do not use eq. (1.1) and the fact that ω_{rf} is commonly tuned to match the Larmor frequency ω_0, to cancel out the term $\mathrm{B}_0 - \omega_{\mathrm{rf}}/\gamma$ in this equation. Such situation is called on-resonance, and only holds for a perfectly homogeneous B_0. In general, eq. (1.1) does not hold everywhere because of B_0 inhomogeneities due to static

field imperfections or to local changes in chemical composition as will be discussed in section 1.3. Introducing an off-resonance term:

$$\Delta\omega = \gamma \mathrm{B}_0 - \omega_{\mathrm{rf}} \tag{1.9}$$

and the complex transverse magnetisation:

$$M_\perp = M_x + \imath M_y \tag{1.10}$$

eq. (1.8) can be expressed (in the rotating frame) as:

$$\frac{\mathrm{d}M_\perp}{\mathrm{d}t} = -\imath\Delta\omega M_\perp(t) + \imath\gamma \mathrm{B}_1^+(t) M_z(t) \tag{1.11}$$

Solving this equation, combined with eq. (1.7), and with the approximation that $M_z(t) \approx M_0$ (small flip angle) eventually gives:

$$\alpha = \gamma \left| \int_0^T \mathrm{B}_1^+(t)\, \mathrm{e}^{\imath\Delta\omega\, t}\ dt \right| \tag{1.12}$$

Since $\mathrm{B}_1^+(t)$ is 0 except during the pulse, the integration limits can be replaced by $-\infty$ to $+\infty$: for small flip angles, an RF pulse shows a spectral selection profile equal to the modulus of the inverse Fourier transform of the envelope. In the specific case of no off-resonance ($\omega = \omega_0 = \omega_{\mathrm{rf}}$), eq. (1.12) boils down to:

$$\alpha = \gamma \int_0^T \mathrm{B}_1^+(t)\ dt \tag{1.13}$$

This relationship is useful to quickly estimate the effect of a pulse on FA. But the Fourier response of the FA to the RF field described by eq. (1.12) is actually what allows us to spatially select a volume to excite, thanks to the introduction of linear static field gradients, produced in all three directions by dedicated coils as we are now going to see.

Selective Excitation

The application of a gradient $\mathbf{G} = \begin{bmatrix} G_X & G_Y & G_Z \end{bmatrix}^T$ modifies the static field at a point $\mathbf{r}$ of coordinates X, Y and Z in the following way:

$$\mathbf{B}(\mathbf{r}) = \mathbf{B_0} + (\mathbf{G} \cdot \mathbf{r})\, \mathbf{e_z} \tag{1.14}$$

where $\mathbf{e_z}$ represents the unit vector along the Z axis. Equation (1.9) now becomes:

$$\Delta\omega(\mathbf{r}) = \gamma \mathrm{B}_0 + \gamma \mathbf{G} \cdot \mathbf{r} - \omega_{\mathrm{rf}} \tag{1.15}$$

With the introduction of these static field gradients, there is now a linear relationship between the off-resonance term $\Delta\omega$ and location $\mathbf{r}$. In particular, when neglecting B_0 inhomogeneity, and when matching ω_{rf} with ω_0, eq. (1.15) simplifies to $\Delta\omega(\mathbf{r}) = \gamma\, \mathbf{G} \cdot \mathbf{r}$. Let us focus on an example with a single gradient G_Z applied in the Z direction as pictured in fig. 1.5: we can write $\Delta\omega(Z) = \gamma\, G_Z Z$. In order to selectively excite a slice of

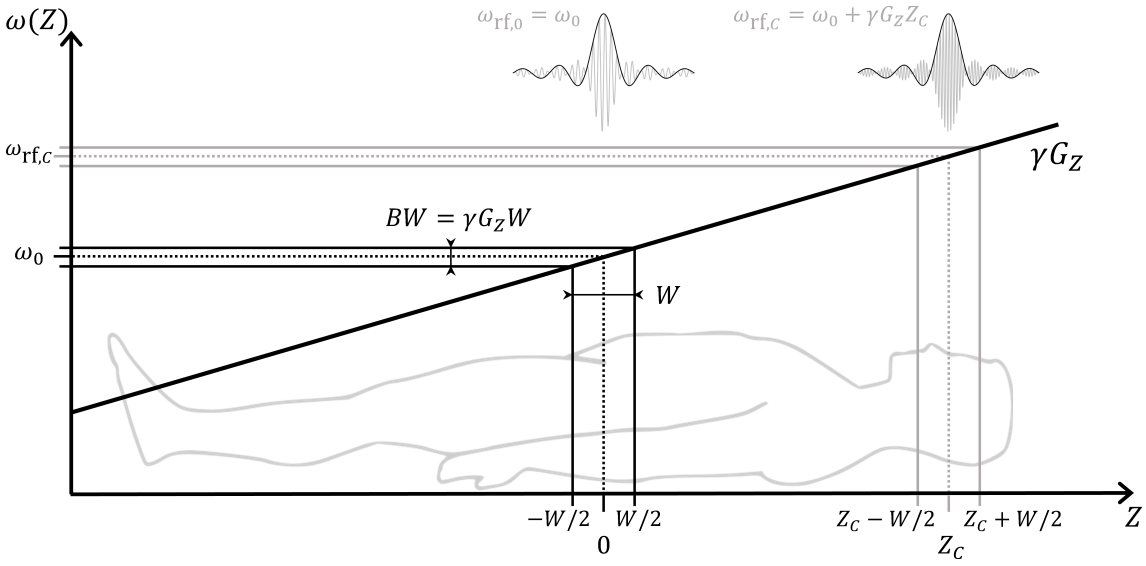

Figure 1.5: Illustration of spatial selection of a transversal slice by coupling a linear static field gradient G_Z along Z and a spectrally selective pulse with a sinc envelope. A slice of thickness W around isocentre (left, in black) is selected by applying a pulse whose carrier frequency ω_{rf} matches ω_0, and whose envelope corresponds to a bandwidth $BW = \gamma G_Z W$. Keeping the same envelope but increasing ω_{rf} to $\omega_{\mathrm{rf,C}} = \omega_0 + \gamma G_Z Z_C$ allows to select a slice of identical thickness W, but centred around Z_C (right, in grey) .

thickness W, comprised between $-W/2$ and $W/2$ around magnet isocentre, we just need to apply a pulse of pass bandwidth $BW = \Delta\omega(W/2) - \Delta\omega(-W/2) = \gamma G_Z W$. According to eq. (1.12), obtaining a rectangular spectral response is achieved with pulse of sinc temporal envelope (in practice a sinc pulse truncated after a few zero-crossings), with a main lobe of duration $2/BW = 2/\gamma G_Z W$. More generally, looking back at eq. (1.15), the same pulse envelope can be used to excite any slice centred around Z_C , by adjusting ω_{rf} accordingly: $\omega_{\mathrm{rf},C} = \omega_0 + \gamma G_Z Z_C$ (*cf.* fig. 1.5).

It should be noted that selective pulses can be utilised without their accompanying gradient to excite a specific range of frequencies, for instance to selectively excite certain chemical compounds (*cf.* section 1.3.2 'Fat Saturation'). In this case they are called spectrally-selective instead of spatially-selective.

Non-Selective Excitation

Sometimes, selectivity is not desired. In order to excite all the volume attainable by the RF field, one should not use any gradient during the pulse. In addition, to make sure all spins isochromats get excited, no matter the local field inhomogeneities, a broadband pulse should be used.

The simplest non-selective pulse is the short rectangular – or *hard* – pulse, whose temporal envelope is simply shaped like a rect function of duration T and amplitude B_1^+. Contrarily to sinc pulses, which need a certain number of zero-crossings to achieve a sharp excitation profile, and therefore are quite long, hard pulses can be very short. The

spectral response of a hard pulse is a sinc, with a bandwidth inversely proportional to the pulse length. For instance, with $T = 100\,\mu s$, the first zero-crossing occurs at $\pm 10\,kHz$. A typical range of off-resonance encountered *in vivo* at 3 T would be $\pm 100\,Hz$ (for a single chemical compound): spins would therefore all be flipped by at least 99.8 % of the nominal FA. Therefore off-resonance can be neglected and, in the small flip angle approximation, eq. (1.13) can be used. The flip angle of a hard pulse is directly proportional to its amplitude and duration:

$$\alpha = \gamma \, B_1^+ \, T \tag{1.16}$$

It is worth noting that a spectrally-selective behaviour can be obtained by combining several rect pulses, as exposed in section 1.3.2 'Water Excitation'.

Non-selective excitation is at the core of this thesis, so we will come across non-selective pulses a lot thereafter. We will see that k_T-points are a form of non-selective excitation, and their performance will be compared to that of hard pulses.

1.1.4 Reception: Spatial Encoding of Signal

So far we have discussed principles related to spin excitation, either for a slice or for the whole volume. We also stated that, once excited, the spin isochromats come back to their equilibrium magnetisation through relaxation, during which it is possible to detect a signal (FID) associated with the precession of $\mathbf{M_{xy}}$. Now let us focus on spatial encoding of signal, considering only modern methods introduced by the works of Mansfield in the seventies [Mansfield 1977a, Mansfield 1977b], and a 'traditional' Cartesian sampling pattern.

2D Imaging

In 2D MRI, the slice to image is first selectively excited as described before, with a *slice-selecting* gradient G_{Slice}. The data corresponding to this slice are then encoded in terms of spatial frequencies along two dimensions; an inverse 2D Fourier transform then allows to turn this so-called 2D k-space (or Fourier plane) into an image of the slice. Two techniques are used together to fill the 2D k-space, line by line:

- Applying a frequency-encoding (or *readout*) gradient G_{Read} orthogonal to G_{Slice} changes the precession frequency of isochromats while signal is acquired, thus allowing to discriminate their position in that direction. We have acquired a line of k-space.
- For now we have only acquired one line, at the centre of k-space. To fill the k-space we need to encode spatial frequencies in the remaining dimension, *i.e.* to encode several lines. We use a third gradient, G_{Phase}, called *phase-encoding* gradient, and orthogonal to both G_{Slice} and G_{Read}. It is applied between excitation and readout, and it induces a variation of phase along its direction, that will hold during the acquisition of signal (readout) described above.

To acquire a full 2D k-space, it is necessary to repeat the $G_{Phase} \rightarrow G_{Read}$ pattern as many times as there are lines in k-space, changing the intensity of G_{Phase} every time, so as to

explore all needed spatial frequencies in its direction. The relationship between a gradient $\mathbf{G}$ – over any combination of axes – applied for a certain duration t and the corresponding encoded spatial frequency $\mathbf{k}$ (in m^{-1}) is:

$$\mathbf{k}(t) = \gamma \int_0^t \mathbf{G}(u)\, du \tag{1.17}$$

At the end of the 2D imaging process described above, we have encoded Fourier data for one slice, and we are able to reconstruct the corresponding image. In 2D imaging, one can repeat the process described above several times, selecting different slices, to acquire a three-dimensional field of view (FOV).

However, resolution is limited in the third dimension (slice thickness), because of three main factors. Firstly, selecting a thinner slice requires higher intensity gradients, which eventually run into hardware limitations. Secondly, it requires increasingly sharp excitation profiles to avoid overlap between adjacent slices (at a lower slice resolution, we usually leave a gap between slices to prevent this overlap). Doing so requires a sinc pulse with more zero-crossings, *i.e.* a longer pulse, which can be undesirable depending on the imaging sequence (see section 1.2). Last but not least, when a slice is excited, the acquired signal comes from all isochromats in it: from a thinner slice comes lower signal, and a loss in imaging quality.

3D Imaging

All these factors make high isotropic resolutions hard – even impossible – to achieve with 2D MRI. Fortunately it is possible to excite the whole FOV at once and perform 3D imaging. The principle is to acquire a three-dimensional k-space, corresponding to the volume. To do so we apply the same steps as described earlier, and we add a second phase-encoding gradient, G_{Part}, along what used to be the slice direction, so as to induce phase variation along that direction. It is called the *partition-encoding* gradient (as the 'slices' obtained in 3D MRI are named 'partitions'), and it is generally played simultaneously with G_{Phase}.

To acquire a full 3D k-space, we have to repeat the $G_{Part} \rightarrow G_{Phase} \rightarrow G_{Read}$ pattern $N_{\mathrm{Part}} \times N_{\mathrm{Phase}}$ times, with N_{Part} the number of partitions to encode, and N_{Phase} the number of lines, and apply an inverse 3D Fourier transform to retrieve the imaged volume. The difference between 2D and 3D imaging in terms of encoding is pictured in fig. 1.6.

One drawback of 3D imaging is its sensitivity to patient motion, as the whole 3D k-space must be filled – which takes time – before reconstructing. Any spatial information corrupted by movement occurring during acquisition affects the quality of all images within the volume. In comparison, in 2D imaging, each slice is reconstructed separately: motion during the acquisition of one slice has no effect on the rest of the FOV.

One last thing to consider: the pulses used for 3D MRI are either selective pulses with a thick excitation profile or non-selective pulses. Non-selective pulses can be used for 3D imaging provided aliasing is avoided in the partition direction (FOV larger than the object in that direction, or minimal selection of reception elements from a receive array). These

two options are called *slab-selective* and *non-selective* 3D imaging, respectively. The latter is the one mostly used in this thesis.

1.2 Pulse Sequences

We have seen how to acquire a volume, either slice by slice or all at once, by repeating an 'excitation – phase encoding – frequency encoding' pattern many times, with signal reception taking place during frequency encoding. This is the basic kernel of what is called an MRI sequence. Today, a multitude of sequences exist, that can incorporate additional gradient or RF elements to manipulate magnetisation, as explained in this section.

One interest of MRI among other imaging modalities is its ability to discriminate tissues based on their respective T_1 or/and T_2 values [Stanisz 2005] (section 1.1.2). A pulse sequence is generally characterised by its echo time (TE) and repetition time (TR). TE corresponds to the time elapsed between spin excitation and signal acquisition. TR is the delay between two applications of the sequence kernel; for basic sequences it corresponds to the time separating the acquisition of two consecutive k-space lines.

Adjusting TR and TE enables the possibility to create different contrasts, or *weightings*. Usually, with a FA high enough:

- A short TR and a short TE give a T_1-weighted (T_1w) image.
- A long TR and a long TE give a T_2^*-weighted image, or possibly T_2-weighted (T_2w) as explained in section 1.2.2.
- A long TR and a short TE give an image not much influenced by either T_1 or T_2, that reflects mostly proton density (PD-weighting).

For instance at 1.5 T, water ($T_1 \approx 4000\,\text{ms}, T_2 \approx 2000\,\text{ms}$) exhibits strong hyposignal in T_1w images and strong hypersignal in T_2w ones. Liver tissue ($T_1 \approx 500\,\text{ms}, T_2 \approx 40\,\text{ms}$ [Bottomley 1984]), on the other hand, has both a low T_1 and a low T_2, so it shows T_1-hyperintensity (T_1H) and T_2-hypointensity (T_2h). Fat ($T_1 \approx 250\,\text{ms}, T_2 \approx 70\,\text{ms}$) contrasts with liver in both weightings, as it is slightly more T_1-hyperintense and produces more T_2w signal.

The aim of this section is to describe the two sequences that will be used in the second part of this work.After an introduction to the gradient-recalled echo (GRE) family, section 1.2.1 focuses on the fast low angle shot (FLASH) sequence. Section 1.2.2 presents the spin-echo (SE) family, then describes the SPACE sequence.

1.2.1 FLASH: a Gradient-Recalled-Echo-Based Sequence

Standard GRE

One of the most basic ways – though historically not the first – to obtain an MRI image is via the GRE sequence, introduced in by Haase *et al.* in 1986 [Haase 1986, Frahm 1986]. In a GRE sequence, one first tilts magnetisation by a flip angle α (with $\alpha \leq 90°$). The kernel of a basic GRE is pictured in fig. 1.6, for both 2D selective and 3D non-selective imaging. As described before, phase-encoding (and partition-encoding in 3D) is ensured

by gradients on G_{Phase} (and on G_{Part} in 3D). Signal in the remaining direction is encoded by a dephasing gradient played on G_{Read} – here of negative polarity – which causes a phase dispersion of the spins. It is followed by a positive gradient whose integral is twice that of the negative lobe: the spins gradually refocus, producing an echo during which signal is sampled, hence the name 'gradient-recalled echo'. Signal is said to be frequency-encoded, as the readout gradient forces spins to precess at different frequencies depending on their location along that axis. Shaded lobes are of equal area in fig. 1.6. Gradient-induced dephasing is fully compensated in the middle of the readout (positive) gradient, thus marking the sequence TE, when the echo peak occurs.

This basic GRE sequence assumes that TR is long enough compared to T_1, so that magnetisation can be considered fully longitudinal before the next RF pulse is applied at each repetition: no previously RF-induced transverse magnetisation remains. In such a situation, acquisition occurs during the FID that immediately follows the excitation: available signal decays at a T_2^* rate (section 1.1.2). Figure 1.7 shows how the echo is generated during an FID by gradient reversal and depends on T_2^*.

Steady-State Magnetisation

If TR is too short, magnetisation does not have enough time to recover to its equilibrium longitudinal state from one repetition to the other. A *steady-state* is formed after a few TRs, in which longitudinal magnetisation M_{SS} available at the beginning of a repetition is smaller than M_0: it is said to be partially saturated (totally saturated if M_{SS} is zero). In addition to this saturation effect, if TR is short relatively to T_2^*, some previously tipped magnetisation may remain in the transverse plane at the end of the repetition, and will be affected by the following pulse. If nothing is done, in some configurations, this magnetisation can be unwillingly rephased during a subsequent TR: uncontrolled bands of varying signal may appear, that substantially degrade the image [Frahm 1987]. Two main approaches to fast (short TR) GRE imaging coexist to handle this issue [Elster 1993]:

- Coherent steady-state GRE techniques in which both longitudinal and transverse components of magnetisation reach a steady-state: M_{SS} is not aligned with the z axis. An example of such sequence is the balanced steady-state free precession (bSSFP) technique[2], widely used in cardiac imaging for the high signal it can produce with a short TR, and its intrinsic resistance to flow artefacts; however it offers no leverage on image contrast (weighted by the ratio T_2/T_1, which highlights well liquids such as blood) [Bieri 2013].
- Incoherent steady-state GRE techniques, which consist in deliberately suppressing the transverse component of magnetisation at the end of each repetition with RF spoiling or gradient spoiling, as explained next; only a longitudinal steady-state has been established. Such sequences are generally referred to as spoiled GRE (SPGR), or as fast low angle shot (FLASH)[3] or VIBE in Siemens nomenclature.

[2]The bSSFP sequence is known as 'TrueFISP' in Siemens nomenclature.

[3]The name 'FLASH' hereby refers to the SPGR sequence in Siemens nomenclature, not to be confused with the original GRE introduced by Haase *et al.*, also coined 'FLASH'.

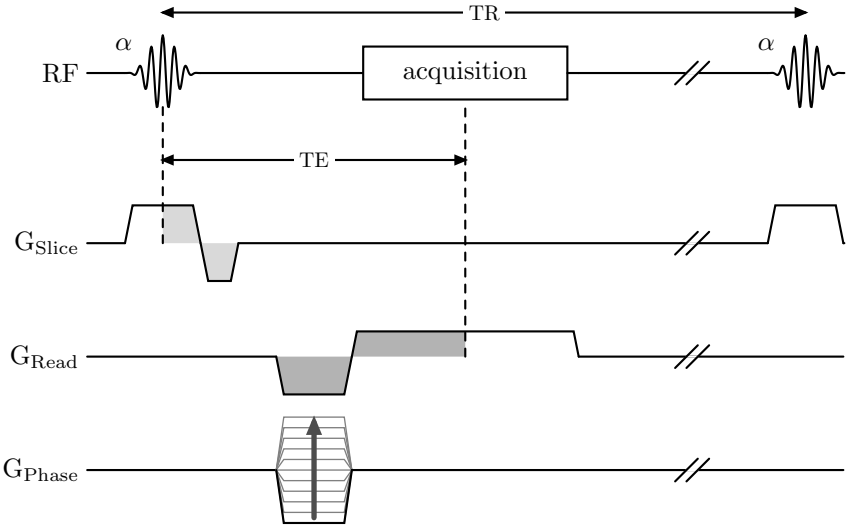

(a) GRE sequence with selective excitation and 2D Cartesian acquisition.

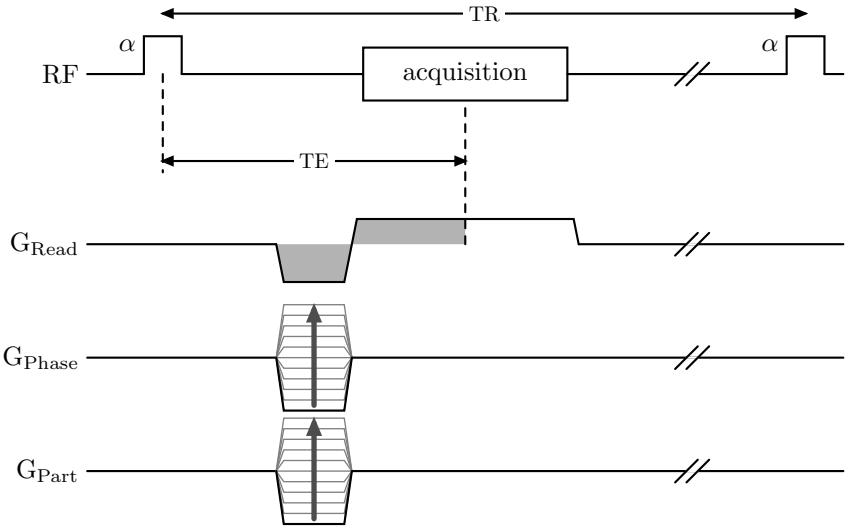

(b) GRE with non-selective excitation and 3D Cartesian acquisition.

Figure 1.6: Timing diagrams for a 'basic' gradient-recalled echo (GRE) pulse sequence, as introduced in [Haase 1986], for (a) 2D and (b) non-selective 3D imaging. This sequence requires $TR \gg T_1$, which is too idealistic; in practice, spoiling is used (fig. 1.8). Notice the slice-selection gradient along with a sinc pulse in (a), and the rect pulse without accompanying gradient in (b). For 3D imaging, a second phase-encoding gradient (G_{Part}) is needed. Greyed-out gradient lobes of a given shade are of identical area (moment). The negative grey G_{Slice} lobe in (a) is a rephasing gradient, to ensure that phase dispersion introduced by the slice-selection gradient is corrected, thus avoiding signal loss due to intra-voxel dephasing.

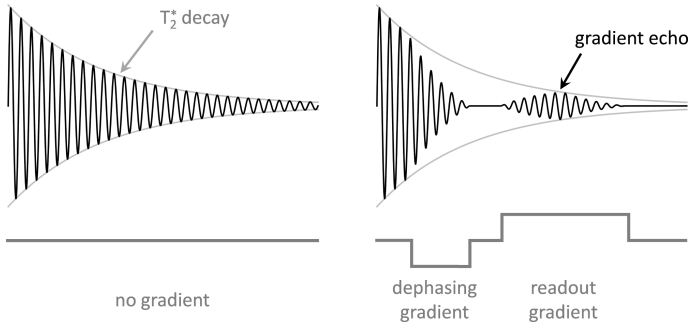

Figure 1.7: Gradient echo formation: received RF signal (top) and encoding gradient shape (bottom). Left-hand side: after a pulse and without application of a gradient, a FID signal is obtained with no spatial information. Right-hand side: dephasing spins with a spatially linear gradient and rephasing them with a gradient of opposite polarity destroys the signal in a controlled way and restores it at a specific echo time (TE); the resulting echo is spatially encoded. Note that this spin manipulation does not compensate for T_2^* decay.

FLASH Sequence

The FLASH sequence is at the core of several studies in this manuscript (chapters 5 and 6) and is therefore described in more detail in its Siemens implementation. Its diagram for 3D non-selective imaging can be found in fig. 1.8, where several differences from the basic GRE (fig. 1.6b) deserve to be highlighted. Firstly, phase- and partition- encoding gradients are counterbalanced by 'rewinder' gradients of identical moment with reversed polarity, guaranteeing the stability of the MR signal phase. This is done to ensure that any user-induced spin incoherence is cancelled out by the end of the repetition. Secondly, a 'spoiler' gradient is added on the readout axis (in grey on the picture). It is not properly *spoiling* (cancelling) transverse magnetisation as it is constant from one repetition to the other; its role is to average the phase of net transverse magnetisation within a voxel. Its moment is large enough to ensure that all phases (0°–360°) exist inside voxels [Van der Meulen 1988]; in practice this corresponds to a moment equal to 0.5 (used in Siemens product FLASH sequence, and pictured in fig. 1.8), 1.5, 2.5, ... times that of the readout lobe to achieve respectively 360°, 720°, 1080°, ... intra-voxel phase dispersion. Finally, proper spoiling is achieved by incrementing the RF phase (represented by φ_i on fig. 1.8) quadratically using a recursive formula from one repetition to the next. The phase-cycling pattern generally applied [Zur 1991] is the following:

$$\begin{cases} \varphi_0 = \varphi_{inc} \\ \varphi_n = \varphi_{n-1} + n\ \varphi_{inc}, \quad n \geq 1 \end{cases} \tag{1.18}$$

where n represents the repetition index, and φ_{inc} is the RF phase increment, selected to be 50° in Siemens product sequences.

Assuming perfect spoiling and that steady-state is reached, the signal obtained by a

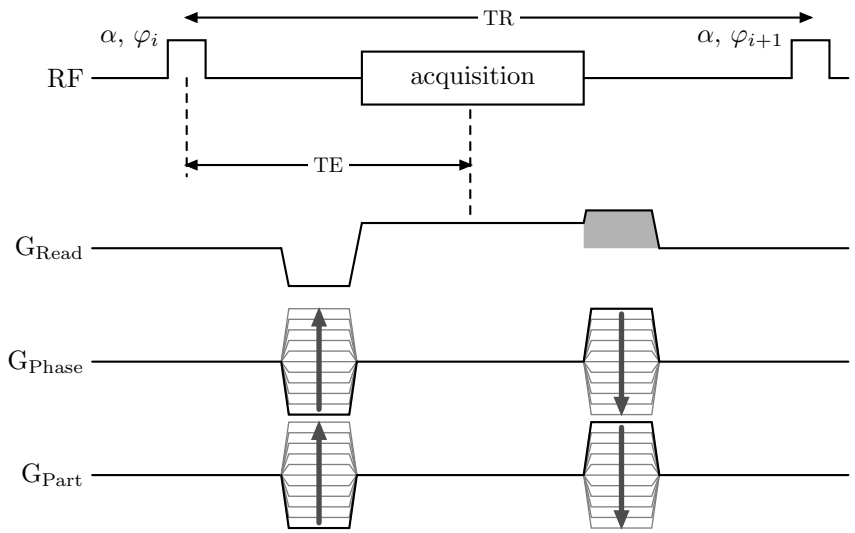

Figure 1.8: 3D fast low angle shot (FLASH) sequence diagram with non-selective excitation. In comparison with the basic GRE (fig. 1.6b), notice the added gradients opposed to phase- and partition-encoding gradients, to counteract the effect of the latter after signal reception by rephasing the spins. A spoiler gradient (grey) is also used in conjunction with RF phase cycling (φ_i) to suppress transverse magnetisation between consecutive TRs.

FLASH sequence for given parameters α, TE, TR and for given T_1 and T_2^*, is [Ernst 1966]:

$$\begin{aligned} S_{\text{FLASH}} &= k\ \text{PD}\ \sin\alpha\ \frac{1-E_1}{1-E_1\cos\alpha}\ E_2^* \\ \text{with}\quad E_1 &= \exp\left(-\frac{\text{TR}}{T_1}\right) \\ \text{and}\quad E_2^* &= \exp\left(-\frac{\text{TE}}{T_2^*}\right) \end{aligned} \tag{1.19}$$

where k is a constant and PD is the proton density. From this equation, it appears that for any T_1 and TR pair, the signal is maximised for $\alpha = \alpha_E$, called the Ernst angle:

$$\alpha_E = \arccos(E_1) \tag{1.20}$$

Intuitively, a small FA will tip some magnetisation into the transverse plane, but will only slightly affect the longitudinal component: less saturation occurs, which means TR can be short (only a few milliseconds). Still, the signal at Ernst angle for a short TR is lower than at Ernst angle for a longer TR. The highest signal one can obtain with a FLASH sequence is with a 90° FA, at the expense of a very long TR (theoretically infinite), and would be:

$$S_{\text{FLASH,max}} = k\ \text{PD}\ E_2^* \tag{1.21}$$

From what we have seen, it appears that the FLASH sequence offers the possibility to perform fast acquisitions with controlled contrast thanks to the leverage offered by the FA. A short repetition time is often appreciated in MRI, especially in 3D imaging where it is not possible to interleave the acquisition of subsequent slices; a long TR is therefore

synonymous with unavoidable dead time and inefficient sequence.[4] Different contrasts can be obtained: proton-density-weighted (PDw), T_1w or T_2w. T_1 weighting will be useful throughout this thesis for contrast-agent-injected imaging (section 1.4 and chapters 5 and 6). However, GRE-based sequences cannot achieve pure T_2 weighting. This is why spin-echo-based sequences, described below, are very common in MRI.

1.2.2 Fast Spin-Echo Sequences

Conventional Spin Echo

The conventional spin-echo (SE) [Hahn 1950b], whose kernel is illustrated in fig. 1.9 for a 2D Cartesian sampling, allows to address different contrasts depending on the TE and TR used: proton-density-, T_1- or T_2-weighting. After a 90° excitation pulse along the x axis, the spins dephase gradually, due to field inhomogeneities and spatially-encoding gradients. Then, applying a 180° refocusing pulse along the y axis at time TE/2 reverts the phase evolution. Spin phases keep evolving as before, but the faster-dephasing ones are now behind the slower ones, such that after another TE/2, all spins are in-phase again. This produces an echo at a time TE after the initial RF pulse. Since all dephasing spins were affected (not only the ones we dephased with the encoding gradients), dephasings induced by B_0 offsets (due to magnetic susceptibility disparities and small magnet defects) are also cancelled, which means that the echo amplitude is affected by T_2 decay, not T_2^*. This decay depends only on tissue properties, and is slower than T_2^*: longer echo times are achievable, and therefore T_2w imaging. It is also possible to acquire multiple echoes for the same k-space line, in order to obtain several contrasts simultaneously [Feinberg 1985]. SE signal for a given TE and TR is given by:

$$S_{\text{SE}} = k \text{ PD } (1 - \text{E}_1) \text{ E}_2, \quad \text{with } \text{E}_2 = \exp\left(-\frac{\text{TE}}{\text{T}_2}\right) \tag{1.22}$$

One can notice, in fig. 1.9, the additional gradient lobes (in dark grey) on G_{Slice} around the slice-selection gradient, applied along with the refocusing pulse. Those are called a 'crusher pair' [Bernstein 2004]. Their role is to get rid of any FID following the refocusing pulse, that may arise in case of an imperfect 180° due to field inhomogeneity. One could also deliberately use a FA lower than 180° to reduce the energy (SAR) deposited in the patient (*cf.* chapter 2).

One issue with T_2 imaging, however, is the need for a long TR to remove the influence of E_1 in eq. (1.22). This implies a long dead time after each line acquisition, during which the system waits for longitudinal recovery before repeating the kernel for another k-space line. In 2D imaging, one way to profit from this dead time is to perform an 'interleaved' acquisition: after acquiring a line within one slice, and while waiting for magnetisation recovery in this slice, we can excite a different slice (in which magnetisation is still pristine) and acquire the equivalent line in it. We can repeat this process with as many slices as

[4] This is particularly true in non-selective 3D imaging: in case of multi-slab imaging, with slab-selective excitation, one can interleave the different slabs. This is very limited however, as only a few slabs are generally used (two or three).

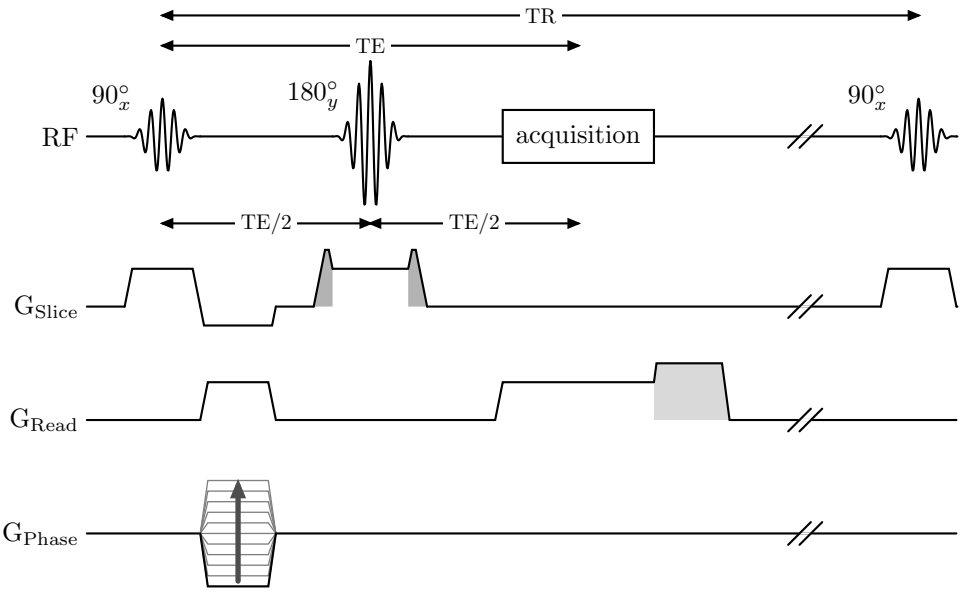

Figure 1.9: 2D conventional spin-echo (SE) sequence diagram. Notice the gradient crusher pair (dark grey) to remove any unwanted FID in case of an imperfect 180°. A gradient spoiler (light grey) is often used to suppress transverse magnetisation, especially when TR is small compared to T_1.

needed, until the required TR is reached, thus saving a lot of dead time and accelerating the sequence. In clinical routine 2D acquisitions, though, slice thickness is coarse compared to in-plane resolution: there are generally many more lines than slices. For instance, for brain imaging at 3 T, a typical T_2 protocol could be the following: TR = 5000 ms, TE = 100 ms, 25 slices of 5.0 mm thickness, and $(0.5 \times 0.5)\,\mathrm{mm}^2$ in-plane resolution (350×450 matrix) [Springer 2016]. With such parameters, acquiring all slices in a row would take about 2500 ms, which would largely fit in one TR. However, there remains an equally long dead-time before the end of the TR: half of the sequence is wasted.

Another limitation is that interleaving cannot be applied to 3D imaging, as in this case the whole imaging volume is excited and refocused for each line and partition. This is why conventional SE imaging, though possible in 3D, is only used for 2D imaging in practice.[5]

Fast Spin-Echo

Given the number of phase lines involved, one could wish to acquire several refocused lines in sequence after an excitation. A different approach to reduce the dead time inherent to T_2 imaging was introduced by Hennig *et al.* in 1986 under the acronym RARE (rapid acquisition with refocused echoes) [Hennig 1986]. This technique was later tuned and refined, and gave rise to commercial sequences known as fast spin-echo (FSE) or turbo spin-echo (TSE).

It is illustrated in its original 2D form in fig. 1.10a, to encode one slice. Similarly to

[5] In T_1w SE, one could lower the flip angle to reduce TR as done in the FLASH sequence, but here we are considering T_2 imaging.

the conventional SE, a 90° excitation pulse is played, followed by a 180° refocusing pulse after a time ΔTE/2. Gradients G_{Phase} and G_{Read} encode locations in phase and frequency to acquire a k-space line during a spin-echo whose peak occurs at a time ΔTE after the initial 90° pulse. Then the refocusing pulse is repeated at regular ΔTE intervals, and successive echoes are acquired. A different phase-encoding gradient is used each time, so that several or all k-space lines corresponding to the selected slice are encoded.

The original RARE sequence, in which all lines are acquired during a refocusing train, suffers from the fact that for a large number of phase-encoding steps, there is a significant difference in signal intensity between the lines acquired at the beginning and at the end of the echo train, due to T_2 decay. As a rule of thumb, one can consider that the contrast of the image is defined by the lines at the centre of the k-space (low spatial frequencies), while the border of the k-space (high frequencies) corresponds to image sharpness. T_2 contrast of a FSE sequence is therefore characterised by a so-called 'effective TE' (TE_{eff}), the time at which the central line is encoded. Echoes acquired towards the end of the echo train generally correspond to high-order phase encoding steps. Because of T_2 decay, image blurring is observed [Sze 1993]. Indeed, signal is getting weaker along the echo train, which weights spatial frequencies with a decreasing exponential function. In image space, this translates into a bell-shaped point spread function, which means a point in the object appears with a Gaussian blur in the image. ΔTE is called echo spacing, and is chosen as short a possible to condense the echo train, so that the difference in T_2 weighting between early and late echoes is not too important. Echo spacing is however limited by gradient performance, RF pulse length and energy constraints. Achievable ΔTEs are around 3 ms for selective refocusing. Acquiring 350 lines as described above would take 1 s, which is for instance ten times as long as the T_2 of grey matter (*cf.* table 2.1 on page 48). Because of its extreme T_2 weighting, this sequence is well suited for highlighting cerebrospinal fluid (liquid, $T_2 \approx 2000$ ms), but not for visualising more subtle T_2 contrast.

In order to overcome those limitations, most modern implementation of the FSE sequence do not encode a whole slice in one train, but rather distribute it across several TRs. The 'useable' time for echo acquisition being about 100 ms after excitation [Li 2003], it is possible to acquire some 30 phase steps at a time. The number of echoes acquired in one TR is called the echo train length (ETL). Of course, interleaving can be applied to make use of the remaining dead time. But once again, this is only possible in 2D imaging. Taking advantage of the isotropic resolution offered by 3D MRI requires to find a way to stretch the useable time, in order to lengthen the ETL. This is what the SPACE (sampling perfection with application-optimised contrasts using different flip angle evolutions) sequence does.

Before moving to the next section, it is important to notice that it is possible to obtain such a train of echoes even with imperfect 180° RF pulses, by respecting a set of conditions, known as CPMG [Carr 1954, Meiboom 1958]:

1. The refocusing pulses must be 90° out of phase with respect to the excitation pulse (as pictured by the indices x and y on fig. 1.10), and evenly positioned with equal spacing between any two consecutive pulses; this spacing must be twice the one

between the excitation pulse and the first refocusing pulse.

2. The phase accumulated by a spin isochromat between any two consecutive refocusing pulses must be equal. This means that any introduced B_0 gradient must be compensated before the end of the kernel.
3. If a pulse has a non-uniform yet smooth phase distribution across the sample, then all other pulses must share the same phase pattern to fulfil both previous conditions everywhere.

Indeed, due to field inhomogeneity or pulse imperfections, the 180° target is not necessarily achieved. In addition, the flip angle of refocusing pulses can be purposely reduced in order to limit energy deposition in the patient (*e.g.* 150° FAs are often used).

SPACE: a 3D Variable Flip Angle FSE

The idea behind 3D FSE sequences is to maintain a useable signal for as long as possible by making use of stimulated echoes in addition to the spin echoes described above, thanks to non-180° refocusing pulses. Here we will consider that the CPMG conditions described above are respected.

Let us have a look at the effect of a pulse on magnetisation of any initial orientation. To follow the evolution of magnetisation, we introduce some notations. An index 0 denotes a longitudinal component (M_z in eq. (1.3)), which regrows towards M_0 during free precession (*i.e.* when no RF pulse is applied). The index 1 denotes a transverse magnetisation component ($M_\perp$ from eq. (1.10)), which dephases under the influence of field inhomogeneity or/and encoding gradients. In addition, the index -1 corresponds to a transverse magnetisation component that rephases during free precession ($M_\perp^*$, the symbol '*' denoting complex conjugation). The history of the evolution of various magnetisation components is remembered as a series of indices. The action of a pulse on some initial magnetisation M, described by Woessner *et al.* [Woessner 1961] and Kaiser *et al.* [Kaiser 1974], is to split it into the three components described above. The weight of each component depends on the pulse's flip angle α:

- a fraction $\cos^2(\alpha/2)$ of M remains unchanged, *e.g.* if M is initially longitudinal (M_0 with the introduced notations), this fraction corresponds to the amount of longitudinal magnetisation after the pulse: $M_0 \to M_{0,0}$
- a fraction $\sin^2(\alpha/2)$ of M is inverted, *e.g.* if M is initially transversal (M_1 or M_{-1}), this corresponds to the amount of magnetisation that sees its phase inverted: if it was dephasing, it is now rephasing ($M_1 \to M_{1,-1}$)
- a fraction $\sin\alpha$ of M is tipped orthogonally to its initial orientation: if M was initially longitudinal (M_0), it is now partly tipped into the transverse plane, rephasing and dephasing in equal parts ($M_0 \to M_{0,1}$ and $M_0 \to M_{0,-1}$); if M was already in the transverse plane (M_1 or M_{-1}), it partly becomes longitudinal ($M_1 \to M_0$ or $M_{-1} \to M_0$).

This framework defines 'phase coherence pathways', *i.e.* the history of the different magnetisation components, that allow to predict easily the formation of echoes, considering

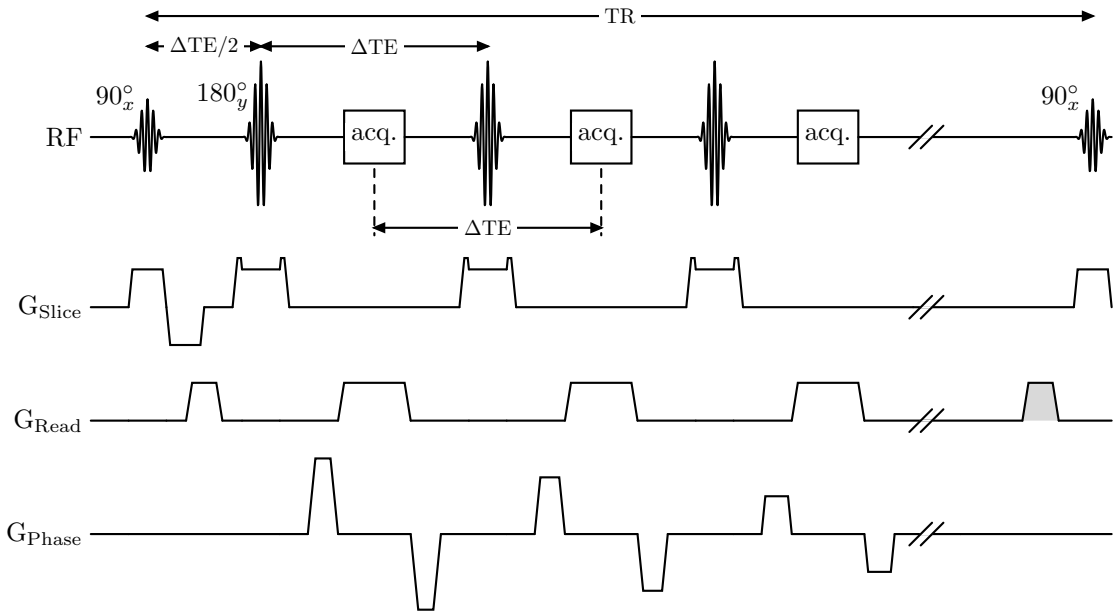

(a) 2D FSE sequence.

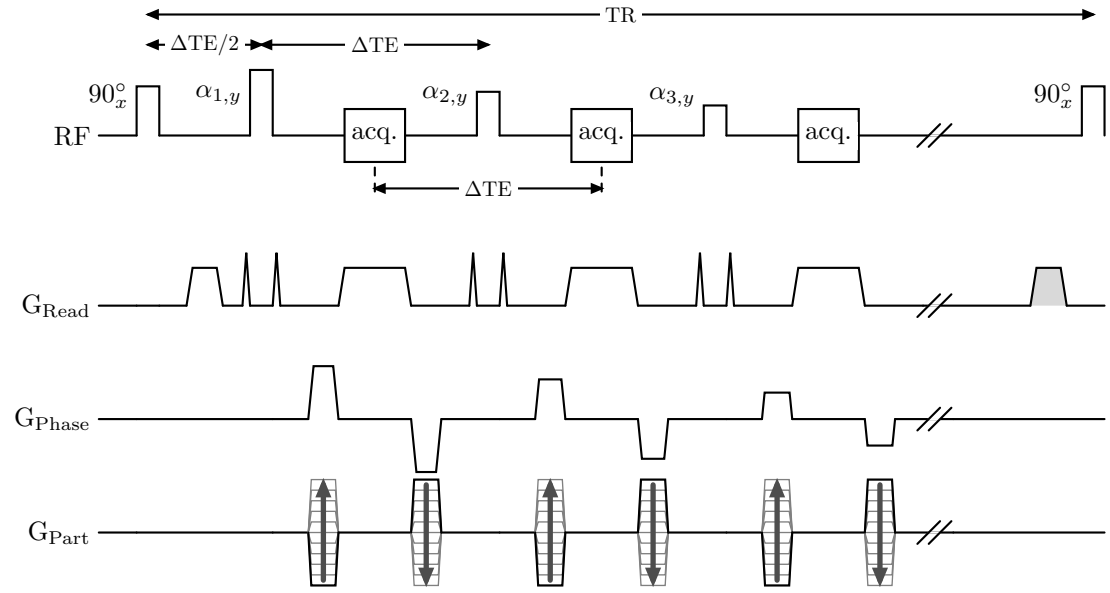

(b) 3D FSE sequence with variable FA, also called SPACE.

Figure 1.10: Timing diagrams for two typical fast spin-echo (FSE) sequences, respectively used for (a) 2D and (b) 3D imaging. Notice in both cases the crusher gradient pairs on G_{Read} (like in fig. 1.9), to get rid of undesired FIDs induced by the non-180° refocusing pulses (b) or imperfect 180° (a), and the gradient spoiler (grey) to ensure that magnetisation is fully longitudinal before every 90° pulse.

we respect the CPMG conditions, especially the first one.

As a first simple example, using a perfect 180° pulse allows to simplify this decomposition: the first and last fractions boil down to 0, and only the second component remains: $\sin^2(180°/2) = 1$. This confirms the purely refocusing property of a 180° pulse: all M_1 becomes $M_{1,-1}$ and vice-versa.

The simple spin-echo process introduced in the beginning of this section can be described as follows. Initial magnetisation is fully along M_0 so when a 90° pulse is applied, all magnetisation is tipped into the transverse plane (the two first components cancel out, only the '$\sin\alpha$' term remains): $M_0 \rightarrow M_1$. Then a 180° refocusing pulse is applied at time TE/2 after excitation, that will generate $M_{1,0}$, $M_{1,1}$ and $M_{1,-1}$[6]. The last one will produce a spin-echo at time TE, as dephasing occuring along the first half of the pathway has been rephased during the second half and is homogeneous again.

The '$\sin\alpha$' fraction of the decomposition ($M_{1,0}$ in the example above) is particularly interesting, as it shows that dephasing or rephasing magnetisation can be 'stored' in a longitudinal state, to be later 'recalled' by a subsequent pulse to form what is called a 'stimulated echo'. For instance, the following pathways produce echoes at time $t = 2\text{TE}$ and $t = 3\text{TE}$ respectively: $M_{1,0,-1}$ and $M_{1,0,0,-1}$. Interestingly enough, several pathways can produce echoes at the same time. For instance, $M_{1,-1,-1,1}$ and $M_{1,1,-1,-1}$ also refocus at $t = 3\text{TE}$. This suggests that a high signal can be maintained for a long time, despite T_2 decay, by determining a succession of non-180° refocusing pulses to create controlled combinations of different spin- and stimulated-echoes.

As more pulses are applied, the number of possible pathways increases exponentially: Hennig has introduced the extended phase graph (EPG) formalism, which allows to keep track of the coherence pathways that can produce echoes at specific times [Hennig 1991, Weigel 2015]. This has inspired, among other techniques, the SPACE sequence [Mugler 2000, Busse 2006, Mugler 2014]. With even spacing of pulses (CPMG №1) and by carefully calculating the pulse train, one can combine spin echoes and stimulated echoes to extend the ETL up to 100 or 150. The SPACE sequence allows to encode significant portions of the k-space (sometimes even an entire partition plane) during a TR, thus reducing the acquisition dead time, making 3D FSE possible in clinical routine. To do so, a variable flip angle train is calculated, that depends on sequence parameters (TR, echo-spacing, desired effective TE) and expected tissue T_1 and T_2. The SPACE kernel is pictured in fig. 1.10, and a typical example of flip angle train is represented in fig. 1.11, along with a comparison between 2D and 3D acquisitions.

SPACE will be the sequence used in chapter 4 for T_2 imaging, in conjunction with a 'SPAIR' module for fat suppression. Questions related to fat and the suppression of its signal are the subject of the next section.

[6] We now start keeping track of the indices only after the first refocusing pulse, when spacing between pulses starts being even: the initial '0' index does not appear in the notation.

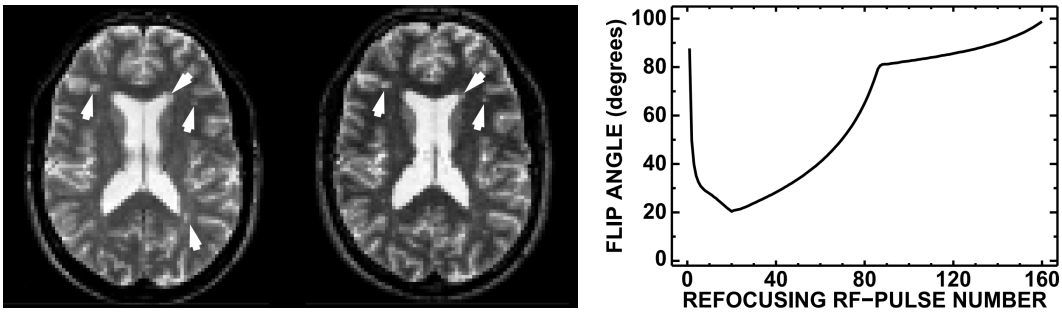

(a) 2D SE (left) and 3D SPACE (right) (b) Variable flip angle train

Figure 1.11: SPACE sequence acquisition and associated flip angle train. (a) Comparison between a 2D slice (thickness: 3 mm) acquired with a conventional spin echo sequence, and a 3D partition (1 mm) from a SPACE acquisition. Arrowheads point to white matter lesions. (b) Variable flip angle train used in the SPACE sequence. The 160-echo train allowed to encode each partition (160 phase lines) in one TR. Notice how the FAs are all much below 180°, with values as low as 20°. Illustration from [Mugler 2000].

1.3 Fat Suppression

Since the beginning of this chapter, we have considered the imaging of ^{1}H nuclei belonging to a single chemical compound. However, depending on their surrounding chemical structure, *i.e.* the molecules they are part of, those nuclei behave differently. In the body, ^{1}H NMR signal mostly arises from two compounds: free water molecules and lipids.

For most tissues, signal from either water or fat generally prevails. For instance, muscle or brain tissues are mostly water-based, while visceral and sub-cutaneous regions are dominated by fat. In some tissues however, water and fat are both present and mixed. This is the case, for instance, for bone marrow, liver with steatosis (see section 1.4.2) or breasts where glandular and fat tissues are sometimes finely intertwined (see section 1.4.2). Since we will later focus on the two latter regions, it is important to briefly review the effect of a mix of water and fat in tissues, as well as some techniques that allow to differentiate them.

1.3.1 Cohabitation of Fat and Water Tissues

Relaxation Properties

Relaxation times T_1 and T_2 of tissues depend on the mobility of the molecules that compose them, and on the efficiency of energy exchange between those molecules and their environment [Bottomley 1984]. As a consequence, one can expect a difference in relaxation times between large, bulky macromolecules that constitute fat, and small, nimble molecules such as free water.

The T_1 of fat tends to be shorter than that of water-based tissues, which leads to a hyper-signal in T_1w imaging. As we will see later on, in section 1.4 and chapters 5 and 6, this can be a problem in sequences that rely on contrast agent injection. In those T_1w sequences, a gadolinium-based agent is injected, that decreases the apparent T_1 of tissues

(*cf.* section 2.1.1). The obtained value is very close to the T_1 of fat: fat signal is barely discernible from that of injected tissue and should be removed. When comparing images before and after injection, a straightforward way to remove fat hypersignal is to subtract images. Accuracy of this method is however heavily challenged in case of patient motion, and cannot be applied in the abdomen, for instance, due to breathing.

T_2 of fat is longer than that of most water-based tissues, which leads to a higher signal for fat in T_2w images. For instance, in breast imaging (section 1.4.1 and chapter 4) this high signal emanating from fat can hinder the analysis of glandular (water-based) tissues. Fat suppression is indicated in those cases.

The difference in relaxation time between fat and water gave rise to a popular fat suppression technique described in section 1.3.2: STIR.

Chemical Shift

The electronic environment of hydrogen protons depends on the chemical structures they belong to, and induces local magnetic field variations. This means that the resonance frequency of a spin depends on its chemical environment. This phenomenon is referred to as chemical shift, and measured in parts per million (ppm) from a reference[7]. For instance, the chemical shift is 4.7 ppm for water, and is 1.3 ppm for the dominant component of fat. Figure 1.12 represents an example of spectrum of the different resonance frequencies found in tissues.

Considering the difference in chemical shift between water and the main component of fat is about 3.5 ppm and that the RF central frequency is tuned to resonate with water, this corresponds to a difference in precession of about 440 Hz at 3 T, with fat precessing slower than water. This difference in frequency corresponds to a period of about 2.3 ms. What follows from this is that during free precession, water and fat components in a voxel will be in phase (IP) every $t_{\mathrm{IP},n} = n\ 2.3\,\mathrm{ms}$, n being a positive integer, and fully out of phase (OP) every $t_{\mathrm{OP},n} = (n+\frac{1}{2})\ 2.3\,\mathrm{ms}$. Signal resulting from the water-fat mix fluctuates in time as shown in fig. 1.13: depending on the TE chosen, water and fat signal can either add up ($\mathrm{TE_{IP}}$) or cancel out ($\mathrm{TE_{OP}}$).

The chemical shift, as we will see in section 2.1.2 can be a source of artefacts that can sometimes justify the need for fat suppression. But it is also an interesting property used by spectral fat suppression techniques introduced below, such as CHESS, water excitation and Dixon.

1.3.2 Fat Suppression Techniques

Fat Saturation

One approach to suppressing fat signal based on its chemical shift, is widely known as 'fat saturation', or by its original acronym: chemical-shift-selective fat suppression

[7] By convention, the 0 ppm reference is the ^{1}H resonance of tetramethylsilane (TMS) [Harris 2001].

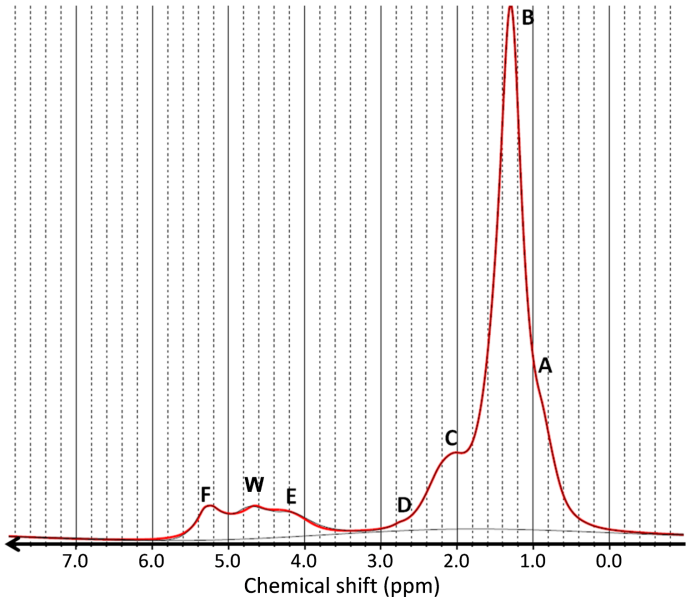

Figure 1.12: Example of a resonance frequency spectrum acquired in the bone marrow in the calcaneum. From [Le Ster 2017]. The tissue was mostly fatty, so the water peak (W) at 4.7 ppm is low. We can clearly see several peaks associated with fat (A–F). The dominant fat peak (B) is at 1.3 ppm. *Note*: NMR spectra are shown with increasing ppm from right to left; in the rest of this document, frequency plots will follow the MRI convention, with increasing frequencies from left to right.

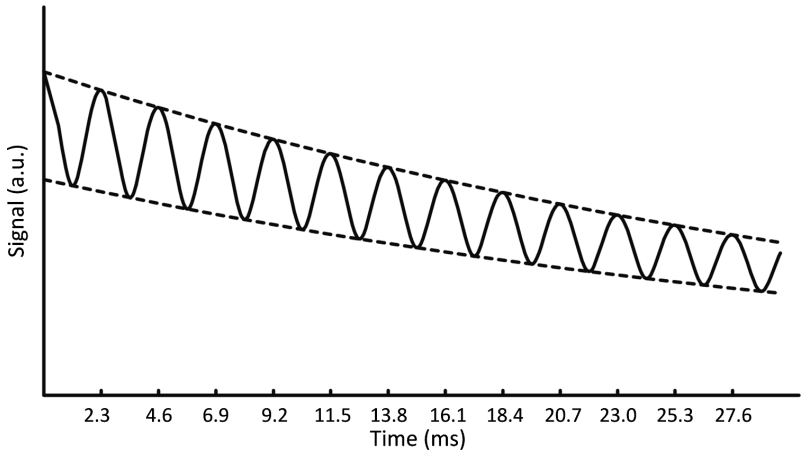

Figure 1.13: Fluctuation of the combined signal of water and fat as a function of time. Markings indicate times at which water and fat subject to the same field are in phase (IP) at 3 T. Adapted from [Haacke 1999].

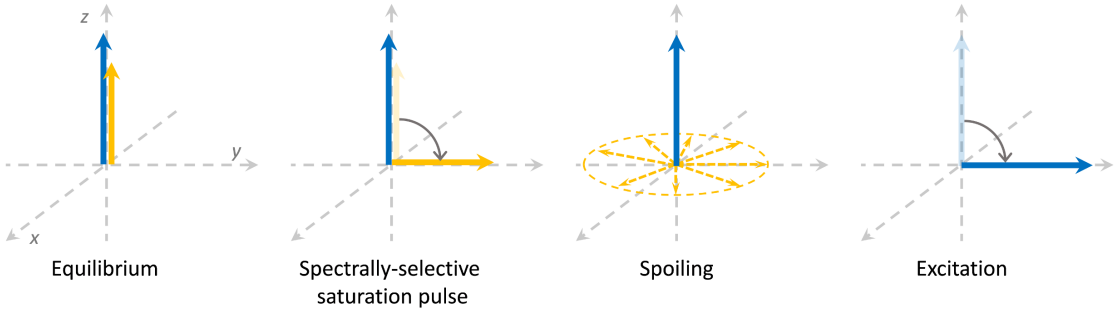

(a) CHESS: fat is selectively saturated and spoiled, so only water magnetisation remains.

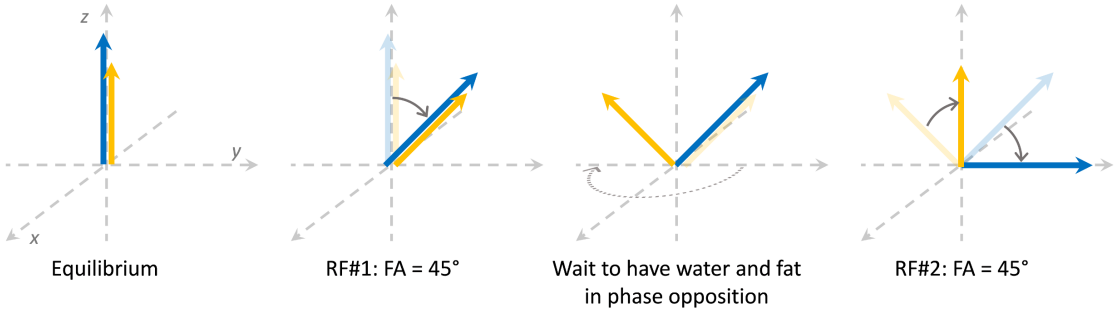

(b) Water excitation: example of 90° excitation with a 45°–45° binomial pulse.

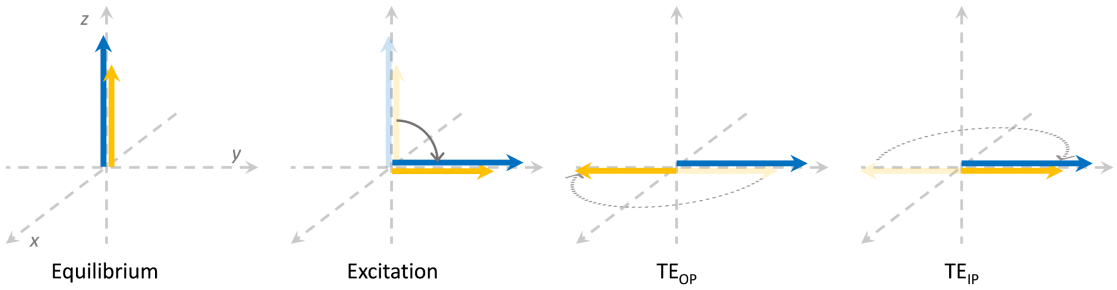

(c) Two-point Dixon: both water and fat are excited, signals cancel out on first echo (they are in phase opposition), and signals add up on second echo (they are in phase).

Figure 1.14: Fat suppression techniques based on chemical shift. Blue arrow = water, yellow arrow = fat.

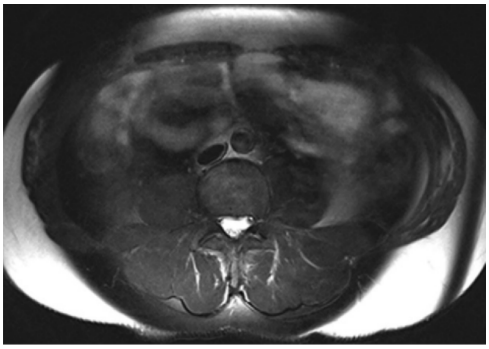

(a) CHESS fat-suppression on a T_2-weighted image, showing incomplete saturation of sub-cutaneous fat due to B_0 inhomogeneity [Del Grande 2014].

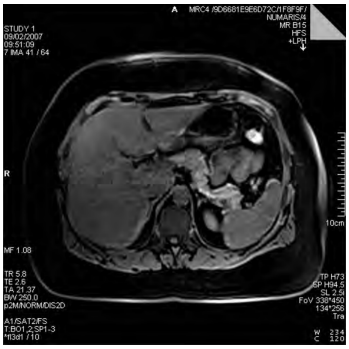

(b) T_1-weighted 3D FLASH with quick-fat-saturation, acquired in one breath-hold [Horger 2007].

Figure 1.15: Images acquired with CHESS-based fat suppression. Note that the two images shown are not meant to be compared: the standard fat saturation (a) works better than the 'quick' one (b) when performed in the same B_0 homogeneity conditions.

(CHESS) [Haase 1985]. The principle is to selectively excite a band of frequencies corresponding to fat with a frequency-selective 90° pulse, followed by a spoiler gradient similar to the one described in section 1.2.1 and fig. 1.8, that dephases the induced fat transverse magnetisation so that all phase values are present in each voxel, thus cancelling it. This is depicted in fig. 1.14a. After that fat suppression module, the usual sequence kernel is played normally, but impacts only water isochromats, at they are the only ones with non-zero net magnetisation. Usually, a Gaussian-shaped pulse is used, with a central frequency shifted by $-440\,\mathrm{Hz}$ (at $3\,\mathrm{T}$) from f_0, and with a bandwidth narrow enough to avoid impacting water, but wide enough to select a sufficient range of fat resonating frequencies (to account for B_0 inhomogeneity).

One advantage of fat saturation is that it has no impact on water-based tissue contrast. Drawbacks include sensitivity to B_0 (*cf.* fig. 1.15a) and B_1^+ inhomogeneity, more pregnant at high field (section 2.1.2) that can reduce the effectiveness of the fat-selective module. Also, significant time is added to the sequence in order to play the RF pulse and the spoiler gradient (about 10 ms per repetition). A consequence is that very small TR values cannot be achieved, which is a problem for T_1w FLASH imaging, and that TA is necessarily longer, preventing breath-hold explorations.

To alleviate the impact of CHESS on TR and TA, the 'quick fat-sat' method [Le 2012] was introduced. It consists in playing the fat-suppression module not on every TR, but only once or twice per imaged slice (in 2D) or partition (in 3D). It now has minimal effect on TA, no effect on TR (except in that it disturbs the steady-state), but at the expense of fat suppression quality. This is the fat suppression method used in conjunction with FLASH for fast T_1-weighted imaging of the abdomen in chapters 5 and 6. An example of image obtained with quick-fat-saturation is shown in fig. 1.15b.

Water Excitation

Water excitation [Levitt 1986, Hauger 2002] is another technique based on the chemical shift between fat and water. In particular, it exploits the dephasing that occurs between the two compounds after excitation, as water protons precess slightly faster than fat ones. The idea, described in fig. 1.14b, is to excite both water and fat with a pulse producing half the desired flip angle (*e.g.* 45° instead of 90°), then to wait for water and fat to be completely out of phase (about 1.15 ms at 3 T) before applying the same half-FA pulse. Water isochromats are tipped to the desired angle, while the second pulse cancels the effect of the first one for the dephased fat spins.

Several comments can be made. Firstly, any pulse can be used to achieve this effect: either selective or non-selective. In the former case, water excitation can be described as a 'spatial-spectral' selection technique. Secondly, the suppression (or rather the *non-excitation*) of fat is very resilient to B_1^+ field inhomogeneity. Indeed, even if the target FA is not reached, the effect on fat is the same as long as the second pulse is the same as the first one. Lastly, water excitation is however by nature very sensitive to static field inhomogeneities, which affect locally the precession frequency of spins. The spectral selectivity can be improved by using more advanced series of pulses. Any binomial combination (1–1, 1–2–1, 1–3–3–1, ...) can be used. Here we have described the 1–1 pulse, but one could achieve 90° with 22.5°–45°–22.5° excitation. The longer the combination, the better the fat suppression. In practice, mostly 1–1 and 1–2–1 pulses are used, to avoid lengthening TR too much.

Dixon

The Dixon method [Dixon 1984] also takes advantage on dephasing between fat and water, but during reception, not excitation. The two-point Dixon principle is exposed in fig. 1.14c. All compounds are excited without distinction, then two echoes are acquired: one when water and fat have their phases opposed (TE_{OP}), the other one when they are in-phase (TE_{IP}). Indeed, we have seen that signal from voxels containing both water and phase fluctuates with time as the phases add up or cancel out (fig. 1.13). Two images are obtained, as shown in figs. 1.16a and 1.16b. Let us denote by S_{IP} and S_{OP} in-phase and opposed-phase signals, respectively, and by S_w and S_f the contributions of water and fat to signal:

$$\begin{cases} S_{IP} = S_w + S_f \\ S_{OP} = S_w - S_f \end{cases} \tag{1.23}$$

Calculating water and phase signals from IP and OP images is straightforward:

$$\begin{cases} S_w = \dfrac{S_{IP} + S_{OP}}{2} \\ S_f = \dfrac{S_{IP} - S_{OP}}{2} \end{cases} \tag{1.24}$$

Figures 1.16c and 1.16d show reconstructed water and fat images.

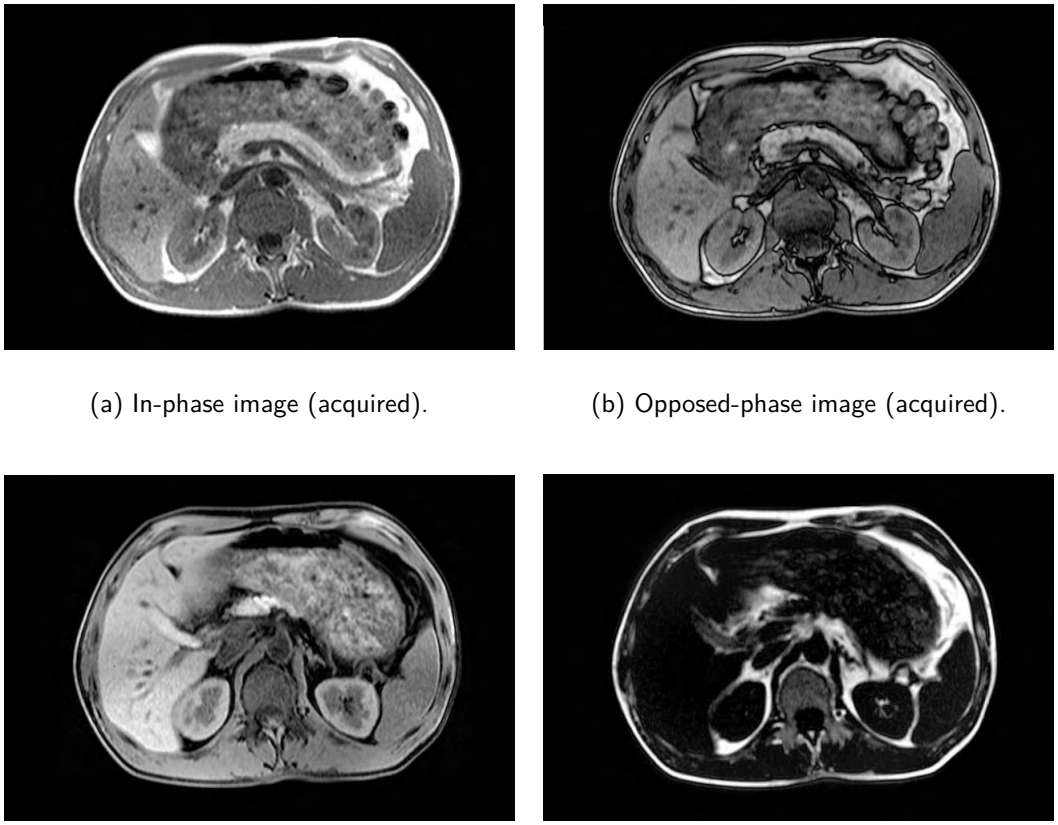

(a) In-phase image (acquired).

(b) Opposed-phase image (acquired).

(c) Water image (computed).

(d) Fat image (computed).

Figure 1.16: Images obtained using the Dixon water-fat separation technique.

This is valid as long as the static field is considered perfectly homogeneous. In general, an extra dephasing term is added to eq. (1.23), and the absolute value of the sum or difference of S_{IP} and S_{OP} must be taken in eq. (1.24). This means that this simple reconstruction fails when B_0 is too inhomogeneous (field inhomogeneity is discussed in section 2.1). Several methods have been proposed to solve this issue, among which the three-point Dixon [Glover 1991, Reeder 2007] that adds a third (in-phase) echo. This can be a problem when TR is desired as short as possible, *e.g.* in T_1w FLASH imaging.

Another way is to determine and remove the extra phase term using a region-growing algorithm [Ma 2004]. Starting from a seed voxel, the phase evolution is progressively analysed, so that 2π shifts corresponding to phase wrapping can be unwrapped.

In its modern implementation, the Dixon acquisition and reconstruction method has many advantages: it is insensitive to both B_0 and B_1^+ field inhomogeneities, and it provides more information than fat suppression techniques as a total of four images is provided. One slight drawback is that it lengthens the minimal TR achievable in T_1 sequences since at least two echoes are needed. Note that a single-point Dixon reconstruction has also been investigated, based solely on region-growing phase unwrapping [Ma 2008].

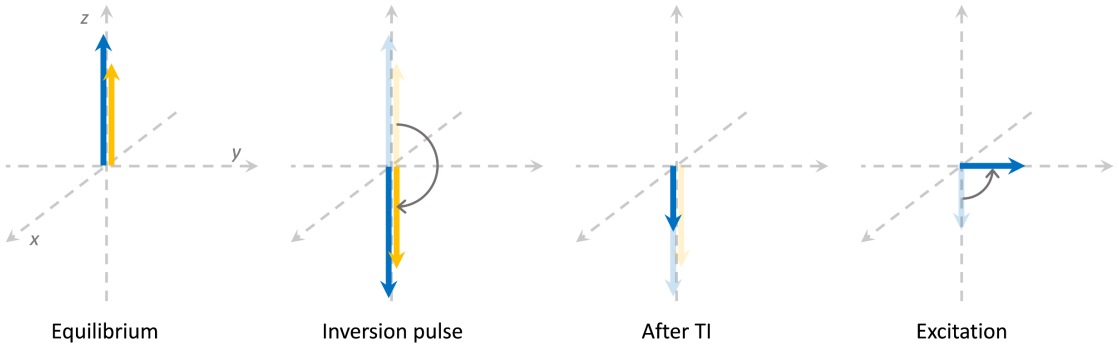

(a) STIR: both water and fat signals are inverted with a non-selective 180° pulse; acquisition begins after the inversion time (TI) that nulls fat magnetisation (shorter T_1). However, contrast in water tissues is changed as excited magnetisation is reduced.

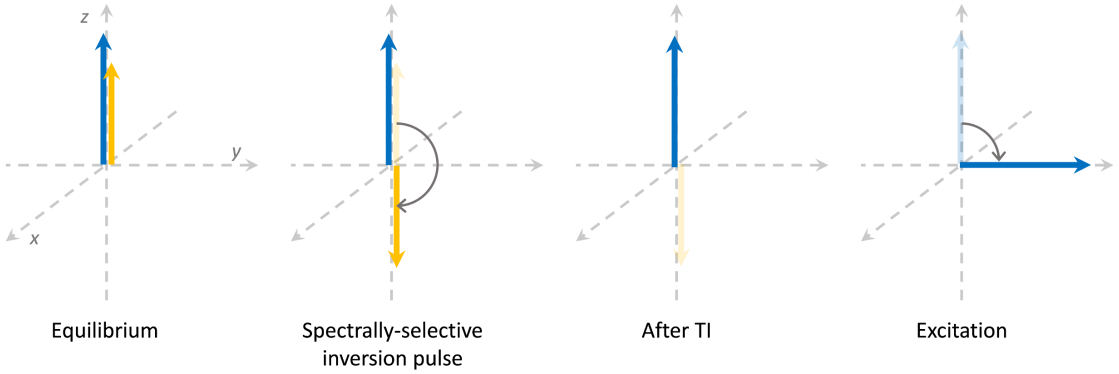

(b) SPIR and SPAIR: only fat magnetisation is inverted by the spectrally-selective 180° pulse. Fat signal is nulled at TI like in (a), but contrast in water tissues is unchanged compared to a non-fat-suppressed sequence.

Figure 1.17: Fat suppression techniques based on (a) relaxation only, and (b) on both relaxation and chemical shift. Blue arrow = water, yellow arrow = fat.

STIR, SPIR and SPAIR

STIR (for 'short TI inversion recovery'), introduced by Bydder and Young [Bydder 1985], makes use of the short T_1 of fat to suppress its signal, as sketched in fig. 1.17a, and is often used in T_2 imaging. A 180° preparation pulse reverses magnetisation for all tissues. A relaxation period ensues, during which fat recovers towards equilibrium more quickly than water, due to its shorter T_1. After a waiting time, called inversion time (TI), fat magnetisation is zero, while that of water still points towards $-z$.[8] At that instant, before fat recovers further towards $+z$, the imaging sequence can start. When the excitation pulse is played, only water isochromats are tipped towards the transverse plane, so fat cannot produce any signal.

[8] To suppress signal for fat, an inversion time $\mathrm{TI} = T_{1,\mathrm{fat}} \times \ln 2$ is chosen. This comes from eq. (1.25), when considering that $\mathrm{TR} \gg T_{1,\mathrm{fat}}$.

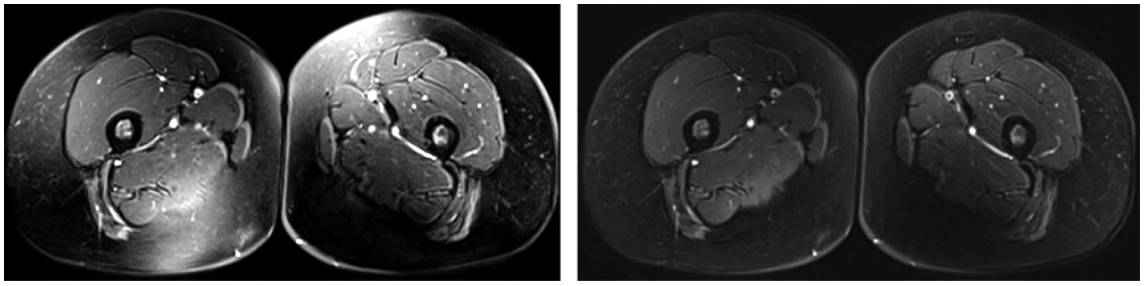

Figure 1.18: Comparison between CHESS and SPAIR fat suppression in the presence of B_1^+ inhomogeneity: in this case, fat is suppressed more uniformly with SPAIR. As we will see in chapter 2, such artefacts often occur in the thighs (*cf.* fig. 2.7). Both images are T_2w and show the same slice in the same subject. From [Del Grande 2014].

Since it does not rely on chemical shift, fat suppression using STIR is robust to local B_0 inhomogeneity. However, it involves an intricate relationship between TR and TI. Indeed, if the signal is recorded by a spin-echo sequence (for instance), the SE signal equation from eq. (1.22) becomes:

$$S_{\text{STIR}} = k \text{ PD } (1 - 2\exp\left(-\frac{\text{TI}}{\text{T}_1}\right) + \exp\left(-\frac{\text{TR}}{\text{T}_1}\right)) \text{ E}_2 \tag{1.25}$$

Magnetisation of other tissues is affected, as shown in fig. 1.17a, which has an impact on signal, but also on contrast between water-based tissues: those with a shorter T_1 regrow faster after the inversion pulse, which means they produce a lower signal. A 'reversed' T_1 contrast adds to the desired T_2 weighting, and must be handled with care. One final limitation is that STIR cannot be used in sequences following contrast agent injection: STIR suppresses all tissues with a T_1 close to that of fat, which includes gadolinium-injected tissues.

Spectral presaturation with inversion recovery (SPIR) [Kaldoudi 1993] is a hybrid fat suppression method similar to STIR, but which affects only fat tissues, and thus respects 'traditional' contrasts. In SPIR (fig. 1.17b), the preparation 180° pulse is spectrally selective, and adjusted to the frequency of fat. Because of its frequency-specific pulse, this method is sensitive to both B_0 and B_1^+ inhomogeneity. A further improvement is spectral adiabatic inversion recovery (SPAIR). It is almost identical to SPIR, but uses an adiabatic inversion pulse [Bernstein 2004] for preparation. Such a pulse is fairly insensitive to B_1^+ inhomogeneity (*cf.* chapter 2), thus ensuring homogeneous suppression of fat. Figure 1.18 shows a comparison between SPAIR and CHESS in a region affected by B_1^+ inhomogeneity. It can however fail, like SPIR and CHESS, when B_0 is strongly inhomogeneous.

1.4 Some Targeted Clinical Applications

In this section we make a short description of two regions in which B_1 artefacts are commonly observed (*cf.* chapter 2), and that will be at the core of the part II of this thesis: the breasts and the liver.

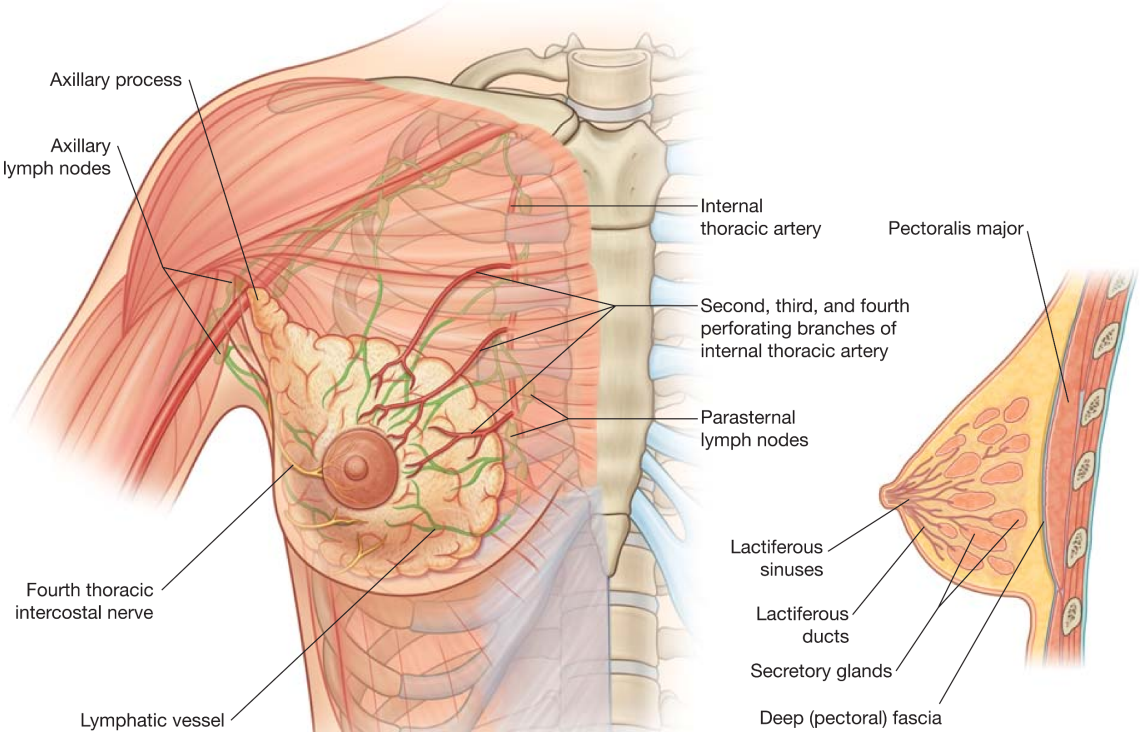

Figure 1.19: Anatomy of the breast. Illustration from [Drake 2009].

1.4.1 Breast MRI

Basic Breast Anatomy

Breasts are mostly constituted of adipose and glandular tissues, as pictured in fig. 1.19. The female adult breast normally contains about 15 irregular secretory glands producing milk, that converge at the nipple via lactiferous ducts. The ratio between fat and glandular tissue varies widely between women and depends on whether the individual is lactating or not.

The lymphatic system[9] (in green on fig. 1.19) is of great importance in breast imaging. Indeed, breast cancer is common in the mammary gland, and cancerous cells can metastasise to other parts of the body through the lymphatic system. Most of the lymph from the breast travels through the axillary lymph nodes on the same side of the body (the rest goes through the parasternal nodes, or to the other breast). This means that before reaching distant regions, metastases can be found in those nodes: it is therefore crucial to examine them during a breast MRI investigation.

Breast Imaging Challenges

Fat Suppression Breast pathologies occur within water-based tissues. However, the surrounding fatty tissues produce strong signal intensity, with a potentially harmful im-

[9]The lymphatic system is a subsystem of the circulatory system, consisting of a complex network of vessels, tissues and organs. It transports lymph, that helps maintain fluid balance in the body and helps defend the body against infection by providing lymphocytes. *Source: Encyclopædia Britannica.*

pact, on T_1w or T_2w images, which are both at the core of the MR diagnosis of breast cancer. Indeed, breast tumours are characterised both by their relative higher T_2 signal and increased angiogenesis, and hence demonstrate increased signal following gadolinium chelates injection on T_1w injected sequences (see below, 'Breast MRI Indications & Protocol'). In some cases, fat signal must be suppressed, following methods described in section 1.3.2. Fat suppression, which is mandatory both in T_2w and T_1w with injection, can be challenging due to potentially large B_0 discrepancies (proximity of the lungs, large field of view). In addition, we will see later (part II) that for k_T-points pulse design, fat voxels can be discarded. This necessitates to create a mask corresponding to water voxels, which is quite difficult in the breast given that secretory glands can be small and are surrounded with fat. Those aspects will be studied in appendix A.

Large FOV As mentioned earlier, it is important to image lymph nodes around the breasts, which means that the FOV is large in the rostrocaudal (head to feet) direction: it should extend up to the axillary nodes (*cf.* fig. 1.19).

Motion Breathing is in general not an issue for breast imaging, as the patient is placed in prone position, on a dedicated breast coil (fig. 1.20a): breathing-related motion concerns only the back, and breasts do not move. Still, great care should be taken regarding motion artefacts induced by elements within the FOV: the back, lungs and most importantly the beating heart. Indeed, a moving part in the FOV propagates along the phase-encoding direction (as well as the partition-encoding direction in 3D MRI). In breast imaging, the acquisitions – whether in 2D or in 3D – are axial. Usually, in MRI, the phase-encoding direction is chosen to be the smallest dimension of the object, to minimise the number of required encoding steps, and therefore the acquisition time (usually in body imaging the anterior-posterior dimension is smaller than the left-right one). Following this principle in breast imaging would propagate motion artefacts towards the breasts. Therefore, the left-right direction is chosen instead for phase-encoding, and the anterior-posterior one for frequency-encoding. This explains the 'square' FOV of breast MRI images.

This consideration, combined with extension of the FOV to reach axillary nodes, and to the relatively fine resolution needed to image small structures makes breast acquisitions rather long.

Implants Finally, one specificity of breast imaging is the possible presence of breast prosthetics, either water- or silicone-based. In the latter case, it is important to know that the chemical shift between the protons in free water and those in silicone gel is about 4.7 ppm [Birkefeld 2003]. At 3 T, this corresponds to a -600 Hz precession frequency offset.

Breast MRI Indications & Protocol

Breast MRI is increasingly used in clinical practice fro breast cancer detection, staging and follow-up either alone or in combination with ultrasound imaging and mammography.

(a) Dedicated surface coil for breast imaging (here with 18 receive channels).

(b) So-called '60-channel' surface body coil: two 30-receive-channel phased arrays (anterior and posterior).

Figure 1.20: Surface coils proposed by Siemens for (a) breast imaging and (b) abdominal imaging. Illustrations from www.healthcare.siemens.com.

It is however indicated in several cases, especially when other techniques fail. Hence, it is now widely accepted that breast MRI is the reference imaging modality for breast cancer screening in patient with genetically demonstrated high risk for breast cancer; in addition, breast MRI is indicated for the precise staging of a primary breast cancer, especially before neoadjuvant chemotherapy and follow-up. Last, breast MRI can be indicated when ultrasound imaging and mammography remain undiagnostic. More recently, breast MRI has been increasingly used to follow patients with silicon implants [Luciani 2017]. A typical protocol includes:

1. A T_1w sequence, either GRE or TSE with a resolution as fine as possible to characterise lesion morphology.
2. A T_2w sequence either TSE (2D) or SPACE (3D), important to differentiate benign lesions (cysts, ganglions or fibroadenomas), and most importantly those that show enhancement in injected sequences (see last point), such as intra-mammary or axillary ganglions or some fibroadenomas. Indeed, malignant lesions tend to produce moderate T_2-hyperintensity, while most benign lesions show strong T_2 signal.
3. If silicone is present, specific sequences with silicone suppression and water suppression (using CHESS, with adapted frequencies).
4. The most important part of the protocol: dynamic contrast-enhanced (DCE) MRI with injection of gadolinium-based contrast agent. A T_1w FLASH sequence is acquired, then contrast agent is injected and the sequence is repeated five to seven times in order to characterise lesions via the temporal evolution of their perfusion. As mentioned before (section 1.3.1), fat suppression must be performed, as gadolinium-perfused tissues mimic the T_1 contrast of fat. A compromise has to be found between spatial and temporal resolution, so that fine details can be observed, while keeping the time between two consecutive acquisitions around 1 min.

1.4.2 Liver MRI

Basic Liver Anatomy

The liver is the largest organ in the human body. It is located within the peritoneal cavity, on the right, and surrounded by several other organs, as pictured in figs. 1.21 and 1.22: stomach, spleen, kidneys, gallbladder (not shown), pancreas (not shown). From fig. 1.22, we can see that the liver is located beneath the lungs (separated from them by the diaphragm): the presence of air can induce a significant B_0 gradient in the liver dome, just below the right lung. The beating heart and the air in the intestines can also cause artefacts, especially in the left liver.

As shown in fig. 1.23, the liver is irrigated by two afferent systems: the hepatic arteries and the portal veins, that bifurcate inside the liver to reach different regions, called segments. Segments are independent from each other in terms of vascularisation and function; for instance they can be removed independently in case of hepatic surgery. Radiologists often refer to segments to locate lesions within the liver. Blood leaves the liver through hepatic veins, which lead to the inferior veina cava (figs. 1.21 and 1.23).

The fact that one of the afferent systems of the liver is venous is rather peculiar, but is explained by the role of the liver in the body. Blood from the portal vein is loaded with digestion-related substances, which are transformed in the liver and released in the body through the hepatic veins. The liver has many functions, including metabolising carbohydrates and lipids, synthesising proteins present in the blood, secreting bile (bile ducts in green on figs. 1.21a and 1.23) or detoxifying some substances (*e.g.* alcohol). However, ethanol and its by-product acetaldehyde (ethanal) are toxic for liver cells and can cause hepatic steatosis, leading to fibrosis, and cirrhosis.

Liver Imaging Challenges

Large FOV The field of view needed to cover the liver depends on the morphology of every patient, but is generally wide in all dimensions. For axial sequences, many slices or partitions must be acquired. The abdomen being wider in the left-right direction than in the anterior-posterior direction, the latter is chosen for phase encoding, thus reducing the number of phase lines needed to avoid aliasing. Still, the overall number of lines to acquire is large, and requires a compromise between resolution and acquisition time.

Breathing Motion In addition, a lot of motion occurs in the abdomen due to breathing. Two approaches coexist to deal with this problem:

- Free-breathing sequences that either use an abdominal belt or a navigator echo [Ehman 1989] measuring the motion of the diaphragm to synchronise the acquisition with breathing, and performing acquisition only during a short window within the breathing cycle. Note that this works best for 2D sequences, where it is possible to acquire full slices during that time window, thus limiting motion artefacts to some

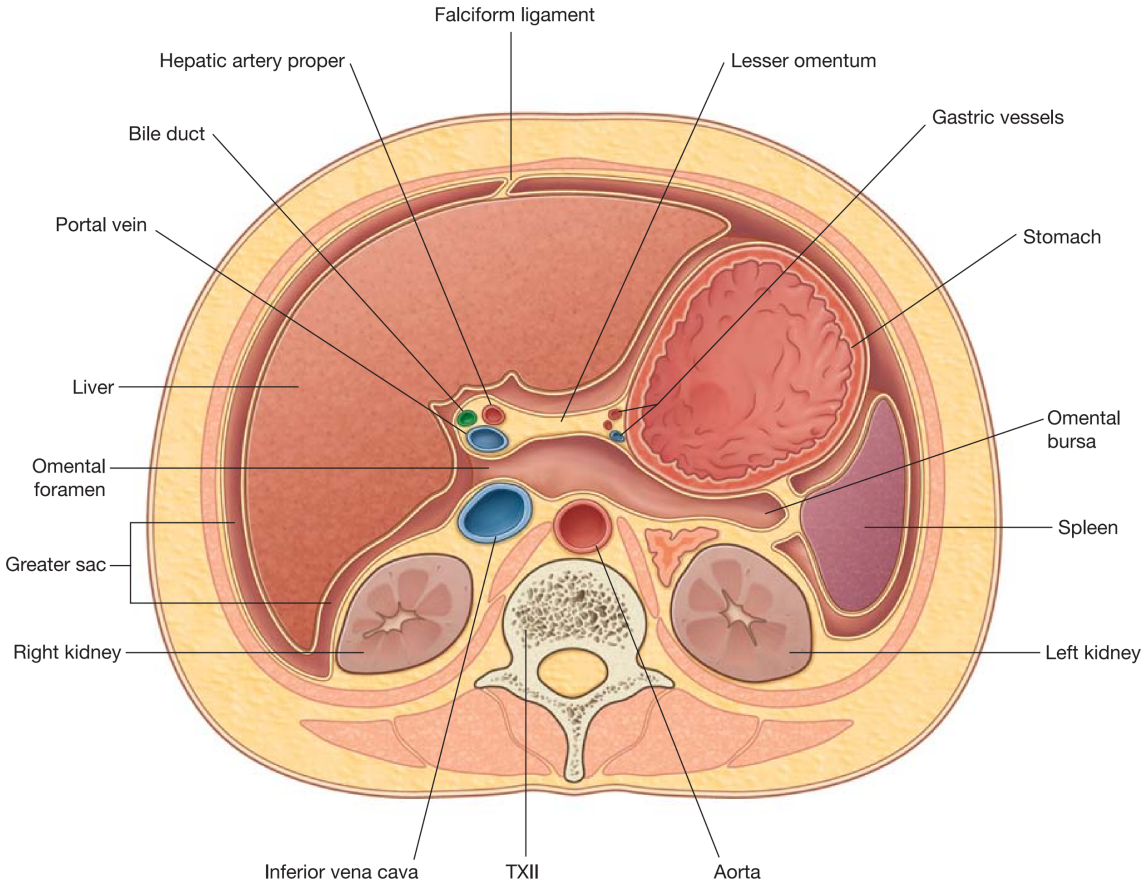

(a) Transverse section of the abdomen (illustration from [Drake 2009]).

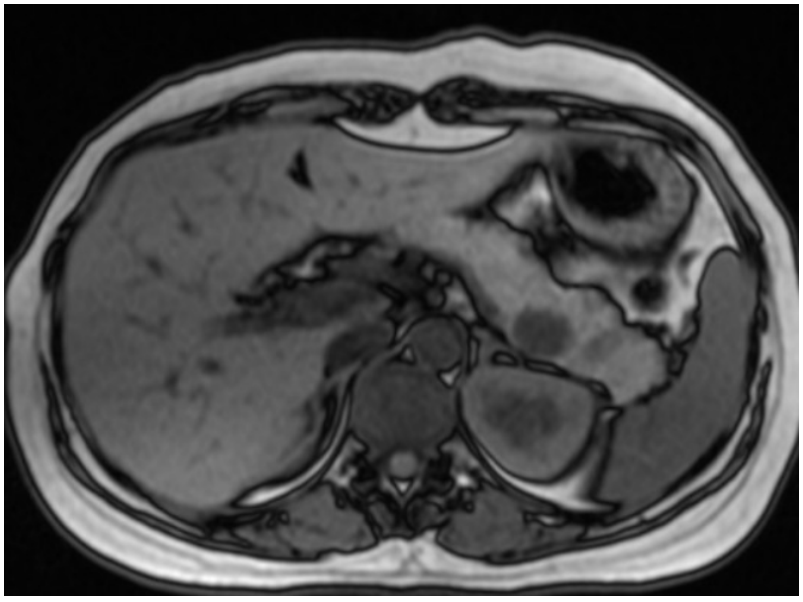

(b) MRI T_1w OP view of a similar section as in (a). Notice the air in the stomach. Only one kidney is visible on this slice. Note that the pancreas also appears on this image.

Figure 1.21: Environment of the liver in the peritoneal cavity.

Figure 1.22: Location and extension of the liver in the abdomen on a T_2-weighted coronal MRI acquisition. The field of view needs to be large in all directions to acquire a whole-liver image. Air in the lungs above the liver and in the intestines below can induce significant B_0 distortion. Image from www.healthcare.siemens.com.

slices. In case of a 3D acquisition, any motion could affect the whole k-space, and deteriorate the quality of the whole volume.

- Breath-hold sequences that require the patient to keep still for 15 to 20 seconds while the acquisition is performed: this is the approach chosen for 3D T_1 sequences.

Reception Profile Finally, for abdominal imaging, a set of two surface array receive coils can be used, as shown in fig. 1.20b, to maximise the number of reception elements, and therefore the signal-to-noise-ratio and the imaging acceleration possibilities. One drawback is the inhomogeneous reception profile (B_1^-) caused by the proximity of coil elements to the surface of the body: received signal is much stronger near the coils. This requires the use of profile correction techniques, either via post-processing, or more elegantly through a small calibration step which compares the reception profile of the whole-body built-in coil, supposedly homogeneous, and that of the coil arrays. This method, referred to as 'Prescan Normalize' is the one used in the abdominal MRI studies in this thesis. Note that it fails to completely remove the reception profile as the RF body coil does not really have a homogeneous B_1 field profile in the human body at high field, be it in transmission (B_1^+) or reception (B_1^-). B_1 inhomogeneity is focused on in chapter 2.

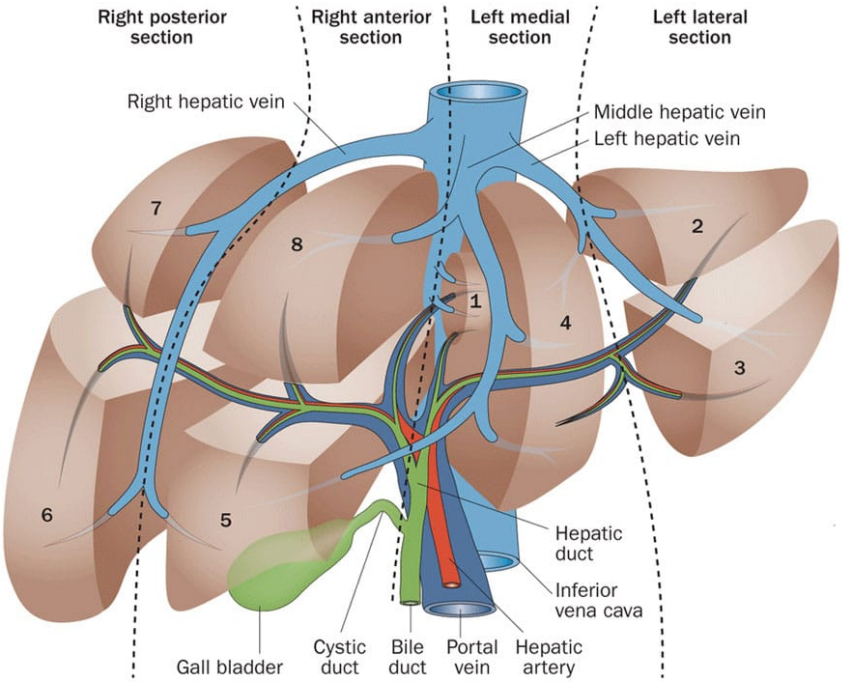

Figure 1.23: Liver irrigation and functional segmentation. From humanbodyanatomy.co.

Liver MRI Indications & Protocol

MRI has become the gold standard for screening and characterisation of liver lesions [Luciani 2017]. Both benign and malignant liver lesions can be characterised on liver MRI. MRI is now the gold standard imaging technique for benign liver lesion characterisation - such as focal nodular hyperplasia (FNH) – as well as for hepatocellular carcinoma (HCC) detection in cirrhotic patients, and for metastatic liver disease staging. In addition, liver MRI is now routinely used for iron and fat quantification in daily practice.

Here are the different MRI sequences typically needed in a liver investigation, along with their clinical use [Luciani 2017, Kierans 2009]:

1. T_1-weighted GRE with Dixon. IP or water images allow to compare T_1 contrast of lesions, while the OP or fat image reveals intra-cellular fat, which can indicate liver steatosis, and a HCC or an adenoma if found in a lesion.
2. T_2-weighted FSE with fat suppression. A FSE is advised because it is rather insensitive to magnetic susceptibility artefacts (*cf.* chapter 2) which can occur when iron is present: this is the case in the liver, especially in a diseased one. T_2 weighting aims at identifying lesions of liquid nature, such as cysts (strong T_2H), but TE should be low enough to keep a moderate T_2 contrast in order to discern lesions with a lower T_2H.
3. A T_2 HASTE (half-fourier acquisition single-shot turbo spin echo imaging) can be used in complement to the T_2 FSE, with a longer TE to identify cysts more clearly.
4. A diffusion-weighted imaging (DWI) sequence, that uses extra gradients to identify regions with mobile protons, and those where movement is restricted. This sequence is important to detect metastatic lesions in the liver, as they are associated with

restricted diffusion (like most malignant hepatic tumours) whereas diffusion is more free in benign lesions.

5. A DCE series of sequences, at the core of chapters 5 and 6, similar to that performed in the breast. However, here the acquisition must be short enough to fit in a breath-hold (TA $\leq 20\,\mathrm{s}$). It is the centremost part of the protocol, decisive to characterise certain lesions such as hepatocellular carcinomas [Goshima 2009], adenomas or focal nodular hyperplasias [Maniam 2010]. After the reference T_1w FLASH acquisition and the injection of gadolinium-based agent, the sequence is repeated at different times to isolate arterial, portal, veinous flows (about 10 s, 40 s and 70 s after injection, respectively), and once again after a two-minute pause to visualise the full vascularisation of the liver (late phase).

* * *
* *
*

Chapter 2

High Magnetic Fields and B_1 Artefacts

Chapter Outline

High field MRI, *i.e.* with a magnetic field of 3 T, is gaining popularity in clinical practice, for multiple reasons exposed in section 2.1. Similarly, ultra-high field (UHF) systems – fields above 3 T, and especially above 7 T – are commonly used in research to push back the limits of human body exploration, and especially brain architecture and functionality. Unfortunately, we will see that increasing the static field does not only come with advantages. One of the challenges associated with high field MRI is called the B_1 artefact and is at the core of the works presented in this thesis. When this artefact

occurs, it results in differences in brightness and contrast across the image. Many solutions have been investigated to counteract this effect; section 2.2 reviews them. But despite the many advances research brought into this area, B_1 artefact reduction in clinical routine is currently set back, as exposed in section 2.3. Since the goal of this thesis is to investigate the implementation in clinical routine of one specific technique – the k_T-points– section 2.4 focuses on its description and on the different demonstrations that have been made in a research environment.

2.1 Benefits and Challenges of High Field Imaging

2.1.1 Advantages

Signal-to-Noise Ratio Increase

Signal-to-noise ratio (SNR) is an important metric to assess the quality of an MRI acquisition, and in the end on image quality. In 3D imaging, the SNR in a voxel can be expressed as:

$$\mathrm{SNR} \propto M_0 \mathrm{B}_1^- \Delta x \Delta y \Delta z \sqrt{\frac{N_{\mathrm{Read}} N_{\mathrm{Phase}} N_{\mathrm{Part}} NEX}{BW}} S_w \tag{2.1}$$

where M_0 is the equilibrium magnetisation, B_1^- is the coil reception profile, Δx, Δy and Δz are the spatial dimensions of the voxels, BW is the readout bandwidth, N_{Read}, N_{Phase} and N_{Part} are the number of readout samples, phase encoding steps and partition steps, respectively, and NEX is the number of averages (repetitions of the whole sequence). S_w is a weighting factor including tissue-dependant parameters (T_1, T_2, proton density), the sequence used and its parameters (TR, TE and flip angle).

We can deduce from eq. (1.2) that a higher static field B_0 leads to a higher equilibrium magnetisation M_0, and as a consequence to a higher SNR. This linear relation between B_0 and SNR [Collins 2006] holds well for a range of relatively low fields (around 1.5 T) but becomes supralinear at UHF as predicted in [Ocali 1998] and recently validated experimentally, with $\mathrm{SNR} \propto {B_0}^{1.65}$ [Pohmann 2016] as pictured in fig. 2.1. The additional SNR obtained at high field can be profitable in several ways:

- Since SNR is also proportional to voxel dimensions, it makes it possible to obtain images of similar quality with a finer resolution.
- Thanks to parallel imaging methods – such as SENSE [Pruessmann 1999], GRAPPA [Sodickson 1999, Griswold 2002] or CAIPIRINHA [Breuer 2004] – making use of receive coils made of multiple elements at different spatial locations (coil arrays), it is possible to reduce either N_{Phase} or N_{Part} (or both) while avoiding aliasing. Thus, faster examinations are obtained at the expense of SNR, which can be compensated by the higher field. If we denote by $\mathrm{SNR}_{\mathrm{full}}$ the signal-to-noise ratio without acceleration (described by eq. (2.1)), by R the time reduction factor, and by $\mathrm{SNR}_{\mathrm{PI}}$ the ratio when using parallel imaging, then [Wiesinger 2004]:

$$\mathrm{SNR}_{\mathrm{PI}} = \frac{\mathrm{SNR}_{\mathrm{full}}}{g\sqrt{R}} \tag{2.2}$$

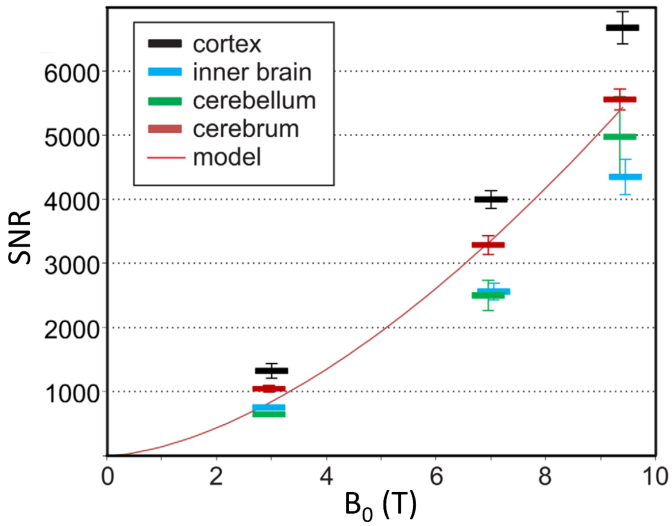

Figure 2.1: Measured SNR values in four different brain compartments at different field strengths. The red line corresponds to the SNR $\propto B_0^{1.65}$ model. From [Pohmann 2016].

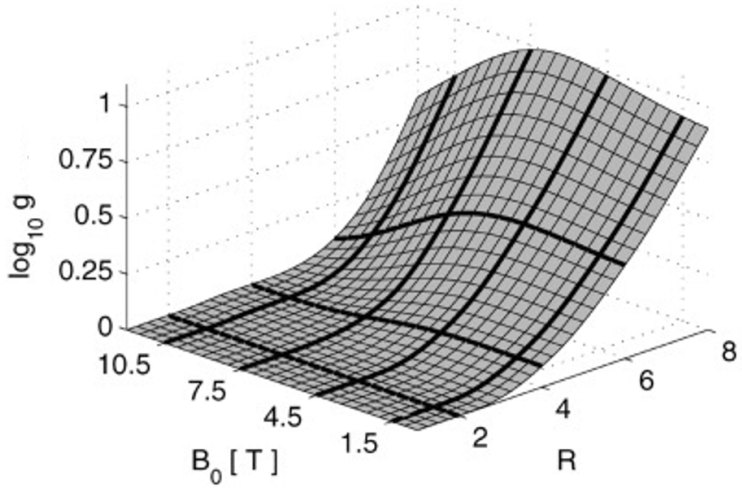

Figure 2.2: Evolution of the geometrical factor g as a function of B_0 and of the acceleration factor R, for a given coil array. This shows an interest of UHF, where g decreases for high acceleration factors. From [Wiesinger 2004].

where g, called geometry factor, is a loss term depending on the configuration of the receive coil array. But this loss factor is also strongly influenced by R and by B_0, as pictured in fig. 2.2.

A Stronger Chemical Shift Leads to Easier Fat-Water Separation

As explained in section 1.3.1 'Chemical Shift', there exists a difference in resonant frequencies between water and fat molecules, generally taken as 3.5 ppm. The difference in resonant frequency between water and fat therefore depends on the magnetic field. For instance, at 1.5 T, Larmor frequency for ^{1}H is about 64 MHz, leading to a water-fat frequency difference $\Delta f \approx -220$ Hz (water is taken as the reference, so the '$-$' sign expresses

that fat resonates at a slower frequency). At 3 T, the Larmor frequency is 128 MHz, so $\Delta f \approx -440$ Hz

This larger frequency offset makes fat saturation (section 1.3.2) easier at high field. More generally, spectroscopy is eased as compounds resonating at different frequencies are more clearly separated one from another. Dixon imaging (section 1.3.2) is eased at 3 T compared to 1.5 T, as the interval between out-of-phase and in-phase echoes is halved, making it possible to achieve a shorter TR. This advantage shows its limit at UHF: if this interval is too short, it requires short readout times to be able to acquire both echoes in the same TR, which implies a higher readout bandwidth – BW in eq. (2.1) – and tends to reduce the SNR.

More generally and beyond fat suppression considerations, an increased chemical shift at high field is a good feature for NMR spectroscopy, where it allows to distinguish compounds whose peaks would be too close to each other at lower field.

Magnetic Susceptibility Disparities Sometimes Deliver Enhanced Image Contrasts

Magnetic susceptibility measures the tendency of a material to become magnetised when placed in an external magnetic field B_0: a field J, called polarisation, is created which can either augment (paramagnetism) or oppose (diamagnetism) the external field. Magnetic susceptibility is denoted as χ and describes the relationship between both fields:

$$\chi = \frac{J}{B_0} \tag{2.3}$$

Its sign depends on the quality of the material (negative for diamagnetic materials, positive for paramagnetic ones). As a result, the observed magnetic field is locally affected by the presence of materials of different susceptibilities, and local static field inhomogeneities appear:

$$B_{observed} = J + B_0 = (1 + \chi)B_0 \tag{2.4}$$

$$\Delta B_0 = \chi B_0 \tag{2.5}$$

Such inhomogeneity increases linearly with the magnet strength, which is generally not a good feature as we will discuss in section 2.1.2, 'Challenges'.

However, it presents an interest in sequences that rely on a measure or estimation of ΔB_0. This is the case for blood-oxygenation-level dependent (BOLD) [Ogawa 1990] functional MRI (fMRI), a technique that measures brain activity based on a T_2^*-weighted (T_2^*w) acquisition. In section 1.1.2, we introduced a distinction between T_2, unrecoverable tranverse relaxation characteristic of a tissue, and T_2^* ($< T_2$) that also accounts for B_0 inhomogeneity inducing additional transverse relaxation, recoverable for instance using a spin-echo pattern (section 1.2.2). Estimating local field variations via T_2^*w imaging allows to monitor changes in the concentration of deoxyhaemoglobyn – a paramagnetic substance – in blood vessels in the brain, which is a marker for oxygen consumption, and therefore brain activity. Additionally, an increase in contrast-to-noise ratio (CNR) is observed in T_2^*w structural imaging [Ciobanu 2012].

Table 2.1: T_1 and T_2 relaxation times at 1.5 T and 3 T for a selection of human tissues. Values are from [Stanisz 2005] (*), [Rakow-Penner 2006] (†) and [Gold 2004] (‡).

Tissue	T_1 (ms)		T_2 (ms)	
	1.5 T	3 T	1.5 T	3 T
Blood*	1441 ± 120	1932 ± 85	290 ± 30	275 ± 50
Brain (grey matter)*	1124 ± 50	1820 ± 114	95 ± 8	99 ± 7
Brain (white matter)*	884 ± 50	1084 ± 45	72 ± 4	69 ± 3
Breast (glandular)†	1266 ± 82	1445 ± 93	58 ± 10	54 ± 9
Fat (breast)†	296 ± 13	367 ± 8	53 ± 2	53 ± 2
Fat (marrow)‡	288 ± 5	365 ± 9	165 ± 5	133 ± 6
Fat (subcutaneous)‡	288 ± 8	371 ± 8	165 ± 6	133 ± 4
Liver*	576 ± 30	812 ± 64	46 ± 6	42 ± 3
Skeletal muscle*	1008 ± 20	1412 ± 13	44 ± 6	50 ± 4

T_1 Increase: Sharper TOF Angiography and Lower Gadolinium Doses

As the magnetic field (and with it also the Larmor frequency) increases, for most tissues T_2 is not affected much, but T_1 tends to increase, as shown in table 2.1.

This gives a clear advantage to high fields in time-of-flight (TOF) MR angiography. TOF is a technique largely used in neuroimaging to isolate blood vessels without resorting to contrast agents. It relies on magnetic saturation of static tissues: as explained in section 1.2.1, repeated excitation of a volume drives down the steady-state magnetisation level within this volume. As a result, 'fresh' blood entering the volume without having been saturated contrasts strongly with static tissues, as its magnetisation before excitation is close to its equilibrium level [Saloner 1995]. The effect of saturation is more noticeable when T_1 is higher, as steady-state magnetisation is lower, which results in a sharper contrast.

A second positive consequence of having a longer T_1 is that it necessitates a smaller concentration of gadolinium in contrast-agent-based sequences, which is appreciable in terms of patient comfort and safety. This is particularly interesting considering the clinical applications focused on in this thesis. First let us consider how contrast agents interact with tissues to enhance T_1 contrast. Because gadolinium is paramagnetic, it decreases the observed T_1 [Tofts 2005, ch. 6] as it accumulates in a tissue[1]:

$$\frac{1}{T_{1,t+Gd}} = \frac{1}{T_{1,t}} + r_1[C] \tag{2.6}$$

where $T_{1,t}$ is the T_1 of tissue without gadolinium, $T_{1,t+Gd}$ is the observed T_1 when gadolinium is present, $[C]$ is the concentration of contrast agent and r_1 is the relaxivity of the contrast agent, characteristic of each product. Dependence of r_1 on field strength is indicated in table 2.2 for two common contrast agent products, that are used in the works presented hereby. A T_1w sequence is used for contrast-based imaging, as gadolinium decreases the observed T_1, making injected tissues brighter than non-injected ones. Contrast enhancement in tissues is linked to the relative change in the observed T_1, given by

[1] T_2 is also affected, but at standard concentrations in tissues, T_1 effects predominate.

Table 2.2: T_1-relaxivity in plasma at 37 °C at 1.5 T and 3 T for two commonly used gadolinium-based contrast agents (adapted from [Rohrer 2005]).

Trade name	Generic name	Short name	r_1 ($L\,mmol^{-1}\,s^{-1}$)	
			1.5 T	3 T
DOTAREM®	Gadoterate meglumine	Gd-DOTA	3.6	3.5
MULTIHANCE®	Gadobenate dimeglumine	Gd-BOPTA	6.3	5.5

$T_{1,t}\,r_1\,[C]$. Now let us have a look at an example. When Gd-DOTA is used at 3 T, the injected dose is typically 0.1 mmol per patient kilogram. Considering a 100-kg patient and $T_{1,t} = 812$ ms (liver, table 2.1), the change in tissue relaxation rate is expected to be 28 %. However, at 1.5 T, tissue T_1 is shorter ($T_{1,t} = 576$ ms in the liver), but r_1 hardly changes (table 2.2). An enhancement ratio similar to the one observed at 3 T would require a dose of about $0.14\,mmol\,kg^{-1}$, *i.e.* 40 % higher.

2.1.2 Challenges

Unfortunately, most aspects of an increased field strength introduced above also come with effects that can impair image quality. Those are summarised in this section, along with additional side-effects of high-field imaging. It has represented a challenge for the MRI community for decades, as the resolution of each one of these issues represents a field of research in itself, and is compulsory in order to benefit fully from stronger magnets.

T_1 Increase: Longer Acquisition or Lower Signal

Having longer T_1 values means that longitudinal magnetisation recovers more slowly. As a consequence, magnetisation saturation is more pronounced, and the available magnetisation is lower: if TR is kept identical, signal is brought down. This impairs the expected SNR gain, unless TR is increased, and with it the acquisition time.

Other inconveniences of a longer T_1 regard sequences including some sort of magnetisation preparation, which consists in waiting for a certain amount of time TI after playing a preparation pulse, before applying the actual imaging kernel to acquire a portion of k-space (be it a line or a larger portion). Examples are sequences such as MP-RAGE [Brant-Zawadzki 1992] or STIR (*cf.* section 1.3.2) [Bydder 1985]. Since the inversion time depends on tissue T_1– for instance T_1 of fat in STIR – the augmentation of T_1 imposes a lengthening of TI, and hence a longer acquisition time overall.

A Stronger Chemical Shift Produces More Displacement Artefacts

We have seen that more chemical shift can be beneficial for spectral fat suppression techniques. But chemical shift is also associated with a fat displacement artefact. As ^1H protons in fat precess at a frequency different from that of protons in water, signal from a fat compound and a water compound located in the same voxel are interpreted as emanating from different locations during readout. This induces a displacement of fat signals

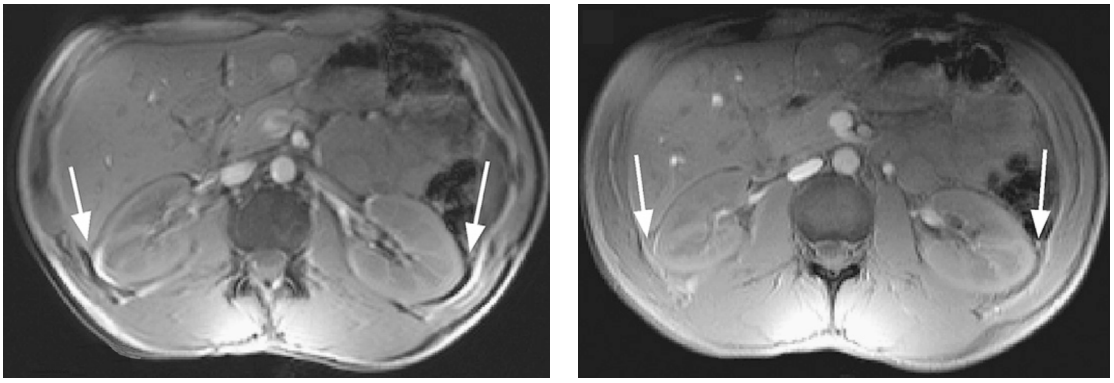

(a) BW = 120 Hz/pixel (b) BW = 480 Hz/pixel

Figure 2.3: Chemical displacement artefacts observed in the abdomen of the same patient at 3 T for different receiver bandwidths. Displacement occurs in the readout direction, here left-right, and provokes light and dark bands (arrows). The receiver bandwidth was increased in (b), resulting in a reduced artefact, at the expense of SNR. Illustration from [Soher 2007].

in the frequency-encoding direction, which is naturally stronger at high field, as shown on fig. 2.3a.

This effect can be circumvented either by suppressing fat signal beforehand when possible, or by increasing the receive bandwidth. Indeed, if the signal is sampled at a frequency of, say, 220 Hz/pixel, fat displacement will be of one pixel in the frequency-encoding direction at 1.5 T, and of two pixels at 3 T. Doubling receiver bandwidth will halve this displacement. However, this comes at a $\sqrt{2}$ cost in SNR (eq. (2.1)).

Magnetic Susceptibility Disparities Spoil the Signal Near Tissue Boundaries

Differences in magnetic susceptibility create local variations in B_0, inducing undesirable off-resonance effects and image distortion, as seen on fig. 2.4. This is somewhat alleviated with careful B_0 shimming at the beginning of the examination: after mapping the B_0 distribution in the FOV, direct current is applied to the gradient coils to counteract linear variations of B_0, and to dedicated shim coils to correct for higher-order deviations. This calibration is performed for all examinations, but it fails to correct very high field distortion, *e.g.* due to air in the sinuses, lungs or colon, let alone near metallic implants, dental hardware or bone screws. In addition, like any calibration, it relies on patient immobility along the exam as the field correction was calculated for a specific patient position. This is typically not the case, considering that even breathing can induce field alterations.

This artefact can occur at all field strengths, but is particularly abundant at high or ultrahigh fields. Mild susceptibility artefacts can however be eased using parallel imaging techniques [Yanasak 2014], in the case of echo-planar imaging [Stehling 1991] where whole k-space planes (slices) are acquired at once with a long readout, which amplifies distortions. Parallel imaging allows to reduce the number of lines in those planes, hence the readout length. Nevertheless, susceptibility artefacts are generally somewhat worsened by parallel

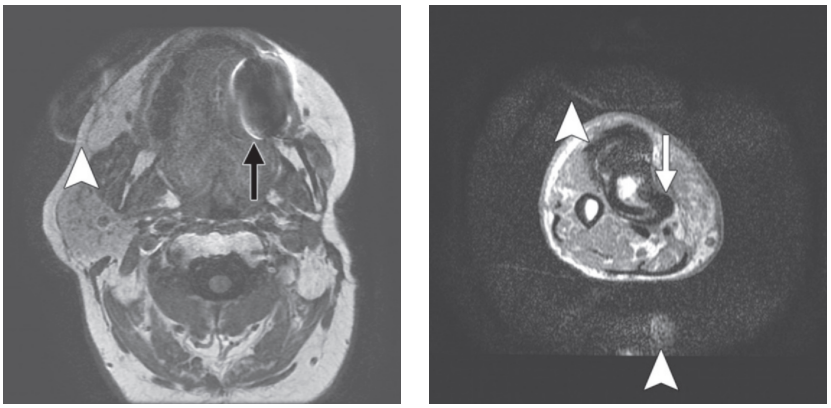

(a) (b)

Figure 2.4: Susceptibility artefacts observed *in vivo* at 3 T. Axial T_1w 2D GRE images show susceptibility artefacts (arrows) and parallel-imaging-induced ghosting particularly pregnant due to susceptibility (arrowheads). Susceptibility artefacts shown arise from (a) dental hardware and (b) a metallic leg implant. Illustration from [Yanasak 2014].

imaging, as important ghosting can be induced (fig. 2.4).

Finally, increased B_0 inhomogeneity provokes a shortened T_2^*, which in turns means a loss of signal, unless TE is reduced.

Energy Deposition: SAR

The energy deposited by the RF field may induce tissue heating, with potential consequences ranging from heatstroke to irreversible damage. For this reason, the International Electrotechnical Commission (IEC) has defined norms to limit the energy deposited in the body [IEC-60601-2-33 2010].

In order to preserve biological tissues, maximal temperature elevation should be limited to 2 °C, and to 1 °C in the eyes. However, to date, it is not possible to measure temperature directly in real time during an MRI exam. An intermediate metric is therefore used instead, called specific absorption rate (SAR), much like in mobile-phone-related safety. It is a time average of the RF power density absorbed by tissues, defined in every location $\mathbf{r}$ in the body as:

$$\mathrm{SAR}(\mathbf{r}) = \frac{1}{T}\frac{\sigma(\mathbf{r})}{2\rho(\mathbf{r})}\int_0^T \|E(\mathbf{r},t)\|_2^2 \, dt \tag{2.7}$$

where T is the time during which the power is averaged, σ is the tissue conductivity, ρ is the volumetric mass density and E is the electric field.

Maximal authorised SAR values were determined via *ex vivo* experimentations and numerical models to enforce aforementioned temperature elevation limits, on a whole body scale as well as at local tissue level. Those depend on several parameters, including the hardware used and the body region considered. In normal operating mode for body imaging, whole body SAR averaged over $T = 6$ min is limited to 2 W/kg. Those limitations will be discussed in more detail in section 2.3.2, 'SAR Control in Clinical Systems'.

Patient safety, and SAR constraints in particular, are relevant for all field intensities. However, several factors make them harder to tackle at 3 T and above. Firstly, SAR is quadratically related to the frequency of the RF field, *i.e.* to the Larmor frequency [Hoult 2000, Collins 2004]. In other words: SAR $\propto {B_0}^2$. This means that SAR is more of a limiting factor and an active constraint at high and ultrahigh fields. Secondly, eq. (2.7) establishes a relationship between SAR and electric field, but the latter is generally unknown. As mentioned before, there are two types of SAR constraints:

- global SAR, which can be estimated comparing measurements of forward and reflected power [Zhu 2012], taking into account the patient's weight
- maximum local SAR encountered – averaged over 10 g of contiguous tissues – which cannot.

At 1.5 T (and lower), at least when using a local transmit coil (such as a head coil) the electric field is quite homogeneous: the peak local SAR is closely related to the global SAR, and can be easily estimated. This is not possible at higher field, where the distribution of E is not longer homogeneous: SAR hotspots can occur, and advanced modelling of its behaviour needs to be performed. This aspect will be developed for a local transmit coil in section 2.2.4, and for a whole-body coil in clinical routine in section 2.3.2. In summary, at high and ultrahigh fields, energy deposition in the patient is a more pregnant issue, and is at the same time harder to estimate.

RF Field Inhomogeneity and B_1 Artefacts

We have now reached the point where we start addressing the high-field-related issue which is at the core of this thesis: the B_1 artefact.

To understand this artefact, we must look at the equation governing the wavelength λ for a RF wave matching the Larmor frequency f_0, passing through a medium of relative permittivity (or dielectric constant) ε_r and magnetic susceptibility χ:

$$\lambda = \frac{c}{f_0 \sqrt{\varepsilon_r (1 + \chi)}} \tag{2.8}$$

where c is the speed of light in a vacuum. Considering that human tissues generally show little susceptibility ($|\chi| \ll 1$) [Bernstein 2006], and keeping in mind eq. (1.1), this equation simplifies to:

$$\lambda \approx \frac{2\pi c}{\gamma} \frac{1}{\sqrt{\varepsilon_r}\, B_0} \propto \frac{1}{\sqrt{\varepsilon_r}\, B_0} \tag{2.9}$$

It follows from eq. (2.9) that a high permittivity or a high magnetic field both tend to shorten the RF wavelength. The wavelength is large in a vacuum or air: $\lambda \approx 4.68$ m at 1.5 T, $\lambda \approx 2.34$ m at 3 T, and $\lambda \approx 1.00$ m at 7 T. However, considering that the permittivity of water-based human tissues is quite high [Gabriel 1996, Haacke 1999] (ranging from 10 to 100), the wavelength is shorter. For a representative value of $\varepsilon_r \approx 80$, this gives a wavelength of about 52 cm, 26 cm and 11 cm in tissue, respectively at 1.5 T, 3 T and 7 T.

When the wavelength comes close to or is shorter than the dimensions of the imaged organ, RF inhomogeneity artefacts can appear [Merkle 2006, Bernstein 2006], resulting

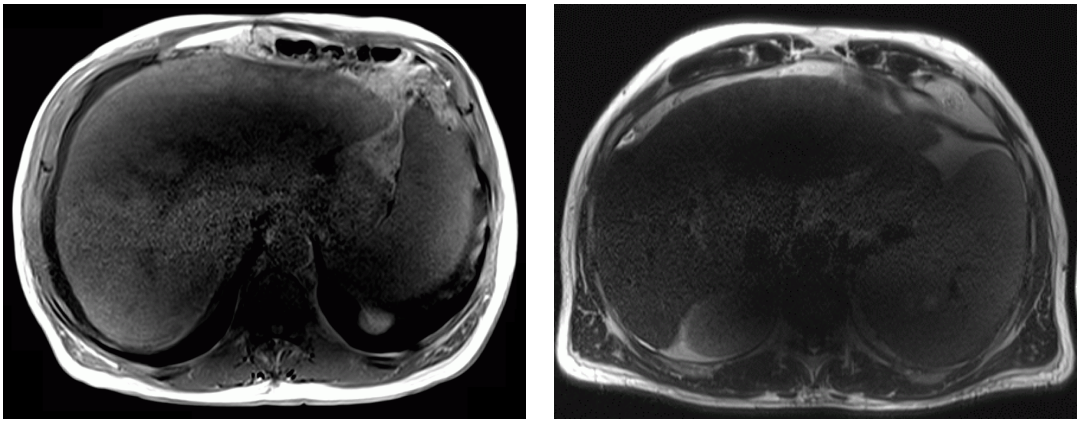

(a) T_1-weighted 3D GRE (b) T_2-weighted 2D HASTE

Figure 2.5: B_1 artefact observed at 3 T in the abdomen, with different imaging sequences. Notice the presence of ascites (T_1 hyposignal around the liver corresponding to liquid) in the patient pictured in (a). *Courtesy of Alexandre Vignaud*.

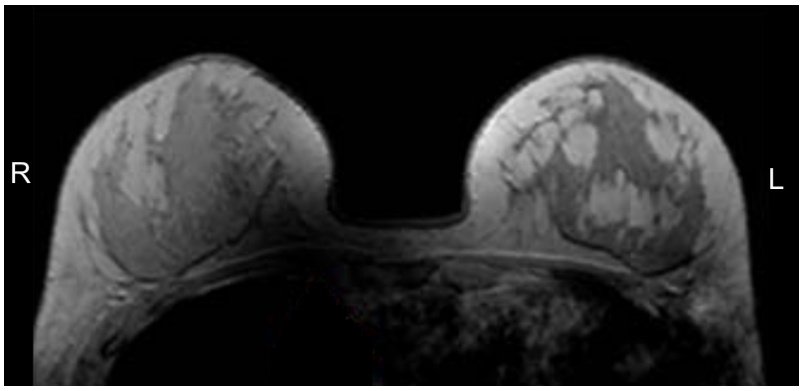

(a) Large bilateral asymmetry in signal intensity in a subject with large dense breasts, and significant signal dropout in the right breast [Brink 2015a].

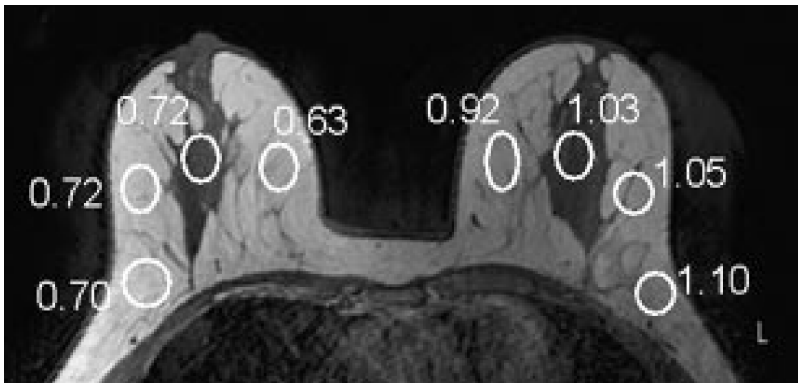

(b) T_1-weighted 2D GRE. TR is 6 ms, target FA is 20°. Numbers in ROIs give FA deviation relative to the target (ideal angle would have the value 1.00). The observed FA varies between 22° and 12.5° [Kuhl 2007].

Figure 2.6: Examples of B_1 artefacts in the breasts..

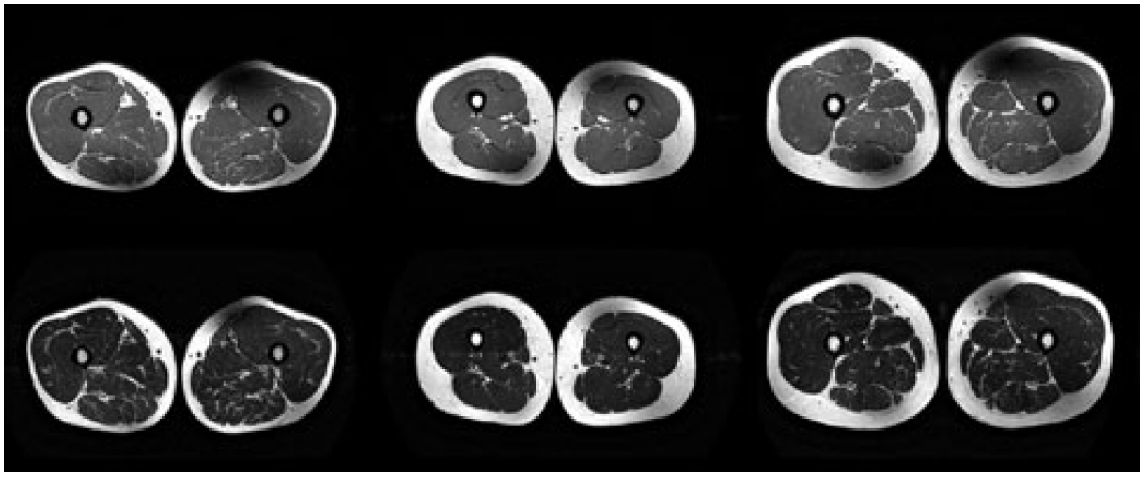

Figure 2.7: B_1 artefact observed at 3 T in the thighs for multiple subjects and different sequences. Top: T_1-weighted 2D TSE. Bottom: T_2-weighted 2D TSE [Childs 2013].

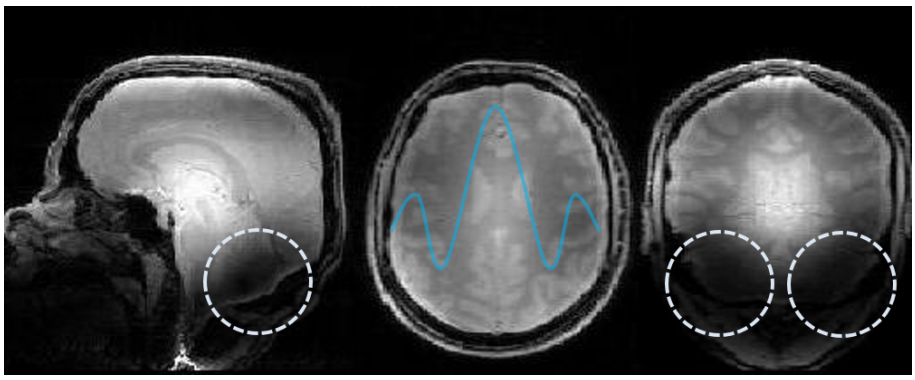

Figure 2.8: Central brightening artefact observed at 7 T with a FLASH sequence [Cloos 2012c]. The blue line in the middle panel outlines the typical pattern, with a higher signal in the centre and loss at the periphery. Dashed circles highlight extreme zones of shade in the cerebellum and near the brainstem.

in regions of bright signal or zones of shade, loss of contrast, and sometimes signal 'holes'. This is very seldom observed at 1.5 T [Soher 2007], but occurs frequently at 3 T, *e.g.* in the abdomen (fig. 2.5), the breasts (fig. 2.6), the thighs (fig. 2.7), the pelvis or the spine. At 7 T and above, those effects are even more pronounced in the aforementioned regions. In addition, the reduced wavelength is lower than the dimension of the head; this results in strong artefacts in the brain. As far as brain imaging is concerned, this is commonly called the 'central brightening artefact', as most signal loss is located in the periphery of the brain, as shown in fig. 2.8 with a 7 T acquisition.

There is no absolute consensus as to the origin of that artefact, which may actually arise from several physical phenomena [Merkle 2006]:

- One widespread explanation is that of dielectric resonance: destructive and constructive interferences (respectively causing shading and brightening) between the primary (forward) field and internally reflected fields can be at the origin of a standing wave explaining the observed patterns. However, the high conductivity of

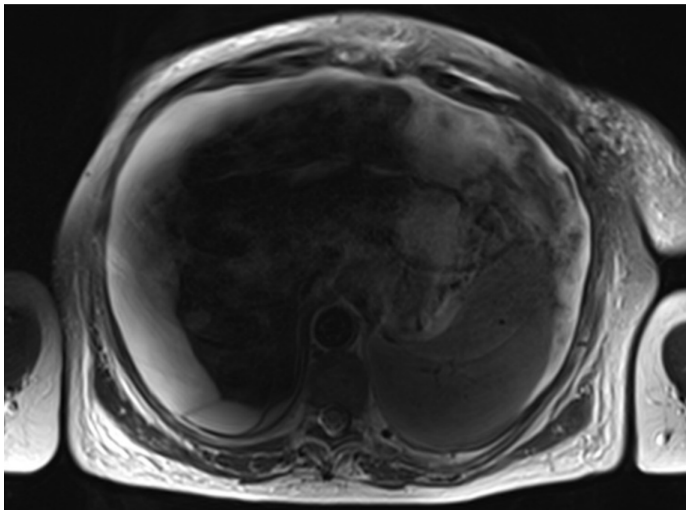

Figure 2.9: Extreme B_1 artefact in an obese patient with severe ascites, on a T_2-weighted TSE sequence [Donato 2017]. Ascites being a liquid characterised by long T_1 and T_2 constants, it appears bright here, and dark on T_1-weighted images (*cf.* fig. 2.5a).

physiological tissues makes this phenomenon unlikely, since the forward propagating field is quickly attenuated, and reflection is limited: dielectric resonance is severely damped [Collins 2005].

- Constructive and destructive interference patterns can however emanate from forward fields transmitted from different coil elements, as they propagate through different media and different geometries [Collins 2005]. This observation leads directly to static RF shimming (introduced later, in section 2.2.2) as an appealing solution to B_1 artefacts.
- Shielding effects, stemming from the presence of highly conductive media. The rapidly-changing RF magnetic field induces eddy currents, in turn resulting in a secondary, opposing, RF magnetic field. As a result the RF field is attenuated. This can be particularly pronounced in ascites[2] (fig. 2.5a), or even amniotic fluid [Soher 2007].

The combination of a shielding effect with interference patterns can cause even stronger artefacts: this happens for pregnant women, or patients with abdominal swelling caused by severe ascites (*cf.* fig. 2.9) [Kukuk 2009].

Note that in fat ($\varepsilon_r \approx 3$ in oil), the wavelength is much larger (*e.g.* 1.35 m at 3 T). This may be an explanation to why larger patients, with a higher fat-to-muscle ratio, do not necessarily produce strong B_1 artefacts in the abdomen [Bernstein 2006]: although such artefacts are more frequently observed in obese patients than in thin ones, there is no direct causality.

[2] Ascites refers to abnormal buildup of fluid in the abdomen that may cause swelling.

2.1.3 Conclusion

As we have seen, the expected supralinear gain in SNR associated with high field MRI does not grant clinical images of higher quality as easily as one could wish. Even more than at low field, preparing an imaging protocol at high or ultrahigh field consists in finding, for each specific application, the right compromise between several parameters, to maximise SNR while maintaining artefacts at an acceptable level.

The advantages associated high field MRI are generally worth the effort. The following sections describe different techniques that have been developed to counteract B_1 artefacts, in research applications as well as in clinical practice. The final section of this chapter focuses specifically on k_T-points, the method used in the rest of this thesis to achieve FA homogeneity in the case of non-selective excitation.

2.2 B_1 Artefacts Reduction: a Dynamic Field of Research

In order to counteract B_1 inhomogeneity, a popular approach is to use a class of amplitude- and frequency-modulated RF pulses, called adiabatic pulses [Tannús 1997, Garwood 2001, Norris 2002], which gradually and slowly sweep through frequencies around resonance. Those pulses are appreciated as they are relatively insensitive to B_1 inhomogeneity, thanks to an inherent 'threshold' effect. They are not exempt from issues, however. For instance, they tend to be long, which makes them unsuitable for use in sequence kernels with short TR such as FLASH or when a short inter-echo time is needed, as in SPACE. Nevertheless, they are often used in magnetisation-prepared, *e.g.* as the inversion pulse in SPAIR[3] (section 1.3.2) which is played only once every few TRs and where complete inversion of fat is expected.

There has therefore been a need for B_1 artefact reduction techniques that can be used in any situation, any sequence, without too many modifications. This is the object of the present section.

2.2.1 Passive RF Shimming

One simple – in the sense of relatively cheap and technically non-demanding – solution to easily reduce B_1 inhomogeneity – or to *shim* the RF field – is to place high-permittivity materials near the most field-deprived regions [Yang 2006, Webb 2011]. At 7 T for brain imaging (and at 3 T *e.g.* in the thighs [Brink 2015b]), dielectric pads made of $CaTiO_3$ (ε_r up to 110) [Teeuwisse 2012b] or $BaTiO_3$ (ε_r up to 210) [Teeuwisse 2012a] powder mixed in a solvent are often used (fig. 2.10) [Neves 2018]. However, those pads have many drawbacks. In particular, they age rapidly and lose their properties within a few months, and they represent an important bulk in the coil and are in direct contact with the patient, which can cause discomfort. In addition, $BaTiO_3$, the most efficient compound, is referenced as highly toxic [ECHA 2015]. For those reasons, research is still going on in

[3] The 'A' in SPAIR stands for 'Adiabatic'.

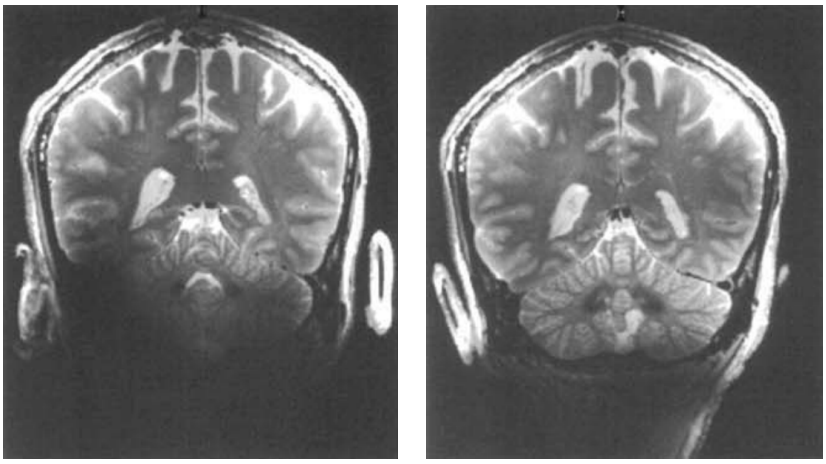

(a) Without pads (b) With pads

Figure 2.10: Effect of $BaTiO_3$ pads, placed at the base of the head, at 7 T on a T_2-weighted TSE acquisition [Teeuwisse 2012a].

the area of passive RF shimming at UHF; for instance, an innovative meta-atom solution has been recently introduced [Leroi 2016].

At 3 T, where B_1 inhomogeneity issues typically occur in the abdomen, an 'RF cushion' solution has long been proposed by several vendors [Schmitt 2004, Franklin 2008]. Those cushions are usually made of ultrasound gel ($\varepsilon_r \approx 60$) mixed with a highly concentrated gadolinium- or manganese-based contrast agent to eliminate the MR signal from the gel itself[4]. See fig. 2.11 for an example result using an RF cushion.

Passive RF shimming solutions are able to locally raise the B_1^+ field where needed the most, while maintaining a limited SAR [Teeuwisse 2012b, Gemert 2017]: due to the high dielectric constant of the pads, the oscillating electric field from the RF coil induces displacement currents that create a secondary magnetic RF field in their vicinity, that reinforces B_1^+. Unfortunately, this is done only at the expense of RF homogeneity loss in the rest of the volume. In addition, these methods rely heavily on the proper positioning of shimming elements, especially for RF cushions as they are not confined in a head coil. The most versatile way to mitigate RF homogeneity over an extended volume while maintaining a safe energy deposition level is to act on the B_1 source itself: *active RF shimming* is the object of the following sections.

2.2.2 Static RF Shimming with Parallel Transmission

Parallel Transmission

We have seen earlier (section 2.1.2) that B_1 artefacts were mostly due to destructive interferences between the RF fields originating from different elements of the transmit coil. According to the principle of superposition, the B_1^+ field observed at a given location $\mathbf{r}$ in the FOV is the sum of the (complex) fields emanating from different coil elements.

[4]We briefly mentioned in section 2.1.1 that a high concentration of gadolinium reduces T_2.

(a) Gel-filled RF cushion; dimensions (L×W×H): 36 cm × 26 cm × 3 cm. Water-based gel mix is located in the white part, while the grey part is a simple foam pad.

(b) Placement on the abdomen for optimal impact on RF homogeneity, with the white side on the patient. This can however induce B_0 distortions.

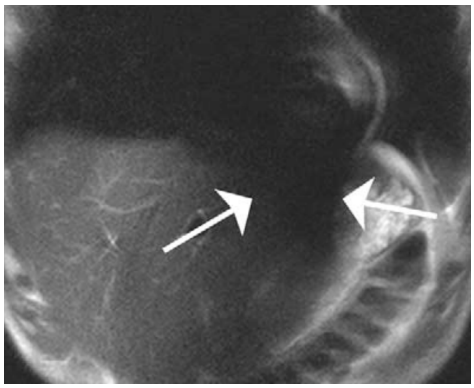

(c) Coronal HASTE image acquired in a healthy male volunteer, without RF cushion.

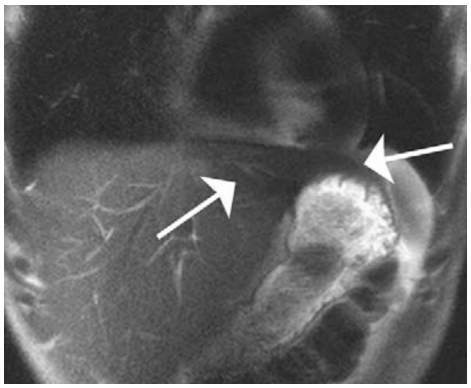

(d) With an RF cushion, the left liver lobe is depicted more clearly, but is not completely free of artefact.

Figure 2.11: RF cushion proposed by Siemens Healthcare for routine abdominal imaging at 3 T. It can be used either with the main (body) coil as receiver, or with abdominal coil arrays. Image from [Merkle 2006].

With N_{Elem} elements:

$$\mathrm{B}_1^+(\mathbf{r},t) = \sum_{\ell=1}^{N_{Elem}} \mathrm{B}_{1,\ell}^+(\mathbf{r},t) \tag{2.10}$$

The idea behind parallel transmission (pTx) is to gain control over the amplitude and phase of the waveforms emanating from those elements. To do so, instead of having one RF amplifier to control the transmit coil (fig. 2.12a) in quadrature – also called circular polarisation (CP) – several amplifiers drive different *transmit channels* independently. Figure 2.12b represents schematically a 'birdcage' coil with four excitation sources, driven with two transmit channels (blue and red): each channel controls two coil elements. If we denote by N_{Ch} the number of independent transmit channels, eq. (2.10) becomes:

$$\mathrm{B}_1^+(\mathbf{r},t) = \sum_{c=1}^{N_{Ch}} \mathrm{B}_{1,c}^+(\mathbf{r},t) \tag{2.11}$$

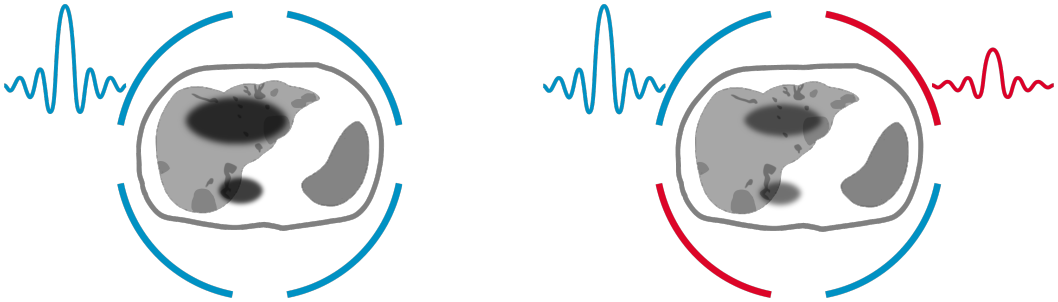

(a) Circular polarisation: one amplifier generates one waveform that is transmitted by different coil elements, with a 90° phase difference between excitation sources in the birdcage coil pictured.

(b) Elliptical polarisation with pTx: several (here two) amplifiers drive different coil elements independently (transmit channels). Amplitude and phase are adjusted to homogenise the B_1 field.

Figure 2.12: Schematic comparison between the traditional circular polarisation (CP) transmit mode (a) and the elliptical polarisation (EP) transmit modes offered by pTx (b) for static RF shimming. Here we represent a body coil transmitting through the abdomen (the liver and the spleen are drawn).

where $B_{1,c}^+$ is the net RF field produced by all elements gathered in the cth controllable channel.

Static RF Shimming

The most basic and widespread use of pTx consists in using the degrees of freedom offered by the different channels to form controlled constructive and destructive RF interferences by transmitting the same waveform through all channels, with adjusted amplitudes and phases. This is often referred to as *static* RF shimming [Padormo 2016], which is the term used in this thesis. The patterns created are called elliptical polarisation (EP) modes, and can be adapted to the patient in the magnet, provided the transmit sensitivity profile ('B_1^+ per applied volt') of each channel is known (see section 2.2.4). When performing static RF shimming, eq. (2.11) is:

$$B_1^+(\mathbf{r}, t) = p(t) \sum_{c=1}^{N_{Ch}} w_c \, S_c^+(\mathbf{r}) \tag{2.12}$$

where p is the pulse temporal waveform, S_c^+ is the (time-independent) sensitivity profile of the cth channel, and w_c is the complex weight – representing the amplitude and phase – applied to the cth channel.

The example in fig. 2.12b describes a two-channel pTx system used for static RF shimming, reducing the typical B_1 artefact in the abdomen. We will see later in section 2.3 'Current State of B_1 Artefacts Reduction in Clinical Routine 3 T MRI' that this is the best set-up currently available on high-end 3 T scanners used in clinical routine. However, scanners with many more transmit channels exist in research facilities. Typically,

7 T MRI are equipped with eight transmit channels, but some exist with 16 or even 32 channels [Brunheim 2018].

As more channels – and hence more degrees of freedom – are added, better B_1^+ homogeneity is expected [Mao 2006, Guérin 2014]. Such hardware is however extremely expensive, and homogeneity achievable over an extended volume with static RF shimming is intrinsically limited to the number of channels available. In addition, there is no guarantee that an infinity of channels would produce a uniform RF field [Harvey 2010]. To circumvent this limitation, we need to look beyond RF interference patterns, and consider that what is eventually expected for a good MRI acquisition is not necessarily a homogeneous B_1^+, but a homogeneous FA distribution. Achieving proper excitation in spite of an imperfect RF field is the purpose of *dynamic* RF shimming, exposed below.

2.2.3 Dynamic RF Shimming

Multidimensional RF Pulses...

While reading this section, let us forget about excitation homogenisation for a moment, and assume a perfectly uniform B_1^+ distribution. Let us also consider a single-channel transmission (sTx) system. In section 1.1.3, we described two principles that are of interest now. Here is a short summary:

1. In the small tip angle (STA) approximation – *i.e.* in practice for angles up to 90° [Boulant 2012] – the FA achieved is related to the Fourier transform of the pulse envelope (eq. (1.12)).
2. To fully describe the effect of an RF pulse, we need to consider any possibly associated gradient, as a gradient relates spatial locations to frequencies, which are then selected (or not) according to the RF waveform applied.

We can go a step further in this Fourier interpretation of RF excitation. Just like spatial locations of received signal can be encoded in terms of spatial frequencies in the k-space (section 1.1.4), it is possible – still in the STA approximation – to describe the effect of any {RF pulse; gradient} pair in terms of excited spatial frequencies, and represent it in the so-called 'transmit k-space' [Pauly 1989]. Applying a gradient $\mathbf{G}$ (possibly over the three axes) for a time T allows to visit spatial frequencies $\mathbf{k}$. At time t, the selected spatial frequency is:

$$\mathbf{k}(t) = -\gamma \int_t^T \mathbf{G}(u)\, du \tag{2.13}$$

This equation is indeed very similar to eq. (1.17), except for the limits of the integral. Figure 2.13 shows two examples with standard pulses introduced in chapter 1 – a slice-selective sinc and a non-selective hard pulse – and describes in detail the k-space interpretation. Rolling back to eqs. (1.11) and (1.15), we can write (neglecting B_0 inhomomogeneity):

$$\Delta\omega(\mathbf{r}) = \mathbf{r} \cdot \mathbf{k} \tag{2.14}$$

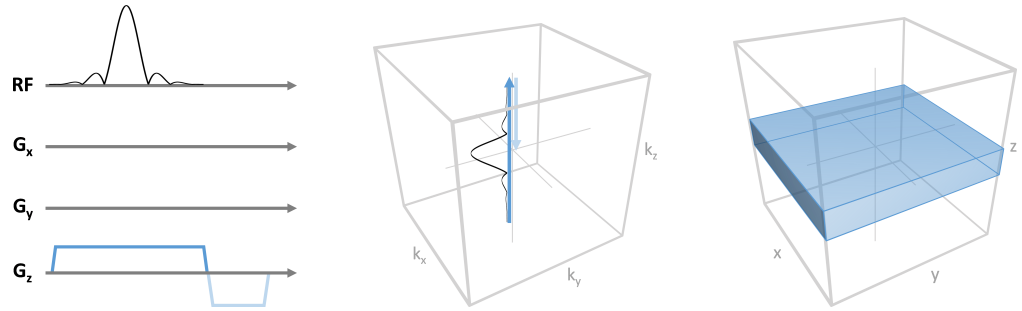

(a) Slice-selective excitation (b) In transmit k-space (c) In image space

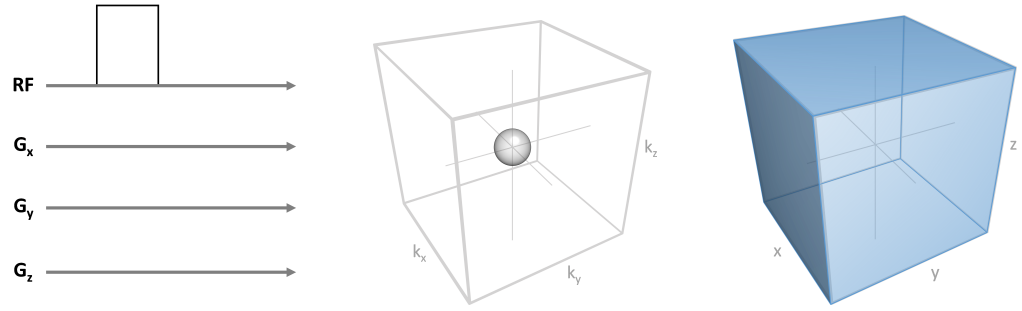

(d) Non-selective excitation (e) In transmit k-space (f) In image space

Figure 2.13: Transmit k-space interpretation of standard pulses. To selectively excite a slice in the z direction, typically a sinc pulse is played along with a B_0 gradient (dark blue) on the z axis (a). In terms of k-space (b), the selection gradient sweeps through k_z while the pulse is applied: energy is deposited along spatial frequencies in the k_z direction according to a sinc pattern (reported here in the k-space picture for better visualisation), which corresponds to exciting a rect in the image space, *i.e.* a slice (c). As no gradients are played in the x and y directions, this trajectory is centred in the (k_x, k_y) plane: only zero-frequencies are explored in those directions (DC components) which means the slice is uniformly excited. Also note the light blue gradient (half the area of the dark blue one) used to refocus the selected slice (see fig. 1.6a for explanation). For non-selective excitation, no gradient is played along with the RF pulse (d): all the energy is deposited in the centre of the transmit k-space (e), so in the image space, the whole volume is excited (f).

Solving eq. (1.11) in the STA approximation gives the impact of a {RF pulse; gradient} pair of duration T on transverse magnetisation:

$$M_\perp(\mathbf{r}) = \imath\gamma M_0 \int_0^T \mathrm{B}_1^+(t)\, \mathrm{e}^{\imath\mathbf{r}\cdot\mathbf{k}(t)}\, dt \tag{2.15}$$

Finally, introducing the complex flip angle $\hat{\alpha} = \alpha\, \mathrm{e}^{\imath\varphi}$ (φ being the phase of $M_\perp$) and recognising that $\hat{\alpha} = \arcsin(M_\perp/M_0)$ for $\alpha < 90°$ [Boulant 2012] :

$$\hat{\alpha}(\mathbf{r}) = \imath\gamma \int_0^T \mathrm{B}_1^+(t)\, \mathrm{e}^{\imath\mathbf{r}\cdot\mathbf{k}(t)}\, dt \tag{2.16}$$

Here we recognise once again the Fourier transform. Equation (2.16) conveys that with the right RF pulse and the right set of gradients, we can excite a volume according to any pattern, provided of course that we can accommodate a pulse long enough. This

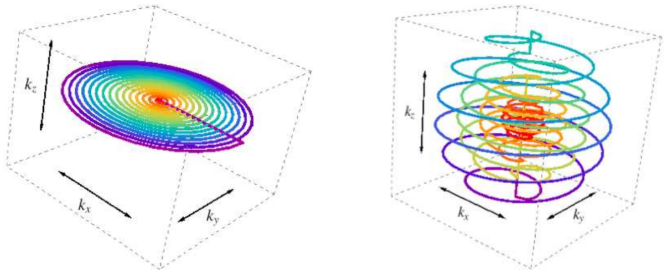

(a) 2D spiral (b) 3D spiral

Figure 2.14: Transmit k-space trajectories of multidimensional RF pulses to selectively excite (a) any 2D pattern repeated along the z axis and (b) a portion of the FOV delimited in the three dimensions. From [Cloos 2012c].

concept gave rise to a plethora of {RF pulse; gradient} strategies, designed for partial volume imaging. We can name a few popular so-called multidimensional pulses:

- 2D spiral trajectories to selectively excite a cylinder, *e.g.* along z, with excitation modulation in the (k_x, k_y) plane only, and $k_z = 0\,\mathrm{m}^{-1}$ everywhere (fig. 2.14a). Those can be used for pencil-beam navigators [Köhler 2011]. With a 2D spiral, one can also select a square beam, and image a zoomed volume by placing the read direction in the beam direction [Amadon 2013].
- 3D spiral trajectories that produce excitation modulation along all transmit k-space dimensions, to select only a small volume (fig. 2.14b) and reduce the acquisition FOV without fear of aliasing, thus gaining either on TA or resolution [Schneider 2013, Malik 2014].

. . . Applied to Flip Angle Homogenisation: dynamic RF shimming

Now that we have introduced, in the STA approximation, the concept of transmit k-space, let us roll back to the harsh reality of B_1^+ inhomogeneity. Multidimensional RF pulses can actually be used to counteract B_1^+ homogeneity: this is commonly called 'dynamic RF shimming'.

In eq. (2.16), we considered that B_1^+ depends only on time (RF pulse shape), not on spatial location $\mathbf{r}$. Still considering a sTx system, we can rewrite it taking into account the transmit sensitivity profile of the coil, with $B_1^+(\mathbf{r}, t) = p(t)S^+(\mathbf{r})$:

$$\hat{\alpha}(\mathbf{r}) = \imath\gamma \underbrace{S^+(\mathbf{r})}_{\substack{\text{transmit}\\ \text{sensitivity}}} \underbrace{\int_0^T p(t)\, \mathrm{e}^{\imath \mathbf{r}\cdot\mathbf{k}(t)}\, dt}_{\substack{\text{excitation}\\ \text{modulation}}} \tag{2.17}$$

where T is the pulse duration, $p(t)$ is the RF pulse shape and $S^+(\mathbf{r})$ the transmit sensitivity at location $\mathbf{r}$. The idea behind multidimensional pulses for excitation inhomogeneity mitigation is to design a {RF pulse; gradient} pair whose excitation pattern (integral term in eq. (2.17)) is the inverse of the transmit sensitivity profile of the coil, so that $\hat{\alpha}$ is

uniformly distributed. This is illustrated in fig. 2.15 where the effect of two dynamic RF shimming implementations are compared with their standard pulse counterparts.

For selective excitation, fast-k_z spokes [Saekho 2006, Yip 2006, Grissom 2012, Wu 2014] are a popular approach. They consist in a succession of sinc RF pulses ('spokes') applied along the k_z direction to excite a slice, interleaved with small G_x and G_y gradient pulses – often called 'blips' – to place each spoke in a different $(k_x; k_y)$ location. The resulting transmit k-space trajectory is pictured on the top-left panel of fig. 2.15b. Doing so, each successive {blip; spoke} pair modulates the in-slice FA distribution with a different pattern, so that at the end of the pulse, the sensitivity profile is compensated (bottom panel).

For non-selective excitation, two notable techniques are SPINS (short for spiral non-selective RF pulses) [Malik 2012] and k_T-points [Cloos 2010, Amadon 2011]. A typical transmit k-space trajectory produced by k_T-points is shown on the top-right panel on fig. 2.15b. Contrarily to fast-k_z spokes, as they are non-selective, they are based on a succession of rect pulses, whose energy is successively deposited at different $(k_x; k_y; k_z)$ locations to modulate excitation patterns over the whole FOV. Note that all RF is transmitted at fixed points in k-space, *i.e.* when all gradients are off.

The principle of dynamic RF shimming boils down to homogenising flip angle, not B_1^+. Some studies have taken a step further by looking at sequence level to homogenise signal itself, for a given tissue. Defining a target tissue (characterised by its T_1 and T_2), this direct signal control (DSC) approach [Malik 2015, Beqiri 2018] takes advantage of the interaction between successive pulses played throughout a sequence, and updates the RF shimming parameters used from one pulse to the next.

As k_T-points constitute the centrepiece of this thesis, various state-of-the-art implementations will be described in section 2.4 (page 72).

More Control with Parallel Transmission

Multidimensional pulses are fantastic tools to precisely control magnetisation, be it for inner volume excitation or for homogenisation. However, their principal limitation lies in their generally long durations, which make them unsuitable for routine applications [Setsompop 2008b]. For instance, more complex excitation patterns require more extensive exploration of the transmit k-space. Similarly, to achieve better homogeneity, k_T-points (or fast-k_z spokes) pulses require more points (spokes) to explore a wider range of spatial frequencies. Ultimately, pulse complexity is limited by hardware and physiological restrictions related to RF energy and gradient amplitude and slew rate. Approaching those limits also makes the pulses prone to system imperfections [Ullmann 2005].

The advent of pTx systems has revived the interest for multidimensional pulses. Making use of different transmit channels by carefully mapping their respective sensitivity profiles has allowed for shorter pulses [Katscher 2003, Grissom 2006], more controlled SAR [Zhu 2004, Beqiri 2017], or both.

In addition, in the particular case of dynamic RF shimming that is of interest for us, pTx is not a fundamental requirement, but it proves useful in practice. Indeed, even if

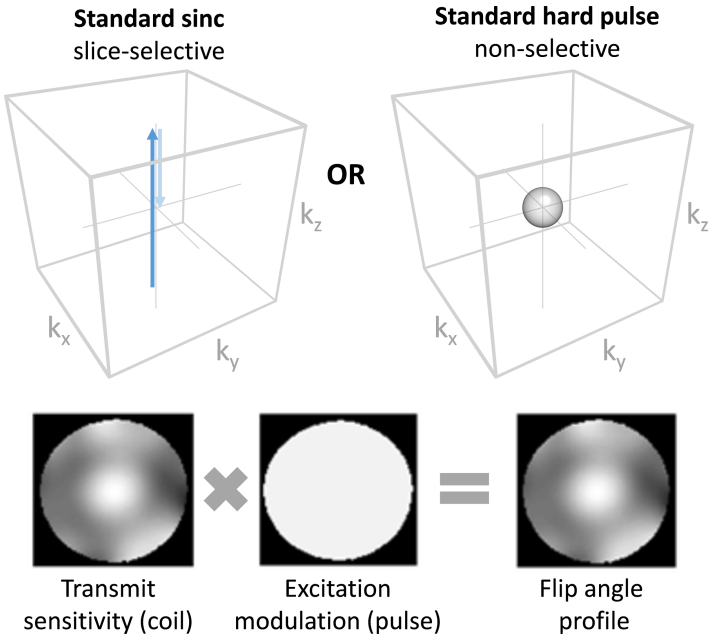

(a) Standard pulses

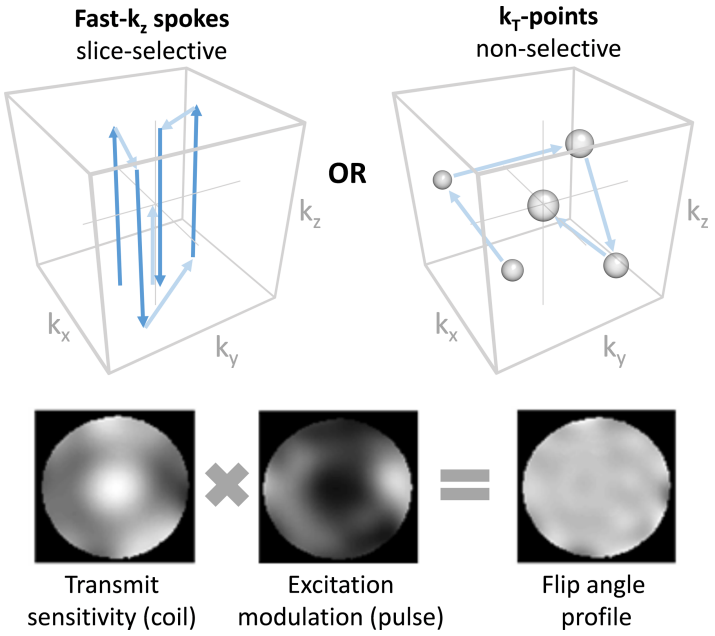

(b) Dynamic RF shimming pulses

Figure 2.15: Illustration of the use of excitation modulation to compensate transmit sensitivity inhomogeneity (eq. (2.17)). Standard pulses (selective and non-selective) (a) and some example dynamic RF shimming pulses (also selective and non-selective) (b) used on a coil with inhomogeneous transmit profile. By modulating the excitation, dynamic RF shimming pulses restore an homogeneous FA distribution. Dark blue arrows show trajectories concomitant with RF, while light blue ones correspond to gradients played alone to reach a different k-space location. For k_T-points, no gradient is played during RF transmission. NB: only one slice shown to demonstrate the effect on FA profile, even though rect and k_T-points pulses excite the whole volume. Adapted from [Setsompop 2008b].

one can homogenise FA despite an inhomogeneous B_1^+, having a less inhomogeneous B_1^+ field in the first place makes the whole operation easier. Rewriting eq. (2.12) in the case of fully independent waveforms (not just independent weightings of the same waveform) gives:

$$B_1^+(\mathbf{r},t) = \sum_{c=1}^{N_{Ch}} p_c(t) S_i^+(\mathbf{r}) \tag{2.18}$$

Now, eq. (2.17) can be extended to express additional control on excitation offered by pTx:

$$\hat{\alpha}(\mathbf{r}) = \imath\gamma \sum_{c=1}^{N_{Ch}} S_c^+(\mathbf{r}) \int_0^T p_c(t)\, \mathrm{e}^{\imath \mathbf{r}\cdot\mathbf{k}(t)}\, dt \tag{2.19}$$

This equation will be used later on when reviewing the k_T-points method more extensively (section 2.4). In the meantime, let us focus on calibration techniques that are needed for pulse design, be it static or dynamic RF shimming, in sTx or pTx.

2.2.4 Calibration Needed for Pulse Design

B_1^+ Mapping

So far, we have seen that, either for static or dynamic RF shimming pulse design, information about the transmit sensitivity profile (amplitude and phase) for each available channel c (if using pTx) in each point $\mathbf{r}$ of the FOV, $S_c^+(\mathbf{r})$, was necessary: this is B_1^+ mapping.

According to eq. (1.13), the FA is proportional to the B_1^+ field when on-resonance, which means pulse sequences can be designed to measure those sensitivity maps. Numerous B_1^+ mapping methods have been proposed with different underlying concepts, many of which are described in [Park 2014]. Among those, the actual flip angle imaging (AFI) sequence [Yarnykh 2007, Amadon 2008, Nehrke 2009, Boulant 2010] is a popular and accurate approach when employed with 3D encoding and non-selective excitation in particular, and can be used to evaluate the performance of designed pulses. It is however quite time-consuming – all the more so when several channels have to be mapped – so it does not fit our need for a fast calibration sequence to play at the beginning of a subject's examination.

Faster yet less accurate techniques have been developed to fulfil this requirement, such as the 2D multi-slice method sat-TFL – known as XFL in the pTx world – [Van de Moortele 2007,Fautz 2008,Chung 2010,Amadon 2010,Amadon 2012]. This is the method used in NeuroSpin for pTx experiments at UHF, and we will also use it for single-channel measurements at 3 T presented in chapter 4. Finally, it was the technique chosen by Siemens Healthcare for B_1^+ mapping on their clinical pTx 3 T imagers (section 2.3), and therefore used in chapters 5 and 6.

Off-Resonance Mapping

For accurate pulse designs, off-resonance (Δf_0) effects need to be taken into account. For non-selective excitation, hard pulses are used in CP or EP mode. As seen in section 1.1.3,

they are generally broadband enough to be rather insensitive to ΔB_0 inhomogeneity or chemical shift effects. The full width at half-maximum (FWHM)[5] of the frequency response is 12 kHz and 3 kHz, for pulse lengths of 100 µs and 400 µs respectively. Off-resonance mapping is therefore unnecessary for non-selective RF shimming pulse design. Frequency response of dynamic RF shimming pulses is however not straightforward and not always as broadband.

To obtain an off-resonance map, the easiest and fastest way is to measure the signal phases φ_1 and φ_2 in each voxel from two echoes acquired at different echo times TE_1 and TE_2:

$$\Delta f_0 = \frac{1}{2\pi} \frac{\varphi_2 - \varphi_1}{TE_2 - TE_1} \tag{2.20}$$

where φ is given in radians, TE in seconds and Δf_0 in Hz. As in all phase measurement, phase wrapping occurs. Without resorting to phase-unwrapping post-processing methods [Chavez 2002], it is not possible to measure Δf_0 if the phase evolution between the two echoes is beyond $\pm\pi$: the range of measurable frequencies is limited by $\Delta TE = TE_2 - TE_1$. At 3 T, minimum achievable ΔTE is about 1 ms, which corresponds to frequencies in the ± 500 Hz range. This can be sufficient for some applications, even when fat is involved (resonance shift of -400 Hz to -450 Hz at 3 T), but sometimes more bandwidth is needed. Such situation will occur in chapter 4, and is dealt with in appendix A.

As ΔTE is reduced, though, phase becomes more influenced by noise-induced random variations, and Δf_0 is less accurately estimated. One way to circumvent this problem, when there are no chemical compounds other than water and fat, and when fat is not important to the pulse design (this is the case for brain imaging), is to set TE_1 and TE_2 at successive water-fat in-phase echo times. At 3 T, this typically corresponds to $TE_1 = 2.46$ ms and $TE_2 = 4.92$ ms. The available bandwidth is reduced (± 200 Hz), but since the water and fat phases coincide, only B_0 variations are mapped, and such bandwidth can be sufficient. Doing so, we no longer map off-resonance (Δf_0) but ΔB_0: this is B_0 mapping.

Another – more elegant – way to improve accuracy is described by Amadon *et al.* and consists in acquiring three echoes or more instead of two. The bandwidth is defined by the time between the two closest echoes, which can be as short as possible without fearing for accuracy. Indeed, the third echo is placed further away to bring leverage, and its phase evolution is unwrapped thanks to the two first ones [Amadon 2008]. This method is slightly longer than the two-echo one because having to acquire a third echo makes the TR longer. However it allows to measure wide ranges of Δf_0 without wrapping.

Patient Safety

Section 2.1.2 introduced, among several challenges associated with high field MRI, the issue of local SAR hotspots. In order to estimate the magnitude of these hotspots and to control the local SAR, knowledge of the electric field at each point in the body is needed

[5] FWHM is the bandwidth over which the response is at least half of the maximum (that is on-resonance).

to solve eq. (2.7). Unfortunately, this field is not directly measurable, and modelling of its distribution is required to get an estimation of the energy deposited in the patient.

In this section only local transmit coils are considered, since most research that led to the control of SAR in pTx as we know it was performed at UHF in the head. A description of SAR control in clinical systems, using whole-body coils will be done in section 2.3.2.

On single-channel transmission (sTx) systems, with a fixed transmission mode and a fixed region of exploration using a local coil, extensive modelling of the electric field distribution in the tissues is possible. For example, in the head, a population of models each describing the various tissue types encountered allows to define *a priori* an upper bound of local SAR [Wang 2007], related to the global SAR: the so-called K factor expresses this relationship. Peak local SAR can be estimated in the head and patient safety be ensured.

However on a pTx system, there is an infinity of possible transmit modes. There has therefore been a need for SAR models that take into account not only the energy of the RF pulse, but the complex RF weights used, describing amplitude and phase relations between the different channels. The Q-matrix formulation was introduced for that purpose [Zhu 2004, Graesslin 2012]. For a 10-g-averaged volume centred in $\mathbf{r}$, the local SAR is defined, for a hard pulse of duration T (*i.e.* $\int_0^{\mathrm{TR}} p(t)dt = T$), as:

$$\mathrm{SAR}_{10\mathrm{g}}(\mathbf{w}, \mathbf{r}) = \frac{T}{\mathrm{TR}}\ \mathbf{w}^{\mathrm{H}}\mathbf{Q}(\mathbf{r})\mathbf{w} \tag{2.21}$$

where $\mathbf{w} = \begin{bmatrix} w_1 & w_2 & \cdots & w_{N_{Ch}} \end{bmatrix}^{\mathrm{T}}$ is the $N_{Ch} \times 1$ vector containing the complex weights for each channel, and $\mathbf{Q}(\mathbf{r})$ is an $N_{Ch} \times N_{Ch}$ matrix summarising tissue properties and electric field in the small volume centred in $\mathbf{r}$. Similarly to what is done in sTx, for a given transmit coil model and exposed region – *e.g.* the head – those Q-matrices can be evaluated via careful modelling.

In order to find the peak local SAR, one must perform this calculation in every point in space. This is time-consuming and computationally expensive when considering the whole head, let alone when considering the whole body (section 2.3.2). In addition, we will see later that some pulse designs algorithms – this is the case for k_T-points – take SAR constraints into account all along the optimisation process, to ensure that the output pulse respects safety regulations. In such a case, faster SAR evaluation is compulsory. This was made possible by the introduction of virtual observation points (VOPs) [Eichfelder 2011]. The set of Q-matrices is compressed up to a factor 5000: the smaller set obtained represents 'virtual locations' whose local SAR would be the highest in any configuration. Now equation eq. (2.21) becomes:

$$\mathrm{SAR}_{10\mathrm{g},i}(\mathbf{w}) = \frac{T}{\mathrm{TR}}\ \mathbf{w}^{\mathrm{H}}\mathbf{Q_i}\mathbf{w} \tag{2.22}$$

where i is the VOP index. Peak local SAR is therefore defined, for N_{VOP} VOPs, as:

$$\mathrm{SAR}_{10\mathrm{g,peak}}(\mathbf{w}) = \frac{T}{\mathrm{TR}}\ \max_i(\mathbf{w}^{\mathrm{H}}\mathbf{Q_i}\mathbf{w}), \quad 1 \leq i \leq N_{VOP} \tag{2.23}$$

Finally, a 'global VOP' can also be defined to account for global SAR in calculations:

$$\mathrm{SAR}_{\mathrm{global}}(\mathbf{w}) = \frac{T}{\mathrm{TR}}\ \mathbf{w}^{\mathrm{H}}\mathbf{Q_{global}}\mathbf{w} \tag{2.24}$$

As a final note, let us keep in mind that SAR is often perceived as a conservative metric, that is only loosely correlated with the real physiological parameter we want to measure: body temperature increase. SAR models do not take tissue perfusion and heat dissipation capacity into account, so they generally overestimate the actual temperature increase [Fiedler 2017]. There is ongoing research to improve patient safety monitoring by directly monitoring temperature, for instance with 'temperature VOPs' [Boulant 2016].

2.3 Current State of B_1 Artefacts Reduction in Clinical Routine 3 T MRI

Passive RF shimming, described in section 2.2.1, and especially the RF cushion for abdominal imaging (fig. 2.11) exists in clinical routine at 3 T. It is however no longer regarded as state-of-the-art, as parallel transmission is now available on some 3 T scanners. Here we will describe the RF transmission modes available on the different clinical scanners utilised throughout this thesis. All are manufactured by Siemens Healthcare GmbH, so we will mostly focus on the products and solutions proposed by this vendor.

As far as pTx is concerned, several manufacturers have proposed clinical two-channel pTx 3 T systems. To my knowledge, as of today, none has provided solutions more advanced than static RF shimming for excitation inhomogeneity mitigation.

2.3.1 RF Transmission Set-Ups

The study on breast MRI presented in chapter 4 was carried out on a Siemens MAGNETOM Verio 3 T scanner at Henri Mondor hospital in Créteil (France). The Verio is a wide-bore (70 cm) single-transmit-channel scanner, equipped with the VQ gradient engine (theoretical maximal performances: 43 mT/m, for a slew rate of 180 T/m/s) and operated by *syngo*.MR VB17A software. Although it is a sTx system, the body coil consists in two ports. RF signal output from a single amplifier is then split into two components, that are adjusted in amplitude and phase before feeding either port. This technology, called *TrueForm* ™ [Nistler 2007, Nistler 2010, Panagiotelis 2009] was introduced in 2007, and permits some degrees of static RF shimming. It is however a very limited implementation as the pulse is not adapted to the patient in the magnet: it is an anatomy-specific static RF shimming. For instance, head imaging is executed in CP mode, while the body coil is used in a fixed EP mode.

Some initial developments were led on a MAGNETOM Prisma 3 T scanner, either in NeuroSpin or within the *Association Institut de Myologie* (AIM) in Paris. This is a 60-cm-bore scanner that comes with the XR gradient engine (theoretical performances: 80 mT/m, for a slew rate of 200 T/m/s), running *syngo*.MR VE11C, and equipped with two-channel pTx as standard. Liver-related clinical studies (chapters 5 and 6), were performed at Henri Mondor hospital on a MAGNETOM Skyra, a wide-bore 3 T scanner with an XQ gradient engine (same performances as the VQ engine), running *syngo*.MR VE11C. Some

Skyras have a two-channel pTx option, which is the case for this scanner. Several transmit modes are offered on these clinical pTx systems [Siemens Healthcare 2013]:

- TrueForm™, a pTx emulation of the anatomy-specific static RF shimming from previous generations (*e.g.* Verio).
- Patient- and volume-specific static RF shimming, based on actual B_1^+ maps acquired on the patient. Patient-specific RF shimming optimises RF coefficients to homogenise the B_1^+ distribution in the whole FOV, while volume-specific focuses on a smaller portion of the volume.
- TrueShape™: this corresponds to the full control of the waveforms produced by each channel. The main product associated with this capability is '*syngo* ZOOMit', which allows to selectively excite a beam through the whole volume, as described earlier when we introduced multidimensional pulses. This transmit mode is not currently used for dynamic RF shimming.

In the two latter cases, B_1^+ maps are needed to compute either the static RF shimming coefficients or the multidimensional 'ZOOMit' pulse. The scanner performs an automated adjustment procedure to measure B_1^+ maps for each channel using a sat-TFL sequence, and provides VOPs for SAR management. In some cases, it also measures ΔB_0 maps.[6]

2.3.2 SAR Control in Clinical Systems

We have introduced notions of patient safety in sections 2.1.2 and 2.2.4, how we estimate global SAR with transmitted and reflected power, and how we could estimate peak local SAR with VOPs. However we have not discussed SAR limitations.

Table 2.3 gathers a few relevant SAR limits imposed by the IEC [IEC-60601-2-33 2010]. First, several sets of limits are defined, of which two are shown: the normal and the first-level operating mode. First-level operating mode allows for higher SAR limits, provided the examination is supervised by a physician; it can be useful in some cases to exceed 'normal' SAR limits to achieve a lower TR (*e.g.* for a shorter TA in a breath-hold acquisition) or a higher flip angle. We will consider the normal operating mode in the works hereby presented.

We used the example of a head coil earlier. When transmitting through a head coil, one must respect two restrictions: a SAR_{global} limit of 3.2 W/kg and a SAR_{10g} limit of 10 W/kg. Those values correspond to both volumic and local transmit coil limitations (table 2.3); indeed, such a coil exposes the head to a far field (as volumic coils do) and to a near field, as local ones do.

All clinical studies conducted here will utilise a body coil, which is the main, default transmit/receive built-in coil, fixed and centred inside the magnet bore. One might notice in table 2.3 that the IEC imposes no limit whatsoever on SAR_{10g} induced by such coils. A 2014 study based on simulations at 1.5 T on several anatomical models, placed at different

[6] All this information is available to users willing to use it for research purpose, at the following location on the scanner console (*syngo*.MR VD13D to VE11C): `C:\MedCom\MriProduct\PhysConfig`. Among the files found here, two MATLAB-compatible ones are of particular interest for us: `AdjDataUser.mat` (B_1^+ and ΔB_0 maps), and `SarDataUser.mat` (patient safety).

Table 2.3: SAR limitations as defined in [IEC-60601-2-33 2010] for body coils and local transmit coils (6-minute average).

	Normal OM[a] (W/kg)	First-level controlled OM[a] (W/kg)
Volumic coils:		
SAR_{global}	2	4
SAR_{global} (head)	3.2	3.2
$SAR_{exposed}$[b]	2–10	4–10
SAR_{10g}	—	—
Local transmit coils:		
SAR_{10g} (head and trunk)	10	20
SAR_{10g} (extremities)	20	40

[a] OM: operating mode. *Normal OM*: default mode of operation of the scanner, in which none of the outputs have a value that may cause physiological stress to patients. *First-level controlled OM*: mode of operation of the MR equipment in which one or more outputs reach a value that may cause physiological stress to patients, which needs to be controlled by medical supervision.
[b] Exposed body sar scales dynamically with the ratio r = exposed patient mass / total patient mass; normal OM: $SAR_{exposed} = 10 - 8\,W/kg$; first-level controlled OM: $SAR_{exposed} = 10 - 6\,W/kg$.

positions in the scanner (centred at head-, torso-, knee-level for instance) has demonstrated that peak local SAR can exhibit large variations, and significantly exceed limitations imposed to local transmit coil, with values over 100 W/kg in first-level controlled operating mode [Murbach 2014]. Still, 1.5 T MRI has existed for more than two decades, and is deemed safe. This can be attributed to the fact that such high SAR values generally occur in extremities, where tissue perfusion and heat dissipation are quite efficient, so a high SAR does not necessarily induce a high temperature elevation.

Figure 2.16 shows the SAR distribution in the body of nine volunteers when torso imaging is performed at 3 T in CP mode. We can notice a large variation of local SAR in the body, with peak values in the arms, that largely exceed the colour-scale range. Stated peak SAR in this study is 80 W/kg [Homann 2012].

Similarly to 1.5 T, 3 T imaging in single-channel mode has been safely performed for a long time. But even though local SAR is not limited by the IEC norm, there is a consensus that it should be supervised, and not exceed that of CP mode when using pTx scanners. The impact of pTx on SAR distribution was recently studied in simulation [Murbach 2016] with a similar approach as [Murbach 2014], *i.e.* several anatomical models – [Christ 2010, Gosselin 2014] – and imaging positions. An interesting result of this study is reported in fig. 2.17. Here we can see, for six different models and 10 imaging positions, the simulated global SAR (in black). The chequered black plot shows the possible local SAR values corresponding to the CP mode on these different models (corresponding values at 1.5 T are shown in light brown for reference). Then, the black line corresponds to the highest SAR achievable in pTx, for each situation. Naturally it is systematically higher than in CP mode, but it is not a useful pTx setting in practice. A more useful setting is a RF shimming that allows highest B_1^+ homogeneity; those are reported in grey, for all anatomies

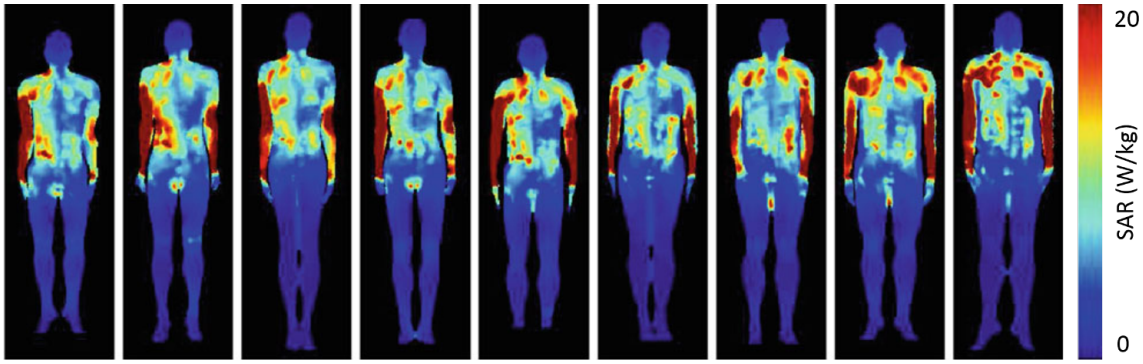

Figure 2.16: SAR distribution in the body of nine volunteers at 3 T with single-channel transmission (CP mode). Local SAR values reach 46 W/kg (average: 31 W/kg) in torso and even up to 80 W/kg (average: 58 W/kg) in extremities. [Homann 2012].

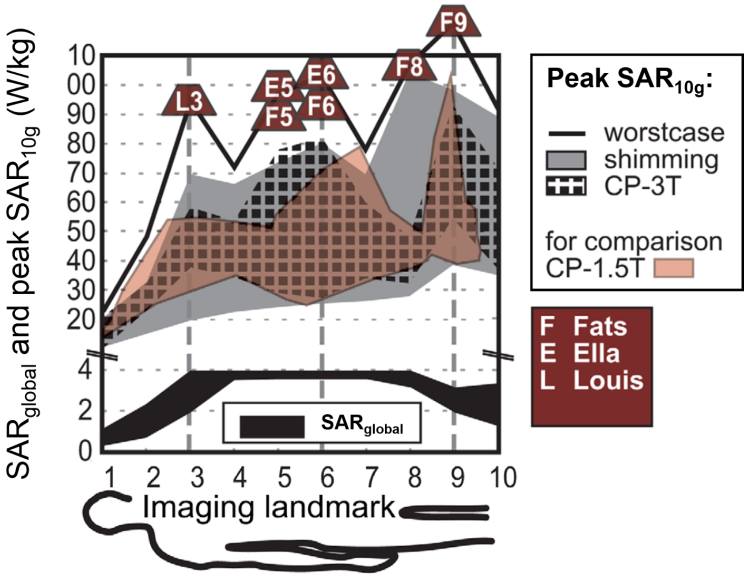

Figure 2.17: Global and 10 g SAR simulations in two-channel pTx at 3 T on 6 anatomical models from the Virtual Population [Christ 2010, Gosselin 2014], as a function of imaging landmark (corresponding to different imaging regions, which means different patient centrings in the body coil), and for different transmit modes: CP, worst-case SAR and static RF shimming. Highest-SAR configurations are indicated, *e.g.* as F9 for the 'Fats' model imaged at knee height. Full study in [Murbach 2016].

and positions. Some of these configurations present higher local SAR than CP: they are discarded from admissible shims. In practice, for a given position, SAR resulting from a RF shimming configuration – or more generally a given RF pulse – is calculated for every model anatomy. It is then expressed as a percentage relatively to the corresponding single-channel SAR (with an additional safety margin). Only pulses yielding less than 100 % relative SAR are accepted. This is what the VOPs provided by clinical 3 T scanners (section 2.3.1) correspond to.

2.3.3 Objectives and Challenges

Although modern high-end 3 T scanners like the Skyra and the Prisma have the ability to routinely implement multidimensional pulses (section 2.3.1), with inline B_1^+ mapping and VOP generation (section 2.3.2), no product currently exists to perform dynamic RF shimming in clinical practice.

The aim of this thesis is to demonstrate the applicability of dynamic RF shimming to clinical protocols, with minimal modification of existing tools. In particular, for studies on the Skyra system, we will use the VOPs provided by the scanner for SAR prediction during pulse design, and we will rely on manufacturer-provided B_1^+ maps measured during automatic adjustment steps. We will focus on non-selective excitation, and will implement dynamic RF shimming through k_T-points.

For studies on the older Verio scanner, no such tools are available, so we had to measure B_1^+ maps by ourselves. On a sTx system, global SAR as well as peak local SAR observed in various body areas are related to power by different constants specific to patient characteristics (mostly weight and position in the scanner). We managed to get hold of SAR calibration information via log files containing those constants, written after each performed sequence. Those parameters depend only on the patient, not on the sequence, so we could retrieve them *e.g.* after a short scout sequence, to predict SAR at pulse design time.

2.4 K_T-Points: State of the Art

Before delving into the work realised along this thesis project, let us review some details about k_T-points implementation, and see the results of some studies involving k_T-points for dynamic RF shimming.

2.4.1 Description

K_T-points are a succession of rectangular RF sub-pulses interleaved with gradient blips [Amadon 2011, Cloos 2010]. In the STA approximation, these blips allow to move through the transmit k-space between each sub-pulse, to excite several spatial frequencies and produce a complex FA pattern. In addition, in pTx systems, each sub-pulse can have different weights, and hence correspond to a different 'RF shim'. Figure 2.18 shows an example of k_T-points pulse shape and corresponding trajectory in transmit k-space.

Optimisation Problem

To obtain a k_T-points pulse, we solve a magnitude least-squares problem to minimise a cost function f, defined as the normalised root-mean-square error (NRMSE) of the FA

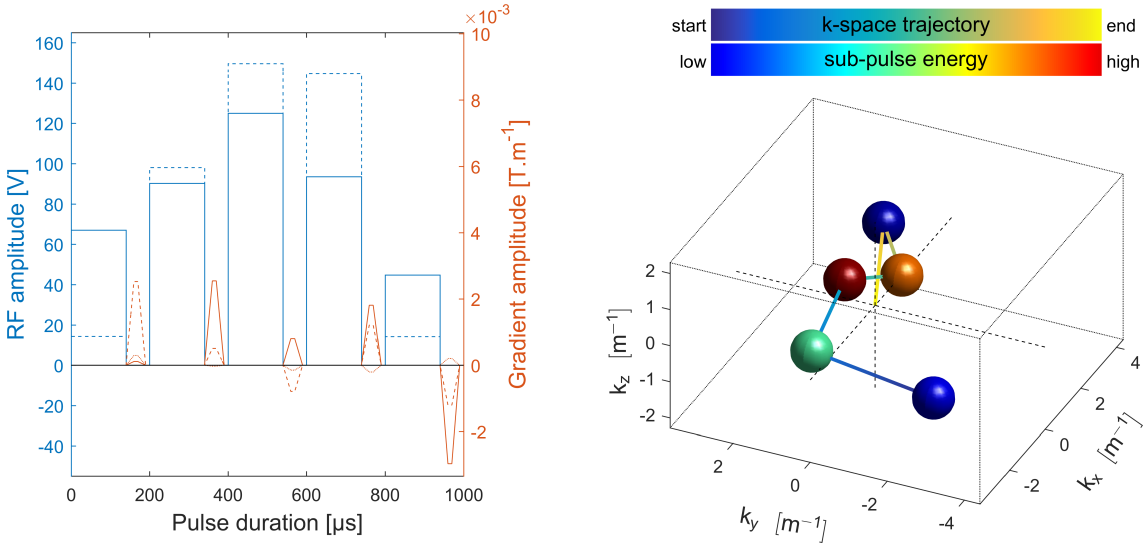

Figure 2.18: Example 5-k_T-points pulse on a two-channel pTx system. Left-hand side: RF amplitudes (blue) for each channel (solid and dashed lines) and gradient amplitudes (orange) for each axis (solid, dashed and dotted lines); RF phase is not shown. Right-hand side: corresponding transmit k-space trajectory.

distribution in the region of interest (ROI) from a FA target α_T:

$$\begin{aligned} f &= \mathrm{NRMSE}(\mathbf{a}) \\ f &= \frac{1}{\alpha_T}\sqrt{\sum_{i=1}^{N}\frac{(|\hat{\alpha}_i| - \alpha_T)^2}{N}} \end{aligned} \tag{2.25}$$

where $\hat{\mathbf{a}}$ is the vector of complex FAs in each voxel and N is the number of voxels in the volume of interest: $\hat{\mathbf{a}} = \begin{bmatrix}\hat{\alpha}_1 & \dots & \hat{\alpha}_i & \dots & \hat{\alpha}_N\end{bmatrix}$.

The FA in each location, and hence f, depends on the sub-pulse complex coefficients for each channel, on their transmit k-space locations and on their durations [Gras 2015]. With fixed sub-pulse durations, if we denote by $\mathbf{w}$ the vector of complex weights for all sub-pulses (concatenated) and by $\mathbf{k}$ the concatenated vector of k-space locations for each sub-pulse, the optimisation problem can be written for N_{Ch} channels and N_{kT} sub-pulses as:

$$\begin{aligned} \underset{\mathbf{w},\mathbf{k}}{\arg\min} \quad & f(\mathbf{w},\mathbf{k}), \qquad (\mathbf{w},\mathbf{k}) \in \mathbb{C}^{N_{Ch}N_{kT}} \times \mathbb{R}^{3N_{kT}} \\ \text{s.t.} \quad & \mathrm{SAR}_{\mathrm{global}}(\mathbf{w}) \leq \mathrm{SAR}_{\mathrm{global,max}}, \\ & \mathrm{SAR}_{10\mathrm{g,v}}(\mathbf{w}) \leq \mathrm{SAR}_{10\mathrm{g,max}}, \quad 1 \leq v \leq N_{VOP}, \\ & \mathcal{P}_c(\mathbf{w}) \leq \mathcal{P}_{\max}, \quad 1 \leq c \leq N_{Ch}, \\ & |w_\ell| \leq V_{\max}, \quad 1 \leq \ell \leq N_{kT}N_{Ch}. \end{aligned} \tag{2.26}$$

As we can see, in addition to patient safety constraints, hardware is also protected, with limits on average power per channel $\mathcal{P}_c(\mathbf{w})$ and maximum voltage $V_{\max}$.

The cost function f is iteratively minimised under strict hardware and patient safety constraints, with a gradient descent algorithm – in practice the *active-set* function from MATLAB's (The Matworks, Natick, MA, USA) *Optimization Toolbox*. On each iteration,

FA needs to be evaluated in each voxel to calculate the cost function f. This can be done in several ways as described below.

STA Approximation

Within the small tip angle approximation, we can calculate the FA in each voxel $\mathbf{r}$ with eq. (2.19). Using the k_T-points formalism, the integral term can be discretised:

$$\int_0^T p_c(t)\, \mathrm{e}^{\imath \mathbf{r}\cdot\mathbf{k}(t)}\, dt = \sum_{p=1}^{N_{kT}} \tau w_{p,c}\, \mathrm{e}^{\imath \mathbf{r}\cdot\mathbf{k}_p} \tag{2.27}$$

where τ is the duration of sub-pulses, $w_{p,c}$ is the complex weight associated to the pth sub-pulse and cth channel, and $\mathbf{k}_p$ the k-space location vector of the pth sub-pulse.

Introducing the normalised complex weights $\mathbf{x}$ such that $\mathbf{w} = V_{\max}\, \mathbf{x}$, and taking off-resonance dephasing and excitation into account, eq. (2.19) can be rewritten as:

$$\hat{\alpha}(\mathbf{r}) = \imath\gamma\, V_{\max} \sum_{p=1}^{N_{kT}} \sum_{c=1}^{N_{Ch}} x_{p,c}\, S_c^+(\mathbf{r}) \tau \mathrm{e}^{\imath \mathbf{r}\cdot\mathbf{k}_p} \underbrace{\mathrm{e}^{\imath 2\pi T_p \Delta f_0(\mathbf{r})}}_{\substack{\text{off-resonance}\\ \text{dephasing}}} \underbrace{\mathrm{sinc}(\pi\tau\Delta f_0(\mathbf{r}))}_{\substack{\text{off-resonance}\\ \text{excitation}}} \tag{2.28}$$

where $\Delta f_0(\mathbf{r})$ is the off-resonance given in Hz, and t_p is the time between the centre of the pth sub-pulse and the end of the pulse. If we denote the duration of gradient blips by τ_b, then $T_p = (N_{kT} - p)(\tau + \tau_b) + \tau_b + 0.5\tau$. The sinc term expressing off-resonance excitation corresponds to the Fourier transform of each individual square sub-pulse.

Since $\mathbf{x}$ is the concatenation of all $x_{p,c}$ as an $N_{kT}N_{Ch} \times 1$ vector, the vector of flip angle in each location, $\hat{\mathbf{a}}$, is calculated as a single matrix product:

$$\hat{\mathbf{a}} = \mathbf{A}\, \mathbf{x} \tag{2.29}$$

where $\mathbf{A}$ is of dimensions $N_{voxels} \times N_{kT}N_{Ch}$ and is called the encoding matrix; its row-vectors $\mathbf{A_r}$ each correspond to a specific voxel at location $\mathbf{r}$:

$$\mathbf{A_r}(\mathbf{k}) = \left[\imath\gamma V_{\max} S_i^+(\mathbf{r}) \tau \mathrm{e}^{\imath \mathbf{r}\cdot\mathbf{k}_i} \mathrm{e}^{\imath 2\pi T_i \Delta f_0(\mathbf{r})}\, \mathrm{sinc}(\pi\tau\Delta f_0(\mathbf{r}))\right]_{1 \le i \le N_{kT}N_{Ch}} \tag{2.30}$$

The minimisation problem can be written, in the STA approximation, as:

$$\begin{aligned}
\underset{\mathbf{x},\mathbf{k}}{\arg\min} \quad & \| |\mathbf{A}(\mathbf{k})\mathbf{x}| - \alpha_T \|_2, \qquad (\mathbf{x},\mathbf{k}) \in \mathbb{C}^{N_{Ch}N_{kT}} \times \mathbb{R}^{3N_{kT}} \\
\text{s.t.} \quad & \mathrm{SAR}_{\mathrm{global}}(\mathbf{x}) \le \mathrm{SAR}_{\mathrm{global,max}}, \\
& \mathrm{SAR}_{10\mathrm{g,v}}(\mathbf{x}) \le \mathrm{SAR}_{10\mathrm{g,max}}, \quad 1 \le v \le N_{VOP}, \\
& \mathcal{P}_c(\mathbf{x}) \le \mathcal{P}_{\max}, \quad 1 \le c \le N_{Ch}, \\
& |x_\ell| \le 1, \quad 1 \le \ell \le N_{kT}N_{Ch}.
\end{aligned} \tag{2.31}$$

SAR and power constraints are monitored by the scanner at runtime, and even during the preparation of the sequence for sTx scanners, or newer pTx scanners (Skyra and Prisma). This means that the sequence will not be executed if patient safety and hardware protection are not ensured, no matter the pulse used. Still, accounting for those constraints at design time guarantees that the pulse will be accepted by the scanner and that the sequence will run to completion, which is an indisputable advantage in clinical routine.

Large Tip Angles

Although the STA approach is computationally efficient, it does not allow to design k_T-points pulses for flip angles over 90°. In particular, a different method should be used for inversion pulses.

When considering large tip angles (LTAs), the visualisation of multidimensional pulses in terms of transmit k-space does not hold. Instead, one should consider the evolution of a magnetisation vector initially pointing along the z axis, when subject to a {RF pulse; static field gradients} pair. This is achieved by numerically integrating Bloch's equation. Rewriting eq. (1.8) in matrix form, adapting the notations to match the current situation gives, at time t and location $\mathbf{r}$:

$$\frac{\partial \mathbf{M}}{\partial t}(\mathbf{r},t) = \begin{bmatrix} 0 & \Delta\omega(\mathbf{r},t) & -\gamma\ \Im(\mathrm{B}_1^+(\mathbf{r},t)) \\ -\Delta\omega(\mathbf{r},t) & 0 & \gamma\ \Re(\mathrm{B}_1^+(\mathbf{r},t)) \\ \gamma\ \Im(\mathrm{B}_1^+(\mathbf{r},t)) & -\gamma\ \Re(\mathrm{B}_1^+(\mathbf{r},t)) & 0 \end{bmatrix} \mathbf{M}(\mathbf{r},t) \tag{2.32}$$

where $\Re(\cdot)$ and $\Im(\cdot)$ respectively stand for the real and imaginary parts of a complex number. When integrating over an infinitesimal time-step δt, this in turn gives:

$$\mathbf{M}(\mathbf{r},t+\delta t) = \begin{bmatrix} 1/\delta t & \Delta\omega(\mathbf{r},t) & -\gamma\ \Im(\mathrm{B}_1^+(\mathbf{r},t)) \\ -\Delta\omega(\mathbf{r},t) & 1/\delta t & \gamma\ \Re(\mathrm{B}_1^+(\mathbf{r},t)) \\ \gamma\ \Im(\mathrm{B}_1^+(\mathbf{r},t)) & -\gamma\ \Re(\mathrm{B}_1^+(\mathbf{r},t)) & 1/\delta t \end{bmatrix} \mathbf{M}(\mathbf{r},t)\ \delta t \tag{2.33}$$

For a pTx system, with RF notations introduced in eq. (2.18), and with a gradient shape $\mathbf{G}(t)$, eq. (2.33) becomes:

$$\mathbf{M}(\mathbf{r},t+\delta t) = \begin{bmatrix} 1/\delta t & 2\pi\Delta f_0(\mathbf{r}) - \gamma\mathbf{G}(t)\cdot\mathbf{r} & -\gamma\sum_{i=1}^{N_{Ch}} \Im\big(p_i(t)S_i^+(\mathbf{r})\big) \\ -2\pi\Delta f_0(\mathbf{r}) + \gamma\mathbf{G}(t)\cdot\mathbf{r} & 1/\delta t & \gamma\sum_{i=1}^{N_{Ch}} \Re\big(p_i(t)S_i^+(\mathbf{r})\big) \\ \gamma\sum_{i=1}^{N_{Ch}} \Im\big(p_i(t)S_i^+(\mathbf{r})\big) & -\gamma\sum_{i=1}^{N_{Ch}} \Re\big(p_i(t)S_i^+(\mathbf{r})\big) & 1/\delta t \end{bmatrix} \mathbf{M}(\mathbf{r},t)\ \delta t \tag{2.34}$$

With notations from eqs. (1.3) and (1.10), the angle and phase (in radians) obtained at time t in location $\mathbf{r}$ are:

$$\alpha(\mathbf{r},t) = \angle\Big(M_z(\mathbf{r},t) + \imath\|\mathbf{M_{xy}}(\mathbf{r},t)\|_2\Big) \quad \text{and} \quad \varphi(\mathbf{r},t) = \angle M_\perp \tag{2.35}$$

In order to determine the magnetisation vector at the end of a pulse, and therefore the FA and phase achieved, assuming fully longitudinal initial magnetisation, one can discretise the pulse and gradient shapes and compute eq. (2.34) as many times as there are time-steps, for each voxel of interest. This operation can be very time-consuming. For instance, with a 1-ms-long pulse, $\delta t = 10\,\mu\mathrm{s}$, and a masked FOV containing 10^5 voxels, 10^7 evaluations of eq. (2.34) are needed.

Fortunately, the k_T-points pulse parametrisation makes this integration much easier. To obtain the final magnetisation vector, one needs only as many evaluations as there are RF sub-pulses and k-space movements. In addition, these calculations are extremely

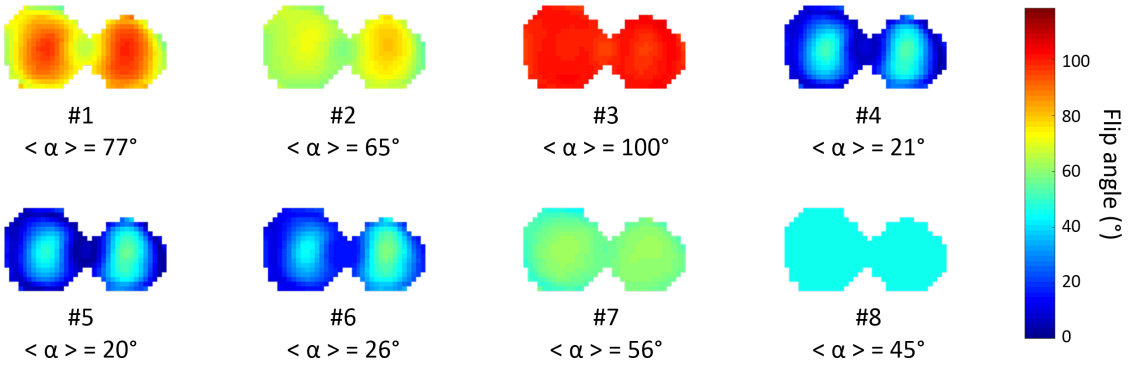

Figure 2.19: Evolution of the flip angle after each sub-pulse of an 8-k_T-point pulse. The average FA in the volume is denoted by $\langle\alpha\rangle$. In this simulation, a FA $\alpha_T = 45°$ is targeted, which lies perfectly within the STA approximation. Nevertheless, much higher FAs are reached after the 3rd sub-pulse, with an average of 100°. This way, the k_T-points pulse can take advantage of the non-linearity of Bloch's equation.

vectorisable, and can be executed relatively quickly with the help of general-purpose computing on graphics processing units (GPGPU), as this allows to compute hundreds of voxels at a time. At the end of the day, it is possible to incorporate large tip angle calculations into the pulse design algorithm, in order to create k_T-points excitation pulses for any target FA.

This method will be used throughout this thesis, even for small flip angles, as it is inherently more precise than the STA approximation and still outputs a k_T-points pulse in a reasonable amount of time. Additionally, it can be more flexible than STA-approximated pulse design. Indeed, even if the FA targeted at the end of the pulse lies relatively well within the approximation (*i.e.* less than 90°), intermediate sub-pulses can produce larger FAs, to exploit the possibilities offered by the Bloch's equation non-linearity to further homogenise excitation. An example of such behaviour is pictured in fig. 2.19.

Scalable K_T-Points

If we want to apply k_T-points pulses to the SPACE sequence (section 1.2.2), we need to design a 90° excitation pulse, and as many refocusing pulses as there are FAs in the variable flip angle train.

A first approach, implemented in [Massire 2015], is to design each of the refocusing pulse successively. An initial waveform is created in the STA approximation, then modified using the GRAPE[7] algorithm that optimises the rotation matrix associated with the pulse in order to make an inversion, regardless of the initial magnetisation state [Massire 2013]. Then each refocusing pulse is designed, targeting the same phase pattern as the first one. Finally, the excitation pulse is similarly designed (with an additional 90° phase to satisfy the CPMG condition). This technique proved very effective in counteracting both B_1^+ and

[7]GRAPE: GRadient Ascent Pulse Engineering.

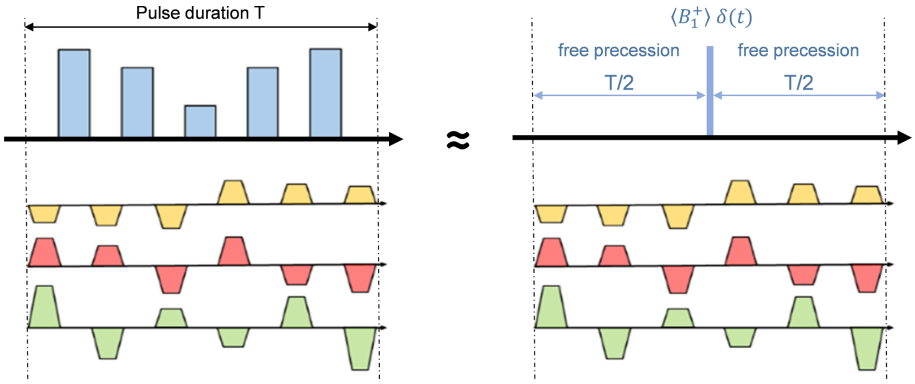

Figure 2.20: Zero-order approximation derived from average Hamiltonian theory. The rotation matrix arising from a k_T-points pulse of duration T producing a FA α can be decomposed into an instantaneous transverse rotation α evaluated under the STA approximation, surrounded by two free-precession periods of duration $T/2$. Adapted from [Gras 2018].

B_0 inhomogeneity at 7 T in the brain. It is however a long, computationally expensive procedure, not directly applicable in clinical routine.

Eggenschwiler *et al.* obtained good mitigation of the RF field inhomogeneity at 7 T by designing k_T-points pulses under the STA approximation, and constraining the RF and gradient waveforms to be respectively symmetric and antisymmetric [Eggenschwiler 2014]. This confers them good scalability properties: one k_T-points pulse can be designed, and scaled in amplitude to match all needed FAs in the SPACE train.

More recently, Gras *et al.* showed that this approach works only on-resonance, and breaks down when Δf_0 is taken into account [Gras 2018]. Using the average Hamiltonian theory (AHT), they demonstrated that the zero-order approximation of a pulse of flip angle α can be seen as an instantaneous STA-approximated RF pulse producing a rotation of α around a purely transverse axis, surrounded by two identical free precession periods (fig. 2.20). Within zero-order AHT approximation, there is therefore no scaling issue. In addition, the RF symmetry and gradient antisymmetry proposed by Eggenschwiler *et al.* lead to a first-order term equal to zero when off-resonance is neglected: this justifies the good scaling properties of their design. Lastly, the decomposition of the pulse shown in fig. 2.20, combined with the overall zero-moment gradients, justifies its inclusion in a refocusing train, as it respects CPMG conditions (p. 23), especially №2. However, the first-order term in the AHT analysis is generally not zero in the presence of Δf_0, which leads to scaling errors. Gras *et al.* went a step further by designing Δf_0-robust scalable k_T-points pulses. Their proposed pulse design is two-fold:

- An on-resonance-scalable k_T-points pulse is designed within the STA approximation, similarly to the method of Eggenschwiler *et al.*, in the absence of Δf_0, and under hardware and safety constraints, following the usual eq. (2.31). Let us denote the pulse obtained by p_0, of RF and location parameters $\mathbf{x}^{(0)}$ and $\mathbf{k}^{(0)}$.
- In a second step, p_0 is optimised again to obtain p_1 of parameters $\mathbf{x}^{(1)}$ and $\mathbf{k}^{(1)}$, this time trying to minimise the scaling error caused by the introduction of Δf_0 information, *i.e.* the distance between the 'true' rotation matrix $\tilde{\mathbf{R}}$ and its STA

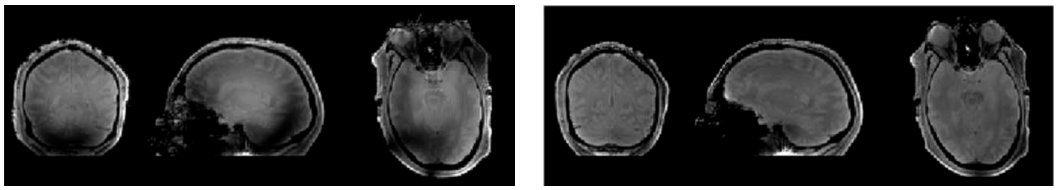

(a) CP mode (b) k_T-points

Figure 2.21: Proton-density-weighted FLASH images obtained at 7 T using CP mode and k_T-points excitations [Cloos 2012a].

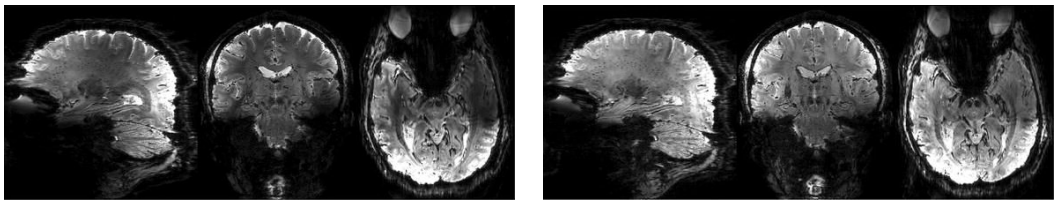

(a) CP mode (b) k_T-points

Figure 2.22: 3D T_2^*-weighted EPI images at 0.75 mm isotropic resolution, obtained at 9.4 T using CP mode and k_T-points excitations [Tse 2016].

approximation $\mathbf{R_{STA}}$. This is done under the added constraint that the NRMSE of p_1 be less than or equal to that of p_0.

The optimisation problem for this second step is:

$$\begin{aligned}
\underset{\mathbf{x}^{(1)},\mathbf{k}^{(1)}}{\arg\min} \quad & \left\| |\tilde{\mathbf{R}}(\mathbf{x}^{(1)},\mathbf{k}^{(1)})\mathbf{R}_{\mathbf{STA}}^{-1}(\mathbf{x}^{(1)},\mathbf{k}^{(1)}) - \mathrm{Id}|_{\mathrm{f}} \right\|_2, \qquad (\mathbf{x},\mathbf{k}) \in \mathbb{C}^{N_{Ch}N_{kT}} \times \mathbb{R}^{3N_{kT}} \\
\text{s.t.} \quad & \left\| |\mathbf{A}(\mathbf{k}^{(1)})\mathbf{x}^{(1)}| - \alpha_T \right\|_2 \leq \left\| |\mathbf{A}(\mathbf{k}^{(0)})\mathbf{x}^{(0)}| - \alpha_T \right\|_2, \\
& \mathrm{SAR}_{\mathrm{global}}(\mathbf{x}) \leq \mathrm{SAR}_{\mathrm{global,max}}, \\
& \mathrm{SAR}_{10\mathrm{g,v}}(\mathbf{x}) \leq \mathrm{SAR}_{10\mathrm{g,max}}, \quad 1 \leq v \leq N_{VOP}, \\
& \mathcal{P}_c(\mathbf{x}) \leq \mathcal{P}_{\max}, \quad 1 \leq c \leq N_{Ch}, \\
& |x_\ell| \leq 1, \quad 1 \leq \ell \leq N_{kT}N_{Ch}.
\end{aligned} \tag{2.36}$$

where $|\cdot|_{\mathrm{f}}$ represents the matrix Frobenius norm, and $\|\cdot\|_2$ is the $\mathcal{L}_2$ norm over voxels. As we will see in the following sections, this two-fold optimisation was successfully applied to T_2w brain imaging at UHF, and will be used for breast imaging at 3 T in chapter 4.

2.4.2 Ultra-High Field Demonstrations

K_T-points have been around since 2011, and many demonstrations of their ability to reduce flip angle inhomogeneity have been carried out at UHF for brain imaging. Among others, we can cite Cloos *et al.* who have successfully applied k_T-points to PDw MRI [Cloos 2012a], as pictured in fig. 2.21. In a subsequent publication, they have also produced homogeneous T_1w acquisitions [Cloos 2012b].

T_2w 3D imaging, which is challenging due to the number of refocusing pulses involved, as well as the constraint on phase, has been tackled by several authors [Massire 2015,

Eggenschwiler 2014, Eggenschwiler 2016]. Recently, Gras *et al.* used the scalable k_T-points approach described above to design a single pulse that was used throughout the entire SPACE excitation-refocusing train [Gras 2018].

Finally, fig. 2.22 shows an example of T_2^*w images acquired at 9.4 T with a 3D echo-planar imaging (EPI) sequence [Tse 2016], opening the door to B_1-artefact-free fMRI at UHF, and hence access to higher temporal SNR and finer cortical resolution.

There is however a number of factors specific to body imaging. For instance, patient motion and breathing make calibration-based pulses difficult to apply as the subjects may have moved between calibration and the actual acquisition. Additionally, a transmit body coil extending far beyond the FOV may be a problem with inherently non-selective k_T-points, inducing aliasing artefacts if nothing is done to counteract them.

2.4.3 Universal Pulses for Calibration-Free Dynamic RF Shimming

Despite those great demonstrations of image quality improvement at UHF, dynamic RF shimming and more generally parallel transmission has so far failed to be widely accepted into routine application. This is attributable to the cumbersome calibration workflow [Setsompop 2008c, Wu 2013, Cloos 2012b, Curtis 2011, Tse 2016, Deniz 2015]: mapping of a subject's B_1^+ and Δf_0, and the subsequent on-the-fly pulse design represent a substantial waste of scanner time. This of course gets worse as more transmission channels are used, adding up to ten minutes calibration time or more. In addition to that, the increased workflow complexity is likely to cause technical or human errors.

Recently, Gras *et al.* proposed a new approach to pTx at UHF for brain imaging: the *universal pulses* method [Gras 2017b]. The concept, illustrated by fig. 2.23, is to bypass the subject-specific calibration steps (maps and pulse design) by incorporating pre-computed pulses into the different sequences in the protocol. Those pulses were designed offline, one for each desired application, on a database of previously-acquired calibration data. From the end-user perspective, it is a completely 'plug-and-play' solution, that gets rid of the burden associated with pTx.

The UP concept was successfully applied on different sequences and with various underlying pulse designs, with only a marginal cost in performance compared to subject-specific optimisation. To date, UPs have been used in a MP-RAGE sequence with k_T-points [Gras 2017b], in SPACE and FLAIR sequences with scalable k_T-points [Gras 2018] (see fig. 2.24), with fast-k_z spokes [Gras 2017a], and with DSC [Beqiri 2018]. They were also implemented with single-channel SPINS for brain imaging at 3 T [Mooiweer 2017].

UPs rely on the relative similarity of B_1^+ and B_0 distributions in subjects' heads, even at ultra-high field, and to some extent to contrast immunity to small FA errors. In chapter 6, we will see that the concept does not translate well to the important inter-subject variability found in abdominal imaging. An alternative, *SmartPulse*, will be proposed instead, based on an appropriate segmentation of the population.

* * *
* *
*

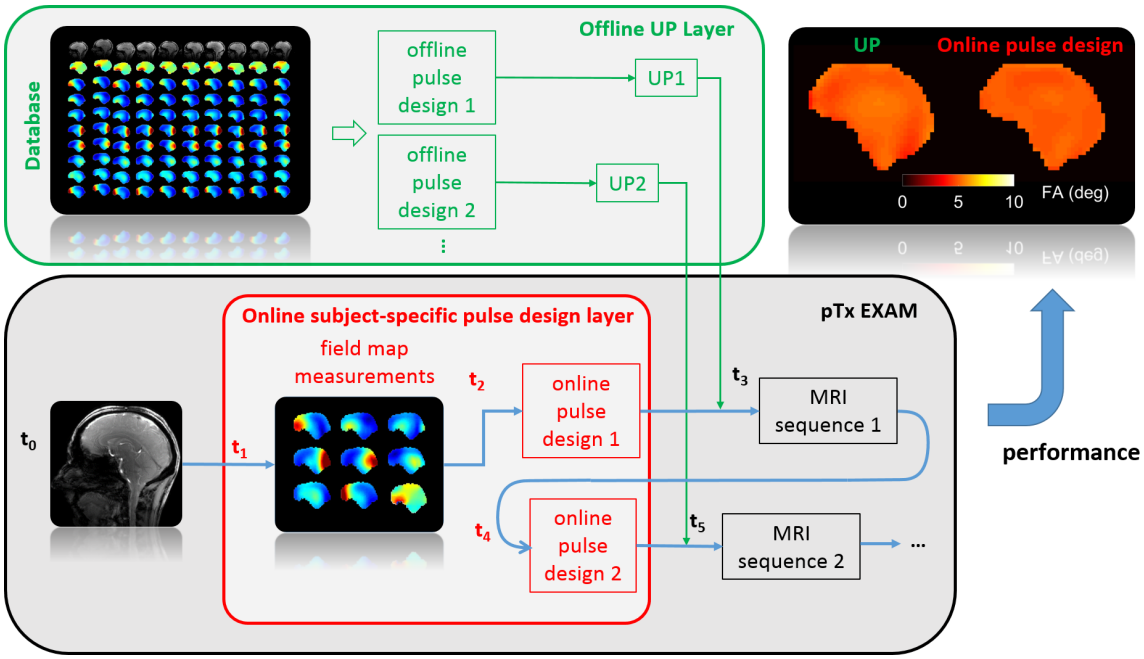

Figure 2.23: Universal Pulses (UPs) concept. Traditional dynamic RF shimming (red box) requires calibration data as well as pulse design for each sequence. These steps are bypassed by pre-computed universal pulses, whose design is made offline on population data (green box). *Courtesy of Vincent Gras*.

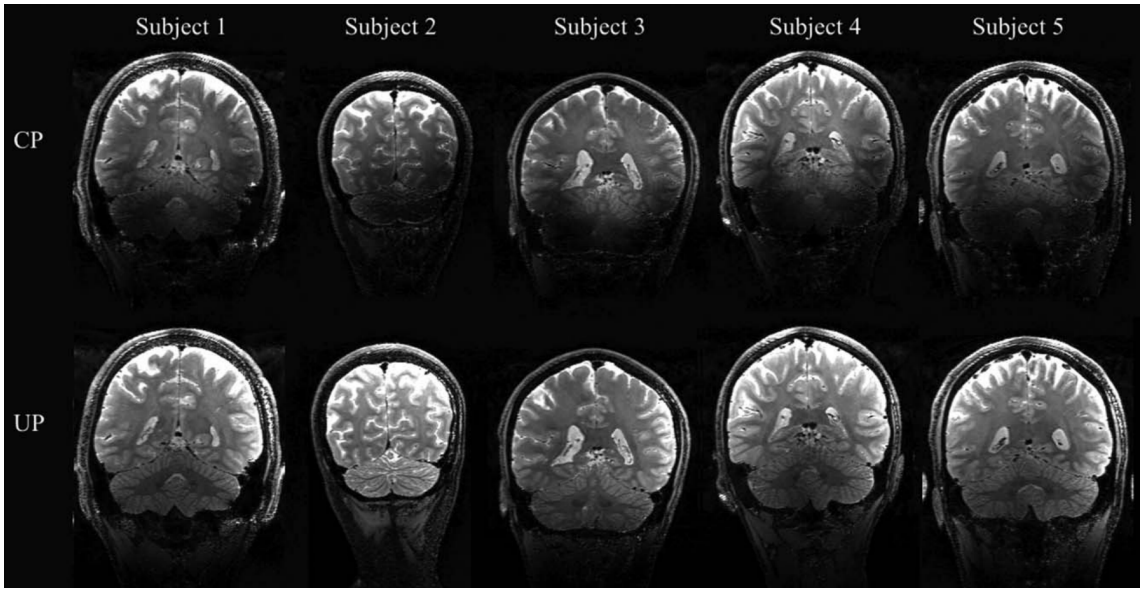

Figure 2.24: Coronal SPACE images acquired in CP mode (top row) and with pTx universal k_T-points pulses (bottom row) at 7 T [Gras 2018]. A clear signal enhancement is observed in the cerebellum and temporal lobes.

Part II

Methodological Developments and Clinical Studies

Chapter 3

Optimisation of K_T-Points Pulse and Sub-Pulse Durations

Chapter Outline

Parts of this chapter (especially section 3.2.4) were presented at the European Society for Magnetic Resonance in Medicine and Biology conference in 2016:

R. Tomi-Tricot, V. Gras, N. Boulant, A. Vignaud and A. Amadon. *K_T-Points Pulse Design at 7T: Optimization of Pulse and Sub-Pulse Durations.* In Magnetic Resonance Materials in Physics, Biology and Medicine, volume 29, pages 247–400, Vienna, AT, September 2016.

This chapter introduces and discusses additions that were made to the k_T-points optimisation algorithm presented in section 2.4.1, described by eq. (2.26) (STA approximation and LTA). The aim is to investigate the impact and interest of letting the algorithm adjust the duration of the generated pulse, as well as that of the different sub-pulses.

We expect better homogeneity thanks the flexibility offered by these additional degrees of freedom.

This work is based on an algorithm developed for the Siemens MAGNETOM 7 T MRI scanner installed in NeuroSpin, using eight parallel transmission channels. The algorithm is however easily adaptable to the Siemens MAGNETOM Prisma or Skyra 3 T two-channel scanner, or to the Verio 3 T single-channel imager.

3.1 Theory

3.1.1 Optimisation Vector

The k_T-points pulse preparation algorithm optimises the following variables, in the continuity of its previous form described in section 2.4.1:

- $\mathbf{x}$, a vector consisting of the concatenation of the RF coefficients corresponding to each channel and each sub-pulse, normalised by the maximum allowed voltage, so that $\mathbf{w} = V_{\max}\ \mathbf{x}$;
- $\mathbf{k}$, the vector of k_T-point locations in the transmit k-space – all three coordinates for each sub-pulse;
- $\mathbf{t}$, the vector of k_T-point durations, one variable for each sub-pulse. This constitutes the addition to the previous algorithm discussed here.

3.1.2 Cost Function

Calculating the Cost Function

Here we keep the same notations as in section 2.4.1, and introduce $\mathbf{t} = \begin{bmatrix}\tau_1 & \dots & \tau_{N_{kT}}\end{bmatrix}$. The cost function to be minimised by the algorithm is still the normalised root-mean-square error (NRMSE), defined by eq. (2.25). Changes were however made to the way each FA is calculated. In the small tip angle (STA) approximation, eq. (2.28) is now:

$$\hat{\alpha}(\mathbf{r}) = \imath\gamma\ V_{\max} \sum_{p=1}^{N_{kT}} \sum_{c=1}^{N_{Ch}} x_{p,c}\ S_c^+(\mathbf{r}) \tau_p \mathrm{e}^{\imath\mathbf{r}\cdot\mathbf{k}_p} \mathrm{e}^{\imath 2\pi T_p \Delta f_0(\mathbf{r})} \operatorname{sinc}(\pi\tau_p \Delta f_0(\mathbf{r})) \tag{3.1}$$

where T_p accounts for the time remaining after the middle of the pth sub-pulse:

$$T_p = \frac{1}{2}\tau_p + \sum_{\ell=p+1}^{N_{kT}} \tau_\ell \tag{3.2}$$

and the encoding matrix – eqs. (2.29) and (2.30) – was modified accordingly. Similarly in the large tip angle (LTA) case, the function that returns the FA map after a numerical evaluation of Bloch's equation was altered to allow for varying sub-pulse durations.

Gradient of the Cost Function

During the optimisation process, to perform gradient descent, the different variables are iteratively updated and the cost function f evaluated. The best solution that respects the

constraints is kept as the starting point for the next iteration. Not all variable modification possibilities are tested, as it would be too time- and resource-consuming. Instead, the gradient of the cost function is calculated, and only the variables leading to the largest decrease in f are considered, *i.e.* those that correspond to the lowest negative partial derivatives of f.

In the LTA case, the cost function gradient is computed using a finite differences approach since those calculations are easily vectorisable. In the STA case, however, it is advisable to use analytical forms of the derivatives to improve performance: this is what is done for RF coefficients and k_T-point locations. So far, only the finite differences method has been implemented for partial derivatives of f relative to k_T-points durations. This is not optimal, but not really a problem either since in this thesis we use the LTA framework even for small target FAs.

3.1.3 Constraints

Addition of Linear Constraints

The new variables must abide by a few constraints; fortunately those are linear, so they do not lead to considerable computational performance drop. First of all, each sub-pulse obviously cannot be shorter than 0 s. Due to hardware limitations, a stronger constraint was set: eventually, each sub-pulse must last at least $\tau_{\min}$, empirically defined as 4 times the 'gradient raster time', *i.e.* the basic unit time used on Siemens scanners for gradient description. This corresponds to a minimum of 40 µs per k_T-point. This is achieved by adding a *lower bound* constraint to the optimisation function.

In addition, an *inequality linear constraint* is needed in order to limit the duration of the total pulse: the sum of the sub-pulse durations must be less than or equal to some user-defined limit $t_{\max}$. This can be useful for instance when a short TR is desired: in that situation, the pulse should not be too long. Note that in some cases the user might want to change this inequality constraint into an equality one, where the total duration is fixed and the algorithm optimises the repartition of the sub-pulses.

Non-Linear Constraints

All added constraints are linear, but the non-linear constraints already present must be modified to account for non-constant sub-pulse durations:

- For calculation of local SAR for each Q-matrix (*cf.* section 2.2.4), eq. (2.21) becomes:

$$\mathrm{SAR}_{10g,i}(\mathbf{x},\mathbf{t}) = \frac{V_{\max}}{\mathrm{TR}} \sum_{p=1}^{N_{kT}} \tau_p \, \mathbf{x_p}^{\mathrm{H}} \mathbf{Q_i} \mathbf{x_p} \tag{3·3}$$

  where i indexes VOPs, and $\mathbf{x_p}$ is the subset of $\mathbf{x}$ corresponding to the pth sub-pulse.
- Similarly for global SAR, eq. (2.24) becomes:

$$\mathrm{SAR}_{\mathrm{global}}(\mathbf{x},\mathbf{t}) = \frac{V_{\max}}{\mathrm{TR}} \sum_{p=1}^{N_{kT}} \tau_p \, \mathbf{x_p}^{\mathrm{H}} \mathbf{Q_{global}} \mathbf{x_p} \tag{3·4}$$

- Peak power is limited by a constraint on maximal voltage, *i.e.* the modulus of each component of $\mathbf{x}$.
- As seen earlier, average power for each channel: $\boldsymbol{\mathcal{P}} = \left[\mathcal{P}_1 \dots \mathcal{P}_{N_{Ch}}\right]$ is also constrained. Here is the expression of the average power on channel c:

$$\mathcal{P}_c(\mathbf{x}, \mathbf{t}) = \frac{V_{\max}^2}{Z \ \mathrm{TR}} \sum_{p=1}^{N_{kT}} \tau_p |x_{p,c}|^2 \tag{3.5}$$

  where $Z = 50\,\Omega$ is the impedance of the system and $x_{p,c}$ is the cth coordinate of $\mathbf{x_p}$.

Gradients of Non-Linear Constraints

When solving the optimisation problem, we also need to compute, on each iteration, the gradient of non-linear constraints, so that the algorithm can determine directions that are more favourable than others in terms of constraint saturation. We have seen that all additional constraints corresponding to durations optimisation are linear: their gradient is trivial. Still, to compute the gradient of existing non-linear constraints, it is necessary to calculate their partial derivatives along the dimensions newly added to the solution space. Note that gradients along other dimensions need not be redefined. Here are the definitions of the partial derivatives of constraints along the k_T-point durations:

- Local SAR: $\forall (i,p) \in \{1,\dots,N_{VOP}\} \times \{1,\dots,N_{kT}\}$,

$$\frac{\partial \mathrm{SAR}_{10g,i}}{\partial \tau_p}(\mathbf{x}) = \frac{V_{\max}^2}{\mathrm{TR}} \ \mathbf{x_p}^{\mathrm{H}} \mathbf{Q_i} \mathbf{x_p} \tag{3.6}$$

- The same definition goes for the partial derivatives of $\mathrm{SAR}_{\mathrm{global}}$, replacing $\mathbf{Q_i}$ with $\mathbf{Q_{global}}$.
- Partial derivatives of RF amplitude constraints relative to $\mathbf{t}$ are zero.
- Average power: $\forall (c,p) \in \{1,\dots,N_{Ch}\} \times \{1,\dots,N_{kT}\}$,

$$\frac{\partial \mathcal{P}_c}{\partial \tau_p}(\mathbf{x}) = \frac{V_{\max}^2}{Z \ \mathrm{TR}} \ |x_{p,c}|^2 \tag{3.7}$$

3.1.4 Expression of the Optimisation Problem

The optimisation problem, previously described by eq. (2.26), is now:

$$\begin{aligned}
\underset{\mathbf{x},\mathbf{k},\mathbf{t}}{\arg\min} \quad & f(\mathbf{x},\mathbf{k},\mathbf{t}), \qquad (\mathbf{x},\mathbf{k},\mathbf{t}) \in \mathbb{C}^{N_{Ch}N_{kT}} \times \mathbb{R}^{3N_{kT}} \times \mathbb{R}^{N_{kT}} \\
\text{s.t.} \quad & \mathrm{SAR}_{\mathrm{global}}(\mathbf{x},\mathbf{t}) \leq \mathrm{SAR}_{\mathrm{global,max}}, \\
& \mathrm{SAR}_{10g,v}(\mathbf{x},\mathbf{t}) \leq \mathrm{SAR}_{10g,\max}, \quad 1 \leq v \leq N_{VOP}, \\
& \mathcal{P}_c(\mathbf{x},\mathbf{t}) \leq \mathcal{P}_{\max}, \quad 1 \leq c \leq N_{Ch}, \\
& |x_\ell| \leq 1, \quad 1 \leq \ell \leq N_{kT}N_{Ch}, \\
& \tau_{\min} \leq \tau_p, \quad 1 \leq p \leq N_{kT}, \\
& \textstyle\sum_{p=1}^{N_{kT}} \tau_p \leq t_{\max}.
\end{aligned} \tag{3.8}$$

3.2 Experiments

The interest of making the pulse duration variable was assessed in two different contexts. The first experiment used a strict constraint on global pulse time, while the second one let the algorithm free to design a pulse as long – or as short – as needed.

3.2.1 Hardware and Methods

As mentioned before, the algorithm was initially developed for a Siemens (Erlangen, Germany) MAGNETOM 7 T scanner with 8 transmission channels. It was implemented in MATLAB r2015b (The Mathworks, Natick, MA, USA) using the built-in *active-set* algorithm from the *Optimization Toolbox*. The cost function and its gradient were evaluated following the LTA framework, by numerical integration of Bloch's equation. In order to speed up the optimisation, extensive use of GPGPU capabilities was made. This was achieved by performing Bloch integrations with CUDA [Nickolls 2008] on an NVIDIA (Santa Clara, CA, USA) Tesla K40c graphics processing unit.

Experiments were made in simulation to compare the algorithm optimising simultaneously RF coefficients and k-space trajectories – referred to as *NoVarDur* – to the new one – *VarDur* – optimising in addition the sub-pulse durations. Two approaches were tested: one with fixed total pulse duration (section 3.2.3) and one with variable total pulse duration (section 3.2.4). Those experiments were performed on B_1^+ and ΔB_0 brain maps acquired on one subject. Using only static RF shimming, the NRMSE in this subject was 29.8 %.

3.2.2 Time Normalisation Factor

One important aspect of iterative optimisation problems is the normalisation of the optimisation vector. All variables defined in section 3.1.1 should be of the same order of magnitude, so that the algorithm would not give too much of an advantage to any of them. In the present situation, by introducing sub-pulse duration variables, great care should be taken in applying a normalisation constant to them. A large normalisation factor applied to a variable would lead to a greater cost function gradient along this dimension, and thus lead to a possibly sub-optimal solution. On the contrary, setting a small normalisation constant to duration variables would encourage the optimisation process to select a path that does not act much on them.

The normalisation factor for durations, K, was defined as $K = K_0 \, |\Delta B_0|_{95\,\%}$, where $|\Delta B_0|_{95\,\%}$ corresponds to the maximum amplitude of B_0 inhomogeneities taken into account (the outlying 5 % highest values of $|\Delta B_0|_{95\,\%}$ are discarded), and K_0 is an arbitrary constant, henceforth referred to as time normalisation constant (TNC). The more inhomogeneous ΔB_0 is, the greater the normalisation factor gets. Sub-pulse lengths become more of a priority for the algorithm, making the pulse more adapted to those inhomogeneities.

A quick experiment was made in order to determine the best K_0 value. A 5 ms 180° 5-k_T-point pulse was designed over 10 random trajectories in two situations: TR = 1000 ms

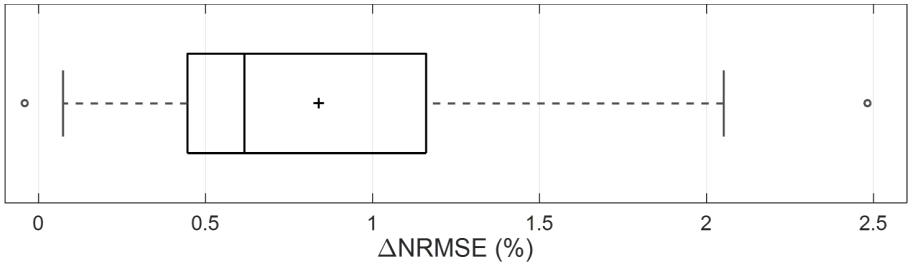

Figure 3.1: Difference in NRMSE from the algorithm with fixed sub-pulse durations to the interleaved one. Positive values express an improvement (lower NRMSE). The cross shows the average value: 0.84 % gain. The line inside the box indicates the median: 0.62 %. The edges of the box correspond to the 25th and the 75th percentiles, while the whiskers delimit the 10th and 90th percentiles. Circles show outliers.

(active SAR constraints) and TR = 20 000 ms (no SAR constraints). The aim was to determine a value of K_0 that would statistically enhance the NRMSE – and never or only seldom degrade it – compared to the fixed-times method. Out of the seven TNC tested (0.002, 0.003, 0.005, 0.01, 0.02, 0.05 and 0.1), $K_0 = 0.01$ prevailed and was used in further experiments.[1]

3.2.3 Fixed Total Pulse Duration: Interleaved Approach

Methods

In this experiment the total pulse time was fixed. That means the linear inequality constraint on the pulse time (last constraint in eq. (3.8)) was changed into an *equality constraint*. This is a case where using an interleaved algorithm [Grissom 2012] could prove useful: (i) designing a pulse without changing the durations, and then (ii) optimising the result by allowing the sub-pulses lengths to vary. Doing so ensured that the final pulse was at least as good as the one designed without variation of durations.

The aim was to design a 5 ms, 7-k_T-point inversion (180°) pulse, with a TR of 1000 ms, so that SAR constraints were active. First the algorithm was launched until convergence without sub-pulse durations optimisation. Then it was launched a second time until convergence, this time with sub-pulse durations optimisation, and with the previous result as a starting point.[2] The TNC used was 0.01. Each sub-impulsion duration was limited to 40 µs, owing to hardware limitations. The algorithm consisting in *NoVarDur* followed by *VarDur* is hereby referred to as *Interleaved*. This procedure was repeated over 10 random trajectories, to compare the *Interleaved* algorithm to the purely *NoVarDur* one.

Results and Discussion

Figure 3.1 shows the statistical repartition of the NRMSE points that the durations-varying algorithm allowed to gain, starting from the output of *NoVarDur*. For each random trajectory, the NRMSE difference is defined as

$$\Delta\text{NRMSE} = \text{NRMSE}_{NoVarDur} - \text{NRMSE}_{Interleaved} \tag{3.9}$$

so that a positive ΔNRMSE value shows an improvement in pulse performance.

As expected, the error with *Interleaved* is systematically lower than the one with fixed durations. On average, the new algorithm achieved a NRMSE gain of 9.48 %, from 8.64 % to 0.84 %. However, this not a staggering improvement considering the additional computation time.

As a side note, one may find intriguing the fact that one ΔNRMSE point lies below zero, meaning that the new algorithm actually worsened the previous result. This is explained by the fact that the first step of the interleaved method reached a local minimum of the cost function that could hardly be improved by varying the sub-pulse durations. The second step of the computation therefore stopped after only one iteration, with a new NRMSE that was only slightly lower. However, after the optimisation, the durations of the RF impulsions are rounded to the nearest higher multiple of the 10 µs gradient raster time – and the amplitudes are slightly decreased accordingly. This usually harms the NRMSE to some extent. In this very case, the result was then somewhat worse than the solution achieved by the *NoVarDur* algorithm alone.

3.2.4 Variable Total Pulse Duration

The most important aspect of the assessment of the *VarDur* algorithm was to compare its performances to those of *NoVarDur*, this time in 'normal' mode: with total freedom on the total pulse length. The *VarDur* algorithm used here is therefore a direct implementation of eq. (3.8), with a $t_{\max}$ high enough to never constrain the optimisation.[3]

This experiment was declined into two sub-experiments, to assess (i) the robustness of the *VarDur* algorithm to initial conditions, and (ii) its resilience to B_0 inhomogeneity.

Methods

The workflows associated with each assessment are described in fig. 3.2. In both cases, the aim was to design a 180° 7-k_T-point pulse on the ΔB_0 and B_1^+ maps from the same subject as before. A TR of 1000 ms was considered for power and SAR prediction, so that SAR constraints were active.

[1] This TNC value is only valid for this particular chapter, where the context is brain imaging at 7 T. In the rest of this thesis, for breast or abdominal imaging at 3 T, a TNC of 1 is generally used.

[2] In both cases a limit of 1000 iterations was set in the eventuality of cases where it took too many iterations to achieve convergence.

[3] Actually, $t_{\max}$ was set to 100 ms, which corresponds to the scanner's limitation for pulse duration. In practice this was never a constraint.

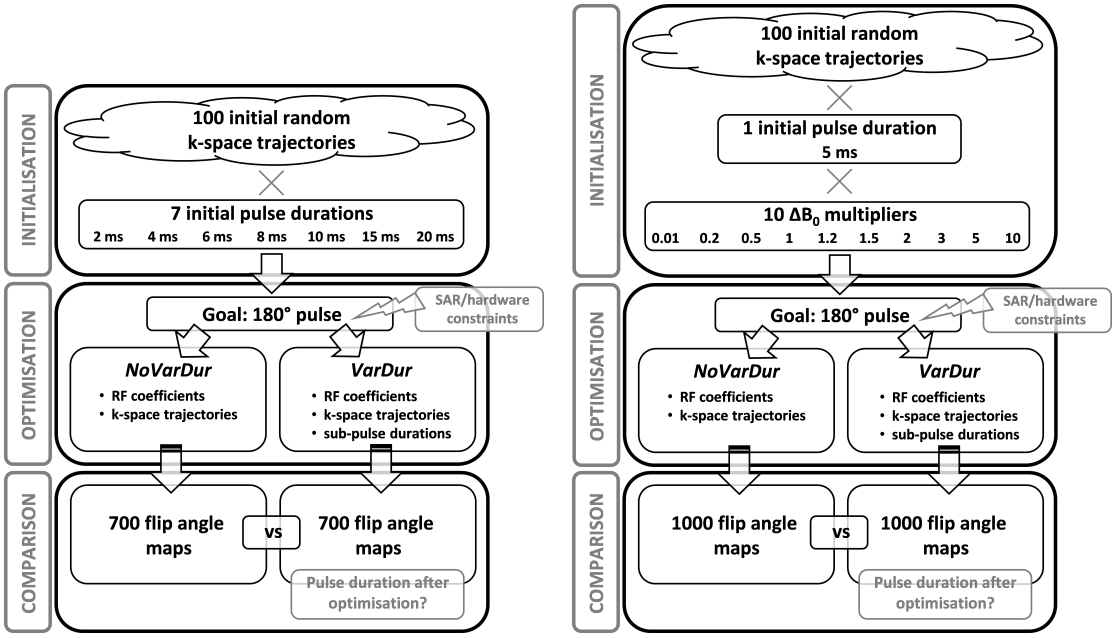

(a) Experiment (i): robustness to initial conditions.

(b) Experiment (ii): resilience to ΔB_0.

Figure 3.2: Simulation workflows used to assess *VarDur* compared to *NoVarDur*.

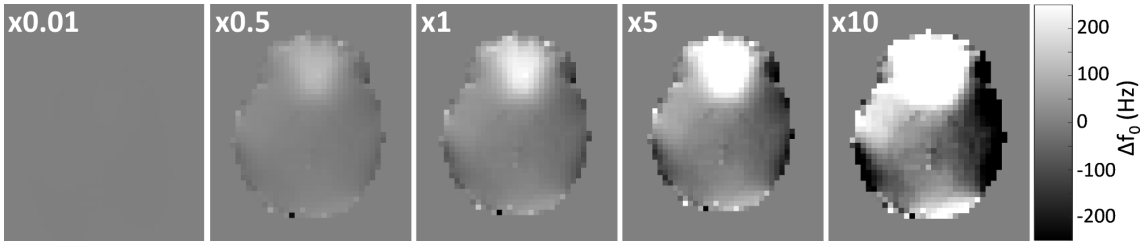

Figure 3.3: Examples of B_0 inhomogeneity maps obtained with different multipliers, as used in experiment (ii). See fig. 3.2b.

For experiment (i) (fig. 3.2a), both *NoVarDur* and *VarDur* algorithms were run until NRMSE convergence[4] over 100 random k-space trajectories, for seven initial pulse durations ranging from 2 to 20 ms.

For experiment (ii) (fig. 3.2b), the same 100 random trajectories were used to compare *NoVarDur* and *VarDur*, this time with only one initial duration (5 ms), but with ten different accentuations of the ΔB_0 map, so as to evaluate the resilience of both algorithms to strong B_0 variations. The map was indeed multiplied by different factors, ranging from 0.01 to 10: fig. 3.3 shows some examples of modified ΔB_0 maps.

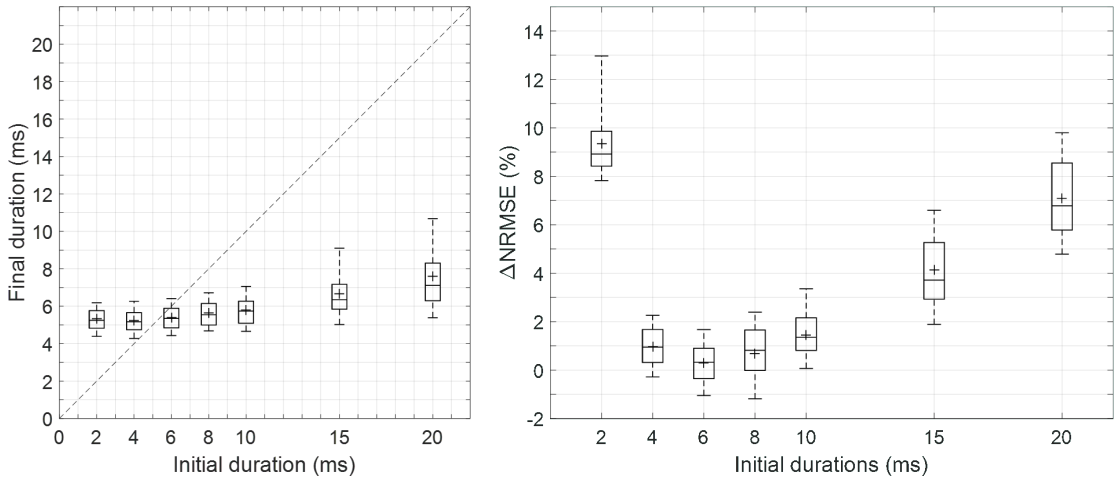

(a) Total pulse duration at the end of *VarDur* optimisation, for each initial duration. The dashed black plot is the 1:1 line. Notice how durations lower than 5-6 ms are increased while higher ones are decreased.

(b) Gain in NRMSE with *VarDur* compared to *NoVarDur*, for each initial duration. In the 2 ms case, *NoVarDur* encounters particularly high SAR limitations. Long pulses (15 and 20 ms) suffer more from B_0 inhomogeneity effects.

Figure 3.4: Robustness of *VarDur* to initial conditions. For each box, the cross shows the average value, the line indicates the median, the edges correspond to the 25th and the 75th percentiles, while the whiskers delimit the 10th and 90th percentiles.

Results and Discussion

Regarding experiment (i), fig. 3.4a reports that with durations optimisation, because ΔB_0 effects are considered, longer pulses do not necessarily yield better NRMSEs. For the situation considered, an optimal total pulse duration seems to be found between 5 and 6 ms. Pulses with lower initial durations see their duration increase to abide by the energy constraint: indeed, SAR increases quadratically with pulse amplitude and only linearly with the pulse length, while the effect on spins increases linearly with both (*cf.* eqs. (1.13) and (2.22)). Indeed, the local SAR limit was reached for both algorithms, in all cases. This 'optimal' duration is harder to achieve for the longest initial pulses (15 and 20 ms), but there is still a tremendous decrease in pulse length. On the contrary, a pulse too long is more subject to ΔB_0 effects, and can be suboptimal in terms of NRMSE. This is confirmed by fig. 3.4b, which highlights a noticeable decrease in NRMSE with *VarDur*, from 13.0 % (*NoVarDur*) to 9.6 % (*VarDur*) overall. In addition, it reveals extra robustness, with lower probability to achieve a high NRMSE when the initial duration is extremely high or low.

Figure 3.5 reports results corresponding to experiment (ii). Those results corroborate the assumption we made before on the effect of high B_0 inhomogeneities on pulse duration in order to guarantee a good NRMSE. On fig. 3.5a, we can see that with *VarDur*, for 'reasonable' ΔB_0 conditions, the pulse duration does not vary much from its initial 5 ms value, which appeared to be optimal in experiment (i). However, in case of exacerbated

[4]See footnote 2 on page 88.

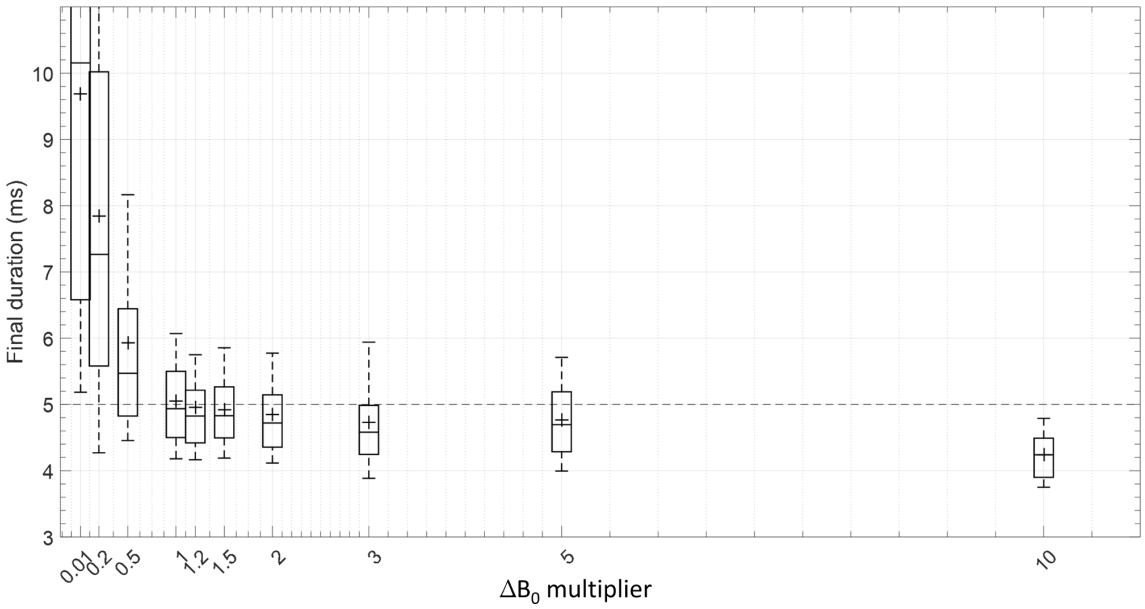

(a) Total pulse duration at the end of *VarDur* optimisation, for each ΔB_0 multiplier. The dashed black plot shows the initial pulse duration (5 ms).

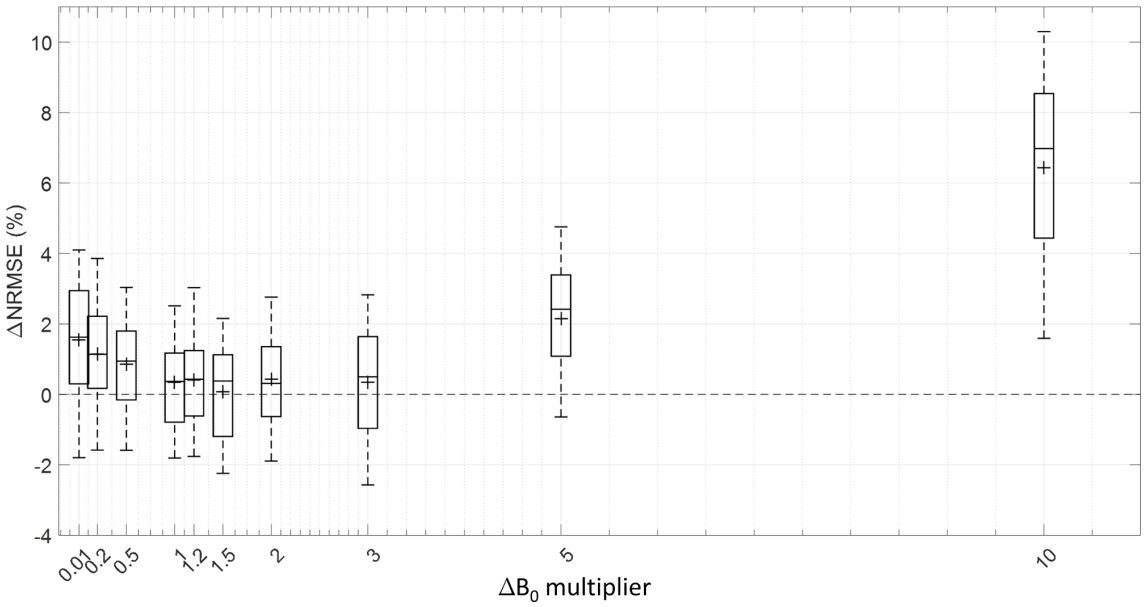

(b) Gain in NRMSE with *VarDur* compared to *NoVarDur*, for each ΔB_0 multiplier.

Figure 3.5: Resilience of *VarDur* to ΔB_0. For each box, the cross shows the average value, the line indicates the median, the edges correspond to the 25th and the 75th percentiles, while the whiskers delimit the 10th and 90th percentiles.

static field inhomogeneity, pulse durations tend to shorten. When ΔB_0 becomes negligible, nothing refrains the pulse to be as long as needed to achieve the best possible NRMSE whithout exceeding SAR limits. In fig. 3.5b, we see that while there is generally no difference between *VarDur* and *NoVarDur* for ΔB_0 multipliers close to 1, *VarDur* offers valuable degrees of freedom to noticeably improve the NRMSE in presence of extreme ΔB_0.

3.3 Conclusion and Perspectives

On the one hand, the interleaved approach presented in section 3.2.3 shows little interest in practice, as it does not improve NRMSE much. But on the other hand, freedom on sub-pulse and on total pulse durations can be highly beneficial as shown in section 3.2.4.

It was demonstrated that the algorithm which includes k_T-point sub-pulse durations as extra optimisation parameters is more robust to initial conditions. Moreover, designed pulses can be more immune to B_0 inhomogeneity as the algorithm finds a compromise between short high-SAR pulses and long pulses that would suffer from off-resonance effects. This behaviour can prove particularly useful for body imaging, where off-resonance is exacerbated by fat-related chemical shift. In abdominal imaging, the presence of the lungs right above the liver also causes important B_0 variations. One could certainly obtain similar results using the former *NoVarDur* algorithm, with some *a priori* knowledge of the off-resonance and some experience, by choosing an appropriate pulse duration. Indeed, as less variables are involved, the optimisation problem can be solved more quickly. However, it is of great help, in a clinical set-up, to have an algorithm that necessitates as little user input as possible, and that can generalise and adapt well to any situation. This is why the *VarDur* approach will be widely used throughout this thesis, for now only on 3D GRE sequences.

This enhanced algorithm could be integrated in the universal pulses framework as it would help finding a better solution for a given {FA; TR; SAR; desired duration} problem. It is used, in particular, in chapter 6 for calibration-free k_T-points in the abdomen, where it helps finding solutions that are robust to off-resonance, as no mapping is performed.

* * *
* *
*

Chapter 4

B_1 Artefacts in Breast Imaging: Exploration of a Single-Channel K_T-Points Solution

Chapter Outline

Parts of this chapter (section 4.2) were presented at the International Society for Magnetic Resonance in Medicine conference in 2018:

R. Tomi-Tricot, V. Gras, T. H. Dao, A. Perrot, F. Mauconduit, N. Boulant, P. Zerbib, A. Rahmouni, A. Vignaud, A. Luciani and A. Amadon. *RF-Induced Potential False-Negative Lesion in Breast T2-weighted MRI at 3T: Exploration of a Single-Channel k_T-Points Solution.* In Proceedings of the 26th Annual Meeting of ISMRM, page 4339, Paris, France, 2018.

Breast MRI can benefit from the improved signal-to-noise ratio brought by high-field systems to achieve finer spatial or temporal resolutions. However, dielectric resonance associated with the shorter RF wavelength provokes inhomogeneous excitation

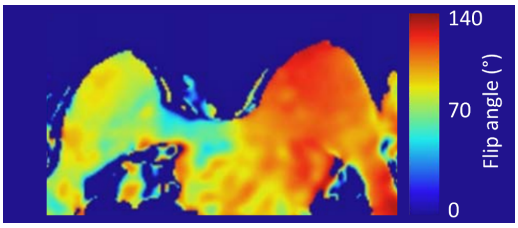

(a)

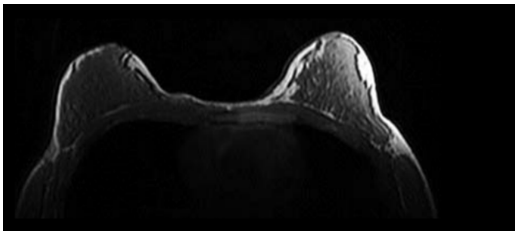

(b)

Figure 4.1: Example of strong B_1 inhomogeneity observed in the breasts at 3 T. (a) Flip angle distribution. (a) T_1w image showing the resulting image shading. From [Winkler 2015].

in the tissues. In this chapter, we see that such artefacts can induce hyperintensity in T_2-weighted images, thus potentially misleading clinicians into excluding malignancy in a lesion. A solution is proposed to reduce the RF artefact on 3D T_2w acquisitions using single-transmit-channel k_T-points, which could be used on any 3 T scanner.

4.1 Introduction

A T_2-weighted sequence is often used in conjunction with dynamic contrast-enhanced (DCE) MRI, in order to help differentiating, in some cases, between benign and malignant breast lesions [Azlan 2010, Moran 2014, Mann 2008, Kuhl 1999]: bright T_2-hyperintensity (T_2H) can indicate either a cyst, a fibroadenoma or an intramammary lymph node, and tends to exclude malignancy [Hochman 1997], associated with moderate T_2H . In the last two cases, contrast enhancement can mimic that of malignant lesions. We saw in part I of this thesis that 3 T MRI is widely recognised for its potential gain in signal-to-noise ratio, which can be used to improve spatial or temporal resolution, but that this gain can be hampered by B_1 artefacts. Examples of such artefacts in the breasts were shown in fig. 2.6 on page 53. An additional example, reported by Winkler and Rutt, can be found in fig. 4.1.

In section 4.2, T_2H clearly identified as related to B_1^+ inhomogeneity is reported, which could lead to false-negative interpretation. The existing solutions to reduce B_1^+ artefacts that we described in sections 2.2.1 and 2.3 – using dielectric pads or dual-transmit RF systems – require either extra hardware or a dedicated setup. Recently, a method similar to k_T-points was specifically proposed for breast imaging to address the problem on single-transmit-channel systems in DCE-MRI sequences [Hsu 2017], but not in T_2-weighted imaging.

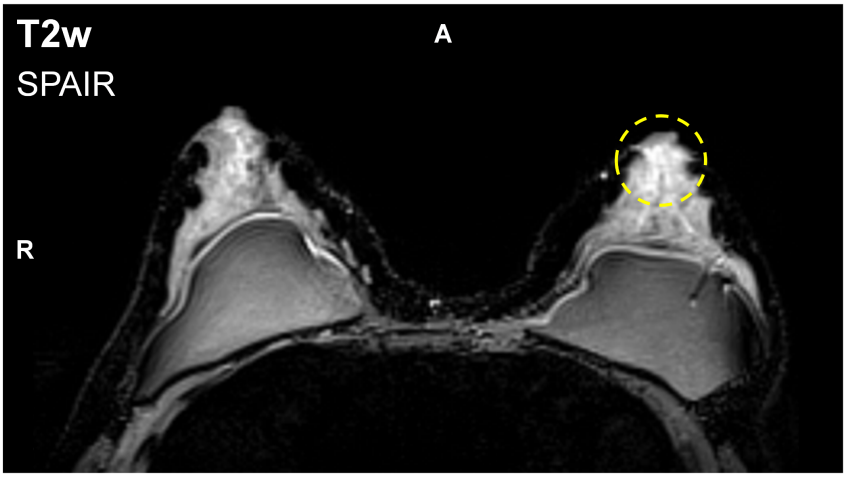

Figure 4.2: *In vivo* acquisition using square pulses. Notice the presence of silicone-based prosthetics. T_2-weighted SPACE with SPAIR fat-suppression. The selected slice highlights substantial local hypersignal in the left breast (circle), which tends to exclude malignancy.

This chapter first aims at analysing the impact of excitation inhomogeneity on T_2-weighted breast imaging. Then, the k_T-points pulse design method is tested to reduce potential B_1^+ artefacts, with no need for parallel transmission.

4.2 Case Report of an RF-Induced Potential False-Negative Lesion in T_2-Weighted Imaging

4.2.1 Methods

Acquisitions were carried out on a single-transmit-channel MAGNETOM Verio 3 T scanner equipped with *TrueForm* [Nistler 2010] (Siemens Healthcare, Erlangen, Germany). An axial T_2-weighted three-dimensional SPACE sequence (*cf.* section 1.2.2) with spectral adiabatic inversion recovery (SPAIR) fat suppression (section 1.3.2) was used. Sequence parameters were the following: $TR = 2800\,ms$, $TE_{effective} = 251\,ms$, $TE_{apparent} = 90\,ms$, $ETL = 100$. Matrix size was $256 \times 256 \times 104$, for a resolution of $(1.4 \times 1.4 \times 2.0)\,mm^3$.

An occurrence of RF-related T_2H has been spotted on a 48-year-old subject (BMI = $21.3\,kg/m^2$). T_2H in the left breast is highlighted in fig. 4.2.

In order to estimate the contribution of RF inhomogeneity to this T_2H, flip angle (FA) map simulations based on B_1^+ and Δf_0 (Larmor frequency offset) maps acquired *in vivo* were performed via numerical integration of Bloch's equations. A FA map was estimated for the largest FA targeted in the refocusing train. SPACE signal simulation was run in every voxel by calculating magnetisation rotations successively induced by each refocusing pulse in the train. Uniform breast tissue relaxation times were considered: $T_1/T_2 = 1500/50\,ms$ [Rakow-Penner 2006].

The B_1^+ field map was acquired using a magnetisation-prepared turbo fast low angle shot sequence [Fautz 2008] at a $(3 \times 3 \times 4)\,mm^3$ isotropic resolution. The Δf_0 map was

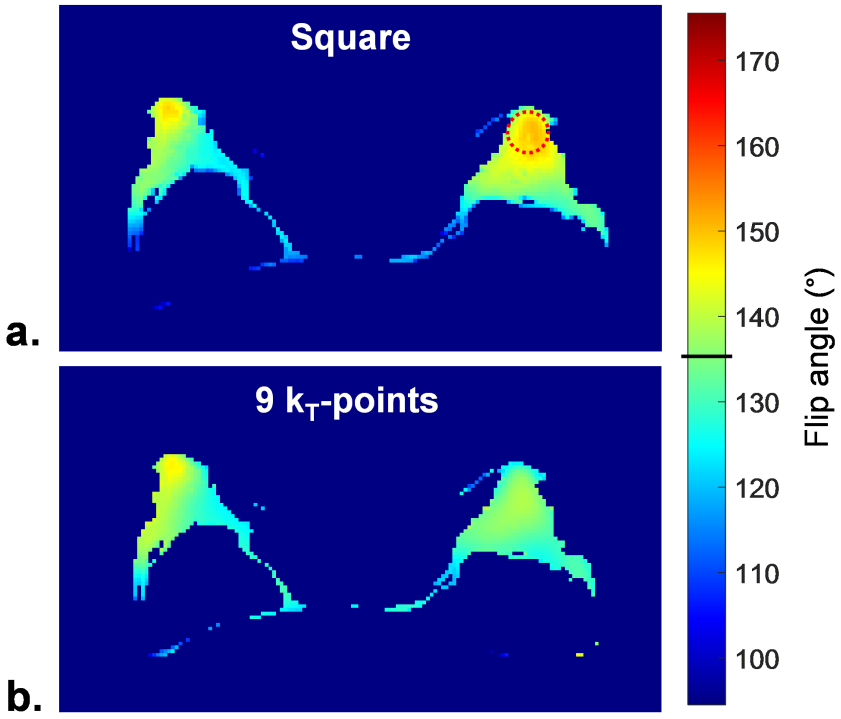

Figure 4.3: Flip angle (FA) simulations, based on actual B_1^+ and Δf_0 maps, of the maximal FA pulse used in the SPACE refocusing train (135°). FAs were calculated in water voxels only, from (a) 700-µs square pulse, and (b) a 9-k_T-point pulse; the waveform was scaled and used for all refocusing pulses and for the 90° excitation. The 20-mm-diameter sphere defining the ROI used to calculate hypersignal in table 4.1 is shown in red on (a).

acquired with a 2-mm isotropic resolution. Three echoes were needed to extract both Δf_0 and water/fat information, acquired over two 3D GRE sequences, with Dixon reconstruction [Dixon 1984] ($TE_1/TE_2/TE_3 = 1.23/2.10/2.46$ ms). Δf_0 was calculated with the phase images from TE_2 and TE_3, using leverage from TE_1 for more precision. More details on Δf_0 mapping and fat-water segmentation are provided in appendix A.

Finally, a Δf_0-robust scalable 9-k_T-point pulse [Gras 2018] was designed, with MATLAB's built-in *active-set* algorithm, under energy and hardware constraints using average Hamiltonian theory (AHT) as described in section 2.4.1 'Scalable K_T-Points'. This tailored pulse was used for the 90° excitation (with a $\pi/2$ phase offset), and for all refocusing pulses (FA = 16° to 135°), which allowed a very quick pulse design (less than one minute). SPACE pulse optimisation was restricted to water voxels, as fat-selective saturation is used in the sequence. Simulated FA and signal were compared with those stemming from the default square pulse.

4.2.2 Results

Figure 4.3a shows the simulated FA map corresponding to the slice pictured in fig. 4.2. A zone of local FA overshoot (red circle) aligns with the highlighted T_2H from fig. 4.2. Table 4.1 gathers FA and signal homogeneity results. In the rightmost column, we reported

Table 4.1: Flip angle (FA) homogeneity simulation results, and SPACE signal simulation at effective TE. FAs were calculated in water voxels only. The ROI mentioned in rightmost column is a 20-mm-diameter sphere whose axial great circle is depicted in red on fig. 4.3. Values represent the relative difference between average SPACE signal in this ROI and in both breasts.

Pulse type	FA NRMSE	SPACE hypersignal in ROI
Square	18.6 %	12.6 %
9 k_T-points	10.7 %	4.1 %

the relative difference between (i) the mean signal in a 20-mm-diameter sphere centred on region of FA overshoot in the left breast, and (ii) the mean signal in both breasts. RF inhomogeneity alone is accountable for a 12.6 % T_2H. Figure 4.3b and table 4.1 report the FA map simulation for the k_T-points pulse. K_T-points substantially lower FA NRMSE. Most importantly, this would translate into reduced RF-induced T_2H.

4.2.3 Conclusion

These results point out potential misinterpretation in T_2-weighted breast MRI due to RF inhomogeneity at 3 T: even if the reported T_2H is not solely RF-induced, the artefact could bring a lesion away from a malignancy threshold, thus implying a false-negative diagnosis. Given how not straightforward the SPACE signal is (section 1.2.2), RF artefacts cannot be removed by post-processing. However, simulations showed that single-channel k_T-points pulses, which can be implemented on any scanner, are promising in reducing RF-related inhomogeneity beforehand.

4.3 Is This a Recurring Situation?

4.3.1 Looking for B_1 Artefacts in More Patients

A study was led on 27 patients from 9th November 2017 to 25th January 2018, to determine whether similar artefacts were actually frequently observed. We focused on T_2w SPACE acquisitions, as done in the first case report. Indeed, we wanted to evaluate T_1w DCE-MRI as well, but the acquisition time for this sequence was about 80 s. Even when playing our two sequences – square pulse and k_T-points – in veinous phase, there was no guarantee that the two acquisitions would have been comparable: it would have been difficult to distinguish between RF-related and time-related differences in contrast enhancement. This time, the goal was also to perform actual SPACE acquisitions with single-channel k_T-points, not just simulations.

In the case report, even though we managed to reduce the overall FA inhomogeneity in the volume, some regions of FA over- or undershoot remained, for instance in the right breast on fig. 4.3. This can be attributable to the fact that, as explained in section 1.4.1, the FOV used for breast imaging is wide in the rostrocaudal direction, so as to include

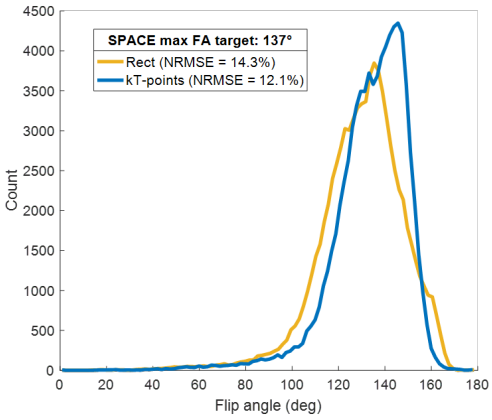

(a)

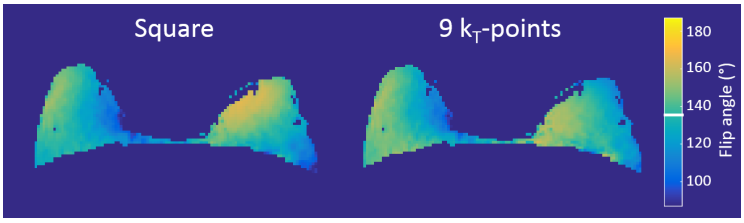

(b)

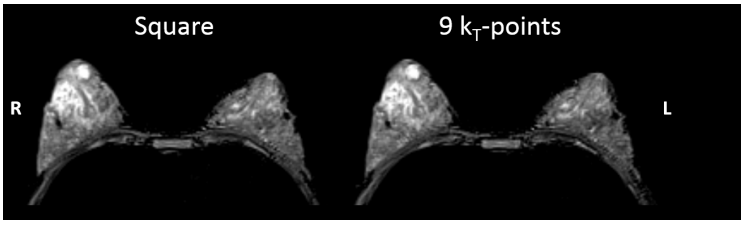

(c)

Figure 4.4: Acquisition example 1: 20-year-old patient with very dense breasts. (a) Histogram of the FA distribution in the whole volume of interest for the square pulse (orange) and the k_T-points (blue); the target is the highest FA in the flip angle train: 137°. (b) FA map in water voxels in a selected slice for both techniques. (c) Corresponding SPACE acquisition; image windowing is the same for both techniques. Despite the dimensions and density of the breasts, no local T_2H is visibly correlated with FA inhomogeneity.

axillary nodes. Those areas suffer from both B_0 and B_1 inhomogeneities, but including them in the volume of interest means including other tissues such as muscles. Those tissues are unnecessary for the examination, but can represent a large portion of water voxels in the volume. This is especially true in patients with mostly adipose breasts, since water voxels – the only ones selected for homogenisation – are scarce. As a consequence, the optimisation algorithm focuses a lot on homogenising excitation in irrelevant areas rather than in the breast. For this study it was decided, as a first step, to use a smaller FOV, strictly limited to the breasts. This could be avoided in the future by using an adequate segmentation method to isolate breast tissues.

For many patients, the breasts were either too small or too adipose to induce significant flip angle inhomogeneity. Here, some of the most notable cases are reported. Figure 4.4

shows an example of a patient with large breasts, with a very high water content: we could expect strong B_1 artefacts. However, we see on the histogram (fig. 4.4a) that the NRMSE is low for both pulses – square and k_T-points. The distributions are similar, and well-centred around the target FA (137°). Still, we can see on the FA map in one specific slice (fig. 4.4b) that excitation shows some inhomogeneity, especially in the square pulse case, with flip angles as low as about 120° and as high as about 160°. Nevertheless, on SPACE acquisitions (fig. 4.4c), both techniques produce similar images, where hyperintensities do not correlate with RF inhomogeneity. The T_2H in the right breast are indeed associated with lesions.

Figure 4.5 introduces a second example. Here k_T-points achieve a clearly better NRMSE over the volume of interest than the standard pulse (13.2 % vs 18.4 %). The histogram is also more narrow. Nevertheless, both techniques are indiscernible in most slices in terms of image quality: a representative slice is shown in figs. 4.5b and 4.5c (FA map and SPACE acquisition respectively). In some regions however, especially in the lower slices, k_T-points achieves significantly better FA homogeneity, as shown in fig. 4.5d. With the square pulse , the important FA undershoot leads to severe signal loss, which is recovered with k_T-points (fig. 4.5e). Note that in the area that lacked signal the most, the flip angle was below 90°–100°, which corresponds to about 70 % of the target: this tends to point out that the SPACE signal is relatively robust to FA inhomogeneity. However, there is not enough breast tissue in this example to comment on contrast.

Finally, fig. 4.6 reports the example of a patient with left mastectomy and silicone implants on both sides. As in fig. 4.4, here the NRMSE for k_T-points is slightly lower than for square pulses, and the histogram is less broad. The slice shown in fig. 4.6b highlights a noticeable local FA overshoot (up to 160°), which correlates with a T_2H in the SPACE acquisition (fig. 4.6c). On the other hand, with k_T-points, the FA distribution is closer to the target and more homogeneous – with a slight undershoot in the anterior part of the breast. In terms of image quality, this translates into a better contrast in breast tissues. Unfortunately, because the contralateral breast is absent, the T_2H observed with the square pulse does not have a real impact on interpretation, unlike on fig. 4.2.

4.3.2 *TrueForm* Works Well in the Breasts

Considering these results, strong FA inhomogeneity is hard to find in the breasts. This seems to be in contradiction with the worried literature exposed in sections 2.1.2 and 4.1 (figs. 2.6 and 4.1). After further inspection of the examples pointed out in the literature, we realised that they were all obtained with 3 T systems different from ours. What was common to those examples is that the body coil was driven in circular polarisation (CP) mode (*cf.* fig. 2.12a on page 59).

Additionally, in [Winkler 2015], the authors compared the results obtained in six subjects when adjusting manually the amplitude and phase of the transmission ports so as to try different elliptical polarisation (EP) modes. They showed that it was possible to find an optimal fixed RF amplitude/phase setting between those ports, that would provide

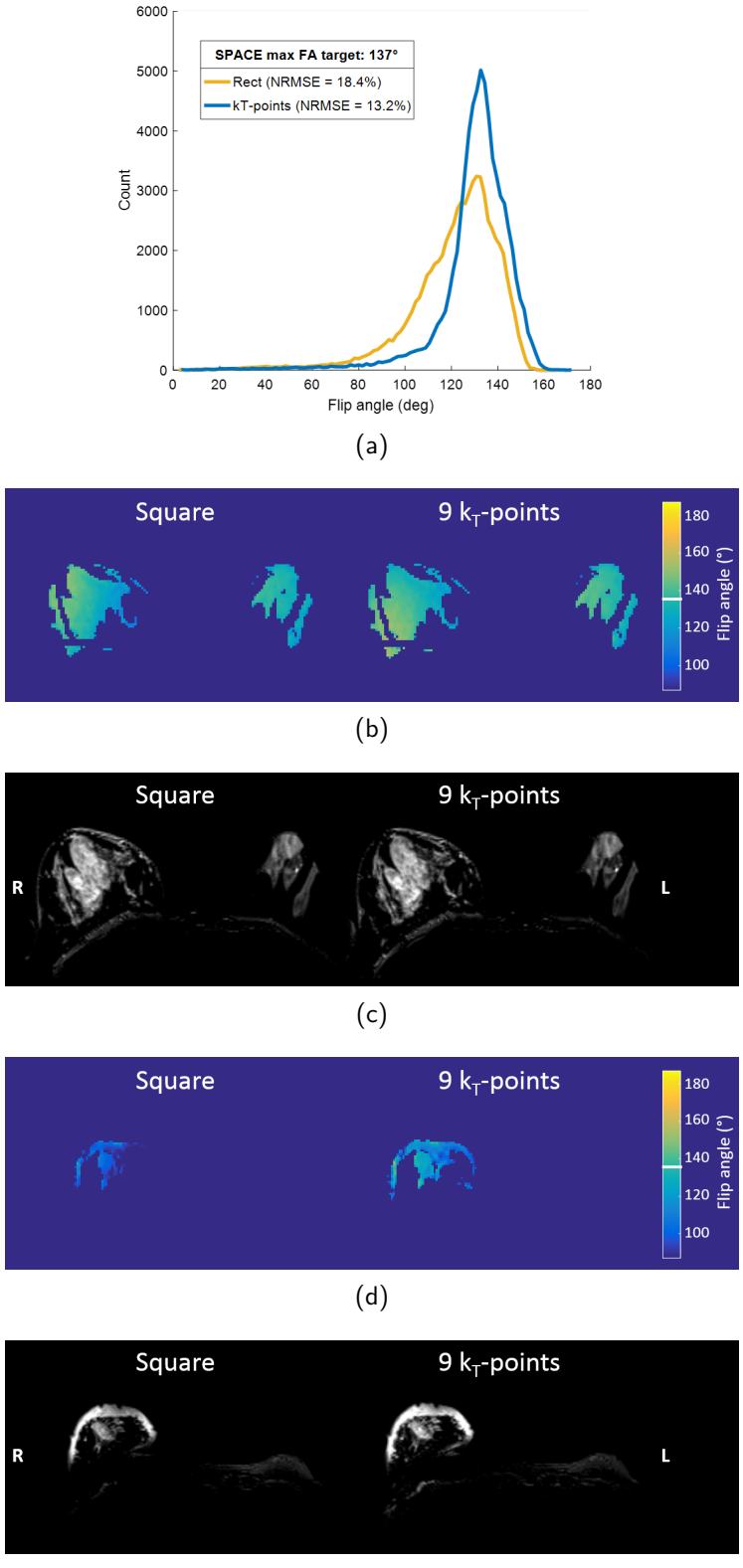

Figure 4.5: Acquisition example 2: 53-year-old patient with dense breasts and reconstruction in the right breast. Same layout as fig. 4.4, for two different slices. (b,c) On the first slice, almost no difference in image quality is visible between techniques. (d,e) On the second slice (lower edge of the FOV), k_T-points show some improvement in FA and signal homogeneity.

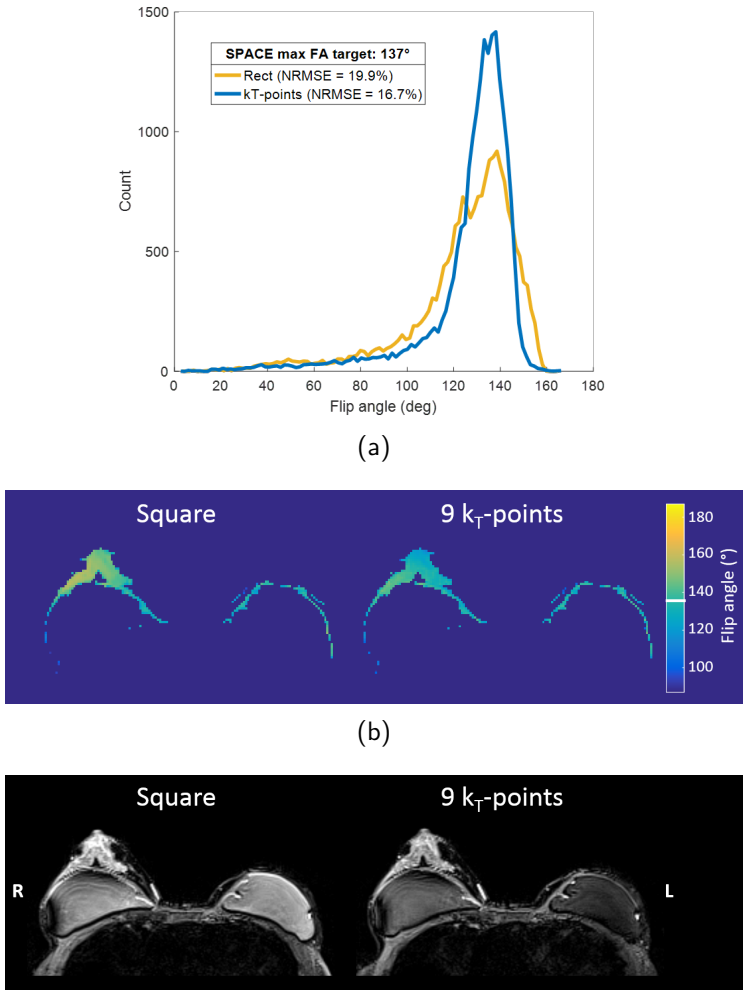

Figure 4.6: Acquisition example 3: 62-year-old patient with left mastectomy and bilateral silicone implants. Figure layout is the same as in fig. 4.4. FA and signal overshoot induced by the square pulse seems to be corrected with k_T-points. Signal in the implants (c) is very different between techniques, because silicone, just like fat, was discarded from the k_T-points optimisation, as one can see in (b).

adequate excitation homogeneity in the 'average' patient.

This is actually what *TrueForm*™, present on Siemens's Verio 3 T, consists in. We saw in section 2.3.1 that this scanner does not offer pTx and therefore cannot provide patient-tailored static RF shimming, but its transmission mode through the body coil is a fixed EP mode, supposed to mitigate RF inhomogeneity correctly in most patients. In the case of breast imaging, a study by Geppert *et al.* [Geppert 2008] endeavoured to assess the impact of *TrueForm* transmission compared to conventional CP. For the sake of the experiment, they modified a Siemens Verio scanner to manually switch between the two modes on the two-port body coil. They were able to measure flip angle maps with the two transmit modes in 11 volunteers, and found that FA deviation was systematically higher in CP mode than in *TrueForm* (fig. 4.7a). On that figure, we can even see that in all subjects, the most inhomogeneous distribution using *TrueForm* was still better than the

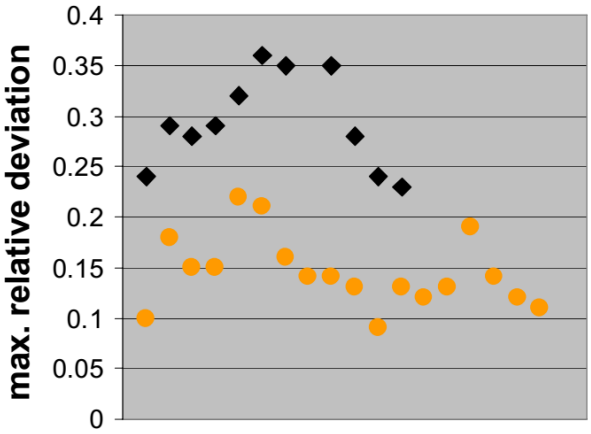

(a) Black: quadrature. Orange: *TrueForm*.

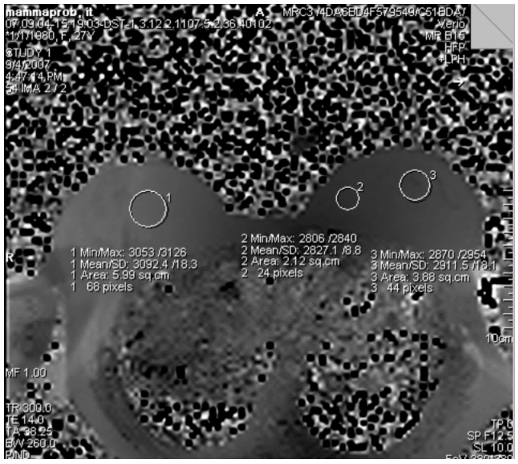

(b) Quadrature RF excitation.

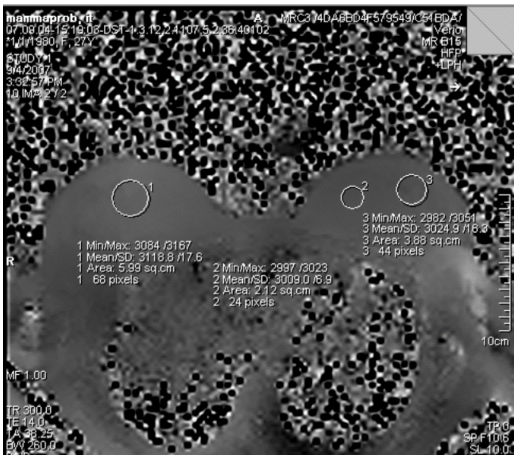

(c) *TrueForm* RF excitation.

Figure 4.7: Comparison between CP and *TrueForm* driving modes on a modified Verio's body coil, for breast imaging. (a) Maximum relative deviation of the measured FA from the nominal FA, with both modes for 11 volunteers, and with *TrueForm* only for 6 additional volunteers. (b,c) Measured FA distribution maps of conventional (CP) and *TrueForm* RF excitation in one volunteer. Greyscale values 0 to 4095 represent −180° to +180°. From [Geppert 2008].

most homogeneous distribution in quadrature. Figures 4.7b and 4.7c show an example of FA distribution in one subject with both methods.

Our results corroborate this study, and the adequacy of *TrueForm* for breast imaging, as in all the subjects we scanned, we did not find any occurrence of RF inhomogeneity strong enough to significantly degrade image quality.

4.4 Conclusion and Perspectives

From that study on single-channel breast MRI at 3 T, we can conclude that k_T-points did not improve FA homogeneity nor image quality much compared to *TrueForm*, which seems to be sufficient for clinical applications in the breasts.

K_T-points could have been more performant, had they not been designed to be scalable:

this restricts the degrees of freedom in the optimisation compared to 'standard' refocusing k_T-points, especially in sTx. Here the choice of scalable k_T-points was justified by the fact that they are more easily incorporated into the product SPACE sequence used and are faster to design since only one scalable pulse is needed to make the whole refocusing train as well as the excitation. Also, as stated before, masking the ROI to focus solely on water voxels corresponding to mammary gland was a difficult task, even with a reduced FOV. The few regions at the edge of the FOV containing, for instance, muscle tissue, could be more strongly affected by RF inhomogeneity. Since the NRMSE metric is a quadratic function of FA deviation from the target, those important FA variations could have a strong impact, even though they corresponded to small volumes, and even if they were not interesting for a breast examination. K_T-points performance could be much improved – and extended to axillary nodes – with anatomy-specific masking of breast tissues. Also, k_T-points could of course benefit from parallel transmission.

After this work on excitation homogenisation in breast imaging on a single-channel scanner, let us move to another body area that is generally associated with B_1 artefacts. The last chapters of this thesis relate two studies focusing on liver MRI, this time with a two-channel transmission system.

* * *
* *
*

Chapter 5

Clinical Assessment of K_T-Points in Abdominal DCE-MRI

Chapter Outline

This chapter was accepted for publication as:

R. Tomi-Tricot, V. Gras, F. Mauconduit, F. Legou, N. Boulant, M. Gebhardt, D. Ritter, B. Kiefer, P. Zerbib, A. Rahmouni, A. Vignaud, A. Luciani and A. Amadon. *B1 artifact reduction in abdominal DCE-MRI using k_T-points: First clinical assessment of dynamic RF shimming at 3T.* Journal of Magnetic Resonance Imaging, vol. 47, no. 6, pages 1562–1571, June 2018.

The methods and principles contained in this chapter were also presented at international conferences as:

R. Tomi-Tricot, V. Gras, F. Mauconduit, F. Legou, N. Boulant, M. Gebhardt, D. Ritter, B. Kiefer, P. Zerbib, A. Rahmouni, A. Vignaud, A. Luciani and A. Amadon. *First Clinical Assessment of k_T-Points Dynamic RF Shimming on Abdominal DCE-MRI in a Commercial 3T MRI Scanner.* In Proceedings of the 103rd Annual Meeting of the Radiological Society of North America, page SSK17:02, Chicago, IL, USA, 2017.

R. Tomi-Tricot, V. Gras, F. Mauconduit, F. Legou, N. Boulant, M. Gebhardt, D. Ritter, B. Kiefer, P. Zerbib, A. Rahmouni, A. Vignaud, A. Luciani and A. Amadon. *K_T-Points Pulses Reduce B1 Shading at 3T: Demonstration in Routine Abdominal DCE-MRI and Evaluation of Reliability.* In Proceedings of the 26th Annual Meeting of ISMRM, page 2689, Paris, France, 2018.

The purpose of this chapter is to assess excitation homogeneity and image quality achieved by k_T-points pulses, compared to static RF shimming, on abdominal imaging in clinical routine with a commercial 3 T scanner.

5.1 Introduction

As we have seen in chapter 2, the abdomen is one of the regions where B_1 artefacts are the most noticeable. They do not systematically appear in every subject, but when they do, the examination quality can drop dramatically, especially in patients with ascites (figs. 2.5a and 2.9).

Several methods have been proposed in order to take advantage of the gain in SNR offered by high-field MRI, with the hope to reduce the variability in examination quality between patients. In clinical routine abdominal imaging, we mentioned passive RF shimming (section 2.2.1) with a gel-filled cushion (fig. 2.11), or static RF shimming (section 2.2.2) on recent scanners equipped with pTx. Researchers have long been developing more advanced techniques, under the general name of dynamic RF shimming (section 2.2.3). However, we have seen in section 2.3 that to date, these methods have not been tested in clinical practice for abdominal and liver imaging, where static RF shimming is still the gold standard.

In this chapter, we propose to assess the applicability of k_T-points for non-selective excitation in the abdomen, and compare them to static RF shimming. We will be using the k_T-points pulse design algorithm described in chapter 3. As k_T-points are spatially non-selective, they are appropriate for 3D imaging provided image aliasing is avoided along phase and partition directions. In particular, they may be used on patients with liver conditions in dynamic contrast-enhanced (DCE) MRI based on a fat-suppressed T_1-weighted 3D FLASH sequence applied in one breath-hold. The clinical interest of DCE-MRI was detailed in section 1.4.2. In such a protocol, one reference 3D image is acquired prior to an injection of contrast agent, then the acquisition is repeated at different times in order for the radiologist to follow the perfusion of tissues, which is crucial to characterise certain focal lesions.

5.2 Materials and Methods

5.2.1 Protocol

Our study was approved by the institutional review board of Centre Hospitalier Universitaire Henri Mondor, and informed consent was waived. On each Wednesday from January 11th to February 15th 2017, measurements were performed on 50 consecutive subjects referred for liver or pancreas MRI. The study included 30 male and 20 female subjects, aged 57 (SD: 14)[1] years (range: 23 – 89 years) and of 25.3 kg/m^2 (SD: 4.1 kg/m^2) body mass index (BMI) (range: 17.6 – 38.8 kg/m^2).

Acquisitions were carried out on a clinical MAGNETOM Skyra 3 T scanner (Siemens Healthcare GmbH, Erlangen, Germany), equipped with a product two-channel pTx system. Transmission was performed through the body coil driven in pTx mode while reception was realised with two – anterior and posterior – 30-channel phased arrays used in routine examinations.

Among the 50 included patients, 20 were scanned in the presence of a pulse designer (Raphaël Tomi-Tricot) while undergoing DCE-MRI. Such subjects constituted the study sample for k_T-points clinical evaluation; they are gathered in table B.1 on page 152, in chronological order. The information corresponding to the subjects shown in the figures of this study can be found in table 5.1 on page 108. One radiologist (Alain Luciani) with 15 years of experience in liver MRI reviewed all images before writing the radiological reports. He was asked to specify within the MRI report, based on the analysis of default DCE-MRI and T_2-weighted fat-suppressed TSE sequence (see fig. 5.1 on the next page), the presence of ascites or iron overload. The information corresponding to the subjects shown in the figures of this study can be found in table 5.1 on page 108.

A FA of 11° was targeted, in accordance with the FA/TR pair used locally for clinical examinations. 3D-FLASH acquisition parameters were: axial partitions, TE/TR = 3/6 ms, $320 \times 220 \times 72$ matrix, $(1.2 \times 1.2 \times 3.5)\,mm^3$ resolution, generalised autocalibrating partially parallel acquisition (GRAPPA) factor 2, 80 %/50 % phase/slice resolution,

[1] SD: sample standard deviation

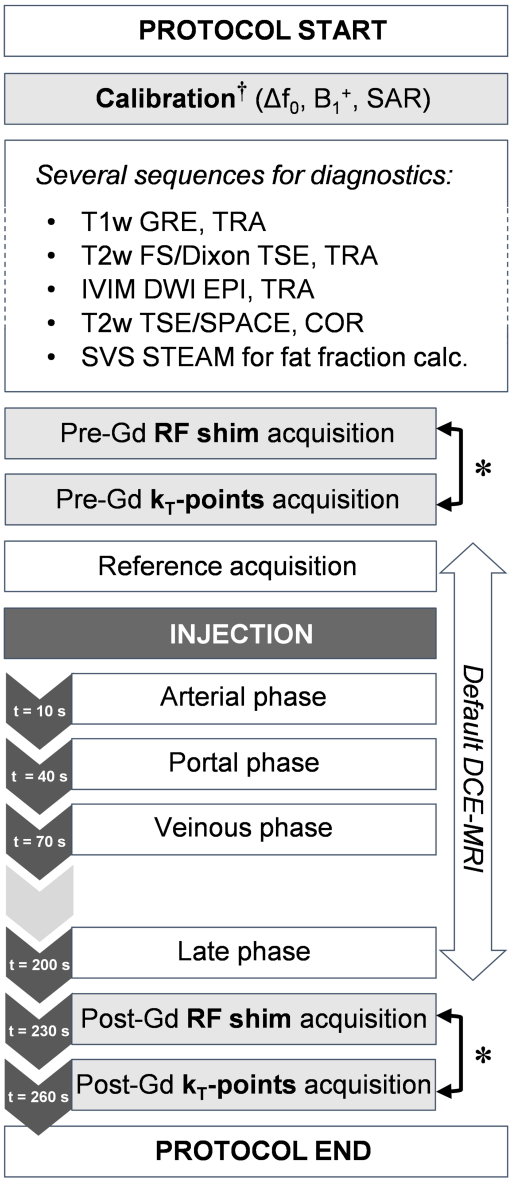

Figure 5.1: Insertion of our sequences (light grey) within the routine liver MRI protocol (white). Injected sequences relevant to this study were acquired at the far end of the acquisition protocol to preserve diagnostics routine timing. ✻ The order of our sequences was regularly reversed. † The calibration procedure included automated manufacturer B_1^+ mapping and a custom-made breath-hold Δf_0 map for proper water-fat resolution. *Abbreviations:* SAR = specific absorption rate; GRE = gradient-recalled echo; TSE = turbo spin-echo; SPACE = sampling perfection with application-optimized contrasts using different flip angle evolutions; IVIM = intravoxel incoherent motion [Luciani 2008]; DWI = diffusion-weighted imaging; EPI = echo-planar imaging; SVS = single-voxel spectroscopy; STEAM = stimulated echo acquisition mode; DCE-MRI = dynamic contrast-enhanced MRI; TRA = transverse plane; COR = coronal plane.

Table 5.1: Clinical information about the five subjects focused on in this study. Data corresponding to the patient population for image analysis (n = 20) is available in table B.1..

Subj.	Sex	Age years	Height cm	Weight kg	BMI kg/m^2	Contrast agent	Investigation	Visual cues*
1	M	66	169	73	25.6	Gd-BOPTA	monitoring after radioembolisation of several HCC nodules in segment 4	ascites
4	M	63	175	85	27.8	Gd-BOPTA	HCC chemoembolisation assessment	ascites (moderate)
17	M	23	171	61	20.9	Gd-DOTA	acute pancreatitis assessment	—
18	M	62	180	88	27.2	Gd-BOPTA	alcohol- and HCV-induced cirrhosis	—
20	M	59	170	85	29.4	Gd-BOPTA	bile duct obstruction in a cirrhotic liver	ascites

Abbreviations: HCC = hepatocellular carcinoma; HCV = hepatitis C virus.
*As indicated in the clinical MRI study reprts by a radiologist with 15 years of experience in liver MRI, based on the analysis of the default DCE-MRI and a T_2-weighted fat-suppressed TSE sequence (fig. 5.1).

partial Fourier (PF) factor of $^6/_8$, 505 Hz/pixel bandwidth, TA $\leq$ 23 s. For some subjects, those parameters had to be slightly adjusted to accommodate for a larger abdomen while maintaining acquisition time (TA) short enough for a single breath-hold. However, special care was taken to ensure that nominal flip angle, TE and TR were left untouched in order to keep the contrast identical for all subjects. In addition, for a given subject, all parameters were preserved between the static RF shimming and the k_T-points acquisition, including B_0 shimming parameters. Only the RF pulse differed: a 100-microsecond square pulse with complex coefficients automatically calculated by the scanner was used for static RF shimming, while for dynamic RF shimming a 9-k_T-point pulse was computed offline and loaded into the scanner. The two post-injection sequences were strictly identical to the pre-injection ones. To avoid aliasing in the partition-encoding direction, oversampling was used, and the required amount was minimised by selecting only the least number of coils necessary to cover the field of view. This selection could be done automatically by the manufacturer MRI software.

Depending on the investigation (table 5.1), the clinical examination procedure required that patients were injected with either gadobenate dimeglumine (Gd-BOPTA) or gadoterate meglumine (Gd-DOTA) at 0.05 mmol/kg and 0.1 mmol/kg body weight respectively, followed in all cases by an adequate saline flush.

The study aimed at assessing the performance of k_T-points compared to subject-tailored static RF shimming (so called 'patient-specific'). Therefore, a total of four series – shown in light grey on fig. 5.1 on page 107 – were acquired for each subject in addition to the routine protocol. After injection, only late-phase images were acquired, so that the timing set for diagnostic series was in no way corrupted. Acquisition delays after injection were therefore about 230 s and 260 s respectively for our two late-phase series. Fatty tissue was suppressed as short-T_1 fat otherwise yields hypersignal and tends to mask small signal enhancement ascribable to contrast agent perfusion [Le 2012, Leyendecker 2008]. The 'quick fat-sat' method [Le 2012] was chosen over a conventional fat saturation, in

order to minimise the impact on acquisition time and SAR. Fat suppression pulses were performed in the 'patient-specific' RF-shimming mode; therefore only the imaging hard pulse was modified into k_T-points in the 3D spoiled GRE sequence.

Acquisitions were somewhat corrected for reception profile through an automated manufacturer procedure known as 'Prescan Normalize', which normalizes individual surface coil images by an equivalent image received by the RF body coil. This assumes homogeneous body coil reception and is expected to yield poor results in this study as the B_1 artifact also affects the reception profile.

5.2.2 K_T-Points Pulse Design

A prototypical k_T-points pulse design algorithm minimised the FA NRMSE, *i.e.* the root-mean-square error normalized to the target FA over the volume of interest, by optimising simultaneously RF complex coefficients, k_T-point locations, pulse and sub-pulse durations under SAR and hardware constraints [Gras 2015, Hoyos-Idrobo 2014, Tomi-Tricot 2016]. This was achieved using MATLAB's (The Mathworks, Natick, MA, USA) built-in *active-set* algorithm on a laptop computer (Intel Core i7-4712HQ CPU, NVIDIA Quadro K1100m GPU). Flip angles were evaluated by numerical integration of Bloch's equation. The number of k_T-points was empirically chosen to be nine as it provides a trade-off between degrees of freedom and pulse duration: with more k_T-points, a lower NRMSE can be expected, but the minimal achievable pulse duration becomes longer. A limit of 1800 µs was set for the maximum allowed pulse duration, to ensure that a 3/6 ms TE/TR was kept. Taking advantage of GPGPU to accelerate critical parts in the optimisation problem allowed to design each tailored pulse in less than one minute.

Even though a quick pulse design and a short RF pulse are desirable features in clinical routine, here priority was given to homogenisation efficiency and generality across subjects: the same algorithm parameters were therefore used for all subjects.

5.2.3 Transmit B_1 and Off-Resonance Mapping, SAR Control

Let Δf_0 represent the Larmor frequency offset relative to the carrier frequency (123.2 MHz at 3 T), due to field inhomogeneity or/and fat-water chemical shift. For each subject, three-dimensional B_1^+ and Δf_0 over the field of view are necessary for pulse design. In order to rely as much as possible on tools available on product scanners, B_1^+ maps for each transmission channel were obtained from the manufacturer standard adjustment procedure used for patient-specific static RF shimming, *i.e.* a magnetisation-prepared turbo FLASH sequence performed in free-breathing in about 30 s. Although a Δf_0 map was also provided, it was subject to breathing artefacts and its spectral resolution was insufficient to identify fatty tissues. A breath-hold Δf_0 mapping sequence (TA = 10 s) was therefore inserted instead, consisting of a two-echo GRE acquisition, with ΔTE = 0.95 ms, short enough to cover the whole frequency range, roughly ±500 Hz, without temporal phase wrapping. Both B_1^+ and Δf_0 maps were down-sampled to an isotropic resolution of 5 mm for pulse design.

The knowledge of Δf_0 across the field of view allowed to discriminate between water and fat voxels, assuming both types of tissue do not mix. Since fat-selective saturation was performed, it was not necessary to target a specific imaging flip angle in fat voxels. Selecting only water voxels for the optimisation allowed to achieve substantially lower computation times and to improve FA homogeneity over the water voxels.

One important aspect of the k_T-points pulse design procedure used in this study lies in the fact that SAR constraints were taken into account jointly with the flip angle optimisation. Resulting pulses therefore systematically complied with the scanner's 'look-ahead' SAR monitoring system. To this end, a set of virtual observation points (VOPs) [Eichfelder 2011] was used, provided by the scanner along with the B_1^+ maps.

5.2.4 Excitation Homogeneity Assessment

FA-map simulations were run for each of the 50 scanned subjects by numerical Bloch simulation performed retrospectively from actual Δf_0 and B_1^+ maps. The FA average, relative standard deviation and NRMSE over water voxels – segmented using the Δf_0 map – in the imaged volume were estimated for both static RF shimming and k_T-points pulses.

5.2.5 Image Analysis

For each subject of the 20-patient subsample (detailed in table B.1), enhancement ratio (ER), given in percent of signal increase, was evaluated for both techniques as:

$$\mathrm{ER} = \frac{S_{late} - S_{ref}}{S_{ref}} \times 100\,\% \tag{5.1}$$

where S_{ref} and S_{late} represent signal before and after injection, respectively. Normalisation by S_{ref} removes the reception profile, allowing a cleaner evaluation of transmission scheme efficiency. For each subject, all series were elastically registered using Siemens software for accurate calculation of ER maps and better comparison between techniques.

In addition, two independent radiologists (Alain Luciani and François Legou, with 15 and 5 years of experience in abdominal MRI, respectively) qualitatively assessed pre- and post-injection acquisitions for the 20 patients. For each subject, the k_T-points and RF shimming series were randomly renamed 'Technique 1' or 'Technique 2' in order to avoid evaluation bias towards either method. Acquisitions were graded on a four-point Likert scale from 0 to 3, according to several criteria:

- Signal homogeneity in the liver:
  - **0:** some liver regions are barely visible; diagnosis is jeopardized;
  - **1:** important shading; major diagnostic discomfort;
  - **2:** some shading; little diagnostic discomfort;
  - **3:** little to no shading, no diagnostic discomfort.

- T_1 contrast (preferably from post-injection images where the 11° target FA is closer to the expected Ernst angle in the liver):

0: missing or inverted contrast in some regions;
1: poor;
2: satisfactory;
3: good.

- Contrast enhancement quality
  0: missing or inconsistent enhancement;
  1: weak or hardly understandable;
  2: satisfactory, but with some unexpected inhomogeneities;
  3: good, matches expectations.

- Details of visible structures
  0: portal vein barely visible, potential lesion(s) indiscernible;
  1: main vessels visible, blurred lesion(s);
  2: most vessels visible, lesion(s) visible;
  3: distal veins clearly visible, lesion(s) well delineated.

- Finally, a global mark expressed the confidence level granted to each technique by the physician:
  0: unusable acquisition;
  1: low level of confidence;
  2: acceptable level of confidence;
  3: full confidence.

5.2.6 Statistical Significance

For quantitative results (NRMSE) and for each aspect of image quality, an exact matched-pairs one-tailed Wilcoxon signed-rank test was computed using the *exactRankTests* R[2] v3.3 package [Hothorn 2017] to compare k_T-points and static RF shimming. All reported *P*-values are exact one-sided significance levels, considered statistically significant when less than 0.05. For the qualitative analysis, Holm-Bonferroni correction [Aickin 1996] was applied to reduce the family-wise error rate.

5.3 Results

5.3.1 Excitation Homogeneity Assessment

Figure 5.2 on the next page compares the NRMSE obtained via simulation with the two techniques for each scanned subject: the 99 %-confidence-interval mean NRMSE was 20.7 % (SD: 1.8 %) for 'patient-specific' RF shimming over the whole population, and improved to 8.5 % (SD: 0.3 %) for k_T-points. 34 % of subjects showed NRMSEs over 20 % with static RF shimming, and none with k_T-points.

[2] www.r-project.org

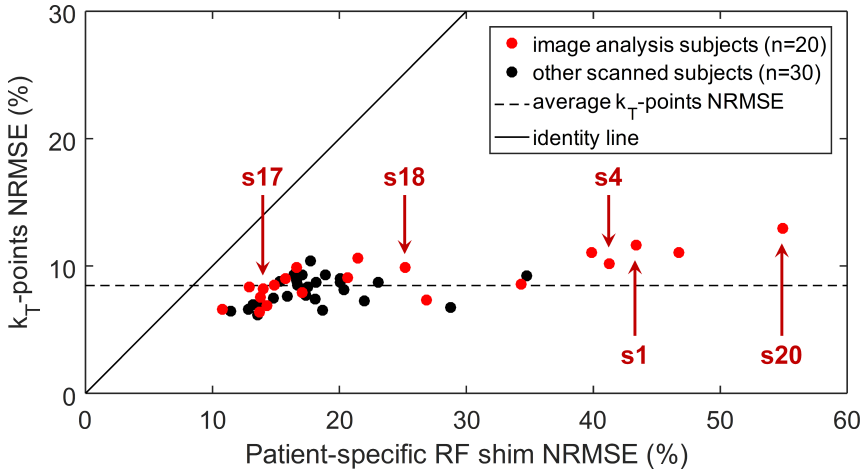

Figure 5.2: Comparison of the flip angle NRMSE obtained for each of the 50 consecutive subjects. Red dots correspond to subjects included in the image quality analysis (table B.1 on page 152). Arrows point out subjects shown in figs. 5.3 and 5.4. Solid line represents identity. Notice how the NRMSEs achieved by k_T-points are systematically lower than the static RF shimming ones, and how they are all gathered close to their mean, pointing to strong robustness of the k_T-points design.

Table 5.2: Detailed results of the quantitative analysis based on simulations of 'patient-specific' static RF shimming and k_T-points on the five subjects from table 5.1. The last line indicates the sample means and standard deviations across all 50 subjects. Targeted flip angle was 11°. While the difference between the two techniques was negligible for many subjects (*e.g.* 17, 18), k_T-points yielded considerably better results in some cases, including the three subjects with ascites (1, 4 and 20). Results for the whole population (n = 50) are available in table B.2.

Subject	Mean FA degrees		FA CV %		FA NRMSE %		Global SAR[a,b] W/kg		10g SAR[a,b] %		Duration[c] µs
	RFS	KTP	RFS	KTP	RFS	KTP	RFS	KTP	RFS	KTP	KTP
1	6.6	10.8	26.8	11.7	43.4	11.7	0.2	0.3	13	29	1750
4	6.7	10.9	21.1	10.2	41.3	10.2	0.2	0.3	14	46	1380
17	10.7	10.9	14.1	8.2	14.0	8.2	0.4	0.4	22	29	1420
18	9.4	10.9	17.4	9.1	20.6	9.1	0.4	0.3	22	27	1430
20	5.4	10.8	42.6	13.1	54.9	13.0	0.2	0.6	12	70	1660
All 50[d]	9.6 (1.4)	10.9 (0.0)	16.6 (5.0)	8.5 (1.5)	20.7 (9.8)	8.5 (1.5)	0.3 (0.1)	0.4 (0.1)	22 (9)	38 (11)	1420 (92)

Abbreviations: FA = flip angle; CV = coefficient of variation; NRMSE = normalized root-mean-squared error from the target; RFS = static RF shimming ; KTP = k_T-points.

[a] Global SAR was measured by the scanner and read directly from the DICOM files. Maximum local SAR was evaluated from the pulse shape, TR, and VOPs provided by the scanner.

[b] 6-minute average SAR limit is $2\,W\,kg^{-1}$ for whole body global SAR (IEC 60601-2-33); local SAR (10 g of contiguous tissue) is expressed as a percentage of the maximal authorised value in quadrature mode.

[c] Duration of static RF shimming square pulses was systematically ser to 100 µs.

[d] For each metric: sample average (sample standard deviation) over the 50 subjects.

Table 5.2 gathers simulation FA homogeneity results (average, coefficient of variation and NRMSE) as well as SAR and pulse duration information for the five subjects from table 5.1 on page 108. Results for all 50 subjects are listed in table B.2 on page 153. K_T-points systematically attained average FA values very close to the 11° target excitation, whereas static RF shimming was not as regular: 10.9° (SD: 0.03°) versus 9.6° (SD: 1.4°) across subjects, respectively. K_T-points achieved lower NRMSEs compared to static RF shimming, with much less variability across subjects: 8.5 % (SD: 1.5 %) (k_T-points) vs 20.7 % (SD: 9.8 %) (RF shimming), $p < 0.0001$. The worst NRMSE encountered was 13.0 % (k_T-points) instead of 54.9 % (RF shimming) for subject 20, who suffered from heavy ascites according to the radiologists (table 5.1).

5.3.2 Image Analysis

Figures 5.3 and 5.4 show examples of images acquired on subjects before and after contrast agent injection, as well as the corresponding ER maps. Figure 5.4 focuses on the three patients (subjects 1, 4 and 20) diagnosed with ascites (amongst the 20-patient group), showing substantial B_1^+ artefacts. ER maps obtained with k_T-points showed higher values in all these subjects. Those results corroborate the simulations from table 5.2: for instance FA NRMSE for subject 1 was 43.4 % with static RF-shimming, while k_T-points achieved 11.7 %. For other subjects, homogeneity was generally already satisfactory with 'patient-specific' static RF shimming; only little to no amelioration was noticeable on anatomical images (subject 17, fig. 5.3), despite slightly better simulation results. However, improvement could be visualized on the ER maps (*cf.* for instance subject 18 in fig. 5.3).

Qualitative grades obtained with k_T-points were higher than with static RF shimming for all criteria, as pictured in fig. 5.5. Statistical significance was established for T_1 contrast (2.4 (SD: 0.4) for k_T-points vs 2.0 (SD: 0.5) for RF shim; $p = 0.002$), contrast enhancement (2.2 (SD: 0.5) vs 1.9 (SD: 0.5); $p = 0.02$), structure details (2.4 (SD: 0.5) vs 2.0 (SD: 0.6); $p = 0.01$) and global image quality (2.3 (SD: 0.5) vs 1.9 (SD: 0.6); $p = 0.008$). The examination of subject 20 (fig. 5.4) was judged unusable (0/3 for all criteria) with RF shim by one reader, whereas no image was deemed unexploitable with k_T-points. 85 % of k_T-points acquisitions were graded at least 2/3, compared to only 55 % in the static RF shimming case.

5.4 Discussion

Our results confirm that the proposed k_T-points approach yields better results in the abdomen than static RF shimming: this is shown here in both the simulation of FA homogenisation and the visual assessment of clinical routine dynamic contrast-enhanced (DCE) images on a commercial 3 T scanner. However, as expected, k_T-points impact spanned from image quality *status quo* for the majority of subjects to large improvement in more 'difficult' cases – ascites, siderotic liver, subject dimensions or muscle/fat proportion [Bernstein 2006] – where static RF shimming was not sufficient to properly reduce

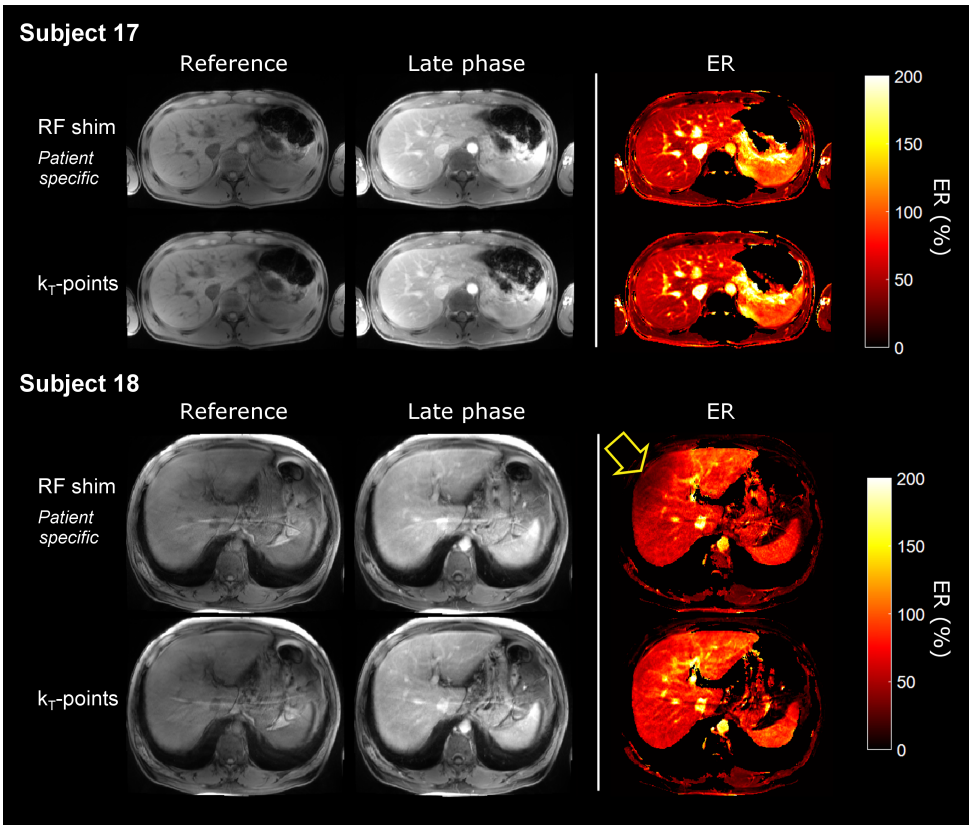

Figure 5.3: From left to right: pre-injection, post-injection and calculated enhancement ratio (ER) images obtained from two subjects (17 and 18) showing no particular *a priori* inhomogeneity. For both subjects, the top row images were obtained using a 'patient-specific' static RF shimming pulse, and the bottom row corresponds to the k_T-points excitation. Anatomical image windowing is the same in all cases for a given subject. Windowing is also the same in all ER images. **Subject 17:** 23-year-old male. Anatomical images are almost identical, and there is no significant gain nor loss of contrast enhancement between static RF shimming and k_T-points. **Subject 18:** 62-year-old male. Although anatomical images look similar, ER calculations highlight a large contrast enhancement gain in segments 8 and 4 (hollow arrow) brought by the k_T-points technique over the 'patient-specific' static RF shimming. For each subject, on bottom row, residual image inhomogeneity (pre- and post-injection) is mostly due to coil array receiving profile, with no impact on ER.

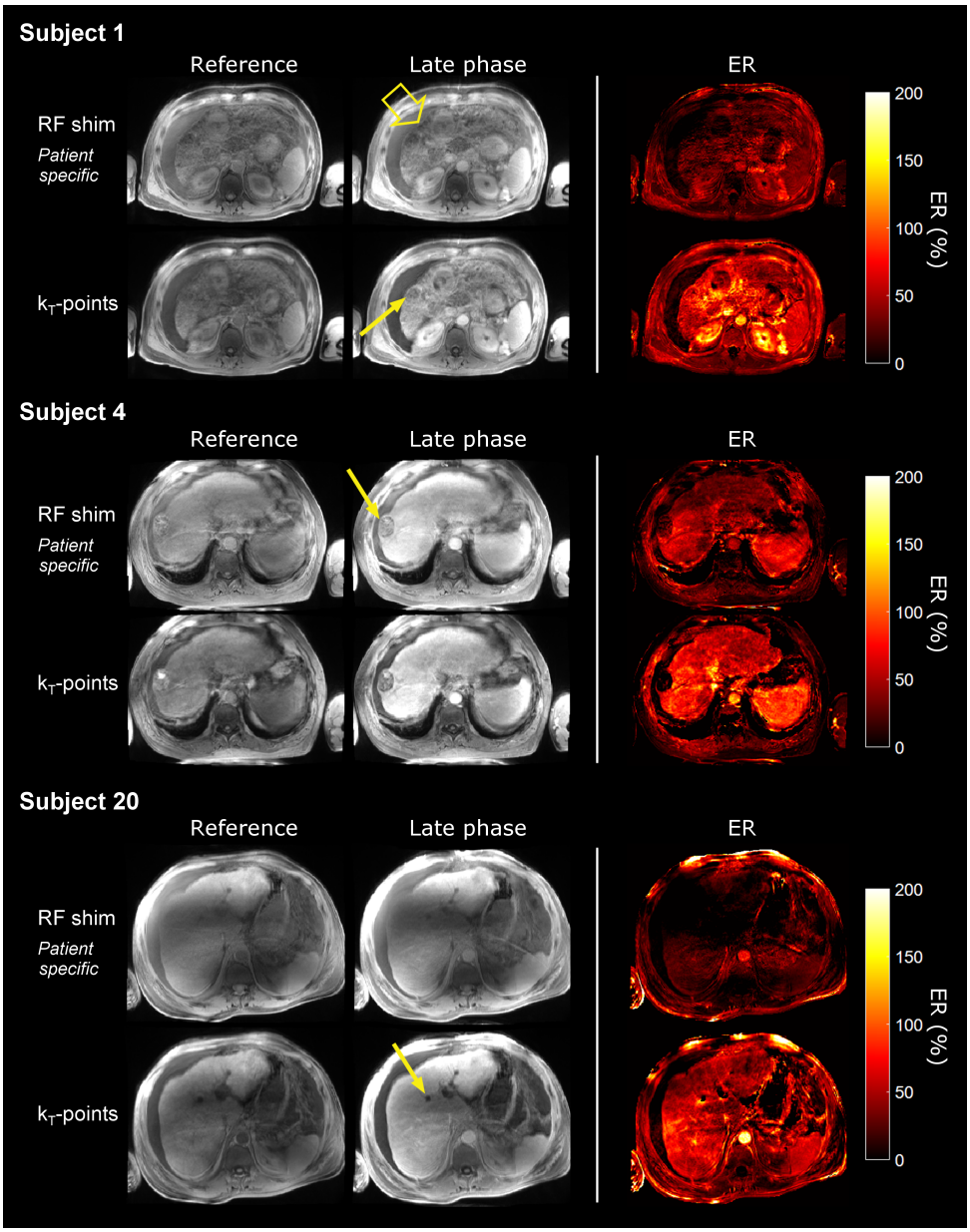

Figure 5.4: Same layout as fig. 5.3, for the three subjects (1, 4 and 20) with ascites. **Subject 1:** 66-year-old male. The contrast between ascites and adjacent liver is better defined with k_T-points; liver signal is more homogeneous (hollow arrow); enhancement ratio (ER) is improved; a siderotic nodule (full arrow) was almost hidden by the zone of shade on the RF shim images. **Subject 4:** 63-year-old male. Signal homogeneity and ER are improved; hypointensity within the embolised HCC lesion (full arrow) is more clearly demarcated. **Subject 20:** 59-year-old male. Shading is present in static RF shimming anatomical images and there is virtually no contrast enhancement in most of the liver. Images acquired with k_T-points are almost free of shading artefact, especially in terms of ER. Also notice the well-defined cystic structure (arrow) in segment 4. For each subject, on bottom row, residual image inhomogeneity (pre- and post-injection) is mostly due to coil array receiving profile, with no impact on ER.

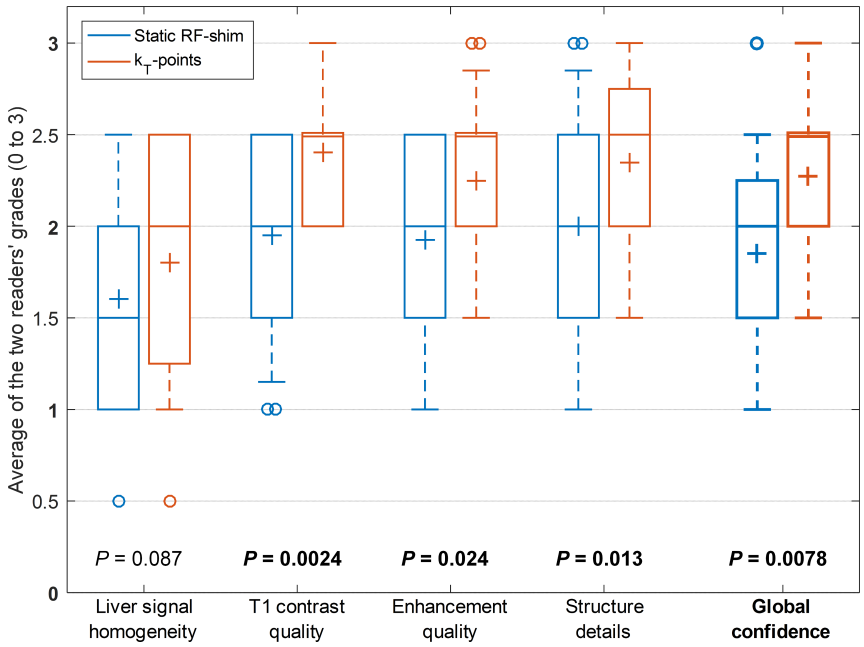

Figure 5.5: Distribution of the qualitative grades, averaged over readers, obtained by static RF shimming (blue) and k_T-points (orange) for all five criteria. *P*-values were calculated from an exact matched-pairs one-tailed Wilcoxon signed-rank test; statistically significant *P*-values ($p < 0.05$) are printed in bold font. Liver signal homogeneity generally received bad grades, even for k_T-points, as reception profiles still alter image quality; in addition, targeting an 11° FA is suitable for contrast enhancement and signal homogeneity on post-injection images, but not for pre-injection ones. Cross in each box = mean value; central mark = median; edges of the box = 25th (Q1) and 75th (Q3) percentiles; whiskers = 10th (D1) and 90th (D9) percentiles; circles = outliers.

the B_1 shading, leading to potential diagnostic changes. All subjects with ascites benefited from the k_T-points, which tends to show that this technique is robust for clinical routine at 3 T, regardless of the subject's abdominal size and composition.

On-the-fly k_T-points pulse design has demonstrated that tailored dynamic pTx can fit in a clinical routine protocol. The FLASH sequence used in this study allowed to exactly compare the two transmission schemes, but more elaborate imaging sequences could have been used instead. The k_T-points pulse design is readily compatible with sophisticated techniques such as CAIPIRINHA [Riffel 2013] and Dixon [Dixon 1984, Ma 2004], and could be integrated into the XD-GRASP framework [Feng 2016]. It is worth mentioning that k_T-points pulses could also be designed to perform better fat suppression.

For some sequences, one improvement would be to reduce the pulse duration: lowering the number of k_T-points sub-pulses could allow designing pulses shorter than a millisecond without damaging FA homogeneity too much. More transmission channels, by offering more degrees of freedom, would also help to find a better trade-off between pulse duration, excitation homogeneity and SAR control. Additionally, better results could be achieved by using the body coil at its full power capabilities. A different choice of optimisation cost function, for instance trying to homogenise the GRE signal (for a given

T_1) rather than the flip angle, can be another solution to ease the pulse design. Spoiled GRE signal homogeneity is indeed rather permissive to flip angle errors around the Ernst angle, especially if the achieved angle is slightly larger than expected. Taking this into account may help reduce the number of needed sub-pulses. Using fewer sub-pulses also implies faster pulse design: the current computation time is a little less than a minute on a powerful laptop, which might prove too slow for everyday clinical use. However this is not a real issue as it can be effortlessly improved through use of better hardware and integration of the procedure into the manufacturer's software.

Only in a few cases, such as subject 12, was acquisition quality slightly lower with k_T-points than with static RF shimming, despite favourable simulation results. This can potentially be attributed to subject-movement-induced Δf_0 fluctuations between calibration and acquisitions, as k_T-points are inherently less broadband than hard pulses. Results could be improved by acquiring Δf_0 (and B_1^+) maps in two successive breath-holds as recently proposed for 7 T heart imaging [Schmitter 2015].

ER is a visual parameter that illustrates the potential gain of contrast obtained with dynamic RF shimming. Quantitative ER assessment in the liver was not performed, as quantitation could have been biased by region of interest (ROI) selection since areas of shade were unevenly distributed.

Comparing anatomical images and ER maps obtained with k_T-points shows that a large part of the remaining shading on the former can be attributed to the non-uniform reception profile, *i.e.* the B_1^- field; the 'Prescan Normalize' B_1^- correction is not sufficient because it wrongly assumes the body coil reception profile is uniform. However, removing the true B_1^- inhomogeneity is beyond the scope of this study. This can explain the generally low qualitative grades obtained for *liver signal homogeneity*, even with k_T-points. Targeting an 11° FA also induces sub-optimal signal in pre-injection acquisitions as liver parenchyma – $T_1 \approx 800$ ms [Stanisz 2005] – Ernst angle is 7° for the TR considered.

One limitation of this study lies in that the pulses designed are strictly non-selective, therefore fit for 3D sequences with some oversampling in the partition-encoding direction. However, the same pulse design procedure can be used to produce slab- or slice-selective excitation, by replacing the rectangular RF sub-pulse waveforms with sinus cardinal ones, accompanied by an appropriate selection gradient. This could be achieved at the expense of pulse duration, so one might need to reduce the number of sub-pulses in that case. This study claims only relative image quality improvement from one technique to another, as there is no absolute reference standard of B_1-artefact-free technique in 3 T abdominal imaging on this type of scanner. A phantom experiment was performed to validate the method, but is not reported here as the k_T-points technique has already been validated extensively both in phantoms and *in vivo* [Cloos 2012a, Massire 2015]. Other study limitations include: a relatively small number of patients, only liver DCE-MRI, and a single 3 T scanner model.

5.5 Conclusion and Perspectives

K_T-points significantly reduce excitation inhomogeneity quantitatively and qualitatively, with a positive impact in DCE-MRI, especially in patients with ascites and prone to B_1 shading artefact at 3 T. Parallel transmission was used to achieve better homogeneity while mitigating SAR deposition; it is however possible to implement k_T-points on single-channel systems [Eggenschwiler 2016,Hsu 2017], where static RF shimming does not exist. These first results in DCE-MRI promise great applications to other anatomical regions at 3 T. K_T-points should indeed improve non-selective preparation and 3D imaging wherever B_1 shading remains, be it in proton-density-, T_1-, T_2^*-, T_2- [Massire 2015] or diffusion-weighted imaging.

* * *
* *
*

Chapter 6

SmartPulse, a Machine Learning Approach for Calibration-Free Body Imaging K_T-Points

Chapter Outline

This chapter is under review for publication in Magnetic Resonance in Medicine as:

R. Tomi-Tricot, V. Gras, B. Thirion, F. Mauconduit, N. Boulant, H. Cherkaoui, P. Zerbib, A. Vignaud, A. Luciani, A. Amadon. *SmartPulse, a Machine Learning Approach for Calibration-Free Dynamic RF Shimming: Preliminary Study in a Clinical Environment.* Magnetic Resonance in Medicine. Submitted.

The methods presented in sections 6.3 and 6.4 were the object of the following patent:

R. Tomi-Tricot, B. Thirion, V. Gras, A. Amadon, N. Boulant, A. Vignaud. *A Computer-Implemented Method of Building a Database of Pulse Sequences for Magnetic Resonance Imaging, and a Method of Performing Magnetic Resonance Imaging Using Such a Database*, no. EP18305909, July 2018. Pending.

We continue our work on clinical routine 3 T MRI in the abdomen by introducing a new concept to remove the burden of calibration and pulse design associated with tailored RF shimming. The proposed method, *SmartPulse*, is a way to adapt the Universal Pulse technique, developed for brain MRI at 7 T and presented in section 2.4.3, to the inter-subject variability typically found in body imaging.

6.1 Introduction

In the previous chapter, using a scanner equipped with pTx in a clinical environment, we demonstrated the superiority of k_T-points dynamic RF shimming on static RF shimming for non-selective excitation in abdominal imaging. Indeed, although tailored static RF shimming is satisfactory for most patients, it fails to offer sufficiently homogeneous excitation in about 10 to 20 % of the population. However, both techniques are tailored, *i.e.* they require calibration consisting at least in the measurement of B_1^+ maps from each transmit channel; moreover, for optimal dynamic RF shimming, a frequency off-resonance Δf_0 map is also required before computation of the RF pulse. All these maps are acquired at the beginning of the examination and thus may become inaccurate in case of subject motion or/and breathing.

On a 3 T scanner with two channels, the whole calibration process can last nearly two minutes: 30 seconds for B_1^+ mapping, 15 seconds for Δf_0 mapping, and between 5 seconds (static RF shimming) and 60 seconds (k_T-points) for pulse design itself. This time naturally scales with the number of transmit channels. For this reason, Gras *et al.* [Gras 2017b] introduced the concept of Universal Pulses (UPs), that allows calibration-free pTx : instead of designing a pulse specific to each subject, a pulse robust to inter-subject variability is created once and for all using calibration data of a population of subjects. We saw in section 2.4.3 that UPs were successfully implemented for a variety of applications in brain imaging.

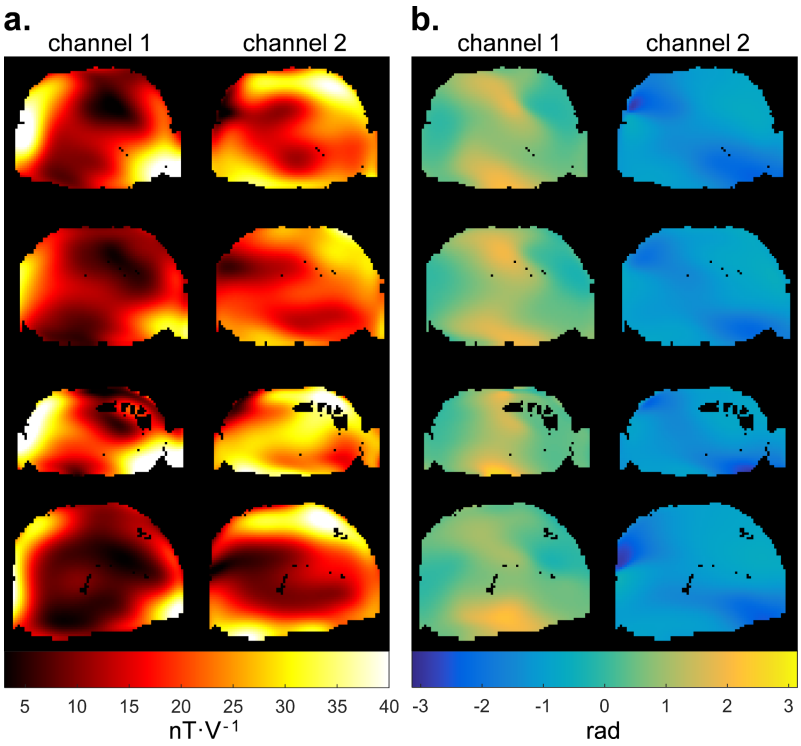

Figure 6.1: Examples illustrating the inter-subject variability of transmit B_1 field in the abdomen for four subjects (top to bottom). (a) B_1^+ magnitude for both transmit channels. (b) B_1^+ phase. Field of view and windowing are identical for all subjects.

Considering that universality could compromise individual homogeneity, some authors have explored machine learning approaches to design tailored pulses while reducing calibration time. Ianni *et al.* for instance developed a method to infer RF coefficients of a static RF shimming pulse using geometrical features of the head and limited B_1^+ information [Ianni Julianna D. 2018] with good accuracy. Mirfin *et al.* investigated a neural network solution to predict dynamic RF shimming pulses [Mirfin 2018], but the produced pulses still lacked performance. Both methods were targeting slice-specific pulses for brain examinations at 7 T.

The present work constitutes a proof-of-concept for a new method, *SmartPulse*, proposed to achieve the simplicity and user-friendliness of universal pulses under the important inter-subject variability found, for instance, in the abdomen at 3 T as shown in fig. 6.1, where a universal design may not suffice. Instead of designing one pulse for all subjects, a population is divided into clusters, and one *smart-universal* pulse is designed for each cluster. Then a machine learning algorithm classifies new subjects to assign the best possible pulse to each one of them. To comply with the calibration-free philosophy of universal pulses, only features that can be extracted automatically from a 'localizer' acquisition – a compulsory step preceding all imaging protocols – are used: no additional data is needed.

In continuation of the works described in chapter 5, this study was led in the context of DCE MRI. Once again, k_T-points being non-selective, they are appropriate for this

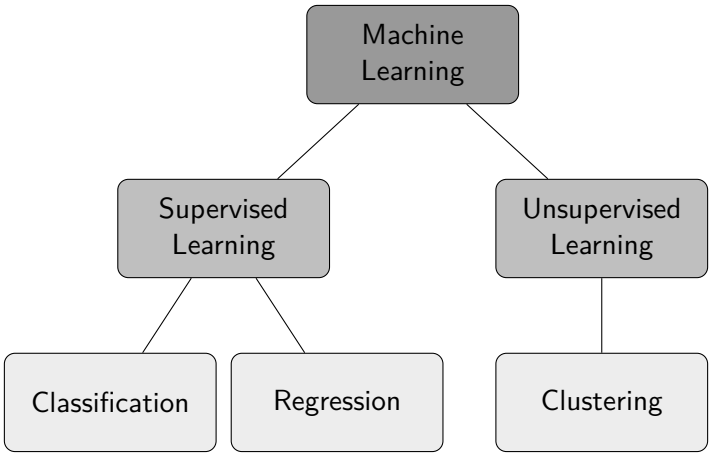

Figure 6.2: Main types of machine-learning-achievable tasks.

sequence where short echo time and repetition time are required: they were chosen as the underlying pulse parametrisation for *SmartPulse*. The performance of this method was assessed on calibration data from various subjects and compared to several other pulses, including universal k_T-points and *TrueForm* – a form of 'universal' static RF shimming (*cf.* section 2.3.1). The effect on DCE images acquired on a 3 T scanner in clinical routine was also investigated.

6.2 Elements of Machine Learning

As the *SmartPulse* method relies heavily on machine learning, let us first discuss what machine learning is, and what tasks and approaches this term encompasses.

Machine learning refers to various methods allowing to 'learn' information directly from data [Kohavi 1998], *i.e.* without a predetermined model. As shown in fig. 6.2, machine learning methods can be subdivided into two main families:

- In *supervised* learning, a predictive model is built from data that has been labelled beforehand: algorithms are trained on a set of examples for which both inputs – called features – and responses (outputs) to these inputs are known.
- *Unsupervised* learning, in contrast, relies solely on inputs: the aim is to reveal intrinsic patterns or structures in data.

Among the various applications of unsupervised learning, the most common one is cluster analysis, or *clustering*. Clustering aims at finding similarities in data in order to group elements together: elements belonging to the same group – or *cluster* – are more similar to one another than to those in other clusters. In order to perform data clustering, one must therefore find a measure of similarity (often a distance function) that best corresponds to the data, and choose a clustering method that best fits the needs. Common clustering approaches include hierarchical, centroid-based (*e.g.* k-means [MacQueen 1967]), distribution-based (*e.g.* Gaussian mixture) or density-based (*e.g.* DBSCAN [Ester 1996]) techniques. As expressed in the introduction, clustering a database of subjects is the first

step of the *SmartPulse* process. We will see in section 6.3.3 that hierarchical clustering presents the advantage to output a *dendogram* showing the bottom-up process of pairwise agglomeration into larger and larger groups (*cf.* fig. 6.3e), along with the distance between the successive groups formed in the process. Thanks to this useful representation of data, the user can then choose the number of clusters that seems most appropriate.

Supervised learning can be further divided into *classification* and *regression* methods. In classification tasks, the output is a set of discrete categories, or *classes*. When one thinks of machine learning, they often have classification in mind, especially as far as medical imaging is concerned. Algorithms commonly used for supervised classification include bayesian methods, support vector machines [Cortes 1995], k-nearest neighbours [Hastie 1996], and decision trees [Breiman 1984]. The latter are the basis for random forests [Ho 1995], an *ensemble* method which consists in aggregating (or bagging) multiple decision trees – each using a different subset of features or/and training examples – and voting the prediction, in order to reduce overfitting to the training set (*i.e.* generalise better to new data). Another classification method relies on artificial neural networks. When such networks are made of many layers, they are referred to as deep neural networks, which are the underlying architecture of deep learning approaches. Deep learning has become increasingly popular in image recognition applications – in particular with convolutional neural networks – since the introduction of *AlexNet* [Krizhevsky 2012] for handwritten digit recognition. Lately, there has been much enthusiasm for deep learning in medical imaging, for applications as varied as lesion classification [Yan 2018] or fat-water separation [Goldfarb 2017]. The second step of the *SmartPulse* process consists in classifying subjects, according to a number of features that do not rely on B_1^+ mapping, into one of the several categories determined during the clustering step. Given the relatively small number of training data available and the few features used, the classifier chosen in this study is based on a random forest and on a non-linear support vector machine (*cf.* section 6.4.4), which should both avoid overfitting and exploit feature non-linearity.

Finally, in regression tasks, the output to predict is a continuous variable. Typical methods are linear or logistic regression, but also decision trees (and random forests), support vector machines or neural networks. There is no regression involved in the *SmartPulse* process, but as we will see in the discussion, it could be used in the future to obtain better performance.

6.3 Theory

Since the goal is to design short non-selective excitation pulses robust to B_1^+ inhomogeneities, we adopted the k_T-points method and its formalism. In this section, we briefly remind subject-specific (tailored) as well as universal k_T-points pulse design (section 2.4). Then we introduce the clustering and pulse design specificities of *SmartPulse*.

6.3.1 Tailored k_T-Points Pulse Design

The k_T-points pulse design consists in homogenising the flip angle (FA) distribution in a region of interest by optimising simultaneously RF complex coefficients, k-space locations [Gras 2015] and durations (chapter 3) of each k_T-point sub-pulse. With N_{kT} sub-pulses on a pTx system equipped with N_{Ch} transmission channels, and using the vectors $\mathbf{x}$, $\mathbf{k}$ and $\mathbf{t}$ to represent, respectively, all sub-pulse RF complex coefficients, three-dimensional k-space locations, and sub-pulse durations, the optimisation problem can be expressed as [Gras 2017b, Setsompop 2008a]:

$$\underset{\mathbf{x},\mathbf{k},\mathbf{t}}{\arg\min} \; \|A(\mathbf{x},\mathbf{k},\mathbf{t}) - \alpha_T\|_2, \qquad (\mathbf{x},\mathbf{k},\mathbf{t}) \in \mathbb{C}^{N_{Ch}N_{kT}} \times \mathbb{R}^{3N_{kT}} \times \mathbb{R}^{N_{kT}} \tag{6.1}$$

where α_T is the targeted FA (a scalar) and A is the Bloch operator that associates a FA with each voxel depending on its B_1^+ and Δf_0 values (see section 2.4.1, either STA or LTA). Optimisation is performed under peak power, average power, and global and local SAR constraints [Hoyos-Idrobo 2014] to comply with hardware limits and patient safety.

6.3.2 Universal k_T-Points Pulse Design

The design of a universal pulse seeks to homogenise excitation simultaneously over the whole population, based on a sample of N_s subjects. In this work, the approach is a compromise between references [Gras 2017b] and [Gras 2017a]: in order to reduce the global FA inhomogeneity in the whole population while avoiding outliers, the mean plus standard deviation of the normalised root-mean-square FA errors (NRMSE) achieved in each subject was chosen as the cost function to be minimized. If we represent by $\mathcal{A} = \{A_1, \ldots, A_{N_S}\}$ the set of Bloch operators associated with each of the N_S subjects in the population, then we solve the following problem:

$$\underset{\mathbf{x},\mathbf{k},\mathbf{t}}{\arg\min} \; \|M(\boldsymbol{\mathcal{E}}) - \alpha_T\|_2, \qquad (\mathbf{x},\mathbf{k},\mathbf{t}) \in \mathbb{C}^{N_{Ch}N_{kT}} \times \mathbb{R}^{3N_{kT}} \times \mathbb{R}^{N_{kT}} \tag{6.2}$$

where $\boldsymbol{\mathcal{E}} = \left(\|A(\mathbf{x},\mathbf{k},\mathbf{t}) - \alpha_T\|_2\right)_{1 \leq i \leq N_S}$ is the residual vector of root-mean-square FA errors applied over all voxels of interest for each subject, and $M\boldsymbol{\mathcal{E}}) = \langle \mathcal{E} \rangle + \mathrm{SD}(\boldsymbol{\mathcal{E}})$. $\langle \cdot \rangle$ and $\mathrm{SD}(\cdot)$ represent the sample mean and the sample standard deviation operators, respectively. Without any additional difficulty, this problem is also solved under all strict constraints as described in the tailored case.

6.3.3 *SmartPulse* Design Process

The *SmartPulse* process can be divided into two steps. First, we create N_C clusters of subjects from a database of $N_{S,0}$ subjects and design one *smart-universal* pulse for each cluster. Then, we train a classifier on N_{train} subjects to assign the most appropriate pulse to a subject, given a set of simple features.

Clustering and Pulse Design

In order to perform database clustering, we design one tailored 9-k_T-points pulse according to eq. (6.1) for each of the $N_{S,0}$ subjects, then form the matrix

$$\boldsymbol{\mathcal{N}} = \left(v_{s,p}\right)_{1\leq s,p\leq N_{S,0}} \tag{6.3}$$

where $v_{s,p}$ denotes the NRMSE achieved by the pth pulse when applied to the sth subject. By defining subject vectors $\mathbf{v_s} = \left(v_{s,p}\right)_{1\leq p\leq N_{S,0}}$ (*i.e.* the pth column of $\boldsymbol{\mathcal{N}}$), we compute $\boldsymbol{\mathcal{D}}$, the distance matrix between subjects:

$$\boldsymbol{\mathcal{D}} = \left(\|\mathbf{v_s} - \mathbf{v_{s'}}\|_2\right)_{1\leq s,s'\leq N_{S,0}} \tag{6.4}$$

We then perform agglomerative hierarchical clustering on $\boldsymbol{\mathcal{D}}$ with *complete* linkage [Müllner 2017], *i.e.* with the distance between two clusters of subjects I and J defined as

$$d(I,J) = \max_{\mathbf{v_s}\in I, \mathbf{v_{s'}}\in J} \|\mathbf{v_s} - \mathbf{v_{s'}}\|_2 \tag{6.5}$$

which tends to produce a few number of large groups of data, as opposed to *single* or *average* linkage, for instance. It is a bottom-up process that starts with each individual subject forming a singleton cluster. A new cluster K is created by joining the two clusters I and J of minimal pairwise distance $d(I,J)$; I and J are then removed from the set. Clusters are iteratively joined two by two to form new larger clusters, until a single cluster containing all subjects is obtained. This process both leverages and represents all the distances between individuals and between groups of subjects. It emphasizes the inherent structure of the set of subjects, and allows to group subjects that display similar behaviour to various RF pulses in terms of NRMSE. Then, given a number of desired clusters N_C, it is possible to stop the merging process to reach this exact number. Finally, if we denote by $\mathcal{C}_j$ the set of indices of subjects belonging to the jth cluster, clustered pulse design boils down to solving eq. (6.2) for each subset $\mathcal{A}_j$:

$$\mathcal{A}_j = \{A_i \mid i \in \mathcal{C}_j\}, \quad 1 \leq j \leq N_C \tag{6.6}$$

to obtain N_C pulses $\mathbf{p_j} = (\mathbf{x_j}, \mathbf{k_j}, \mathbf{t_j})$.

Assigning Additional Subjects to Groups

For the second step, a classification algorithm is trained on N_{train} labelled subjects. For good classifier performance, a large number of training subjects is desirable. To expand the training set, $N_{S,1}$ additional subjects are acquired ($N_{train} = N_{S,0} + N_{S,1}$); they were not included in the clustering as some of them induced the creation of a fourth cluster, too small for training.

The $N_{S,0}$ subjects used for clustering are labelled from 1 to N_C according to the cluster they belong to. Since the performance criterion used eventually is the NRMSE obtained by applying a pulse to a subject, each of the $N_{S,1}$ new subjects is labelled according to

the cluster pulse $\mathbf{p_j}$ that yields the lowest NRMSE. If we denote by y_i the class assigned to the ith subject:

$$y_i = \begin{cases} j \in \{1, \ldots, N_C\} \text{ such that } i \in \mathcal{C}_j & \text{if } i \in \{1, \ldots, N_{S,0}\} \\ \underset{j \in \{1,\ldots,N_C\}}{\arg\min} \left\| A_i(\mathbf{x_j}, \mathbf{k_j}, \mathbf{t_j}) - \alpha_T \right\|_2 & \text{if } i \in \{N_{S,0}+1, \ldots, N_{S,0}+N_{S,1}\} \end{cases} \tag{6.7}$$

This is a simple and fast way to expand the training database, making the proposed method easily scalable.

6.4 Methods

6.4.1 Subjects and Scanner

Data acquired for the study from chapter 5 on 50 consecutive subjects were reused here as the clustering set: it corresponds to subjects 1 through 50 ($N_{S,0}$). For the present work, measurements were performed over a three-week period on 30 ($N_{S,1}$) additional subjects, thus forming a training population of 80 subjects (N_{train}). Finally, a testing population of 53 consecutive subjects (N_{test}) was acquired over four weeks. A total of 133 patients (69 men, 64 women, age: 22–89 years, height: 1.45 to 1.91 m, weight: 45 to 140 kg, BMI: 17.6 to 43.7 kg/m^2) were therefore included. 23 subjects from the testing population underwent DCE-MRI while in the presence of a pulse designer (Raphaël Tomi-Tricot), over the last two weeks of the study; they constitute the imaging population.

Our study was approved by the institutional review board of Centre Hospitalier Universitaire Henri Mondor; informed consent was waived. Acquisitions were carried out on a MAGNETOM Skyra (Siemens Healthcare GmbH, Erlangen, Germany) 3 T scanner, equipped with a two-channel pTx system used in clinical routine. Two 30-channel coil arrays (anterior and posterior) were used for reception.

6.4.2 Transmit B_1 and Off-Resonance Mapping

B_1^+ maps were measured through a manufacturer automatic adjustment procedure, a free-breathing magnetisation-prepared turbo FLASH sequence performed in about 30 seconds. They were the same maps as the ones used for patient-specific static RF shimming.

Δf_0 maps were needed for pulse design and FA simulations *per se*, but also to discriminate between water and fat voxels. Indeed, the pulses were intended for a fat-suppressed sequence, so only water voxels were considered for FA homogenisation, leading to increased pulse performance in water as well as lower computation times. Assuming that both tissues do not mix, this was achieved with a two-echo FLASH acquisition acquired in one breath-hold (10 seconds) with $\Delta\text{TE} = 0.95$ ms, short enough to avoid phase wrapping over a ± 500 Hz frequency range.

Pulse design was performed from a 3D mesh of 5-mm isotropic voxels, so both B_1^+ and Δf_0 maps were down-sampled to match that resolution.

6.4.3 Pulses Compared

For each subject of the testing population (Subjects 81 through 133), six pulse types were used:

- p_{TF}: *TrueForm*, the scanner default elliptically polarised pulse (*cf.* section 2.3.1);
- p_{TSS}: manufacturer's patient-tailored static RF shimming (*cf.* section 2.3.1) with coefficients automatically calculated by the scanner based on the subject's B_1^+ maps, but with a maximum voltage constrained to be less than or equal to that of *TrueForm*;
- p_{OTSS}: optimal static RF shimming, computed offline;
- p_{TKT}: patient-tailored k_T-points dynamic RF shimming, computed offline;
- p_{UKT}: universal k_T-points;
- p_{SP}: *SmartPulse* k_T-points.

Duration of hard pulses p_{TF}, p_{TSS} and p_{OTSS} was set to 100 µs. Pulse design for other techniques is described below.

Tailored and Universal K_T-Points Pulse Design

9-k_T-point-point tailored pulses (p_{TKT}) were designed, under SAR and hardware constraints, as done in chapter 5 and explained in section 2.4.1 and chapter 3. With the goal of using them for DCE-MRI, a FA of $\alpha_T = 11°$ was targeted, for a TR of 6 ms, and a 1300-µs pulse duration limit was set. For local SAR prediction, virtual observation points (VOPs) [Eichfelder 2011] provided by the scanner were used.

A universal pulse was also designed on Subjects 1 through 50, according to eq. (6.2). The pulse used throughout this study, p_{UKT}, had five sub-pulses and was 770-µs-long: it was returned shorter than the tailored version, most likely to achieve more broadband behaviour.

All pulse designs were performed using the active-set constrained optimisation algorithm from MATLAB R2016a (The Mathworks, Natick, MA) on a laptop computer (Intel Core i7-4712HQ CPU, NVIDIA Quadro K1100m GPU).

SmartPulse Clustering and Pulse Design

Clustering and *SmartPulse* design was based on Subjects 1 through 50 ($N_{S,0}$), as pictured in fig. 6.3, where matrices $\boldsymbol{\mathcal{N}}$ and $\boldsymbol{\mathcal{D}}$ (eqs. (6.3) and (6.4)), obtained using tailored k_T-points described above, are shown both before and after clustering. Agglomerative hierarchical clustering was done using Python v2.7 (Python Software Foundation[1]) and the *fastcluster* package [Müllner 2017]. Given the relatively small number of training data, a limited number of clusters (3) was chosen. Subject 24 behaved as an outlier and formed its own cluster, so it was manually assigned to cluster $\mathcal{C}_3$ (fig. 6.3e).

[1] www.python.org

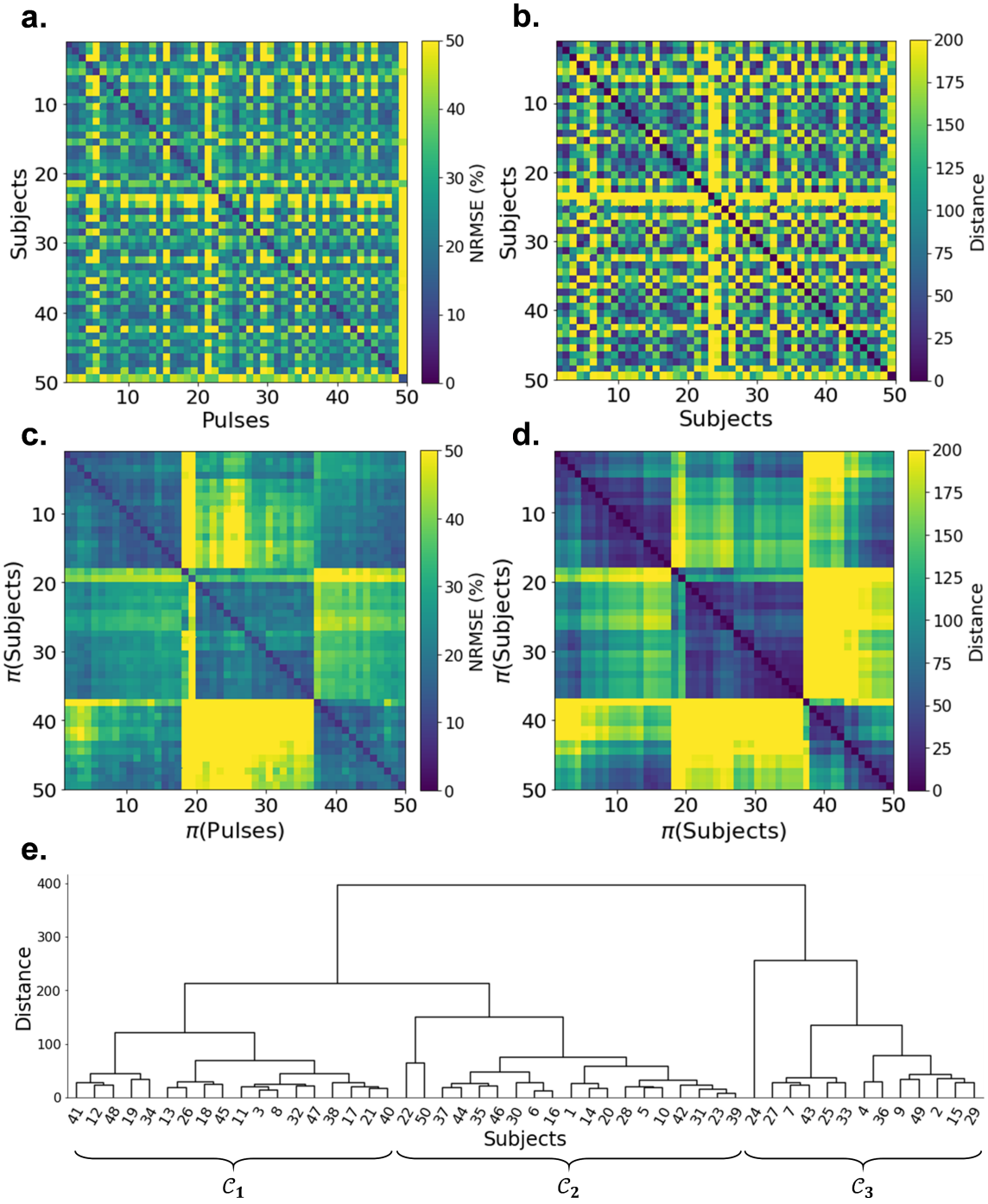

Figure 6.3: Creation of three clusters from subjects 1 through 50. (a) Matrix $\mathcal{N}$ (eq. (6.3)) of NRMSEs. (b) Matrix $\mathcal{D}$ of subject pairwise distance (eq. (6.4)). (c-d) Reorganised matrices $\mathcal{N}$ and $\mathcal{D}$ (respectively) using permutation π output by agglomerative hierarchical clustering applied on $\mathcal{D}$. Cluster structure becomes visible. (e) Dendogram output by agglomerative clustering applied on $\mathcal{D}$. Definition of $\mathcal{C}_1$, $\mathcal{C}_2$ and $\mathcal{C}_3$, the three clusters used for *SmartPulse* pulse design in this study.

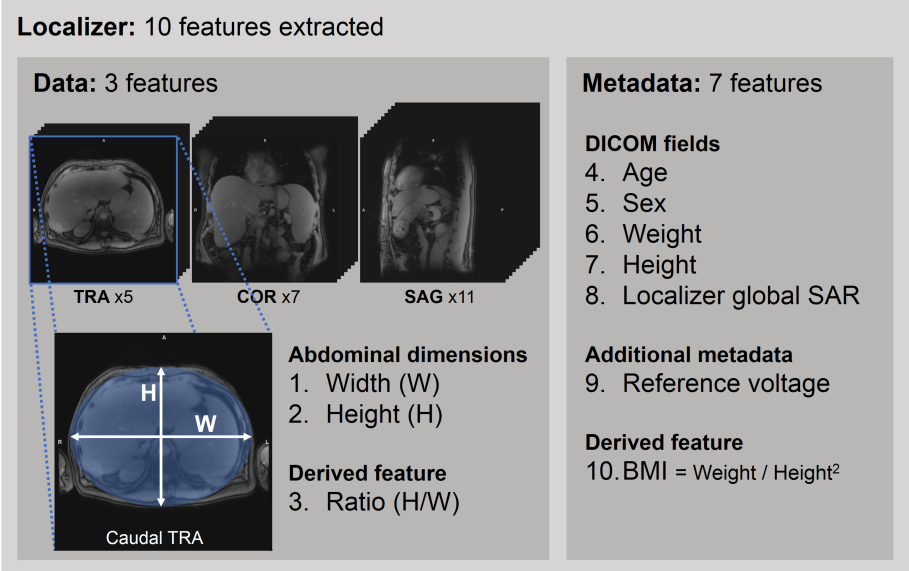

Figure 6.4: Features extracted from a 'localizer' acquisition (compulsory sequence at the beginning of any protocol). Abdomen dimensions were measured by fitting an ellipse in one axial slice; more slices could be analysed with the help of automated patient and field of view positioning, allowing finer patient characterisation. Additionally and with some post-processing, coronal and sagittal views could provide useful liver and spleen geometry information. TRA/COR/SAG = transverse/coronal/sagittal planes; SAR = specific absorption rate; BMI = body mass index; reference voltage = voltage required for a 500-µs hard pulse to perform 90° excitation.

Pulses *SmartPulse* 1 ($p_{SP,1}$), *SmartPulse* 2 ($p_{SP,2}$) and *SmartPulse* 3 ($p_{SP,3}$) were created for cluster $\mathcal{C}_1$, $\mathcal{C}_2$ and $\mathcal{C}_3$ respectively, with the same 5-k_T-point design parameters as for p_{UKT}. Their optimized durations were 700, 720 and 690 µs, respectively.

All p_{SP} and p_{UKT} were applied to every subject without voltage scaling.

6.4.4 Subject Classification

Ten features likely to influence abdominal composition and geometry, and therefore B_1^+ distribution, were used for classification, all of them extracted from data from the localizer (fig. 6.4), which is a compulsory sequence placed at the very beginning of the protocol and used to set up the field of view (FOV) of subsequent acquisitions. The localizer sequence used locally for liver imaging consists in 5 axial, 7 coronal and 11 sagittal T_1-weighted 7.0-mm-thick slices of 0.8-mm in-plane resolution, all acquired in one breath-hold (TA = 17 s).

Table 6.1 gathers the features corresponding to the subjects shown in the figures of this study, as well as a population summary. Subject's *age*, *sex*, *weight* and *height*, given by the patients during registration, are compulsory data for any MRI examination on this scanner, and are available as DICOM fields, as specified in PS3.6: Data Dictionary [The National Electrical Manufacturers Association 1997]. The *global SAR* measured by the machine during the localizer acquisition was also retrieved from DICOM fields. Subject's *body mass index* (BMI) was derived from height and weight. Additional manufacturer-

Table 6.1: Features extracted from the localizer for the five subjects focused on in this study.

Subject number	Age	Sex	Height	Weight	BMI	Abdomen AP[a]	Abdomen LR[a]	Abdomen ratio[a]	V_{ref}[b]	Localizer SAR_g[c]
	years		m	kg	kg/m^2	mm	mm	%	V	W/kg
110	62	M	1.76	119	38.4	338	408	83	494	0.064
113	40	F	1.65	65	23.9	198	285	69	430	0.075
115	58	M	1.80	85	26.2	232	333	70	633	0.099
127	65	M	1.70	79	27.3	237	353	67	571	0.087
132	48	M	1.80	90	27.8	282	363	78	460	0.070
N_{test}[d]	53 (16)	M: 26 F: 27	1.68 (0.09)	78 (22)	27.4 (6.3)	242 (36)	332 (38)	73 (4.8)	509 (75)	0.078 (0.016)

[a] Abdomen dimensions measured in the anterior-posterior (AP) and left-right (LR) directions, and ratio: AP/LR.
[b] Reference voltage measured by the scanner: voltage required for a 500-µs hard pulse to perform 90° excitation.
[c] Global specific absorption rate due to the localizer acquisition, as measured by the scanner.
[d] For all columns except sex: Mean (SD) over the testing set ($N_{test} = 53$). For sex: number of male (M) and female (F) subjects.

specific metadata was available, among which the *reference voltage*, calibrated by the scanner for each subject, and defined as the voltage necessary for a 500-µs hard pulse to create 90° excitation in a 1-cm-thick transversal slice at magnet isocentre [Feiweier 2009]. In the default transmit configuration, this value is related to the B_1^+ distribution within this slice. The subject's abdominal *width* and *height* (2 features) were estimated by fitting an ellipse inscribed in the most caudal axial slice, and retrieving its major and minor axes (respectively). The most inferior slice was picked to ensure the ellipse fitting was performed in the abdomen, not in the thorax. In this pilot study, however, for some patients, the localizer was really off-centred; in those cases, the ellipse fitting was performed on the central slice of the magnitude images associated with the Δf_0 map. One last feature was derived from these measurements: the *abdominal ratio* (height over width).

The classification algorithm was implemented using Scikit-learn [Pedregosa 2011] and trained on the population of $N_{train} = 80$ subjects. Two algorithms were separately tuned by repeated stratified cross-validation on this set, with 50 shuffles and 5 splits. An *extremely randomised trees algorithm* [Geurts 2006] with 4000 trees reached 84.3 % cross-validation accuracy. A *support vector machine* multiclass classifier [Cortes 1995, Wu 2004] with a radial basis function kernel achieved 84.9 % accuracy. The algorithm selected for this study was a voter classifier averaging the output class probabilities of both algorithms; its cross-validation accuracy was 85.4 %. Prediction score on the whole training set was 100 %.

To assess classification performance, a prediction accuracy score was calculated on the training test, *i.e.* the proportion of subjects who were assigned the pulse yielding minimal NRMSE. A relaxed accuracy score was also determined, which regarded subjects as misclassified only if the NRMSE associated with their assigned pulse was 2% above the lowest possible.

Finally, the time needed for feature extraction and pulse prediction time on individual subjects from the testing population was measured.

6.4.5 Excitation Homogeneity

FA maps obtained with each technique were simulated by numerical integration of Bloch's equations based on actual B_1^+ and Δf_0 maps measured in subjects. FA average, coefficient of variation (CV) and NRMSE over water voxels in the volume of interest were estimated.

In the *SmartPulse* case, all three cluster pulses were tested, and the one yielding the best NRMSE was defined as $p_{SP,best}$, and used to assess the performance of an 'ideal' process with no prediction errors.

Matched-pair Wilcoxon signed-rank tests were computed using the SciPy [Jones 2001] stats package whenever FA NRMSE, CV or means of different techniques were compared. Reported p-values are two-sided significance levels; null hypothesis of equality of distribution medians was rejected for p less than 0.05.

6.4.6 *In Vivo* Acquisitions

Additional sequences were run on subjects from the imaging population to compare images obtained with p_{TF}, p_{TSS}, p_{TKT} and the predicted p_{SP}. To avoid disturbing the diagnostic DCE-MRI protocol, those sequences were only inserted prior to contrast agent injection and in late phase, as pictured in fig. 6.5.

The sequence used was a T_1-weighted 3D FLASH, with 'quick fat-saturation' [Le 2012] to remove hypersignal due to the short T_1 of fat that could mask contrast-agent-related enhancement. Fat saturation was achieved with a fat-selective 90°-pulse of Gaussian shape, identical in all sequences. Sequence parameters were: FA = 11°, TR/TE = 6/3 ms, $320 \times 220 \times 72$ matrix, $(1.2 \times 1.2 \times 3.5)\,\mathrm{mm}^3$ resolution, GRAPPA factor 2 in the phase encoding direction (anterior-posterior), 80 %/50 % phase/slice resolution, PF = 6/8, 505 Hz/pixel bandwidth, for an acquisition time of less than 23 seconds. The matrix size or/and resolution was sometimes slightly adjusted to accommodate larger patients while ensuring an acquisition time compatible with a breath-hold. Up to 33 % oversampling was needed in the partition-encoding direction to avoid aliasing. Two 30-channel surface coils (anterior and posterior) were used for reception. Only the channels necessary to cover the FOV were selected; this was done automatically by the scanner, and allowed to keep oversampling to a minimum. The manufacturer's 'Prescan Normalize' procedure was applied to all series in order to correct images for reception profile. However, this technique assumes homogeneous body coil reception, which is not the case in the abdomen as the corresponding reception profile is also affected by the B_1 artefact; some inhomogeneity may therefore remain.

Elastic registration was applied to all acquisitions using Siemens software. This allowed to calculate, for each technique, the contrast enhancement (CE) and the enhancement ratio (ER) defined as:

$$\mathrm{CE} = S_{late} - S_{ref} \tag{6.8}$$

and

$$\mathrm{ER} = \frac{\mathrm{CE}}{S_{ref}} \times 100\,\% \tag{6.9}$$

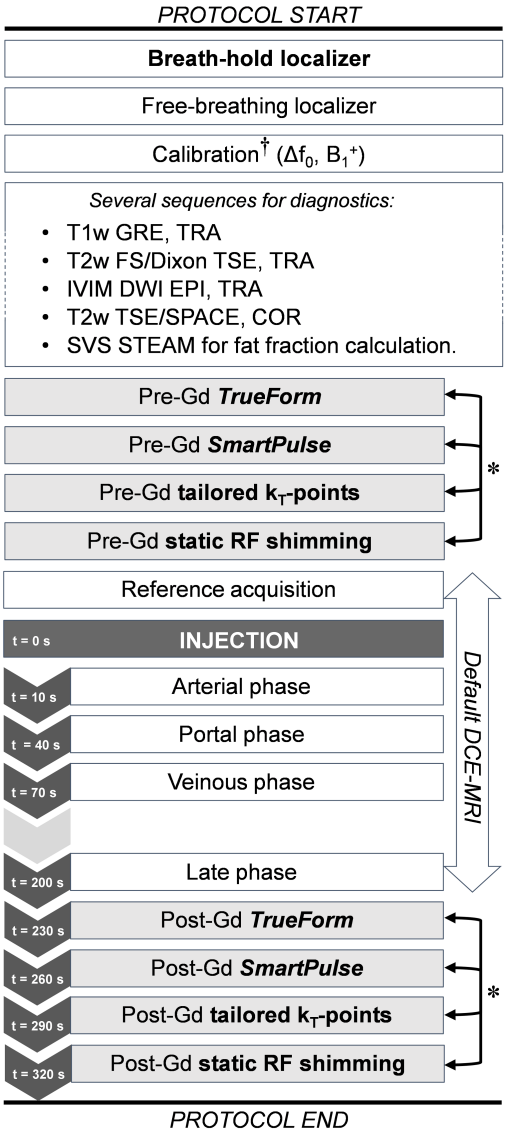

Figure 6.5: Insertion of our sequences (light grey) within the routine liver MRI protocol (white). Injected sequences relevant to this study were acquired at the far end of the acquisition protocol to preserve diagnostics routine timing. Data from the breath-hold localizer was used for subject classification. ✻ The order of our sequences was randomly assigned. † The calibration procedure was needed for flip angle simulations and for tailored pulse design, not for *SmartPulse* nor *TrueForm*. It included automated manufacturer transmit B_1^+ mapping and a custom-made breath-hold Δf_0 map for proper water fat resolution. Abbreviations: GRE = gradient-recalled echo; TSE = turbo spin-echo; SPACE = sampling perfection with application optimized contrasts using different flip angle evolutions; IVIM = intravoxel incoherent motion; DWI = diffusion-weighted imaging; EPI = echo-planar imaging; SVS = single-voxel spectroscopy; STEAM = stimulated echo acquisition mode; DCE-MRI = dynamic contrast-enhanced MRI; TRA = transverse plane; COR = coronal plane.

where S_{ref} and S_{late} represent signal before and after contrast agent injection, respectively. ER presents the advantage of completely removing the reception profile; however it will artificially increase with FA overshoot, contrarily to CE.

6.5 Results

6.5.1 Subject Classification

Once the localizer sequence was acquired, the full process of feature extraction and *SmartPulse* prediction for one subject systematically took less than two seconds. Strictly speaking, the accuracy of the algorithm on test data was 74 %. However, in many cases two pulses would perform similarly well, so the second best pulse may not necessarily be regarded as a 'wrong' option. This is illustrated on fig. 6.6a where, for each testing subject, coloured circles represent the NRMSE of the different p_{SP} options; filled circles correspond to the actual prediction. Relaxed accuracy (with a +2 % NRMSE tolerance) was 81 %.

6.5.2 Excitation Homogeneity

Figure 6.6b compares *SmartPulse* to *TrueForm*, the default calibration-free pulse provided by the vendor. Universal pulse performance is also indicated. Considering the same +2 % tolerance, predicted p_{SP} yielded lower NRMSE than p_{TF} or was at least the best available p_{SP} for 46 subjects (87 %). Figure C.1 on page 154 gathers individual NRMSE results for all tested pulse designs. p_{SP} performed consistently better than p_{TF}, p_{TSS} and p_{UKT}; they were comparable to p_{OTSS} for the majority of subjects, but the latter showed their limit for the most difficult ones (*cf.* subject 132 on fig. C.1). All were unsurprisingly outperformed by p_{TKT}.

In addition, p_{SP} allowed 93 % of subjects to get a NRMSE below 25 % (dashed line on fig. 6.6), which is much more than p_{UKT} (72 % of subjects), p_{TSS} (77 %) and p_{TF} (79 %); comparable to p_{OTSS} (96 %), but less than p_{TKT} (100 %). However, $p_{SP,best}$ would also have allowed 100 % of subjects below that threshold. Yet, in three cases, even the optimal *SmartPulse* ($p_{SP,best}$) gave a lower performance than *TrueForm*: subject 96 (18 % NRMSE for $p_{SP,best}$, 14 % for p_{TF}), subject 103 (18 % instead of 15 %) and subject 114 (18 % against 13 %).

Sample average and SD of NRMSE, CV and mean of FA are available in table 6.2, with more detail on their distribution in fig. 6.7. Average p_{SP} NRMSE was 16 % (SD: 5 %), lower than that of p_{TF}, p_{TSS} and p_{UKT}, respectively 20 % (SD: 9 %, $p = 0.002$), 21 % (SD: 10 %, $p = 0.0005$) and 20 % (SD: 5 %, $p < 0.0001$). Again, p_{OTSS} were slightly more efficient, with 14 % (SD: 4 %, $p = 0.001$), but this difference would disappear ($p = 0.44$, not significant), with perfect classification ($p_{SP,best}$). Other metrics allow deeper understanding of pulse performance: FA CV expresses sheer homogeneity, while FA average measures a possible FA bias as compared to the nominal value. With a mean CV of 13 %, p_{SP} outperformed all pulses but p_{TKT}. Although p_{TSS} yielded better homogeneity than p_{TF} ($p < 0.0001$), it drifted further away from the FA target average: 9.6° (SD: 1.3°) and 9.3°

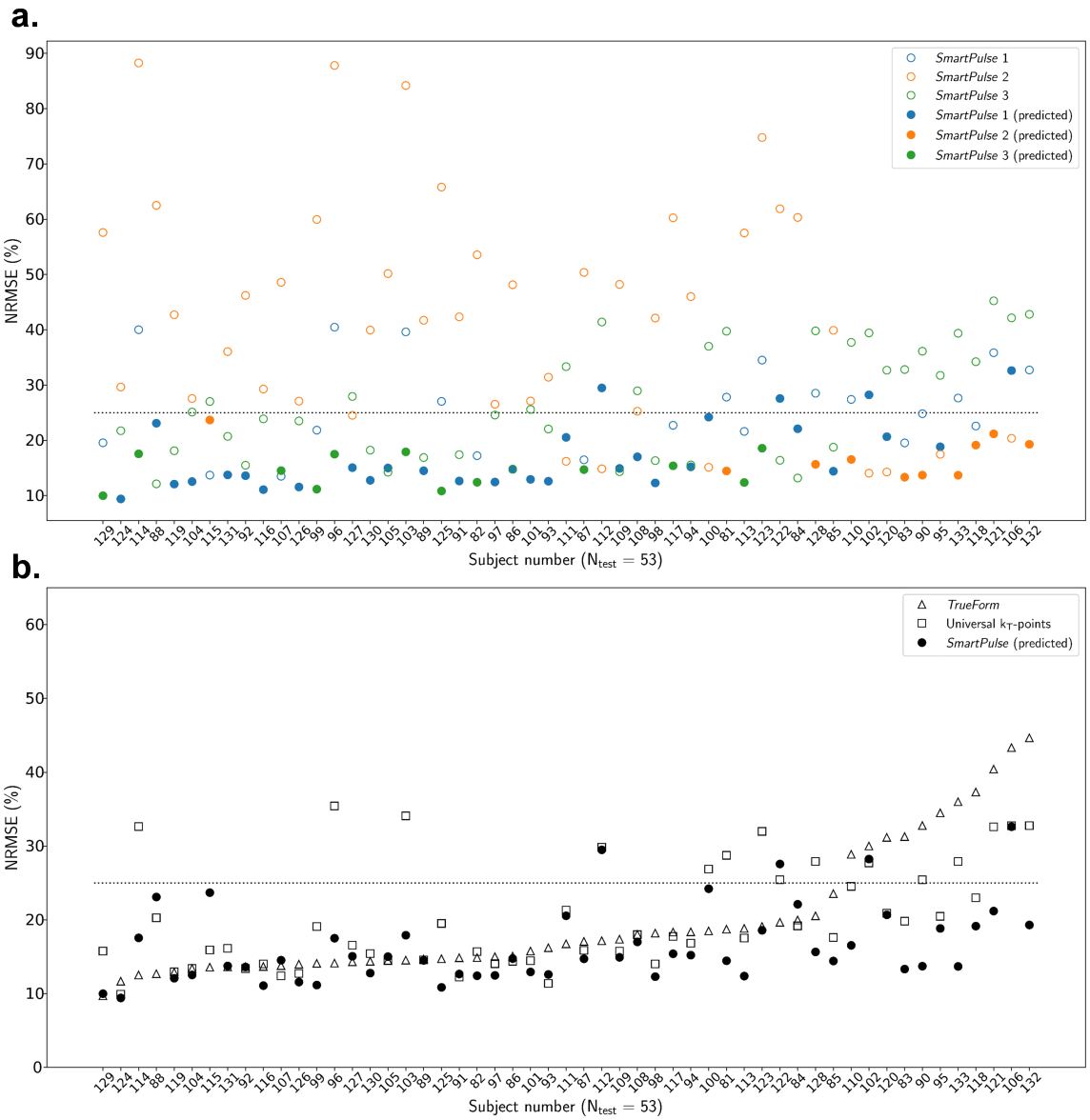

Figure 6.6: NRMSE simulation results for all test subjects, sorted in increasing *TrueForm* inhomogeneity. (a) Performance of predicted *SmartPulse* (filled circles) compared to other *SmartPulse* options (hollow circles). Colours render the three different possible *SmartPulse* classes. For instance, for subject 129 (first entry), $p_{SP} = p_{SP,best} =$ *SmartPulse* 3, while for subject 88 (fourth entry), $p_{SP} =$ *SmartPulse* 1 and $p_{SP,best} =$ *SmartPulse* 3. (b) Comparison of *TrueForm*, Universal and *SmartPulse* pulse designs. For each subject, only the predicted *SmartPulse* is shown, not all three possibilities. The dashed line indicates 25 % NRMSE. Notice how subjects with a high *TrueForm* NRMSE are brought towards more acceptable values.

Table 6.2: Detailed homogeneity assessment results of all tested pulses for the five subjects from table 6.1.

Subject	p_{TF}	p_{TSS}	p_{OTSS}	p_{TKT}	p_{UKT}	p_{SP}	$p_{SP,best}$[a]
Flip Angle NRMSE (%)							
110	29	32	15	8	25	17	17
113	19	20	14	8	18	12	12
115	14	13	13	7	16	23	**14**
127	14	14	12	7	17	15	15
132	45	49	26	9	33	19	19
All N_{test}[b]	20 (9)	21 (10)	14 (4)	8 (2)	20 (5)	16 (5)	14 (3)
Flip Angle Coefficient of Variation (%)							
110	18	14	15	8	14	17	17
113	15	15	14	8	12	12	12
115	14	13	13	7	14	14	**10**
127	14	13	12	7	13	11	11
132	28	27	27	9	27	17	17
All N_{test}[b]	16 (4)	15 (4)	14 (4)	8 (2)	14 (4)	13 (3)	13 (2)
Flip Angle Average (degrees)							
110	8.2	7.7	10.4	10.9	8.6	10.5	10.5
113	9.5	9.3	10.8	10.9	12.2	10.4	10.4
115	10.8	10.4	10.8	10.9	9.9	12.9	**9.9**
127	10.6	10.3	10.8	10.9	9.7	9.8	9.8
132	6.4	5.9	10.0	10.9	8.1	9.7	9.7
All N_{test}[b]	9.6 (1.3)	9.3 (1.3)	10.7 (0.2)	10.9 (0.0)	10.7 (1.8)	10.7 (1.3)	10.8 (0.8)
Maximal SAR[c] (%)							
110	17	28	48	58	33	25	25
113	16	18	29	38	50	20	20
115	19	19	27	42	29	22	**17**
127	21	23	38	29	31	18	18
132	15	18	47	58	43	31	31
All N_{test}[b]	17 (4)	18 (5)	33 (12)	38 (12)	38 (12)	21 (4)	21 (5)

p_{TF} = *TrueForm*; p_{TSS} = patient-tailored static RF shimming calculated by the scanner; p_{OTSS} = optimal patient-tailored static RF shimming; p_{TKT} = tailored k_T-points; p_{UKT} = universal k_T-points; p_{SP} = predicted *SmartPulse*; $p_{SP,best}$ = optimal *SmartPulse*.

[a] $p_{SP,best}$ values are in bold in case of misprediction (when different from p_{SP}).

[b] For each metric and each pulse: Mean (SD) over the testing set. $N_{test} = 53$.

[c] Maximum local SAR, estimated from the pulse shape, TR and virtual observation points provided by the scanner for each subject, expressed as a percentage of the maximal value authorized in quadrature mode.

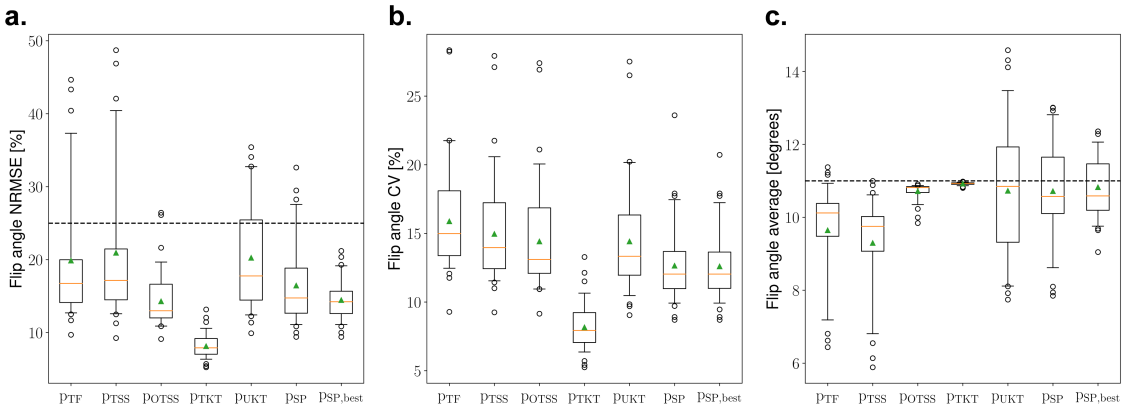

Figure 6.7: Distribution of the different metrics used to assess pulse performance: p_{TF} = *TrueForm*; p_{TSS} = patient-tailored static RF shimming calculated by the scanner; p_{OTSS} = optimal patient-tailored static RF shimming; p_{TKT} = tailored k_T-points; p_{UKT} = universal k_T-points; p_{SP} = predicted *SmartPulse*; $p_{SP,best}$ = optimal *SmartPulse*. Green triangle = mean value; orange lin = median; edges of the box = 25th (Q1) and 75th (Q3) percentiles; whiskers = 5th and 95th percentiles; circles = outliers. (a) Flip angle (FA) NRMSE; the dashed line corresponds to the 25 % threshold. (b) FA coefficient of variation. (c) FA average; the dashed line corresponds to the 11° target.

(SD: 1.3°) respectively ($p < 0.0001$). This was not the case for p_{SP}, which achieved better performance on FA average as well, with 10.7° (SD: 1.3°), and even 10.8° (SD: 0.8°) for $p_{SP,best}$ ($p < 0.0001$ in both cases).

Finally, table 6.2 and fig. 6.7 also point out that while p_{OTSS} and p_{TKT} yield better NRMSE than p_{TF} and p_{TSS}, SAR is much higher on average ($p < 0.0001$ in all cases). This is not the case for p_{SP}: associated SAR is significantly higher ($p = 0.003$) than that of p_{TSS}, but not by much. p_{SP} SAR was 21 % (SD: 4 %) of the maximal authorized value vs 38 % (SD: 12 %) for both p_{UKT} and p_{TKT}, and 18 % (SD: 5 %) for p_{TSS}. One may be concerned about implications of mispredictions in terms of SAR, but *SmartPulse* seems to behave favourably in this respect. Indeed, out of the 53 test subjects, the highest SAR encountered was 37 % of the maximal allowed value, considering all three p_{SP} options.

6.5.3 *In Vivo* Acquisitions

Figures 6.8 and 6.9 show examples of images acquired before contrast agent injection and in late phase, with CE and ER maps calculated according to eqs. (6.8) and (6.9).

Figure 6.8 focuses on two subjects whose p_{TF} NRMSE was above 25 %. In both cases, using *TrueForm* (p_{TF}) and tailored static RF shimming (p_{TSS}) pulses, the enhancement and ER maps lacked intensity and homogeneity. This artefact was largely alleviated with tailored k_T-points (p_{TKT}) and *SmartPulse* (p_{SP}). For subject 132, T_1 contrast was quite poor with p_{TF} and p_{TSS}. Some lesions (yellow arrowheads) were harder to see and less delineated than with p_{SP}. Scarcely no difference was visible between p_{SP} and p_{TKT} images or enhancement maps, despite sensible disparity in NRMSE. For subject 110 the ER map was even slightly better defined with *SmartPulse* in outer regions of the liver.

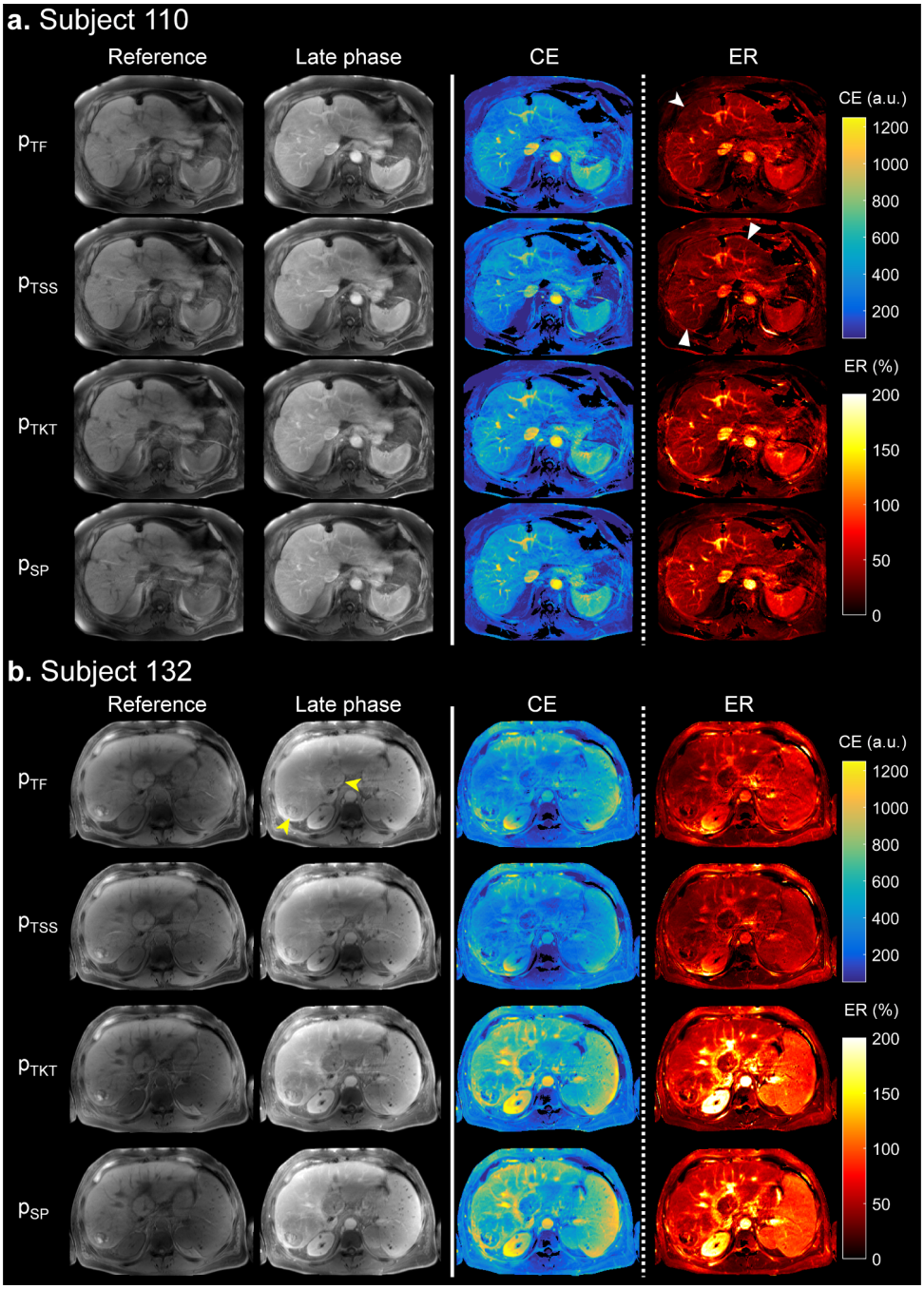

Figure 6.8: From left to right: pre-injection, post-injection, calculated CE and ER obtained with four pulse techniques applied to two 'difficult' subjects (*TrueForm* NRMSE over 25 %, fig. 6.6). See table 6.1 for patient characteristics and table 6.2 for performance metrics. p_{TF}: TrueForm; p_{TSS}: patient-tailored static RF shimming; p_{TKT}: patient-tailored k_T-points; p_{SP}: *SmartPulse* attributed to the subject. (a) Notice the lack of ER in liver segment 5 with p_{TF} (notched arrowhead) also visible on the CE image. p_{TSS} results in a more homogeneous ER, but at the expense of global enhancement (full arrowheads). ER is improved with p_{TKT}, and even more with p_{SP}. (b) Substantial shading is visible on anatomical, CE and ER images with both p_{TF} and p_{TSS}. Two hepatocellular carcinomas (yellow arrowheads) are barely visible. T_1 contrast is retrieved with both p_{TKT} and p_{SP}, and no shading remains in CE nor ER. Additional inhomogeneity can be noticed on anatomical and CE images, due to coil array receiving profile; only ER images are completely free of it.

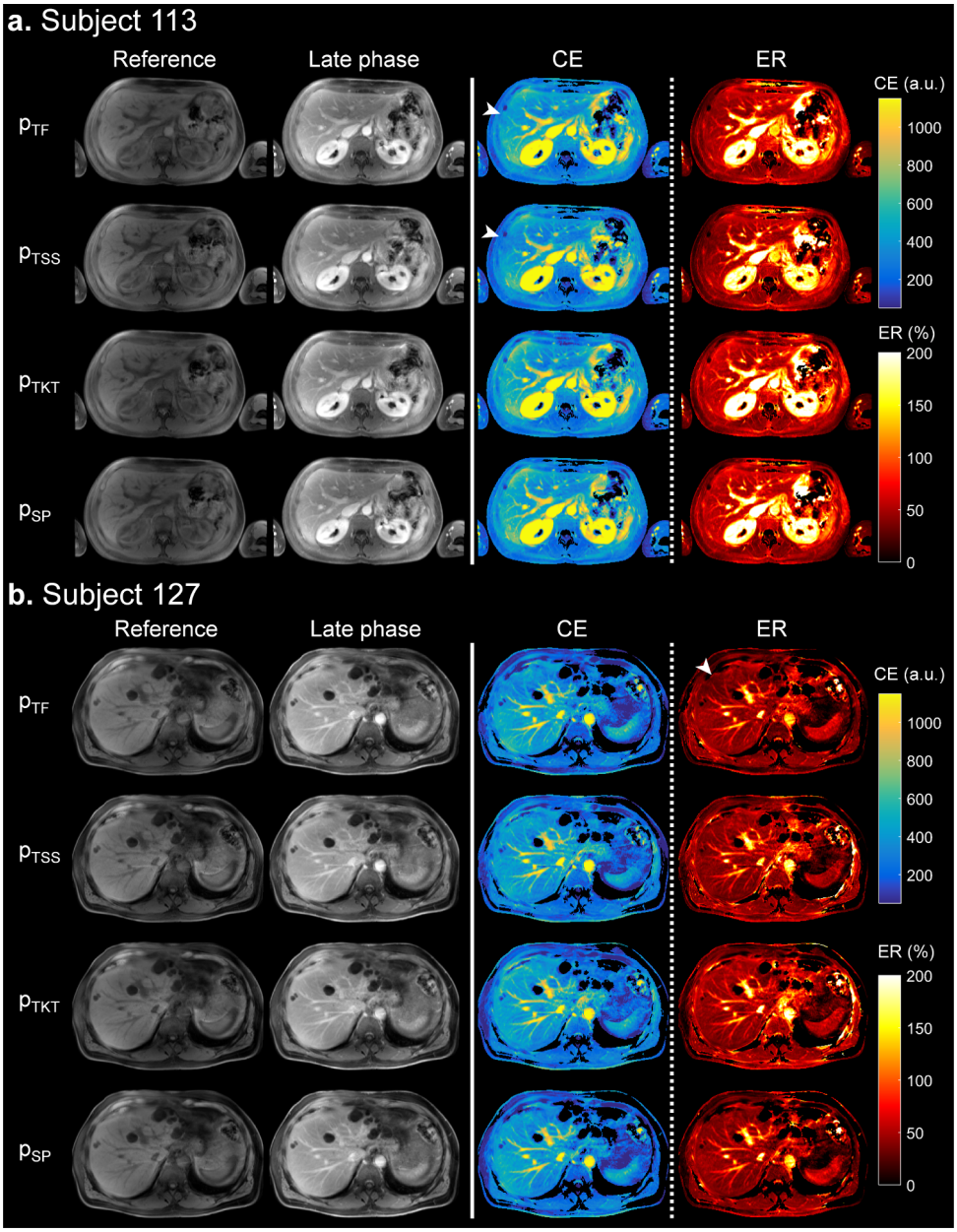

Figure 6.9: From left to right: pre-injection, post-injection, calculated CE and ER obtained with four pulse techniques applied to two 'standard' subjects (*TrueForm* NRMSE below 25 %, fig. 6.6). See table 6.1 for patient characteristics and table 6.2 for performance metrics. p_{TF}: TrueForm; p_{TSS}: patient-tailored static RF shimming; p_{TKT}: patient-tailored k_T-points; p_{SP}: *SmartPulse* attributed to the subject. (a) Arrowhead points out lack of CE in segment 8, also noticeable in ER maps, for both p_{TF} and p_{TSS}. This artefact is absent from p_{TKT} and p_{SP} maps, which look very much alike. (b) All techniques perform similarly, except for a slight CE abnormality (arrowhead) with p_{TF}.

In fig. 6.9, one can compare the different pulses on two 'easier' cases: subject 113 (p_{TF} NRMSE of 19 %) and subject 127 (p_{TF} NRMSE of 14 %). Here, all techniques yielded similar results, all satisfying. Yet, some slight localised enhancement underestimations remained on p_{TF} and p_{TSS} acquisitions (arrowheads), but not with p_{TKT} nor p_{SP}.

Finally, fig. C.2 on page 155 shows an example of *SmartPulse* misprediction, with subject 115. The difference between p_{TF} and p_{SP} was clear on ER maps and on the signal level of native images. However all images showed reasonable inhomogeneity. Indeed, one can see from table 6.2 that NRMSE was 14 % with p_{TF} and 23 % with p_{SP}. However, CV values are the same. The main difference lies in the fact that the mispredicted p_{SP} overshot the average FA in subject 115, while p_{TF} was close to the target. Note however that $p_{SP,best}$ showed much better behaviour than p_{SP}, and so that an improved *SmartPulse* decision would have solved the problem here.

6.6 Discussion

6.6.1 Results Summary

The *SmartPulse* process as presented here provided correct pulse assignments in 87 % of the cases. NRMSE simulation results were generally better with p_{SP} than either with p_{TF}, p_{TSS} and p_{UKT}, and comparable to those obtained with p_{OTSS}. This is even more salient when considering perfect predictions ($p_{SP,best}$). *SmartPulse* was especially convincing in tempering inhomogeneity in the most difficult subjects. Moreover, these results are obtained almost instantly after completion of the introducing localizer sequence.

Comparing actual acquisition results brought out that *SmartPulse* does not produce images worse than tailored k_T-points pulse design, despite simulations favourable to the latter. Due to their 'universal' nature, *SmartPulse* k_T-points may be more robust to patient motion during the acquisition or between calibration and DCE than their tailored counterpart, not forgetting that B_1^+ maps are acquired in free-breathing, and thus generally do not correspond to breath-hold positions of subjects. Bias in CE and ER was avoided by randomly assigning sequence order for each subject.

Better results can be obtained by further improvement of the two main aspects of this work: subject classification and pulse performance.

6.6.2 Improving Subject Classification

The difference between training and testing accuracy indicates model overfitting. This can be alleviated by using a larger training set, but this alone may not be enough.

Firstly, the way additional subjects are labelled for training and testing – *i.e.* selecting the pulse yielding the best NRMSE – is different from the way clusters are made. High machine learning performance, for these subjects, expresses that the selected pulses are the best in terms of NRMSE. Of course, this is an interesting metric, as the aim is to obtain a low NRMSE eventually, but it is only loosely connected to the clustering scheme. Even though it is not really a problem, as such errors would occur between pulses with similar

NRMSE on a given subject, it would still result in lower test scores. This is why a tolerance margin of +2 % on NRMSE was used to further analyse classification performance.

Secondly, there were a few imprecisions in the features used for extraction. Subject's height and weight were provided by the patients themselves, not measured on site, thus leading to slight approximations as people tend to give round values or to understate their weight, for instance. Most importantly, abdomen measurements could be much improved by automating localizer placement. This would ensure consistent localizer axial slice locations in the body, and would allow using more than one slice for abdominal dimensions estimation. Measurements at different locations in the abdomen would discard the assumption of a somewhat cylindrical body, while making the database more consistent. Another refinement would be to analyse other slice orientations, such as the coronal view – which is already acquired (fig. 6.4). For instance, subject 106 suffered from massive splenomegaly, which probably explains its misclassification. Because of its mostly rostrocaudal extension, the abnormal spleen did not impact much abdominal dimensions in the axial plane; still it had an influence on excitation inhomogeneity.

6.6.3 Improving Pulse Performance

Flawless class prediction would make NRMSE of all subjects in a 9 % to 21 % range, which could induce perfectly acceptable examinations for every patient. Still, those results could be improved. In some cases (subjects 96, 103, 114), $p_{SP,best}$ NRMSE was slightly higher than that of p_{TF}. Also, because of an inadequate average FA, some subjects showed relatively high NRMSE despite having low CV.

This issue could be addressed by defining more (finer) clusters. This would require the acquisition of more subjects in order to train the classifier to discriminate between even more categories.

Another – more seductive – approach would be to train a regression model to infer the average FA that the predicted pulse is expected to yield on a given subject, and to adapt the pulse's amplitude accordingly. Preliminary works on this aspect are ongoing and seem promising, but indicate that such a regression model would require more training data to make precise average FA estimates.

6.7 Conclusion and Perspectives

Universal pulse design does not suffice to homogenize excitation in 3 T abdomen imaging consistently for the whole population. Once implemented, the proposed method provides a simple and efficient trade-off between tailored and full universal pulse design approaches. Although *SmartPulse* did not systematically provide better homogenisation than the best possible tailored static RF shimming, it performed equally well or better in most difficult subjects without sacrificing easier ones. Interestingly also, *SmartPulse* could be used on single-channel systems [Eggenschwiler 2016], where patient-tailored RF shimming does not exist.

The proposed approach is extremely fast as it gets rid of all calibration and optimisation. This could prove useful especially for ultra-high field explorations of the body, where the increased number of transmit channels used to perform RF shimming makes calibration and pulse design even more tedious and challenging.

SmartPulse is not particularly demanding in terms of SAR. Energy deposition was not a limiting factor in this DCE study, but this property would be of interest in more SAR-inducing sequences.

Finally, the *SmartPulse* approach with underlying k_T-points pulses is readily implementable for non-selective preparation and 3D imaging to tackle B_1^+ inhomogeneity in T_1-, T_2^*-, T_2- [Gras 2018, Massire 2015], or proton-density-weighted imaging. As universal selective pulses, it could also be extended to fast-kz spokes to achieve slab- or slice-selective behaviours and thereby tackle full protocol optimisation.

* * *
* *
*

General Conclusions and Perspectives

After reaching the end of this three-year project, we hope we have helped giving a fresh boost to RF inhomogeneity management in clinical practice MRI at 3 T. The aim of this thesis was to demonstrate the applicability of the k_T-points technique in clinical applications. The works conducted in this thesis may contribute in convincing the industry of the usefulness of k_T-points.

Allowing the optimisation of k_T-point pulse and sub-pulse durations at design time in addition to complex RF coefficients and k_T-point locations proved useful in brain imaging at 7 T, especially in presence of large static field inhomogeneities. This improvement to the original algorithm was also included in the pulse design in clinical liver studies at 3 T as it gave more flexibility and required less user involvement to find a good compromise between pulse length and homogeneity performance.

Our breast imaging study on a single-channel scanner showed that the default *TrueForm* transmission mode implemented on Siemens scanners was already satisfactory for almost all subjects we encountered, and that there was no particular need for more homogeneity in clinical applications. The k_T-points implementation on the sTx scanner could be improved in the future by better masking breast tissues.

On the contrary, k_T-points proved essential in liver imaging, even on a dual-transmit-channel scanner capable of performing patient-tailored static RF shimming. We demonstrated the superiority of k_T-points in terms of quantitative performance as well as image quality. Indeed, considering that an acquisition is of good quality when it receives a global confidence grade of at least 2 on a scale from 0 to 3, static RF shimming produced good quality images in only 55 % of the population. With k_T-points, 85 % of the patients received a good examination. K_T-points therefore enforce equality for all in diagnosis quality.

With the *SmartPulse* method, a step forward has been taken towards the integration of dynamic RF shimming solutions in the clinical world. This proof of concept with underlying k_T-points pulses for non-selective excitation in abdominal imaging is very promising. From a pre-formed database of pulses, the classifier algorithm managed to select the one yielding the best homogeneity in 87 % of the patients. The result was generally more homogeneous than with subject-tailored static RF shimming, even though it did not require

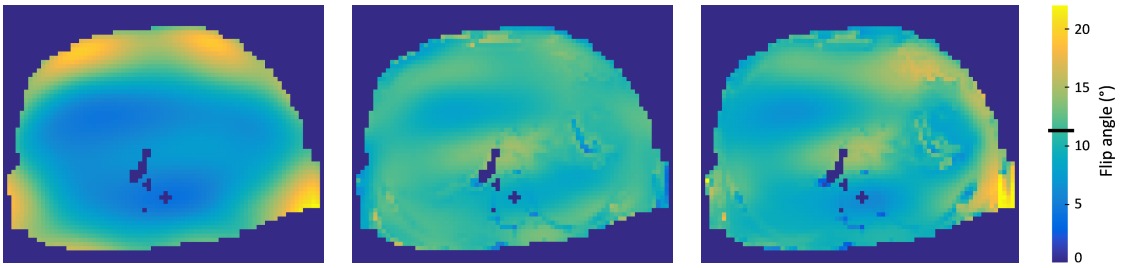

(a) Static RF shimming, pTx. (b) K_T-points, pTx. (c) K_T-points, sTx.

Figure GC.1: Performance of single-channel k_T-points compared to other pulse designs on subject 20 from chapter 5. The sTx k_T-points pulse was obtained by enforcing quadrature between the two channels. All pulses fit in the protocol used in chapter 5 (in particular TE/TR = 3/6 ms). Simulated NRMSEs over the volume: (a) 38 %; (b) 14 %; (c) 23 %.

any specific calibration (neither mapping nor in-line pulse design), which saves precious time for the examination. Additionally, some subjects showed strong RF inhomogeneity: in those cases, tailored static RF shimming showed its limits, while *SmartPulse* was still performant.

Future developments could consist in including dynamic RF shimming in as many clinical protocols as possible. In this thesis, we focused on the k_T-points technique, which is suited for non-selective excitation, inversion, or refocusing, in particular for 3D imaging. Having implemented k_T-points on a FLASH sequence for DCE MRI, and on a SPACE for T_2w imaging, we can address most of the 3D sequences portfolio needed in clinical applications. Additional demonstrations could be considered in other regions where B_1 artefacts remain, such as the spine or thighs. Applications would be, for instance, MR angiography of the lower limbs (using a similar FLASH sequence) or T_1w SPACE imaging. Still, many routine protocols include 2D or slab-selective 3D sequences: to achieve selective excitation, one would need to use fast-k_z spokes. Moreover, homogeneous excitation seems essential in the fast-growing field of quantitative imaging. Indeed, whereas in 'conventional' MRI radiologists rely on the contrast of tissues compared to their surroundings, in quantitative imaging actual values are measured (T_1, T_2, diffusion coefficient, ...) to characterise lesions. Inappropriate flip angles could shift those values, thus dramatically corrupting the diagnosis.

One interest of dynamic RF shimming compared to static methods is that, although it takes advantage of parallel transmission, it does not require it. This means that k_T-points can be used on any scanner, with no need for additional hardware, as done in chapter 4 for our study in breast MRI. Figure GC.1c is an example of the flip angle homogeneity that could be obtained in the liver with k_T-points on a single-channel transmission system. This result was obtained in simulation on one of the most difficult patients we encountered, and we can see that sTx k_T-points, although they are not as effective as pTx ones, clearly surpass the best possible two-channel static RF shimming. Considering that contrast is quite immune to small flip angle errors, this should be enough to radically improve acquisition quality.

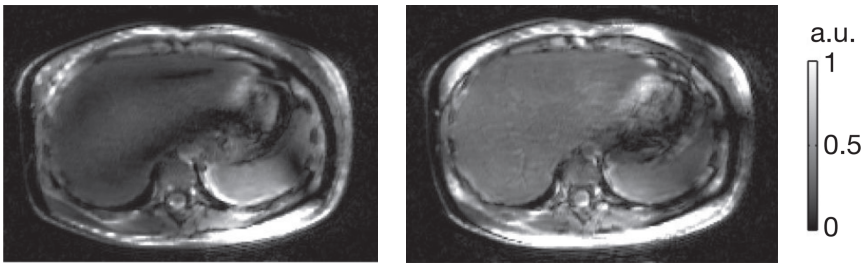

(a) Static RF shimming (b) Dynamic RF shimming

Figure GC.2: Excitation profiles obtained in the liver on a 7 T scanner equipped with eight-channel pTx. (a) Static RF shimming excitation; (b) 4-spoke dynamic RF shimming excitation. Image from [Wu 2014].

Finally, Siemens Healthineers have recently introduced the MAGNETOM Terra, a clinical 7 T scanner, that received both CE (European Conformity) and FDA (US Food an Drug Administration) markings. This imager has two operating modes: sTx and eight-channel pTx. Although today clinical use of the Terra is legally restricted to single-channel transmission, it seems likely that pTx will be authorised in the upcoming years, thus opening the door to ultra-high field exploration of the body. However, we expect that static RF shimming will not be sufficient to overcome the strong flip angle inhomogeneity encountered in body imaging – especially in the liver – even with eight channels as shown in fig. GC.2. Furthermore, B_1^+ mapping will be longer. The TIAMO technique has already demonstrated good mitigation of signal voids due to B_1^+ inhomogeneity in the liver at 7 T by acquiring two time-interleaved images with a different excitation mode for each [Orzada 2010]. However it requires every sequence to be played twice: in addition to being a burden in clinical routine, it is hardly compatible with breath-hold examinations. Therefore, we can easily imagine that the k_T-points method will be a promising alternative to obtain high quality 3D imaging. Moreover, with the *SmartPulse* approach, the need for complex and time-consuming calibration usually associated with static or dynamic RF shimming will simply vanish away.

* * *
* *
*

Appendices

Appendix **A**

Fat Management for Pulse Design in Breast Imaging

Off-resonance mapping, as we have seen throughout this manuscript, is necessary for accurate pulse design. Additionally, in the two liver studies, the Δf_0 map was used to discriminate water voxels from fat ones. Indeed, as the imaging sequence used eventually performed fat suppression, it was not necessary to homogenise the excitation in fat, and those voxels could be removed from the optimisation problem. For the study on breast imaging, a Δf_0 map and a water mask were needed for the same reasons. In this appendix, we will describe by what aspects the study on breast MRI was different from the liver ones in terms of fat management, and what process we used to perform mapping and masking. The intention is not to provide guidance, as better solutions could be imagined, but rather to describe what methods we implemented at the time, so that future readers could consider improvements.

A.1 Off-Resonance Mapping and Fat Mapping: Comparison Between Liver and Breast

In the liver, we could not use the off-resonance map provided by the scanner (see footnote 6 on page 69), mostly because it was not acquired in breath-hold. Fat and water tissues could occupy the same spatial location at different time points along the acquisition, and the apparent measured frequency at that location was the temporal average of the observed voxel. We therefore used the vendor's product FLASH sequence with an isotropic resolution of 4 mm, acquired in one breath-hold, with two echoes as close as possible to distinguish a wide range of spatial frequencies without ambiguity due to phase wrapping. The shortest ΔTE achievable was 0.96 ms, which allowed to map frequency offsets between -520 Hz and $+520$ Hz. With some quick and trivial unwrapping work based on the asymmetry of the spectrum, this was enough to map all frequencies present in the region of interest, as shown in fig. A.1. In addition, water and fat peaks almost did not overlap, so it was easy to discriminate both tissue types by setting an arbitrary limit

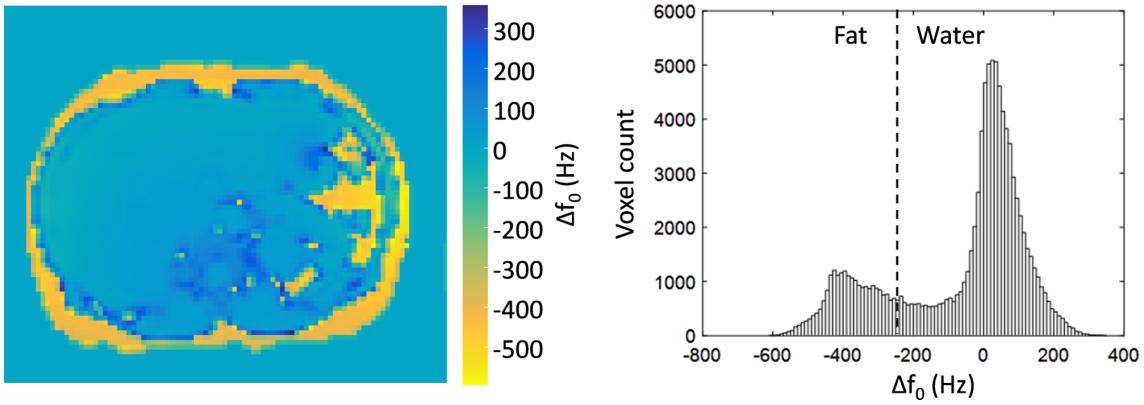

Figure A.1: Typical off-resonance map and associated histogram obtained in the liver in one subject. Most of the FOV is occupied by the liver, and water voxels dominate the histogram. Water and fat peaks are easy to distinguish and a threshold can be picked to isolate water tissues (here $-250\,\mathrm{Hz}$).

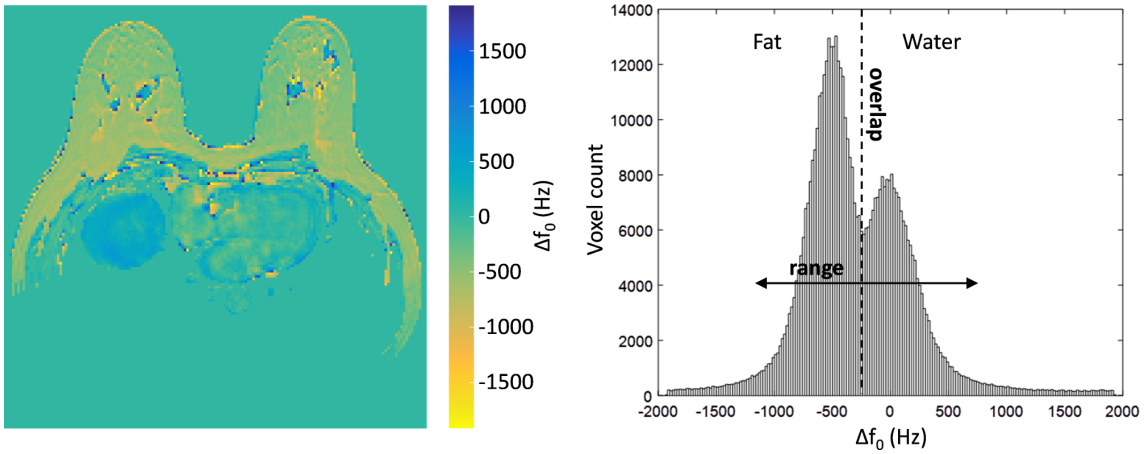

Figure A.2: Example of off-resonance map (left) and associated histogram (right) in the breast in one subject. Compared to the liver (fig. A.1), a wider range of frequencies must be acquired, and the water and fat peaks significantly overlap. In addition, we can see on the left panel that both tissues are finely intertwined. Here, water voxels in the breast are very sparse. Also notice the liver dome and the heart in the FOV.

at $-250\,\mathrm{Hz}$.

In comparison, when looking at fig. A.2, the situation was much more difficult in the breast, giving rise to three challenges:

1. Due to stronger B_0 inhomogeneities (because of the extended FOV and the presence of the lungs), we needed to acquire a wider range of frequencies, corresponding to $\Delta\mathrm{TE} \leq 0.4\,\mathrm{ms}$.
2. Fat and water voxels were finely intertwined so a higher resolution was needed. Additionally, on the spectrum, we can see significant overlap between water and fat peaks, making discrimination between both tissues difficult.
3. We needed to clean the FOV from isolated voxels and from a number of irrelevant organs and tissues: liver dome, heart, pectoral muscles, etc.

In addition, there is a wide variety of breast sizes and compositions, including patients with mastectomy (unilateral or bilateral), or with silicone-based prostheses (off-resonance peak at −600 Hz). Sometimes, the water peak is insignificant, sometimes it dominates fat. Fortunately, breast examinations are performed in free-breathing and breathing does not induce significant breast movement, so increasing the acquisition time of the Δf_0 mapping sequence was not really an issue.

A.2 Mapping a Wide Range of Off-Resonance Frequencies

To solve the first issue, and acquire a range of frequencies as large as needed, we acquired two distinct single-echo FLASH sequences, each with a slightly different TE. Choosing $\Delta\text{TE} = 0.25\,\text{ms}$ allowed to distinguish frequencies in a $\pm 2000\,\text{Hz}$ bracket, which was more than enough to cover the entire spectrum. Both echo times were picked so that water and fat were in phase or close (for instance 2.20 ms and 2.45 ms), so that signal was maximal in every voxel, and phases as precise as possible in voxels containing a mix of water and fat. Also, this two-sequence scheme allowed us to use a readout bandwidth narrower than with a single two-echo acquisition, which increased the SNR.

Running two sequences, of course, means doubling the time needed to acquire the Δf_0 map. To achieve an isotropic resolution of 2 mm, a total acquisition time of about one minute was needed.

In order to increase the precision of the Δf_0 mapping, we decided to acquire a third echo – using a 2+1 or 1+2 echo acquisition scheme – as suggested in section 2.2.4 'Off-Resonance Mapping'. As we are about to see, choosing adequate echo times enabled us to easily segment fat and water voxels, despite the overlap between their respective peaks on the histogram.

A.3 Using Dixon Reconstruction to Mask Water and Fat

Here we consider a 2+1 echo acquisition. The first sequence can be acquired with a Dixon scheme, *i.e.* with $\text{TE}_{\text{OP}} = 1.23\,\text{ms}$ and $\text{TE}_{\text{IP}} = 2.46\,\text{ms}$. As seen in section 1.3.2, Dixon reconstruction provides water and fat signal images. In order to use this information to create water and fat masks, we need to estimate the water and fat fractions in every voxel.

Let us call S_w and S_f the measured water and fat signals (respectively), and S'_w and S'_f the theoretical water and fat signals. Introducing the water and fat fractions τ_w and τ_f, such that $\tau_w = 1 - \tau_f$, we can write:

$$\begin{cases} S'_w = \tau_w \; S'_{w,0} \\ S'_f = \tau_f \; S'_{f,0} \end{cases} \tag{A.1}$$

with $S'_{w,0}$ and $S'_{f,0}$ the theoretical signals in voxels containing solely water or solely fat,

respectively. $S'_{w,0}$ and $S'_{f,0}$ are given by eq. (1.19):

$$\begin{cases} S'_{w,0} = k\ \mathrm{PD}_w\ \sin\alpha\ \dfrac{1-\mathrm{E}_{1,w}}{1-\mathrm{E}_{1,w}\cos\alpha}\ \mathrm{E}^*_{2,w} \\ S'_{f,0} = k\ \mathrm{PD}_f\ \sin\alpha\ \dfrac{1-\mathrm{E}_{1,f}}{1-\mathrm{E}_{1,f}\cos\alpha}\ \mathrm{E}^*_{2,f} \end{cases} \tag{A.2}$$

Let us make a few approximations: we consider that $\mathrm{PD}_w = \mathrm{PD}_f$, and we consider identical T_2^* values for both tissue types (*cf.* table 2.1 on page 48). We know that the ratio between theoretical signals from both tissues should be equal to that of measured signals:

$$\frac{S_f}{S_w} = \frac{S'_f}{S'_w} \quad\Longleftrightarrow\quad \frac{S_f}{S_w} = \frac{\tau_f\ S'_{f,0}}{(1-\tau_f)\ S'_{w,0}} \tag{A.3}$$

This gives:

$$\tau_f = \frac{1}{1 + \dfrac{S_w}{S_f}\ \dfrac{S'_{f,0}}{S'_{w,0}}} \tag{A.4}$$

For a given {TR, α} pair, the only relevant parameters in the ratio $\frac{S'_{f,0}}{S'_{w,0}}$ are the T_1 constants for water and fat. We can choose $\mathrm{T}_{1,f} = 300\,\mathrm{ms}$, and $\mathrm{T}_{1,w} = 1500\,\mathrm{ms}$ (breast glandular tissue). An example of obtained fat fraction map is shown in fig. A.3, along with the corresponding water and fat masks. We picked a τ_f threshold of 60 % to separate water from fat.

We developed an *ICE* functor (image reconstruction program for Siemens systems) that incorporates default Dixon reconstruction along with 3-echo $\Delta\mathrm{B}_0$ calculation, that outputs water and fat signal images along with the off-resonance map. This way, we only had to retrieve a compact file on the scanner that we would use for pulse design, rather than working with raw data or DICOM images.

A.4 Additional Masking Steps

Apart from water and fat separation considerations, it was necessary to have a mask clean enough to avoid including background noise voxels in the pulse design, thus improving its robustness. Figure A.4 illustrates the different steps we implemented to process this mask:

(a) A first mask was obtained by applying a threshold on a magnitude image from the Δf_0 mapping acquisition (*e.g.* the in-phase image): most of the background was removed.

(b) This mask was cleaned from remaining isolated voxels and from voxels at the border between the background and the region of interest by morphological erosion.

(c) We were not interested in the liver dome nor the heart. Taking advantage of the convexity of the torso, we could easily remove most of them. Indeed, any horizontal line of the mask should include at most four interfaces.

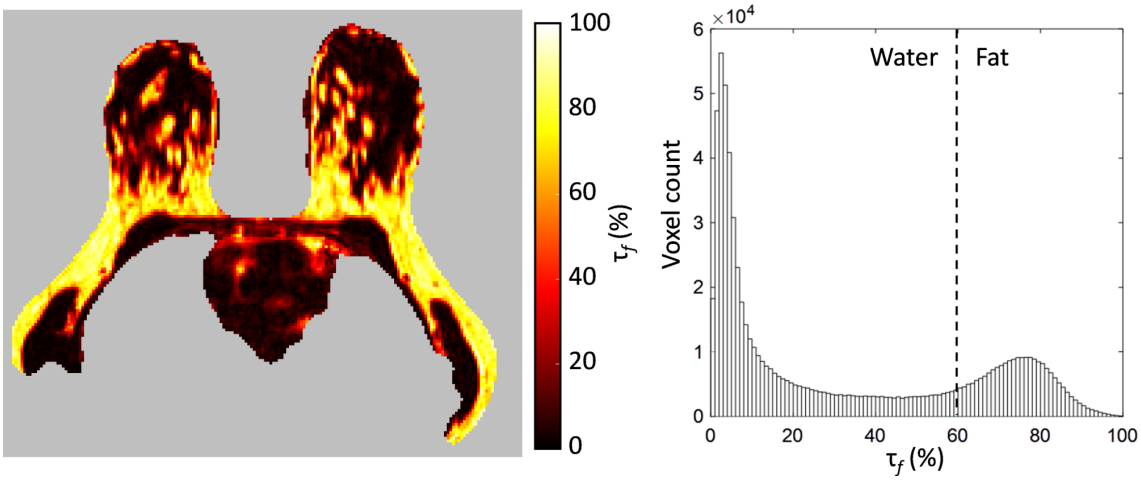

(a) Fat fraction map, and associated histogram

(b) Water mask

(c) Fat mask

Figure A.3: Example of a fat fraction map obtained from Dixon images, and the associated masks. To obtain the water and fat masks, voxels associated with a fat fraction below 60 % were regarded as water, and included in the pulse optimisation.

(a) (b) (c) (d)

Figure A.4: Additional steps to clean the mask. See the text for a description of each step.

(d) For breast imaging acquisitions, the B_0 shimming 'FOV' is much smaller than the imaging FOV. The coordinates of the shimming box were included in our *ICE* functor's output file, so that the volume could be cropped accordingly in post-processing.

Additional semi-automated processing of the mask was also performed (not shown here), that consisted of 'cropping out' a 3D ellipsoid from the torso, to remove as much pectoral muscle tissues as possible.

* * *
* *
*

Appendix B

Additional Data from Chapter 5

Table B.1: Patient population for image analysis from chapter 5: extended version of table 5.1.

Subject	Sex	Age *years*	Height *cm*	Weight *kg*	BMI	Contrast agent	Investigation	Visual cues
1	M	66	169	73	25.6	Gd-BOPTA	monitoring after radioembolization of several HCC nodules in segment 4	ascites
2	F	42	165	69	25.3	Gd-BOPTA	investigation of area hypo-dense on CT in segment 4	polycystic liver and kidney disease
3	M	47	169	81	28.4	Gd-BOPTA	follow-up: right posterior segmentectomy due to HCC	—
4	M	63	175	85	27.8	Gd-BOPTA	HCC chemoembolization assessment	ascites (moderate)
5	M	64	165	95	34.9	Gd-BOPTA	bile ducts monitoring	—
6	M	45	173	60	20.0	Gd-BOPTA	characterisation of hypervascular areas in segments 4+8 in chronic HCV context	—
7	F	41	160	62	24.2	Gd-BOPTA	liver injury screening	—
8	M	78	187	78	22.1	Gd-DOTA	mantle cell lymphoma treatment follow-up	significant shading
9	M	66	168	75	26.6	Gd-BOPTA	monitoring after left lateral segmentectomy for HCC (NASH)	—
10	F	54	160	52	20.3	Gd-BOPTA	monitoring prior to liver transplantation for HCC (chronic HBV infection)	—
11	F	83	164	69	25.7	Gd-DOTA	cystic mass in pancreas tail	—
12*	M	54	170	70	24.2	Gd-BOPTA	cured HCV follow-up; HCC nodule found	—
13	M	60	166	68	24.7	Gd-BOPTA	HBV-induced cirrhosis follow-up; segments 5+7 resected	—
14	F	23	160	45	17.6	Gd-BOPTA	adenomatosis follow-up; tumorectomy in segments 7+8	—
15	M	70	175	97	31.7	Gd-BOPTA	HCC radioembolization assessment	significant shading
16	F	53	158	68	27.2	Gd-DOTA	screening for cholangitis or lithiasis in common bile duct	—
17	M	23	171	61	20.9	Gd-DOTA	acute pancreatitis assessment	—
18	M	62	180	88	27.2	Gd-BOPTA	alcohol- and HCV-induced cirrhosis	—
19	F	73	172	73	24.7	Gd-BOPTA	HCV-induced cirrhosis follow-up	iron overload
20	M	59	170	85	29.4	Gd-BOPTA	bile duct obstruction in a cirrhotic liver	ascites

Abbreviations: HCC= hepatocellular carcinoma; HBV/HCV= hepatitis B/C virus; NASH= non-alcoholic steatohepatitis.

*A different set of receive coils was used: 18-channel anterior phased array and 32-channel posterior "spine" phased array.

Table B.2: Detailed results of the quantitative analysis based on simulations of 'patient-specific' static RF shimming and k_T-points on all 50 subjects. Extreme values are printed in bold. The last line indicates the means and standard deviations across subjects. Targeted flip angle was 11°. While the difference between the two techniques was negligible for many subjects, k_T-points yielded considerably better results in some cases (*e.g.* 1, 4, 8, 15 and 20). These include the three subjects with ascites (table B.1).

Subject[a]	Mean FA *degrees*		FA CoV *%*		FA NRMSE *%*		Global SAR[b,c] *W.kg^{-1}*		10g SAR[b,c] *W.kg^{-1}*		Duration[d] *µs*
	RF shim	k_T-points	RF shim	k_T-points	RF shim	k_T-points	RF shim	k_T-points	RF shim	k_T-points	k_T-points
1	6.6	**10.8**	26.8	11.7	43.4	11.7	**0.2**	0.4	1.3	2.9	**1750**
2	8.3	10.9	15.5	7.3	26.9	7.3	**0.2**	0.3	1.5	3.2	1530
	9.9	10.9	16.9	8.8	18.1	8.7	0.4	**0.6**	2.1	5.3	1360
	9.4	10.9	13.7	6.5	18.7	6.5	**0.2**	0.4	1.6	3.7	1340
	9.7	10.9	18.2	9.1	20.1	9.0	0.4	0.4	2.4	4.2	1570
	9.8	10.9	19.1	8.1	20.4	8.1	0.5	0.4	3.3	3.6	1580
	9.7	10.9	14.5	8.2	17.3	8.2	**0.2**	0.3	1.7	3.6	1350
	11.0	10.9	16.5	9.3	16.4	9.3	0.4	0.5	1.9	2.6	1410
	9.6	**11.0**	15.1	7.4	18.1	7.4	0.3	0.4	1.8	3.8	1390
3	10.3	10.9	13.7	6.9	14.3	6.9	0.5	0.5	4.1	3.8	1720
	11.4	10.9	14.4	8.8	15.3	8.8	0.5	0.4	2.3	2.3	1440
	8.0	10.9	13.9	6.8	28.8	6.8	**0.2**	0.4	1.3	2.6	1400
	9.9	10.9	16.0	7.7	17.3	7.7	0.3	0.5	1.8	4.0	1360
4	6.7	10.9	21.1	10.2	41.3	10.2	**0.2**	0.4	1.4	4.6	1380
	10.1	10.9	17.2	10.5	17.8	10.4	0.4	0.3	2.4	3.7	1390
5	9.7	10.9	20.2	10.7	21.4	10.6	0.5	0.4	3.1	3.7	1450
6	9.7	10.9	13.9	7.9	17.1	7.9	0.3	0.3	2.0	3.7	1350
7	8.6	10.9	16.4	9.9	25.2	9.9	0.3	0.3	1.5	3.1	1360
	7.5	10.9	20.3	9.2	34.7	9.2	**0.2**	0.5	1.3	5.4	1360
8	6.9	10.9	22.5	11.1	39.8	11.1	**0.2**	0.3	1.3	4.6	1460
	10.3	10.9	15.5	7.7	15.9	7.6	0.4	0.4	2.0	5.4	1360
	9.1	10.9	16.8	7.3	21.9	7.3	0.4	0.3	3.8	5.5	1470
9	10.5	10.9	15.7	9.1	15.7	9.0	0.5	0.4	3.9	3.7	1390
10	10.7	**11.0**	**10.7**	6.6	**10.8**	6.6	**0.2**	0.3	1.3	**1.3**	1370
	9.8	10.9	15.3	8.4	17.5	8.4	0.3	0.3	1.4	5.0	1420
	10.4	10.9	13.7	8.2	14.0	8.2	0.4	0.4	2.4	2.6	1430
	10.0	**11.0**	11.4	**6.1**	13.6	**6.1**	0.3	0.4	1.5	2.4	1380
	10.0	10.9	13.2	7.5	14.8	7.5	0.5	0.3	**4.7**	4.2	1410
11	10.2	10.9	12.6	6.4	13.7	6.4	0.3	0.5	1.8	3.2	1320
	10.6	10.9	19.3	9.3	18.9	9.3	0.5	0.4	3.2	4.3	1420
12	10.2	10.9	14.1	8.5	14.8	8.5	0.5	0.3	3.5	4.5	1420
13	11.0	10.9	13.8	7.5	13.8	7.5	0.4	0.4	2.2	2.7	1410
14	10.1	10.9	15.7	9.9	16.6	9.9	0.3	**0.2**	1.8	4.2	1370
	10.5	10.9	13.7	7.1	13.8	7.0	0.4	0.3	2.5	5.0	1380
15	6.1	10.9	23.9	11.1	46.7	11.1	**0.2**	0.4	1.3	4.9	1420
16	10.3	10.9	12.2	8.4	12.9	8.3	0.3	0.3	1.7	2.4	1390
	10.0	10.9	15.9	9.3	17.1	9.3	0.5	0.3	3.2	2.7	1410
17	10.7	10.9	14.1	8.2	14.0	8.2	0.4	0.4	2.2	2.9	1420
	10.4	10.9	16.6	8.5	16.7	8.5	0.5	0.3	3.5	4.7	1420
	10.3	**11.0**	13.0	6.8	13.6	6.8	0.3	0.4	1.9	4.3	1410
	10.6	**11.0**	13.2	7.0	13.2	7.0	0.4	0.3	2.8	4.1	1340
	11.0	10.9	16.6	9.5	16.6	9.4	0.5	0.4	3.8	4.1	1410
	10.7	**11.0**	11.4	6.5	11.5	6.4	0.3	0.3	1.7	3.5	1350
18	9.4	10.9	17.4	9.1	20.6	9.1	0.4	0.4	2.2	2.7	1430
	9.5	10.9	16.7	8.8	20.1	8.7	**0.2**	0.4	1.6	3.0	1340
	11.6	10.9	21.3	8.7	23.1	8.7	**0.6**	0.5	3.7	5.4	1450
	10.5	**11.0**	12.6	6.6	12.8	6.6	0.4	0.4	2.0	2.7	1380
19	7.5	10.9	17.3	8.6	34.3	8.5	**0.2**	0.3	**1.2**	2.8	1370
	10.4	10.9	16.5	8.9	16.6	8.8	0.3	0.4	2.1	2.9	**1300**
20	**5.4**	**10.8**	**42.6**	**13.1**	**54.9**	**13.0**	**0.2**	0.4	**1.2**	**7.0**	1660
All[e]	**9.6 ± 1.4**	**10.9 ± 0.0**	**16.6 ± 5.0**	**8.5 ± 1.5**	**20.7 ± 9.8**	**8.5 ± 1.5**	**0.3 ± 0.1**	**0.4 ± 0.1**	**2.2 ± 0.9**	**3.8 ± 1.1**	**1420 ± 92**

Abbreviations: FA = flip angle; CoV = coefficient of variation; NRMSE = normalised root-mean-squared error from the target.
[a]Only subjects included in image analysis were numbered.
[b]Global SAR was measured by the scanner and read directly from the DICOM files. Local SAR was evaluated from the pulse shape, TR, and VOPs (virtual observation points) provided by the scanner.
[c]6-minute average SAR limits (IEC 60601-2-33): 2 W.kg^{-1} for whole body global SAR; 10 W.kg^{-1} for local SAR (10g of contiguous tissue).
[d]Duration of static RF shimming square pulses was systematically set to 100 µs.
[e]For each metric: mean ± standard deviation over the 50 subjects.

Appendix C

Additional Figures from Chapter 6

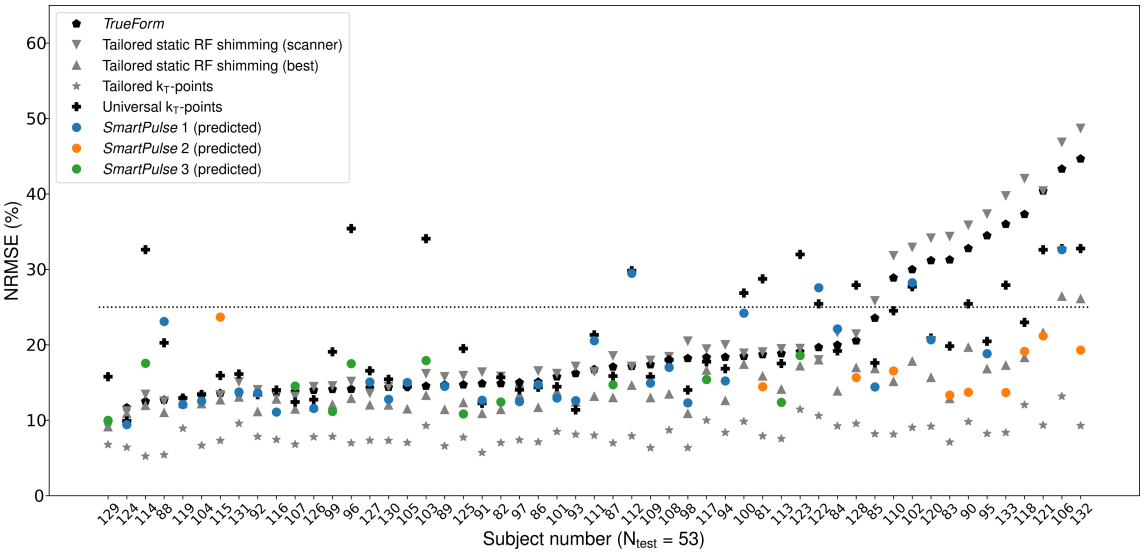

Figure C.1: Complementary to fig. 6.6: comparison of all simulated pulse designs: Normalized root-mean-square error from the target flip angle (NRMSE) simulation results for all test subjects, sorted in increasing *TrueForm* inhomogeneity. For each subject, only the predicted *SmartPulse* is shown. The dashed line indicates 25 % NRMSE. Notice how subjects with a high *TrueForm* NRMSE are brought towards more acceptable values with *SmartPulse*.

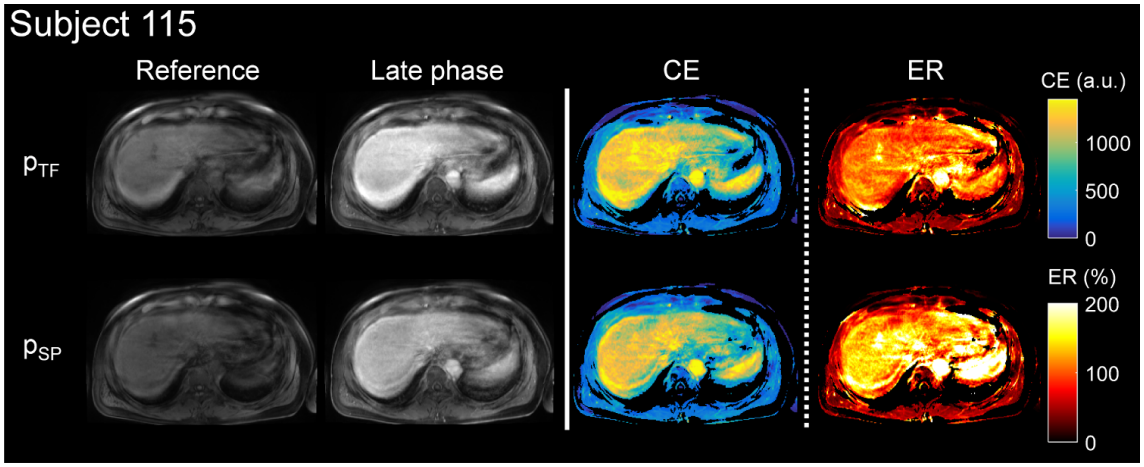

Figure C.2: From left to right: pre-injection, post-injection, calculated contrast enhancement (CE) and enhancement ratio (ER) obtained with *TrueForm* (p_{TF}) and *SmartPulse* (p_{SP}) in a case where predicted p_{SP} was not at all optimal, yielding 23 % NRMSE, compared to 14 % for p_{TF} and $p_{SP,best}$ (table 6.2). Homogeneity is the same for both pulses, but p_{SP} overshoots the flip angle target, hence the overall excessive ER.

Appendix **D**

Résumé en français

Abstract in French

Sujet : Applications cliniques de la méthode des points k_T pour homogénéiser l'excitation des spins en IRM à 3 teslas.

Nous résumons ici les différents aspects abordés au cours de cette thèse. Après un exposé des contextes stratégique et technique qui ont conduit à la mise en œuvre de ces travaux, nous nous attacherons à décrire l'état de l'art antérieur de la méthode des points k_T (ou *k_T-points*), au cœur de cette thèse. Dans un second temps, nous présenterons quelques développements méthodologiques autour de cette méthode et de son implémentation. Enfin, trois études en milieu hospitalier ont été menées pour démontrer l'intérêt pratique des points k_T en routine clinique, en imagerie du sein et du foie.

Contexte et état de l'art

L'imagerie par résonance magnétique (IRM) est une technique relativement récente (années 70–80) qui a su révolutionner l'imagerie médicale, en particulier des tissus mous, par son caractère non-ionisant – contrairement aux rayons X – et par la grande variété de « contrastes » offerts. Un même examen permet d'obtenir un atlas anatomique des différents organes, mais aussi une caractérisation de nombreuses pathologies, et même une exploration fonctionnelle. On pensera par exemple à la visualisation des activations cérébrales.

Un scanner IRM est organisé autour d'un puissant aimant, et est donc caractérisé en particulier par le champ magnétique produit par cet aimant. Le principe de l'imagerie de résonance magnétique nucléaire est le suivant. Lorsqu'un volume est placé dans le champ magnétique statique généré par l'aimant, appelé B_0 et noté $\mathbf{B_0}$ sous forme vectorielle, les spins des protons d'hydrogène ^1H le composant[1] s'alignent sur le champ de manière paral-

[1] Nous nous intéressons au noyau d'hydrogène car il est présent en grande quantité dans les tissus (eau, graisse, ...). L'imagerie d'autres noyaux, dits « exotiques », existe, mais n'est pas étudiée ici.

lèle ou anti-parallèle et, d'un point de vue macroscopique, on voit apparaître un moment magnétique moyen : c'est l'aimantation à l'équilibre $\mathbf{M_0}$, alignée avec $\mathbf{B_0}$ et dont la valeur augmente linéairement avec B_0. Pour l'instant, aucun signal n'est mesurable. Pour cela, une onde radiofréquence (RF) est appliquée, qui permet de faire basculer tout ou partie de cette aimantation dans un plan transverse à $\mathbf{B_0}$. Le champ RF utilisé est dénommé $\mathbf{B_1^+}$, et sa fréquence doit être ajustée pour résonner avec les spins : elle est proportionnelle à B_0. Une fois l'aimantation basculée, le champ B_1^+ est arrêté, et l'aimantation revient lentement vers son état d'équilibre purement longitudinal en « tournant » autour de $\mathbf{B_0}$: on parle de précession libre. C'est durant cette période qu'un signal correspondant à cette relaxation peut être mesuré : la FID (de l'anglais *free induction decay*). Ce mouvement de précession, et donc la FID, est empiriquement décrite par deux constantes de temps :

- T_1 correspond à la relaxation spin-réseau, qui décrit le retour à l'équilibre de la composante longitudinale de l'aimantation ;
- T_2 correspond à la relaxation spin-spin, qui correspond à la disparition progressive de la composante transverse de l'aimantation.

Ces deux constantes varient selon les tissus et permettent de les caractériser. En pratique, le champ B_0 n'est pas parfaitement homogène, ce qui accélère la disparition de la composante transverse, que l'on décrit alors par T_2^*.

IRM à haut et très haut champ : plus de signal, mais de nombreux défis

L'amplitude du signal mesuré est, entre autres, proportionnelle à M_0, et donc à la valeur du champ statique B_0. Partant de ce constat, depuis les débuts de l'IRM, des aimants de plus en plus puissants ont été construits afin d'améliorer le rapport signal sur bruit des acquisitions et ainsi obtenir des images de meilleure résolution par exemple. Actuellement, en pratique clinique, on rencontre des aimants de 1.5 T et de 3 T. En recherche, les champs de 7 T sont courants – et ont même été très récemment introduits en clinique – et montent aujourd'hui jusqu'à 10.5 T. Dans ce cadre, les laboratoires IRFU et NeuroSpin du CEA se sont lancés en 2007 dans le projet ISEULT, qui consiste en la conception et la mise en œuvre d'un imageur à 11.7 T, qui deviendrait l'IRM la plus puissante au monde. L'aimant a été livré en juillet 2017 (figure D.1), et à ce jour les premières images sont attendues fin 2019. L'objectif de ce projet est à terme d'obtenir des images de cerveau d'une résolution inégalée.

Néanmoins, de nombreux défis se présentent lorsque l'on augmente le champ magnétique. Par exemple, il devient plus difficile d'obtenir un champ B_0 homogène. De plus, la résolution d'image accrue impose de trouver des méthodes d'acquisition rapides. Un problème qui nous intéresse tout particulièrement, et que nous allons développer plus loin, est celui de l'inhomogénéité du champ B_1^+. Tous ces défis à relever pour obtenir des images de qualité ont donné lieu à autant de champs de recherche en IRM, sur lesquels travaillent de nombreuses équipes dans le monde. En particulier, dans le cadre du projet ISEULT, des financements ont été attribués au sein du CEA pour préparer l'arrivée de cet imageur hors normes et assurer autant que possible une bonne qualité d'image. Un de ces finan-

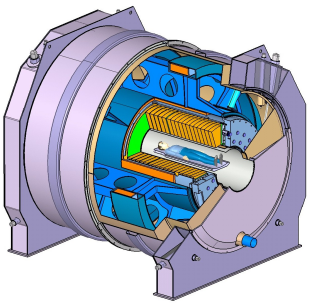

(a) Ecorché de l'IRM 11.7 T.

(b) Livraison de l'aimant.

Figure D.1 : Projet ISEULT d'IRM à 11.7 T, en cours de construction à NeuroSpin.

cements a donné lieu à une méthode originale pour surmonter l'inhomogénéité du champ B_1^+ dans le cerveau à 7 T, brevetée en 2011 par Alexis Amadon et Martijn A. Cloos : les points k_T. C'est dans la continuité de ce brevet que se sont inscrits les travaux de thèse présentés ici. Dans un souci de valorisation, et pour susciter l'intérêt des industriels envers cette technique, l'idée est d'effectuer la démonstration de l'applicabilité et de l'intérêt des points k_T en routine clinique.

Méthode des points k_T pour homogénéiser l'excitation des spins

La fréquence de l'onde RF utilisée pour exciter les spins, *i.e.* basculer l'aimantation d'un certain *angle de bascule*, est ajustée à la fréquence de Larmor, proportionnelle à B_0. La longueur d'onde dans les tissus humains est d'environ 50 cm à 1.5 T, 25 cm à 3 T et seulement 11 cm à 7 T. Or, lorsque la longueur d'onde RF est inférieure à la taille des objets ou organes imagés, des artéfacts apparaissent en raison d'interférences constructives et destructives. En effet, l'onde RF est émise par une antenne généralement constituée de plusieurs éléments, ajustés en amplitude et phase pour permettre une polarisation circulaire, en quadrature, du champ B_1^+. Lorsque l'antenne est chargée par des tissus physiologiques et que la longueur d'onde diminue, la propagation des ondes est modifiée par la géométrie de l'objet et ces ajustements de phase ne sont plus optimaux. On parle fréquemment « d'artéfact de B_1 », caractérisé par des zones d'ombre et de perte de contraste dans le champ de vue. Cet effet est souvent observé dans le cerveau à 7 T (figure D.2a) et dans les cuisses, les seins ou l'abdomen à 3 T (figure D.2b). Notons que cet artéfact peut être amplifié par la présence de liquide conducteur : c'est le cas du liquide amniotique chez les femmes enceintes, ainsi que de l'ascite, épanchement liquidien inflammatoire dans l'abdomen.

Parmi les solutions traditionnellement implémentées pour résoudre ces problèmes, on peut citer l'utilisation de coussins à haute constante diélectrique, et le *shim* RF statique. La première méthode permet de rehausser le champ B_1^+ localement, dans les régions proches du coussin, mais au détriment des autres zones du champ de vue. Quant au *shim* RF statique, il repose sur l'utilisation d'antennes émettrices pilotables par différents canaux : on parle de transmission parallèle (pTx, pour *parallel transmission*). Un canal pilote un

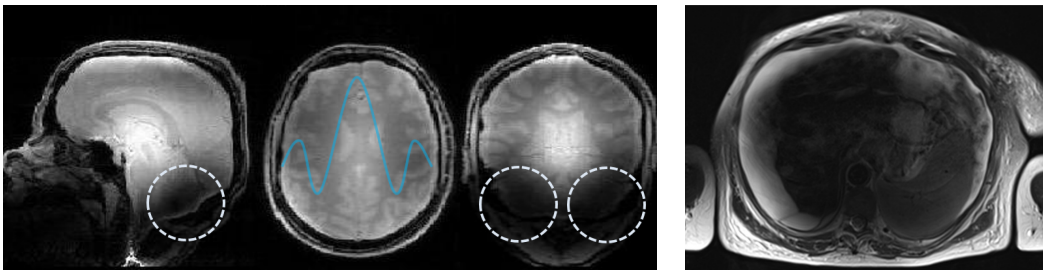

(a) (b)

Figure D.2 : Exemples d'artéfacts de B_1 observés (a) dans le cerveau à 7 T, et (b) dans l'abdomen à 3 T. L'artéfact est particulièrement marqué dans l'abdomen en raison de la présence d'ascite.

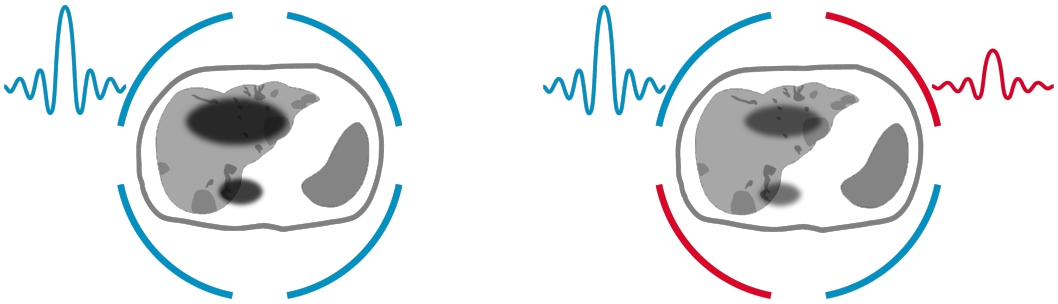

(a) Polarisation circulaire : un amplificateur génère une forme d'onde, transmise à différents éléments d'antenne avec une différence de phase fixée (90° dans l'exemple ci-dessus d'antenne *birdcage*).

(b) Polarisation elliptique avec pTx : plusieurs amplificateurs RF (ici deux) pilotent indépendamment certains éléments d'antenne, qui forment des canaux d'émission. Amplitudes et phases peuvent être ajustées pour homogénéiser le champ B_1.

Figure D.3 : Schéma comparant le mode de transmission CP traditionnel (a) avec les modes EP de RF *shim* statique offerts par la pTx (b). N.B. : certains systèmes sTx sont ajustés non pas en CP, mais avec un mode EP fixé..

ou plusieurs éléments d'antenne simultanément ; chaque canal peut se voir attribuer une amplitude et une phase RF différente, permettant de contrôler les motifs d'interférences. La figure D.3 illustre la différence entre un système mono-canal (sTx) et un scanner avec pTx. Les systèmes ultra-haut champ de recherche (7 T et plus) utilisent en général huit canaux d'émission, voire plus (jusqu'à 32 à ce jour). En pratique clinique à 3 T, étant donné le coût important de cette technologie, le nombre de canaux est plus modeste : les systèmes dotés de pTx ont au plus deux canaux.

Pour dépasser les limites du RF *shim* statique, on peut chercher à obtenir une excitation des spins homogène – ce que l'on veut *in fine* – malgré un champ B_1^+ inhomogène : c'est le RF *shim* dynamique. En appliquant des gradients de champ magnétique statique pendant et/ou entre des impulsions RF, il est possible de moduler l'excitation des spins. En particulier, le motif de modulation peut être défini comme l'inverse du motif d'inhomogénéité de transmission afin de compenser ce dernier. Les points k_T sont une paramétrisation

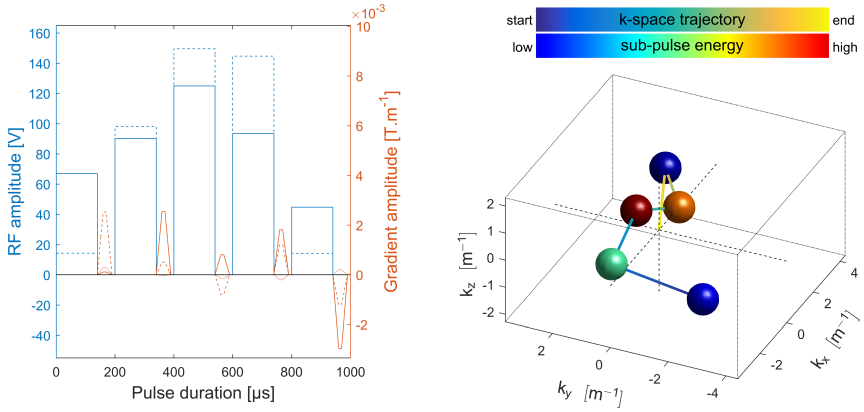

Figure D.4 : Exemple de points k_T à 5 sous-impulsions sur un système pTx à deux canaux, et trajectoire correspondante dans l'espace réciproque d'émission. A gauche : amplitudes RF (en bleu) sur chaque canal (lignes continue et en pointillés) et forme des gradients (en orange) sur chaque axe ; la phase RF n'est pas représentée. A droite : trajectoire associée dans l'espace réciproque.

d'impulsions de *shim* RF dynamique permettant une excitation non-sélective, c'est-à-dire ayant un effet sur l'intégralité du volume à imager (et non une coupe ni une tranche), qui consiste à alterner des impulsions RF rectangulaires et des « *blips* » – petites impulsions – de gradients. Dans l'approximation des petits angles de bascule (moins de 90°), on peut considérer que les gradients permettent de se déplacer dans « l'espace réciproque d'émission » : le motif de modulation de l'excitation correspond à la transformée de Fourier des points k_T. Pour obtenir une bonne homogénéité, un grand nombre de sous-impulsions RF peut être nécessaire. Aussi, même si le RF *shim* dynamique fonctionne en sTx, les degrés de liberté offerts par la pTx sont appréciables. Un exemple de points k_T avec deux canaux de transmission est représenté figure D.4. Les points k_T ont fait leurs preuves à ultra-haut champ dans le cerveau, avec de nombreuses pondérations et séquences d'imagerie 3D (GRE, MP-RAGE, SPACE).

Que ce soit en RF *shim* statique ou dynamique, il est nécessaire de réaliser des cartographies de B_1^+ et parfois de B_0 avant de calculer des impulsions adaptées au motif d'inhomogénéité du patient. Cette étape de calibration (cartes et calculs) prend d'autant plus de temps qu'il y a de canaux d'émission disponibles : le processus complet peut prendre entre deux et dix minutes selon le matériel. Il faut ajouter à cela le risque d'erreur de la part du manipulateur, ainsi que les mouvements potentiels du patient entre le moment de la cartographie et l'examen lui-même. Pour ces raisons, Vincent Gras *et al.* ont récemment introduit le concept d'impulsion universelle (UP pour *Universal Pulse*) : des impulsions sont calculées sur une base de données de sujets de sorte à optimiser l'homogénéité de l'excitation sur la population entière, et non plus sur un sujet unique. La méthode a été testée avec succès en imagerie cérébrale à 7 T, notamment avec des points k_T comme le montre la figure D.5. Etant donné la variabilité morphologique importante dans l'imagerie du corps, en particulier de l'abdomen, la méthode des UP ne peut cependant pas s'appliquer en l'état dans les gros organes à 3 T.

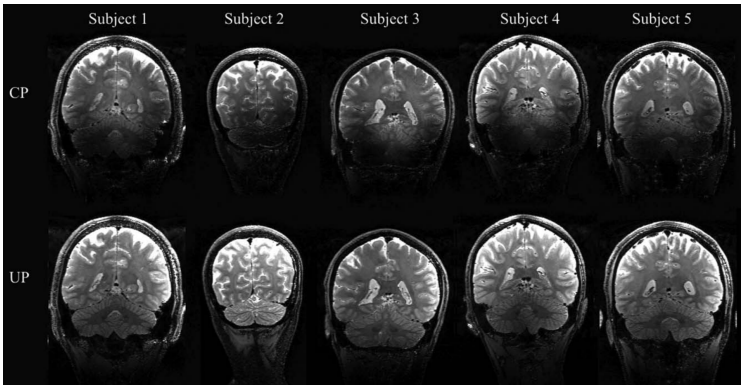

Figure D.5 : Images SPACE pondérées en T_2 acquises à 7 T en mode CP (en haut) et avec des points k_T universels (en bas).

Développements méthodologiques

L'algorithme de conception de points k_T utilisé jusqu'à présent à NeuroSpin optimise simultanément les coefficients complexes de chaque sous-impulsion RF (amplitude et phase sur chaque canal) ainsi que leur position dans l'espace réciproque d'émission, c'est-à-dire les amplitudes des *blips* de gradients. Ces paramètres sont optimisés de sorte à minimiser, sous contraintes de puissance et de dépôt d'énergie dans le patient (débit d'absorption spécifique, ou DAS), une fonction de coût correspondant à l'homogénéité d'angle de bascule, définie par la NRMSE (erreur moyenne quadratique normalisée, *normalised root-mean-square error* en anglais) :

$$\mathrm{NRMSE}(\mathbf{a}) = \frac{1}{\alpha_T}\sqrt{\sum_{i=1}^{N}\frac{(\alpha_i - \alpha_T)^2}{N}} \tag{D.1}$$

où $\mathbf{a}$ est le vecteur des angles de bascule en chaque voxel et N est le nombre de voxels pris en compte dans le champ de vue : $\mathbf{a} = \begin{bmatrix}\alpha_1 & \dots & \alpha_i & \dots & \alpha_N\end{bmatrix}$.

Optimisation des durées d'impulsion et de sous-impulsions de points k_T

Un développement apporté à l'algorithme a été d'optimiser, en plus des coefficients complexes et des positions dans l'espace k, les durées de sous-impulsion, ainsi que la durée totale de l'impulsion points k_T. L'intérêt de cette optimisation a été démontré sur des simulations réalisées dans le cerveau à 7 T. Les degrés de liberté permettent certes de gagner quelques points de NRMSE de manière générale, mais c'est en particulier face à des inhomogénéités importantes de champ statique (en plus des inhomogénéités RF) que le gain est tout à fait intéressant. En effet, une impulsion longue permet de réduire la NRMSE tout en limitant la puissance (qui évolue linéairement avec la durée d'impulsion, mais avec le carré de l'amplitude) par rapport à une impulsion équivalente plus courte, avec une amplitude plus élevée. Mais une impulsion courte est moins sensible aux inhomogénéités de B_0. Cette flexibilité peut s'avérer intéressante en imagerie du corps, où les gradients de B_0 peuvent être importants, notamment près des poumons.

Gestion de la présence de graisse

Une grande différence entre l'imagerie cérébrale et celle des régions du corps considérées dans cette thèse est la présence de grandes quantités de graisse dans le champ de vue, que l'on peut souhaiter imager ou préférer masquer. En effet, si l'impulsion est conçue pour être utilisée dans une séquence avec suppression de graisse, il n'est alors pas nécessaire d'optimiser l'excitation dans les voxels contenant de la graisse. Du fait du déplacement chimique entre l'eau et la graisse, ceux-ci peuvent être discriminés à partir d'une carte de différentiel de fréquence par rapport à la porteuse (Δf_0) : dans la graisse, les spins résonnent dans une bande de fréquence centrée autour de $-440\,\mathrm{Hz}$ environ (contre $0\,\mathrm{Hz}$ pour l'eau).

Une telle carte est fournie par le scanner au cours de séquences standard de calibration, au côté d'une carte de champ RF sur chaque canal, et de données permettant d'estimer le DAS. Si cette carte s'avère satisfaisante pour l'imagerie des cuisses, il nous a fallu procéder nous-mêmes à la mesure pour l'abdomen du fait de la respiration du patient. La carte automatique est réalisée en respiration libre, le résultat est donc une moyenne temporelle de la fréquence observée en chaque point au cours du temps, tantôt eau, tantôt graisse, ce qui ne convient pas du tout.

Dans le cas de l'imagerie du sein, la situation est également délicate. Il n'y a pas de mouvement lié à la respiration, mais la structure même du sein, mélange entre tissus glandulaires (aqueux) et adipeux finement entremêlés rend également la carte automatique inopérante du fait de sa résolution spatiale trop faible. Dans certains cas, très peu de voxels peuvent être identifiés comme aqueux, à cause d'effets de volume partiel. De plus, les variations parfois importantes de champ statique entraînent un chevauchement partiel des pics d'eau et de graisse, rendant inopérante la séparation eau/graisse basée uniquement sur le spectre. La solution retenue pour l'IRM du sein a donc été d'acquérir les cartes de Δf_0 en deux étapes. Une séquence Dixon à deux échos est d'abord acquise, qui permet d'isoler le signal de l'eau de celui de la graisse et donc de créer un masque pour chacune des composantes. Dans un second temps, un troisième écho est acquis, avec un TE proche de l'un des deux échos précédents, afin de mesurer un spectre fréquentiel large.

Etudes cliniques

Trois études cliniques ont été réalisées au Centre Hospitalier Universitaire Henri Mondor (Créteil), en IRM du sein et du foie. En voici un résumé.

Imagerie du sein avec des points k_T en mono-canal

Le cas d'une patiente présentant un hypersignal sur une séquence T_2 de type SPACE avec une impulsion standard (rectangulaire) laisse penser à un artéfact lié aux inhomogénéités RF (figure D.6). Or, une lésion présentant un hypersignal T_2 est interprétée comme bénigne : cet artéfact, s'il était avéré, pourrait conduire à un faux négatif. Une simulation du signal SPACE à partir de la carte de champ RF et de Δf_0, en considérant un tissu

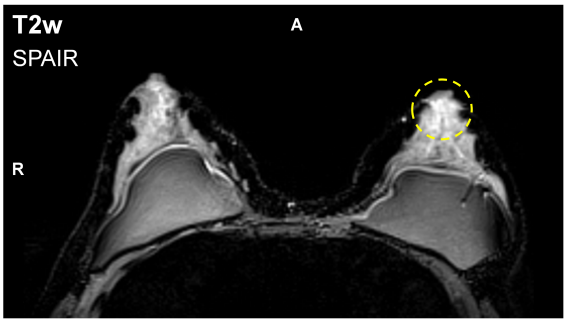

Figure D.6 : Acquisition *in vivo* T_2 SPACE avec suppression de graisse utilisant une impulsion rectangulaire standard. Présence de prothèses en silicone. On remarque un hypersignal local important dans le sein gauche (cercle), tendant à exclure un diagnostic de malignité.

mammaire uniforme en termes de T_1 et T_2 (donc en l'absence de lésion), a mis en évidence un hypersignal d'environ 13 %, lié uniquement à un dépassement de l'angle de bascule par rapport au reste du champ de vue. Une impulsion points k_T a été conçue pour tenter d'homogénéiser l'angle de bascule, sachant que le système utilisé – Siemens MAGNETOM Verio – ne possédait qu'un seul canal de transmission, donc ne proposait pas de *shim* RF statique adapté au patient : l'hypersignal n'était que de 4 % avec les points k_T. En termes de NRMSE, l'impulsion rectangulaire se situait à 18.6 %, contre 10.7 % pour les points k_T. Cependant, certains « points chauds » d'angle de bascule subsistaient par endroits.

Une étude a par la suite été menée sur 27 patientes consécutives afin de déterminer s'il s'agissait d'un cas récurrent ou isolé, et de déterminer l'impact des points k_T pour résoudre ce problème. Seules quelques patientes présentaient des inhomogénéités visibles, malgré une littérature assez alarmiste quand aux problèmes de transmission RF dans le sein. D'une part, assez peu de sujets présentaient des seins denses, c'est-à-dire comprenant beaucoup de glande mammaire ; or la graisse tend à atténuer les inhomogénéités de RF. D'autre part, le système utilisé dans cette étude utilise la technologie dite *TrueForm*, qui consiste à transmettre la RF selon un mode elliptique prédéfini au lieu du traditionnel mode CP, généralement rencontré dans la littérature. Il s'avère que les paramètres de *TrueForm* sont bien adaptés à l'imagerie du sein dans la plupart des cas. Certaines patientes présentaient toutefois une NRMSE relativement élevée, mais les points k_T, en monocanal, ne parvenaient pas à l'améliorer nettement.

Les deux études qui suivent ont quant à elles été réalisées sur un imageur plus moderne – Siemens MAGNETOM Skyra pTx – équipé de deux canaux de transmission, permettant donc de mettre en concurrence les points k_T avec un *shim* RF statique personnalisé.

Imagerie du foie avec des points k_T en transmission parallèle à deux canaux

L'acquisition de cartes de champ RF et statiques de l'abdomen sur 50 patients consécutifs a permis de comparer quantitativement, en simulation, les performances du *shim* RF statique et des points k_T, tous deux personnalisés pour chaque sujet. Pour vingt de ces patients, une comparaison qualitative a pu être réalisée par deux radiologues, indépendamment, à partir

d'images obtenues au cours d'un examen DCE (*dynamic contrast-enhanced imaging*). Pour les deux techniques, des images ont été acquises avant injection et en phase tardive, en employant exactement la même séquence (notamment angle de bascule, TE et TR) : seul l'impulsion RF différait.

Dans le cas du *shim* RF statique, les coefficients RF sur les deux canaux ont été calculés automatiquement par le scanner ; les points k_T ont quant à eux été optimisés sur un ordinateur hors ligne.

La comparaison qualitative a fait ressortir un gain systématique en termes de NRMSE avec les points k_T, et en particulier pour certains sujets « difficiles ». C'est le cas par exemple des patients présentant de l'ascite (*cf.* figure D.2b). En moyenne, la NRMSE offerte par le *shim* RF statique était de $(20.7 \pm 9.8)\,\%$, contre $(8.5 \pm 1.5)\,\%$ pour les points k_T : la NRMSE est généralement meilleure, et la variabilité réduite à l'échelle de la population observée.

D'un point de vue qualitatif, les points k_T ont surpassé le *shim* RF statique en contraste T_1, qualité du rehaussement de contraste, détail des structures et confiance générale dans l'image. En particulier, seuls 55 % des patients scannés ont reçu un examen de bonne qualité générale (*i.e.* noté au moins 2/3) avec le *shim* RF statique, contre 85 % avec les points k_T.

On peut conclure que les points k_T permettent d'obtenir des images au moins équivalentes en qualité comme le montre la figure D.7a dans le cas d'un patient « standard », tout en permettant de rendre exploitables les examens très difficiles, comme sur la figure D.7b.

Approche par apprentissage automatique pour utiliser des points k_T en IRM du corps sans calibration

Enfin, dans une dernière étude, nous avons présenté une nouvelle technique, dénommée *SmartPulse*, qui s'appuie sur la méthode des pulses universels, présentée plus haut, et l'étend à l'imagerie du corps où la variabilité morphologique est plus importante que dans le cerveau, et où une impulsion unique ne fonctionne pas pour toute la population.

A partir des cartes de champ acquises sur les 50 sujets de l'étude précédente, nous avons pu séparer la population en trois groupes. Pour cela, nous avons simulé l'effet de chaque impulsion points k_T personnalisée (une par sujet) sur chacun des sujets (soit 2500 simulations) : l'impulsion conçue pour un patient donné pouvait donner de bons résultats sur certains, et une mauvaise homogénéité chez d'autres. Pour chacun des trois groupes ainsi déterminés, une impulsion universelle de type points k_T a été optimisée, qui permette d'obtenir une homogénéité d'angle de bascule aussi bonne que possible chez tous les sujets du groupe. L'étape suivante a été d'entraîner un algorithme d'apprentissage automatique à classifier un nouveau sujet dans le groupe qui lui correspond le mieux, afin de lui attribuer l'impulsion points k_T qui permette la meilleure homogénéité, et ce à partir de données morphologiques et d'informations de base (taille poids, âge, ...) obtenues à partir d'une simple séquence de *localizer*, jouée systématiquement au début de tout protocole. Cet algorithme a été entraîné sur les 50 sujets initiaux ainsi que sur 30 sujets supplémentaires.

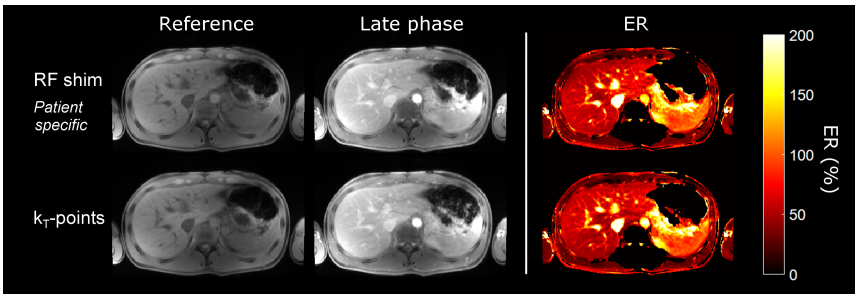

(a) Sujet standard, sans inhomogénéité RF *a priori* : les deux techniques sont équivalentes.

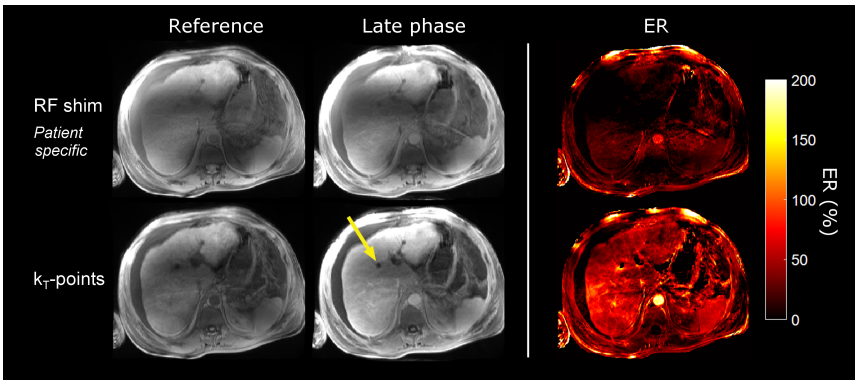

(b) Sujet difficile, avec de l'ascite : l'image en *shim* RF statique est très marquée par l'artéfact de champ RF (ombrage, perte de contraste), contrairement avec celle en points k_T.

Figure D.7 : De gauche à droite : images pré-injection, post-injection et taux de rehaussement obtenues, pour chaque sujet, avec un *shim* RF statique (rangée du haut) et des points k_T (en bas), pour un patient « standard » et un présentant de l'ascite.

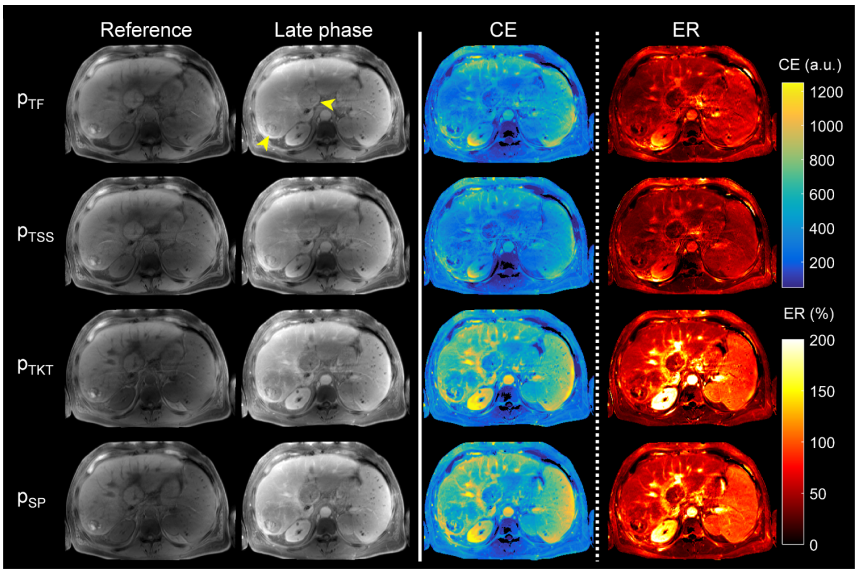

Figure D.8 : De gauche à droite : images pré-injection, post-injection, de rehaussement et de taux de rehaussement obtenues, de haut en bas, avec *TrueForm* (p_{TF}), un *shim* RF statique personnalisé (p_{TSS}), des points k_T personnalisés (p_{TKT}), et *SmartPulse* (p_{SP}), pour un patient « difficile ».

L'efficacité de cette méthode a été testée sur 53 patients consécutifs par simulation d'homogénéité d'angle de bascule, et des images ont pu être acquises chez 23 de ces patients. La figure D.8 montre un exemple de ces acquisitions. Différentes techniques d'impulsion ont été comparées : *TrueForm*, l'impulsion standard « universelle » du constructeur (avec les mêmes coefficients RF prédéterminés que ceux utilisés sur le scanner Verio), le *shim* RF statique personnalisé optimisé par le scanner, des points k_T personnalisés et *SmartPulse*. Sur cet exemple, l'acquisition avec *SmartPulse* est bien meilleure qu'avec *TrueForm* et même qu'avec le *shim* RF statique personnalisé, et très proche de celle avec les points k_T personnalisés. Pourtant, aucune calibration particulière n'a été requise – ni carte de champ, ni optimisation d'impulsion – ce qui est tout à fait appréciable en clinique, où le temps est précieux.

SmartPulse a réussi à attribuer l'impulsion points k_T optimale, parmi les trois possibles, chez 87 % des sujets de test, offrant des résultats d'homogénéité généralement meilleurs qu'avec les techniques de *shim* RF statique. L'effet s'est avéré particulièrement convaincant pour les sujets les plus difficiles (comme celui de la figure D.8), pour lesquels le *shim* statique montre vraiment ses limites.

Conclusion

Par ces travaux de thèse, nous espérons donner un nouveau souffle à la gestion des inhomogénéités RF en routine clinique à 3 T, en convainquant les industriels de l'intérêt pratique de la méthode des points k_T par rapport aux techniques de *shim* RF statique, ce d'autant plus qu'aucun élément matériel additionnel n'est nécessaire.

Nous nous sommes ici attachés exclusivement aux points k_T, qui permettent une excitation non sélective. Afin d'améliorer l'homogénéité de l'excitation dans l'intégralité des protocoles cliniques, dans lesquels les séquences 2D sont nombreuses, il faudra également démontrer l'applicabilité de méthodes de *shim* RF dynamique adaptées à la sélection de coupe, comme les *fast-k_z spokes*.

Enfin, Siemens a récemment mis sur le marché un imageur clinique à 7 T, le MAGNETOM Terra, agréé CE (Conformité Européenne) et FDA (*Food and Drug Administration* américaine). Si l'utilisation de ce scanner en pTx est possible, avec huit canaux d'émission, elle reste à ce jour réservée à la recherche, les applications cliniques étant cantonnées au mono-canal. On peut néanmoins envisager une autorisation de la pTx dans les années à venir, ouvrant la porte à des applications cliniques d'IRM du corps à ultra-haut champ. Dans ce cas, il est à craindre que le *shim* RF statique, même avec huit canaux, ne sera pas suffisant pour obtenir une bonne homogénéité d'excitation, notamment dans l'abdomen. La méthode *SmartPulse* pourrait alors permettre de réaliser des examens de qualité tout en évitant la perte de temps et la complexité que constitue la calibration généralement associée au *shim* RF statique comme aux points k_T.

* * *
* *
*

Publications

Articles in Peer-Reviewed Journals

Raphaël Tomi-Tricot, Vincent Gras, Bertrand Thirion, Franck Mauconduit, Nicolas Boulant, Hamza Cherkaoui, Pierre Zerbib, Alexandre Vignaud, Alain Luciani, Alexis Amadon. *SmartPulse, a Machine Learning Approach for Calibration-Free Dynamic RF Shimming: Preliminary Study in a Clinical Environment.* Magnetic Resonance in Medicine. Submitted.

Vincent Gras, Benedikt A. Poser, Xiaoping Wu, **Raphaël Tomi-Tricot** and Nicolas Boulant. *Improving Human Connectome Project Style Resting-State fMRI at 7 Tesla Using Calibration-Free Parallel Transmit Universal Pulses.* NeuroImage. Submitted.

Raphaël Tomi-Tricot, Vincent Gras, Franck Mauconduit, François Legou, Nicolas Boulant, Matthias Gebhardt, Dieter Ritter, Berthold Kiefer, Pierre Zerbib, Alain Rahmouni, Alexandre Vignaud, Alain Luciani and Alexis Amadon. *B_1 Artifact Reduction in Abdominal DCE-MRI Using k_T-points: First Clinical Assessment of Dynamic RF Shimming at* 3 T. Journal of Magnetic Resonance Imaging, vol. 47, no. 6, pp. 1562-1571, 2018.

Abstracts Presented at International Conferences with Reading Committee and Proceedings

Raphaël Tomi-Tricot, Vincent Gras, Franck Mauconduit, François Legou, Nicolas Boulant, Matthias Gebhardt, Dieter Ritter, Berthold Kiefer, Pierre Zerbib, Alain Rahmouni, Alexandre Vignaud, Alain Luciani and Alexis Amadon. *K_T-Points Pulses Reduce B_1 Shading at* 3 T*: Demonstration in Routine Abdominal DCE-MRI and Evaluation of Reliability.* Proceedings of the 26th Annual Meeting of the International Society for Magnetic Resonance in Medicine, Paris, France, 2018. Poster.

Raphaël Tomi-Tricot, Vincent Gras, Thu Ha Dao, Antoine Perrot, Franck Mauconduit, Nicolas Boulant, Pierre Zerbib, Alain Rahmouni, Alexandre Vignaud, Alain Luciani and Alexis Amadon. *RF-Induced Potential False-Negative Lesion in Breast T_2-Weighted MRI at* 3 T*: Exploration of a Single-Channel k_T-Points Solution.* Proceedings of the 26th Annual Meeting of the International Society for Magnetic Resonance in Medicine, Paris, France, 2018. ePoster.

Gaël Saïb, **Raphaël Tomi-Tricot**, Vincent Gras, Franck Mauconduit, Nicolas Boulant, Alexandre Vignaud, Michel Luong, Eric Giacomini, Edouard Chazel, Denis Le Bihan, Laurent Le Brusquet and Alexis Amadon. *Z-Segmentation of a Transmit Array Head Coil Improves RF Ramp Pulse Design at* 7 T. Proceedings of the 26th Annual Meeting of the International Society for Magnetic Resonance in Medicine, Paris, France, 2018. ePoster.

Raphaël Tomi-Tricot, Vincent Gras, Franck Mauconduit, François Legou, Nicolas Boulant, Matthias Gebhardt, Dieter Ritter, Berthold Kiefer, Pierre Zerbib, Alain Rahmouni, Alexandre Vignaud, Alain Luciani and Alexis Amadon. *First Clinical Assessment of k_T-Points Dynamic RF Shimming on Abdominal DCE-MRI in a Commercial* 3 T *MRI Scanner.* Proceedings of the 103rd Annual Meeting of the Radiological Society of North America, Chicago, IL, USA, 2017. Oral and ePoster.

Raphaël Tomi-Tricot, Vincent Gras, Franck Mauconduit, Nicolas Boulant, Pierre Zerbib, Alain Rahmouni, Alexandre Vignaud, Alain Luciani and Alexis Amadon. *SAR-Constrained k_T-Points Pulse Design Applied to B_1 Inhomogeneity Mitigation in the Human Abdomen at* 3 T. Proceedings of the 25th Annual Meeting of the International Society for Magnetic Resonance in Medicine, Honolulu, HI, USA, 2018. ePoster.

Raphaël Tomi-Tricot, Vincent Gras, Nicolas Boulant, Alexandre Vignaud and Alexis Amadon. *K_T-Points Pulse Design at* 7 T*: Optimization of Pulse and Sub-Pulse Durations.* Proceedings of the 33rd Annual Meeting of the European Society for Magnetic Resonance in Medicine and Biology, Vienna, Austria, 2016. Oral and ePoster.

Patent

Raphaël Tomi-Tricot, Bertrand Thirion, Vincent Gras, Alexis Amadon, Nicolas Boulant, Alexandre Vignaud. *A Computer-Implemented Method of Building a Database of Pulse Sequences for Magnetic Resonance Imaging, and a Method of Performing Magnetic Resonance Imaging Using Such a Database*, no. EP18305909, July 2018. Pending.

Bibliography

[Aickin 1996] M. Aickin and H. Gensler. *Adjusting for multiple testing when reporting research results: the Bonferroni vs Holm methods.* American journal of public health, vol. 86, no. 5, pages 726–728, 1996. (Cited on page 111.)

[Amadon 2008] A. Amadon and N. Boulant. *Simultaneous measurement of Bo-and B1-maps with modified Actual Flip Angle Imaging sequence.* In Proc ISMRM, page 1248, 2008. (Cited on pages 65 and 66.)

[Amadon 2010] A. Amadon, N. Boulant, M. A. Cloos, E. Giacomini, C. J. Wiggins, M. Luong, G. Ferrand and H. P. Fautz. *B1-mapping of an 8-channel TX-array over a human-head-like volume in less than 2 minutes: The XEP sequence.* In Proc. Intl. Soc. Mag. Reson. Med, volume 18, page 2828, 2010. (Cited on page 65.)

[Amadon 2011] A. Amadon and M. A. Cloos. *Method and apparatus for compensating for B1 inhomogeneity in magnetic resonance imaging by nonselective tailored RF pulses*, no. WO2011/128847A1, October 2011. (Cited on pages 63 and 72.)

[Amadon 2012] A. Amadon, M. A. Cloos, N. Boulant, M.-F. Hang, C. J. Wiggins and H.-P. Fautz. *Validation of a very fast B1-mapping sequence for parallel transmission on a human brain at 7T.* In Proceedings of the 20th Annual Meeting of ISMRM, Melbourne, Australia, page 3358, 2012. (Cited on page 65.)

[Amadon 2013] A. Amadon, A. Vignaud, A. Massire, M. Bottlaender and N. Boulant. *Is a 2D-spiral excitation trajectory sufficient for 3D Inner Volume Imaging?* In Proc. Intl. Soc. Magn. Reson. Med, page 4251, 2013. (Cited on page 62.)

[Azlan 2010] C. A. Azlan, P. Di Giovanni, T. S. Ahearn, S. I. Semple, F. J. Gilbert and T. W. Redpath. *B1 transmission-field inhomogeneity and enhancement ratio errors in dynamic contrast-enhanced MRI (DCE-MRI) of the breast at 3T.* Journal of Magnetic Resonance Imaging, vol. 31, no. 1, pages 234–239, January 2010. (Cited on page 94.)

[Beqiri 2017] A. Beqiri, A. N. Price, F. Padormo, J. V. Hajnal and S. J. Malik. *Extended RF shimming: Sequence-level parallel transmission optimization applied to steady-*

state free precession MRI of the heart. NMR in Biomedicine, vol. 30, no. 6, page e3701, 2017. (Cited on page 63.)

[Beqiri 2018] A. Beqiri, H. Hoogduin, A. Sbrizzi, J. V. Hajnal and S. J. Malik. *Whole-brain 3D FLAIR at 7T using direct signal control.* Magnetic Resonance in Medicine, vol. 0, no. 0, February 2018. (Cited on pages 63 and 79.)

[Bernstein 2004] M. A. Bernstein, K. F. King and X. J. Zhou. Handbook of MRI pulse sequences. Elsevier, 2004. (Cited on pages 6, 11, 21, and 35.)

[Bernstein 2006] M. A. Bernstein, J. Huston and H. A. Ward. *Imaging artifacts at 3.0T.* Journal of Magnetic Resonance Imaging, vol. 24, no. 4, pages 735–746, 2006. (Cited on pages 52, 55, and 113.)

[Bieri 2013] O. Bieri and K. Scheffler. *Fundamentals of balanced steady state free precession MRI.* Journal of Magnetic Resonance Imaging, vol. 38, no. 1, pages 2–11, July 2013. (Cited on page 17.)

[Birkefeld 2003] A. B. Birkefeld, R. Bertermann, H. Eckert and B. Pfleiderer. *Liquid- and solid-state high-resolution NMR methods for the investigation of aging processes of silicone breast implants.* Biomaterials, vol. 24, no. 1, pages 35–46, January 2003. (Cited on page 37.)

[Bloch 1946] F. Bloch. *Nuclear Induction.* Physical Review, vol. 70, no. 7-8, pages 460–474, October 1946. (Cited on pages 7 and 11.)

[Bottomley 1984] P. A. Bottomley, T. H. Foster, R. E. Argersinger and L. M. Pfeifer. *A review of normal tissue hydrogen NMR relaxation times and relaxation mechanisms from 1–100 MHz: Dependence on tissue type, NMR frequency, temperature, species, excision, and age.* Medical Physics, vol. 11, no. 4, pages 425–448, July 1984. (Cited on pages 16 and 27.)

[Boulant 2010] N. Boulant, M. Cloos and A. Amadon. *A simple and analytical way to correct for DB0 inhomogeneity in the evaluation of B1 maps relying on flip angle measurements and non-selective square pulses.* Proc. Intl. Soc. Mag. Reson. Med. Stockholm, Sweden, page 4918, 2010. (Cited on page 65.)

[Boulant 2012] N. Boulant and D. I. Hoult. *High tip angle approximation based on a modified Bloch–Riccati equation.* Magnetic Resonance in Medicine, vol. 67, no. 2, pages 339–343, 2012. (Cited on pages 60 and 61.)

[Boulant 2016] N. Boulant, X. Wu, G. Adriany, S. Schmitter, K. Uğurbil and P.-F. Van de Moortele. *Direct control of the temperature rise in parallel transmission via temperature virtual observation points: simulations at 10.5 T.* Magnetic resonance in medicine, vol. 75, no. 1, pages 249–256, January 2016. (Cited on page 68.)

[Brant-Zawadzki 1992] M. Brant-Zawadzki, G. D. Gillan and W. R. Nitz. *MP RAGE: a three-dimensional, T1-weighted, gradient-echo sequence–initial experience in the brain.* Radiology, vol. 182, no. 3, pages 769–775, March 1992. (Cited on page 49.)

[Breiman 1984] L. Breiman, J. Friedman, R. Olshen and C. Stone. *Classification and Regression Trees, 1984: Belmont.* CA: Wadsworth International Group, 1984. (Cited on page 123.)

[Breuer 2004] F. A. Breuer, M. Blaimer, M. M. Müller, R. M. Heidemann, M. A. Griswold and P. M. Jakob. *Controlled aliasing in parallel imaging.* 2004. (Cited on page 45.)

[Brink 2015a] W. M. Brink, V. Gulani and A. G. Webb. *Clinical applications of dual-channel transmit MRI: A review.* Journal of Magnetic Resonance Imaging, vol. 42, no. 4, pages 855–869, 2015. (Cited on page 53.)

[Brink 2015b] W. M. Brink, M. J. Versluis, J. M. Peeters, P. Börnert and A. G. Webb. *Passive radiofrequency shimming in the thighs at 3 Tesla using high permittivity materials and body coil receive uniformity correction.* Magnetic Resonance in Medicine, vol. 76, no. 6, pages 1951–1956, December 2015. (Cited on page 56.)

[Brunheim 2018] S. Brunheim, M. Gratz, S. Johst, A. K. Bitz, T. M. Fiedler, M. E. Ladd, H. H. Quick and S. Orzada. *Fast and accurate multi-channel B1+ mapping based on the TIAMO technique for 7T UHF body MRI.* Magnetic Resonance in Medicine, vol. 79, no. 5, pages 2652–2664, May 2018. (Cited on page 60.)

[Busse 2006] R. F. Busse, H. Hariharan, A. Vu and J. H. Brittain. *Fast spin echo sequences with very long echo trains: Design of variable refocusing flip angle schedules and generation of clinical T2 contrast.* Magnetic Resonance in Medicine, vol. 55, no. 5, pages 1030–1037, May 2006. (Cited on page 26.)

[Bydder 1985] G. M. Bydder and I. R. Young. *MR imaging: clinical use of the inversion recovery sequence.* Journal of Computer Assisted Tomography, vol. 9, no. 4, pages 659–675, August 1985. (Cited on pages 34 and 49.)

[Carr 1954] H. Y. Carr and E. M. Purcell. *Effects of diffusion on free precession in nuclear magnetic resonance experiments.* Physical review, vol. 94, no. 3, page 630, 1954. (Cited on page 23.)

[Chavez 2002] S. Chavez, Q.-S. Xiang and L. An. *Understanding phase maps in MRI: a new cutline phase unwrapping method.* IEEE Transactions on Medical Imaging, vol. 21, no. 8, pages 966–977, August 2002. (Cited on page 66.)

[Childs 2013] A. S. Childs, S. J. Malik, D. P. O'Regan and J. V. Hajnal. *Impact of number of channels on RF shimming at 3T.* Magma (New York, N.y.), vol. 26, no. 4, pages 401–410, 2013. (Cited on page 54.)

[Christ 2010] A. Christ, W. Kainz, E. G. Hahn, K. Honegger, M. Zefferer, Esra Neufeld, W. Rascher, R. Janka, W. Bautz, J. Chen, B. Kiefer, P. Schmitt, Hans-Peter Hollenbach, J. Shen, M. Oberle, D. Szczerba, A. Kam, J. W. Guag and N. Kuster. *The Virtual Family—development of surface-based anatomical models of two adults and two children for dosimetric simulations.* Physics in Medicine & Biology, vol. 55, no. 2, page N23, 2010. (Cited on pages 70 and 71.)

[Chung 2010] S. Chung, D. Kim, E. Breton and L. Axel. *Rapid B1+ mapping using a preconditioning RF pulse with TurboFLASH readout.* Magnetic Resonance in Medicine, vol. 64, no. 2, pages 439–446, 2010. (Cited on page 65.)

[Ciobanu 2012] L. Ciobanu, O. Reynaud, L. Uhrig, B. Jarraya and D. L. Bihan. *Effects of Anesthetic Agents on Brain Blood Oxygenation Level Revealed with Ultra-High Field MRI.* PLOS ONE, vol. 7, no. 3, page e32645, March 2012. (Cited on page 47.)

[Cloos 2010] M. A. Cloos, N. Boulant, M. Luong, G. Ferrand, C. J. Wiggins, E. Giacomini, A. France, D. Le Bihan and A. Amadon. *Kt points: Fast Three-Dimensional Tailored RF Pulses for flip-angle homogenization over an extended volume.* In Proceedings of the 18th Annual Meeting of ISMRM, Stockholm, Sweden, page 102, 2010. (Cited on pages 63 and 72.)

[Cloos 2012a] M. A. Cloos, N. Boulant, M. Luong, G. Ferrand, E. Giacomini, D. Le Bihan and A. Amadon. *kT-points: Short three-dimensional tailored RF pulses for flip-angle homogenization over an extended volume.* Magnetic Resonance in Medicine, vol. 67, no. 1, pages 72–80, January 2012. (Cited on pages 78 and 117.)

[Cloos 2012b] M. Cloos, N. Boulant, M. Luong, G. Ferrand, E. Giacomini, M.-F. Hang, C. Wiggins, D. Le Bihan and A. Amadon. *Parallel-transmission-enabled magnetization-prepared rapid gradient-echo T1-weighted imaging of the human brain at 7T.* NeuroImage, vol. 62, no. 3, pages 2140–2150, September 2012. (Cited on pages 78 and 79.)

[Cloos 2012c] M. A. H. Cloos. *Parallel transmission for magnetic resonance imaging of the human brain at ultra high field : specific absorption rate control & flip-angle homogenization.* phdthesis, Université Paris Sud - Paris XI, April 2012. (Cited on pages 54 and 62.)

[Collins 2004] C. M. Collins, W. Liu, J. Wang, R. Gruetter, J. T. Vaughan, K. Ugurbil and M. B. Smith. *Temperature and SAR calculations for a human head within volume and surface coils at 64 and 300 MHz.* Journal of Magnetic Resonance Imaging, vol. 19, no. 5, pages 650–656, 2004. (Cited on page 52.)

[Collins 2005] C. M. Collins, W. Liu, W. Schreiber, Q. X. Yang and M. B. Smith. *Central brightening due to constructive interference with, without, and despite dielectric*

resonance. Journal of Magnetic Resonance Imaging, vol. 21, no. 2, pages 192–196, 2005. (Cited on page 55.)

[Collins 2006] C. Collins, P. Robitaille and L. Berliner. *Ultra high field magnetic resonance imaging*. 2006. (Cited on page 45.)

[Cortes 1995] C. Cortes and V. Vapnik. *Support-vector networks*. Machine Learning, vol. 20, no. 3, pages 273–297, September 1995. (Cited on pages 123 and 130.)

[Coste 2017] A. Coste. *Methodological Developments for Sodium, Phosphorus and Lithium MRI at high magnetic field : Applications to clinical research at 3 and 7 Tesla*. PhD thesis, 2017. (Cited on page 7.)

[Curtis 2011] A. T. Curtis, K. M. Gilbert, L. M. Klassen, J. S. Gati and R. S. Menon. *Slice-by-slice B1+ shimming at 7 T*. Magnetic Resonance in Medicine, vol. 68, no. 4, pages 1109–1116, 2011. (Cited on page 79.)

[Del Grande 2014] F. Del Grande, F. Santini, D. A. Herzka, M. R. Aro, C. W. Dean, G. E. Gold and J. A. Carrino. *Fat-Suppression Techniques for 3-T MR Imaging of the Musculoskeletal System*. RadioGraphics, vol. 34, no. 1, pages 217–233, January 2014. (Cited on pages 31 and 35.)

[Deniz 2015] C. Deniz M., L. Alon, R. Brown and Y. Zhu. *Subject- and resource-specific monitoring and proactive management of parallel radiofrequency transmission*. Magnetic Resonance in Medicine, vol. 76, no. 1, pages 20–31, July 2015. (Cited on page 79.)

[Dixon 1984] W. T. Dixon. *Simple proton spectroscopic imaging*. Radiology, vol. 153, no. 1, pages 189–194, October 1984. (Cited on pages 32, 96, and 116.)

[Donato 2017] H. Donato, M. França, I. Candelária and F. Caseiro-Alves. *Liver MRI: From basic protocol to advanced techniques*. European Journal of Radiology, vol. 93, pages 30–39, August 2017. (Cited on page 55.)

[Drake 2009] R. Drake, A. W. Vogl and A. W. Mitchell. Gray's Anatomy for Students E-Book. Elsevier Health Sciences, 2009. (Cited on pages 36 and 40.)

[Décorps 2012] M. Décorps. Imagerie de résonance magnétique. EDP Sciences, December 2012. (Cited on page 9.)

[ECHA 2015] ECHA. *Guidance on the Application of the CLP Criteria; Guidance to Regulation (EC) No 1272/2008 on classification, labelling and packaging (CLP) of substances and mixtures*. 2015. (Cited on page 56.)

[Eggenschwiler 2014] F. Eggenschwiler, K. R. O'Brien, R. Gruetter and J. P. Marques. *Improving T_2 -weighted imaging at high field through the use of k_T -points: k_T -Pointing T_2 -Weighted Images at 7 T*. Magnetic Resonance in Medicine, vol. 71, no. 4, pages 1478–1488, April 2014. (Cited on pages 77 and 78.)

[Eggenschwiler 2016] F. Eggenschwiler, K. R. O'Brien, D. Gallichan, R. Gruetter and J. P. Marques. *3D T 2-weighted imaging at 7T using dynamic kT-points on single-transmit MRI systems.* Magnetic Resonance Materials in Physics, Biology and Medicine, vol. 29, no. 3, pages 347–358, June 2016. (Cited on pages 78, 118, and 140.)

[Ehman 1989] R. L. Ehman and J. P. Felmlee. *Adaptive technique for high-definition MR imaging of moving structures.* Radiology, vol. 173, no. 1, pages 255–263, 1989. (Cited on page 39.)

[Eichfelder 2011] G. Eichfelder and M. Gebhardt. *Local specific absorption rate control for parallel transmission by virtual observation points.* Magnetic Resonance in Medicine, vol. 66, no. 5, pages 1468–1476, November 2011. (Cited on pages 67, 110, and 127.)

[Elster 1993] A. D. Elster. *Gradient-echo MR imaging: techniques and acronyms.* Radiology, vol. 186, no. 1, pages 1–8, 1993. (Cited on page 17.)

[Ernst 1966] R. R. Ernst and W. A. Anderson. *Application of Fourier Transform Spectroscopy to Magnetic Resonance.* Review of Scientific Instruments, vol. 37, no. 1, pages 93–102, January 1966. (Cited on page 20.)

[Ester 1996] M. Ester, H.-P. Kriegel, J. Sander, X. Xu and others. *A density-based algorithm for discovering clusters in large spatial databases with noise.* In Kdd, volume 96, pages 226–231, 1996. (Cited on page 122.)

[Fautz 2008] H. P. Fautz, M. Vogel, P. Gross, A. Kerr and Y. Zhu. *B1 mapping of coil arrays for parallel transmission.* In Proceedings of the 16th Annual Meeting of ISMRM, Toronto, Canada, page 1247, 2008. (Cited on pages 65 and 95.)

[Feinberg 1985] D. Feinberg, C. Mills, J. Posin, D. Ortendahl, N. Hylton, L. Crooks, J. Watts, L. Kaufman, M. Arakawa and J. Hoenninger. *Multiple spin-echo magnetic resonance imaging.* Radiology, vol. 155, no. 2, pages 437–442, 1985. (Cited on page 21.)

[Feiweier 2009] T. Feiweier, P. Heubes and T. Speckner. *Method and magnetic resonance system for adjustment of the field strength of rf pulses*, August 2009. (Cited on page 130.)

[Feng 2016] L. Feng, L. Axel, H. Chandarana, K. T. Block, D. K. Sodickson and R. Otazo. *XD-GRASP: Golden-angle radial MRI with reconstruction of extra motion-state dimensions using compressed sensing.* Magnetic Resonance in Medicine, vol. 75, no. 2, pages 775–788, February 2016. (Cited on page 116.)

[Fiedler 2017] T. Fiedler, M. Ladd and A. Bitz. *RF safety assessment of a 32-channel integrated body coil for 7 Tesla: Thermal dose evaluation at high SAR level.* In

Proceedings of the 25th Annual Meeting of ISMRM, page 5577, Honolulu, HI, USA, 2017. (Cited on page 68.)

[Frahm 1986] J. Frahm, A. Haase and D. Matthaei. *Rapid NMR imaging of dynamic processes using the FLASH technique.* Magnetic Resonance in Medicine, vol. 3, no. 2, pages 321–327, 1986. (Cited on page 16.)

[Frahm 1987] J. Frahm, W. Hanicke and K.-D. Merboldt. *Transverse coherence in rapid FLASH NMR imaging.* Journal of Magnetic Resonance, vol. 72, no. 2, pages 307–314, 1987. (Cited on page 17.)

[Franklin 2008] K. Franklin M., B. Dale M. and E. Merkle M. *Improvement in B1-inhomogeneity artifacts in the abdomen at 3T MR imaging using a radiofrequency cushion.* Journal of Magnetic Resonance Imaging, vol. 27, no. 6, pages 1443–1447, May 2008. (Cited on page 57.)

[Gabriel 1996] C. Gabriel, S. Gabriel and E. Corthout. *The dielectric properties of biological tissues: I. Literature survey.* Physics in Medicine and Biology, vol. 41, no. 11, pages 2231–2249, November 1996. (Cited on page 52.)

[Garwood 2001] M. Garwood and L. DelaBarre. *The Return of the Frequency Sweep: Designing Adiabatic Pulses for Contemporary NMR.* Journal of Magnetic Resonance, vol. 153, no. 2, pages 155–177, December 2001. (Cited on page 56.)

[Gemert 2017] J. H. F. v. Gemert, W. M. Brink, A. G. Webb and R. F. Remis. *Designing High-Permittivity Pads for Dielectric Shimming in MRI using Model Order Reduction and Gauss-Newton Optimization.* In 2017 International Conference on Electromagnetics in Advanced Applications (ICEAA), pages 417–420, September 2017. (Cited on page 57.)

[Geppert 2008] C. Geppert, J. Nistler, W. Renz, I. Panagiotelis and T. Speckner. *Reduced B1-inhomogeneities in breast MRI using optimized RF excitation.* In Proc. ISMRM, volume 2726, 2008. (Cited on pages 101 and 102.)

[Geurts 2006] P. Geurts, D. Ernst and L. Wehenkel. *Extremely randomized trees.* Machine Learning, vol. 63, no. 1, pages 3–42, April 2006. (Cited on page 130.)

[Glover 1991] G. H. Glover and E. Schneider. *Three-point Dixon technique for true water/fat decomposition with Bo inhomogeneity correction.* Magnetic Resonance in Medicine, vol. 18, no. 2, pages 371–383, April 1991. (Cited on page 33.)

[Gold 2004] G. E. Gold, E. Han, J. Stainsby, G. Wright, J. Brittain and C. Beaulieu. *Musculoskeletal MRI at 3.0 T: relaxation times and image contrast.* American Journal of Roentgenology, vol. 183, no. 2, pages 343–351, 2004. (Cited on page 48.)

[Goldfarb 2017] J. W. Goldfarb. *Separation of Water and Fat Magnetic Resonance Imaging Signals Using Deep Learning with Convolutional Neural Networks.* arXiv:1711.00107 [cs], October 2017. arXiv: 1711.00107. (Cited on page 123.)

[Goshima 2009] S. Goshima, M. Kanematsu, H. Kondo, Y. Shiratori, M. Onozuka, N. Moriyama and K. T. Bae. *Optimal Acquisition Delay for Dynamic Contrast-Enhanced MRI of Hypervascular Hepatocellular Carcinoma.* American Journal of Roentgenology, vol. 192, no. 3, pages 686–692, March 2009. (Cited on page 43.)

[Gosselin 2014] M.-C. Gosselin, E. Neufeld, H. Moser, E. Huber, S. Farcito, L. Gerber, Maria Jedensjö, I. Hilber, F. D. Gennaro, B. Lloyd, E. Cherubini, D. Szczerba, Wolfgang Kainz and N. Kuster. *Development of a new generation of high-resolution anatomical models for medical device evaluation: the Virtual Population 3.0.* Physics in Medicine & Biology, vol. 59, no. 18, page 5287, 2014. (Cited on pages 70 and 71.)

[Graesslin 2012] I. Graesslin, H. Homann, S. Biederer, P. Börnert, K. Nehrke, P. Vernickel, G. Mens, P. Harvey and U. Katscher. *A specific absorption rate prediction concept for parallel transmission MR.* Magnetic Resonance in Medicine, vol. 68, no. 5, pages 1664–1674, November 2012. (Cited on page 67.)

[Gras 2015] V. Gras, M. Luong, A. Amadon and N. Boulant. *Joint design of kT-points trajectories and RF pulses under explicit SAR and power constraints in the large flip angle regime.* Journal of Magnetic Resonance, vol. 261, pages 181–189, December 2015. (Cited on pages 73, 109, and 124.)

[Gras 2017a] V. Gras, M. Boland, A. Vignaud, G. Ferrand, A. Amadon, F. Mauconduit, D. L. Bihan, T. Stöcker and N. Boulant. *Homogeneous non-selective and slice-selective parallel-transmit excitations at 7 Tesla with universal pulses: A validation study on two commercial RF coils.* PLOS ONE, vol. 12, no. 8, page e0183562, August 2017. (Cited on pages 79 and 124.)

[Gras 2017b] V. Gras, A. Vignaud, A. Amadon, D. L. Bihan and N. Boulant. *Universal pulses: A new concept for calibration-free parallel transmission.* Magnetic Resonance in Medicine, vol. 77, no. 2, pages 635–643, February 2017. (Cited on pages 79, 120, and 124.)

[Gras 2018] V. Gras, F. Mauconduit, A. Vignaud, A. Amadon, D. Le Bihan, T. Stöcker and N. Boulant. *Design of universal parallel-transmit refocusing kT -point pulses and application to 3D T2 -weighted imaging at 7T.* Magnetic Resonance in Medicine, vol. 80, no. 1, pages 53–65, July 2018. (Cited on pages 77, 79, 80, 96, and 141.)

[Grissom 2006] W. Grissom, C.-y. Yip, Z. Zhang, V. A. Stenger, J. A. Fessler and D. C. Noll. *Spatial domain method for the design of RF pulses in multicoil parallel excitation.* Magnetic Resonance in Medicine, vol. 56, no. 3, pages 620–629, September 2006. (Cited on page 63.)

[Grissom 2012] W. A. Grissom, M.-M. Khalighi, L. I. Sacolick, B. K. Rutt and M. W. Vogel. *Small-tip-angle spokes pulse design using interleaved greedy and local optimization methods.* Magnetic resonance in medicine, vol. 68, no. 5, pages 1553–1562, 2012. (Cited on pages 63 and 87.)

[Griswold 2002] M. A. Griswold, P. M. Jakob, R. M. Heidemann, M. Nittka, V. Jellus, J. Wang, B. Kiefer and A. Haase. *Generalized autocalibrating partially parallel acquisitions (GRAPPA).* Magnetic Resonance in Medicine, vol. 47, no. 6, pages 1202–1210, June 2002. (Cited on page 45.)

[Guérin 2014] B. Guérin, M. Gebhardt, P. Serano, E. Adalsteinsson, M. Hamm, J. Pfeuffer, J. Nistler and L. L. Wald. *Comparison of simulated parallel transmit body arrays at 3 T using excitation uniformity, global SAR, local SAR, and power efficiency metrics.* Magnetic Resonance in Medicine, vol. 73, no. 3, pages 1137–1150, April 2014. (Cited on page 60.)

[Haacke 1999] E. M. Haacke, R. W. Brown, M. R. Thompson and R. Venkatesan. Magnetic Resonance Imaging - Physical Principles And Sequence Design. Wiley-Liss, 1999. (Cited on pages 6, 29, and 52.)

[Haase 1985] A. Haase, J. Frahm, W. Hanicke and D. Matthaei. *1 H NMR chemical shift selective (CHESS) imaging.* Physics in Medicine and Biology, vol. 30, no. 4, page 341, 1985. (Cited on page 31.)

[Haase 1986] A. Haase, J. Frahm, D. Matthaei, W. Hanicke and K.-D. Merboldt. *FLASH imaging. Rapid NMR imaging using low flip-angle pulses.* Journal of Magnetic Resonance, vol. 67, no. 2, pages 258–266, 1986. (Cited on pages 16 and 18.)

[Hahn 1950a] E. L. Hahn. *Nuclear Induction Due to Free Larmor Precession.* Physical Review, vol. 77, no. 2, pages 297–298, January 1950. (Cited on page 10.)

[Hahn 1950b] E. L. Hahn. *Spin Echoes.* Physical Review, vol. 80, no. 4, pages 580–594, November 1950. (Cited on page 21.)

[Harris 2001] R. K. Harris, E. D. Becker, d. M. S. M. Cabral, R. Goodfellow and P. Granger. *NMR nomenclature. Nuclear spin properties and conventions for chemical shifts(IUPAC Recommendations 2001).* Pure and Applied Chemistry, vol. 73, no. 11, pages 1795–1818, 2001. (Cited on page 28.)

[Harvey 2010] R. P. Harvey, P. Cecilia and J. Simons. *B1 Shimming Performance Versus Channel/Mode Count.* In Proc Int Soc Magn Reson Med, 2010. (Cited on page 60.)

[Hastie 1996] T. Hastie and R. Tibshirani. *Discriminant adaptive nearest neighbor classification.* IEEE Transactions on Pattern Analysis and Machine Intelligence, vol. 18, no. 6, pages 607–616, June 1996. (Cited on page 123.)

[Hauger 2002] O. Hauger, E. Dumont, J.-F. Chateil, M. Moinard and F. Diard. *Water Excitation as an Alternative to Fat Saturation in MR Imaging: Preliminary Results in Musculoskeletal Imaging.* Radiology, vol. 224, no. 3, pages 657–663, September 2002. (Cited on page 32.)

[Hennig 1986] J. Hennig, A. Nauerth and H. Friedburg. *RARE imaging: A fast imaging method for clinical MR.* Magnetic Resonance in Medicine, vol. 3, no. 6, pages 823–833, 1986. (Cited on page 22.)

[Hennig 1991] J. Hennig. *Echoes—how to generate, recognize, use or avoid them in MR-imaging sequences. Part II: Echoes in imaging sequences.* Concepts in Magnetic Resonance, vol. 3, no. 4, pages 179–192, 1991. (Cited on page 26.)

[Ho 1995] T. K. Ho. *Random Decision Forests.* In Proceedings of the Third International Conference on Document Analysis and Recognition (Volume 1) - Volume 1, ICDAR '95, pages 278–, Washington, DC, USA, 1995. IEEE Computer Society. (Cited on page 123.)

[Hochman 1997] M. G. Hochman, S. G. Orel, C. M. Powell, M. D. Schnall, C. A. Reynolds and L. N. White. *Fibroadenomas: MR imaging appearances with radiologic-histopathologic correlation.* Radiology, vol. 204, no. 1, pages 123–129, July 1997. (Cited on page 94.)

[Homann 2012] H. Homann, I. Graesslin, H. Eggers, K. Nehrke, P. Vernickel, U. Katscher, O. Dössel and P. Börnert. *Local SAR management by RF Shimming: a simulation study with multiple human body models.* Magnetic Resonance Materials in Physics, Biology and Medicine, vol. 25, no. 3, pages 193–204, June 2012. (Cited on pages 70 and 71.)

[Horger 2007] W. Horger. *Fat suppression in the abdomen.* MAGNETOM Flash SIEMENS, vol. 3, pages 114–119, 2007. (Cited on page 31.)

[Hothorn 2017] T. Hothorn and K. Hornik. exactRankTests: Exact Distributions for Rank and Permutation Tests. 2017. (Cited on page 111.)

[Hoult 1997] D. I. Hoult and B. Bhakar. *NMR signal reception: Virtual photons and coherent spontaneous emission.* Concepts in Magnetic Resonance, vol. 9, no. 5, pages 277–297, 1997. (Cited on page 10.)

[Hoult 2000] D. I. Hoult. *Sensitivity and Power Deposition in a High-Field Imaging Experiment.* Journal of Magnetic Resonance Imaging, vol. 12, no. 1, pages 46–67, 2000. (Cited on page 52.)

[Hoyos-Idrobo 2014] A. Hoyos-Idrobo, P. Weiss, A. Massire, A. Amadon and N. Boulant. *On variant strategies to solve the magnitude least squares optimization problem in parallel transmission pulse design and under strict SAR and power constraints.*

IEEE Transactions on Medical Imaging, vol. 33, no. 3, pages 739–748, 2014. (Cited on pages 109 and 124.)

[Hsu 2017] Y.-C. Hsu, S. Littin, Y.-H. Chu, F.-H. Lin and M. Zaitsev. *Uniform Flip Angle 3D Tailored Excitation for MR Breast Imaging at 3T.* In Proc. Intl. Soc. Mag. Reson. Med, page 4927, Honolulu, HI, USA, 2017. (Cited on pages 94 and 118.)

[Ianni Julianna D. 2018] Ianni Julianna D., Cao Zhipeng and Grissom William A. *Machine learning RF shimming: Prediction by iteratively projected ridge regression.* Magnetic Resonance in Medicine, vol. 0, no. 0, March 2018. (Cited on page 121.)

[IEC-60601-2-33 2010] IEC-60601-2-33. *Medical electrical equipment-Part 2-33: Particular requirements for the basic safety and essential performance of magnetic resonance equipment for medical diagnosis, IEC 60601-2-33: 2010/AMD2: 2015.* Technical report, International Electrotechnical Commission, 2010. (Cited on pages 51, 69, and 70.)

[Jones 2001] E. Jones, T. Oliphant, P. Peterson and others. SciPy: Open source scientific tools for Python. 2001. (Cited on page 131.)

[Kaiser 1974] R. Kaiser, E. Bartholdi and R. R. Ernst. *Diffusion and field-gradient effects in NMR Fourier spectroscopy.* The Journal of Chemical Physics, vol. 60, no. 8, pages 2966–2979, April 1974. (Cited on page 24.)

[Kaldoudi 1993] E. Kaldoudi, S. C. Williams, G. J. Barker and P. S. Tofts. *A chemical shift selective inversion recovery sequence for fat-suppressed MRI: theory and experimental validation.* Magnetic resonance imaging, vol. 11, no. 3, pages 341–355, 1993. (Cited on page 35.)

[Katscher 2003] U. Katscher, P. Börnert, C. Leussler and J. S. van den Brink. *Transmit SENSE.* Magnetic Resonance in Medicine, vol. 49, no. 1, pages 144–150, January 2003. (Cited on page 63.)

[Kierans 2009] A. S. Kierans, P. Leonardou, F. Shaikh and R. C. Semelka. *Body MR imaging: Sequences we use and why.* Appl Radiol, vol. 38, no. 5, pages 7–12, 2009. (Cited on page 42.)

[Kohavi 1998] R. Kohavi. *Glossary of terms.* Special issue on applications of machine learning and the knowledge discovery process, vol. 30, no. 271, pages 127–132, 1998. (Cited on page 122.)

[Krizhevsky 2012] A. Krizhevsky, I. Sutskever and G. E. Hinton. *ImageNet Classification with Deep Convolutional Neural Networks.* In F. Pereira, C. J. C. Burges, L. Bottou and K. Q. Weinberger, editors, Advances in Neural Information Processing Systems 25, pages 1097–1105. Curran Associates, Inc., 2012. (Cited on page 123.)

[Kuhl 1999] C. K. Kuhl, S. Klaschik, P. Mielcarek, J. Gieseke, E. Wardelmann and H. H. Schild. *Do T2-weighted pulse sequences help with the differential diagnosis of enhancing lesions in dynamic breast MRI?* Journal of Magnetic Resonance Imaging, vol. 9, no. 2, pages 187–196, February 1999. (Cited on page 94.)

[Kuhl 2007] C. K. Kuhl, H. Kooijman, J. Gieseke and H. H. Schild. *Effect of B1 Inhomogeneity on Breast MR Imaging at 3.0 T.* Radiology, vol. 244, no. 3, pages 929–930, September 2007. (Cited on page 53.)

[Kukuk 2009] G. M. Kukuk, J. Gieseke, M. Nelles, R. König, M. Andersson, E. Muschler, P. Mürtz, J. Stout, M. Nijenhuis, F. Träber and others. *Clinical liver MRI at 3.0 Tesla using parallel RF transmission with patient-adaptive B1 shimming.* In Proc. Intl. Soc. Mag. Reson. Med, volume 17, page 119, 2009. (Cited on page 55.)

[Köhler 2011] M. O. Köhler, B. Denis de Senneville, B. Quesson, C. T. Moonen and M. Ries. *Spectrally selective pencil-beam navigator for motion compensation of MR-guided high-intensity focused ultrasound therapy of abdominal organs.* Magnetic Resonance in Medicine, vol. 66, no. 1, pages 102–111, July 2011. (Cited on page 62.)

[Lauterbur 1973] P. C. Lauterbur. *Image Formation by Induced Local Interactions: Examples Employing Nuclear Magnetic Resonance.* Nature, vol. 242, no. 5394, pages 190–191, March 1973. (Cited on page 7.)

[Le Ster 2017] C. Le Ster. *Exploration de la moelle osseuse en Imagerie par Résonance Magnétique : quantification de biomarqueurs.* PhD Thesis, Université Rennes 1, 2017. (Cited on page 29.)

[Le 2012] Y. Le, R. Kroeker, H. D. Kipfer and C. Lin. *Development and evaluation of TWIST Dixon for dynamic contrast-enhanced (DCE) MRI with improved acquisition efficiency and fat suppression.* Journal of Magnetic Resonance Imaging, vol. 36, no. 2, pages 483–491, August 2012. (Cited on pages 31, 108, and 131.)

[Leroi 2016] L. Leroi, A. Vignaud, P. Sabouroux, E. Georget, B. Larrat, S. Enoch, G. Tayeb, N. Bonod, A. Amadon, D. Le Bihan and R. Abdeddaïm. *B1+ homogenization at 7T using an innovative meta-atom.* In International Society for Magnetic Resonance in Medicine, page 3531, 2016. (Cited on page 57.)

[Levitt 1986] M. H. Levitt. *Composite pulses.* Progress in Nuclear Magnetic Resonance Spectroscopy, vol. 18, no. 2, pages 61–122, 1986. (Cited on page 32.)

[Leyendecker 2008] J. R. Leyendecker, M. Gakhal, K. M. Elsayes, R. McDermott, V. R. Narra and J. J. Brown. *Fat-suppressed dynamic and delayed gadolinium-enhanced volumetric interpolated breath-hold magnetic resonance imaging of cholangiocarcinoma.* Journal of Computer Assisted Tomography, vol. 32, no. 2, pages 178–184, April 2008. (Cited on page 108.)

[Li 2003] T. Li and S. A. Mirowitz. *Fast T2-weighted MR imaging: impact of variation in pulse sequence parameters on image quality and artifacts.* Magnetic Resonance Imaging, vol. 21, no. 7, pages 745–753, September 2003. (Cited on page 23.)

[Liney 2007] G. Liney. MRI in Clinical Practice. Springer Science & Business Media, April 2007. Google-Books-ID: xpCffxNrCXYC. (Cited on page 6.)

[Luciani 2008] A. Luciani, A. Vignaud, M. Cavet, J. Tran Van Nhieu, A. Mallat, L. Ruel, A. Laurent, J.-F. Deux, P. Brugieres and A. Rahmouni. *Liver cirrhosis: intravoxel incoherent motion MR imaging—Pilot study 1.* Radiology, vol. 249, no. 3, pages 891–899, 2008. (Cited on page 107.)

[Luciani 2017] A. Luciani and A. Rahmouni. IRM en pratique clinique: Imagerie neuroradiologique, musculosquelettique, abdominopelvienne, oncologique, hématologique, corps entier, et cardiovasculaire. Elsevier Health Sciences, September 2017. (Cited on pages 6, 8, 38, and 42.)

[Ma 2004] J. Ma. *Breath-hold water and fat imaging using a dual-echo two-point dixon technique with an efficient and robust phase-correction algorithm.* Magnetic Resonance in Medicine, vol. 52, no. 2, pages 415–419, August 2004. (Cited on pages 33 and 116.)

[Ma 2008] J. Ma. *A single-point dixon technique for fat-suppressed fast 3D gradient-echo imaging with a flexible echo time.* Journal of Magnetic Resonance Imaging, vol. 27, no. 4, pages 881–890, April 2008. (Cited on page 33.)

[MacQueen 1967] J. MacQueen and others. *Some methods for classification and analysis of multivariate observations.* In Proceedings of the fifth Berkeley symposium on mathematical statistics and probability, volume 1, pages 281–297. Oakland, CA, USA, 1967. (Cited on page 122.)

[Malik 2012] S. J. Malik, S. Keihaninejad, A. Hammers and J. V. Hajnal. *Tailored excitation in 3D with spiral nonselective (SPINS) RF pulses.* Magnetic Resonance in Medicine, vol. 67, no. 5, pages 1303–1315, May 2012. (Cited on page 63.)

[Malik 2014] S. Malik and J. Hajnal. *3D-FSE Inner Volume Imaging using 3D selective excitation.* In Proc. Intl. Soc. Magn. Reson. Med, page 948, 2014. (Cited on page 62.)

[Malik 2015] S. J. Malik, A. Beqiri, F. Padormo and J. V. Hajnal. *Direct signal control of the steady-state response of 3D-FSE sequences.* Magnetic Resonance in Medicine, vol. 73, no. 3, pages 951–963, March 2015. (Cited on page 63.)

[Maniam 2010] S. Maniam and J. Szklaruk. *Magnetic resonance imaging: Review of imaging techniques and overview of liver imaging.* World Journal of Radiology, vol. 2, no. 8, pages 309–322, August 2010. (Cited on page 43.)

[Mann 2008] R. M. Mann, C. K. Kuhl, K. Kinkel and C. Boetes. *Breast MRI: guidelines from the European Society of Breast Imaging.* European Radiology, vol. 18, no. 7, pages 1307–1318, July 2008. (Cited on page 94.)

[Mansfield 1977a] P. Mansfield. *Multi-planar image formation using NMR spin echoes.* Journal of Physics C: Solid State Physics, vol. 10, no. 3, page L55, 1977. (Cited on page 14.)

[Mansfield 1977b] P. Mansfield and A. A. Maudsley. *Medical imaging by NMR.* The British Journal of Radiology, vol. 50, no. 591, pages 188–194, March 1977. (Cited on pages 7 and 14.)

[Mao 2006] W. Mao, M. B. Smith and C. M. Collins. *Exploring the limits of RF shimming for high-field MRI of the human head.* Magnetic Resonance in Medicine, vol. 56, no. 4, pages 918–922, October 2006. (Cited on page 60.)

[Massire 2013] A. Massire, M. A. Cloos, A. Vignaud, D. Le Bihan, A. Amadon and N. Boulant. *Design of non-selective refocusing pulses with phase-free rotation axis by gradient ascent pulse engineering algorithm in parallel transmission at 7T.* Journal of Magnetic Resonance, vol. 230, pages 76–83, May 2013. (Cited on page 76.)

[Massire 2015] A. Massire, A. Vignaud, B. Robert, D. Le Bihan, N. Boulant and A. Amadon. *Parallel-transmission-enabled three-dimensional T2-weighted imaging of the human brain at 7 Tesla: 3D T2-Weighted Brain Imaging at 7T.* Magnetic Resonance in Medicine, vol. 73, no. 6, pages 2195–2203, June 2015. (Cited on pages 76, 78, 117, 118, and 141.)

[McRobbie 2006] D. W. McRobbie. MRI from picture to proton. Cambridge University Press, Cambridge, UK; New York, 2006. (Cited on pages 6 and 10.)

[Meiboom 1958] S. Meiboom and D. Gill. *Modified spin-echo method for measuring nuclear relaxation times.* Review of scientific instruments, vol. 29, no. 8, pages 688–691, 1958. (Cited on page 23.)

[Merkle 2006] E. M. Merkle, B. M. Dale and E. K. Paulson. *Abdominal MR Imaging at 3T.* Magnetic Resonance Imaging Clinics of North America, vol. 14, no. 1, pages 17–26, February 2006. (Cited on pages 52, 54, and 58.)

[Mirfin 2018] C. Mirfin, P. Glover and R. Bowtell. *Optimisation of parallel transmission radiofrequency pulses using neural networks.* In Proc. Intl. Soc. Mag. Reson. Med, Paris, France, 2018. (Cited on page 121.)

[Mooiweer 2017] R. Mooiweer, J. V. Hajnal and S. J. Malik. *A single-channel universal SPINS pulse for calibration-free homogeneous excitation without PTX.* In Proceedings of the 25th Annual Meeting of the ISMRM, page 390, 2017. (Cited on page 79.)

[Moran 2014] C. J. Moran, B. A. Hargreaves, M. Saranathan, J. A. Lipson, J. Kao, D. M. Ikeda and B. L. Daniel. *3D T2-weighted spin echo imaging in the breast.* Journal of Magnetic Resonance Imaging, vol. 39, no. 2, pages 332–338, February 2014. (Cited on page 94.)

[Mugler 2000] J. P. Mugler, B. Kiefer and J. R. Brookeman. *Three-dimensional T2-weighted imaging of the brain using very long spin-echo trains.* In Proceedings of the 8th Annual Meeting of ISMRM, page 687, 2000. (Cited on pages 26 and 27.)

[Mugler 2014] J. P. Mugler. *Optimized three-dimensional fast-spin-echo MRI.* Journal of Magnetic Resonance Imaging, vol. 39, no. 4, pages 745–767, April 2014. (Cited on page 26.)

[Murbach 2014] M. Murbach, E. Neufeld, W. Kainz, K. P. Pruessmann and N. Kuster. *Whole-body and local RF absorption in human models as a function of anatomy and position within 1.5T MR body coil.* Magnetic Resonance in Medicine, vol. 71, no. 2, pages 839–845, February 2014. (Cited on page 70.)

[Murbach 2016] M. Murbach, E. Neufeld, E. Cabot, E. Zastrow, J. Córcoles, W. Kainz and N. Kuster. *Virtual population-based assessment of the impact of 3 Tesla radiofrequency shimming and thermoregulation on safety and B1+ uniformity.* Magnetic Resonance in Medicine, vol. 76, no. 3, pages 986–997, September 2016. (Cited on pages 70 and 71.)

[Müllner 2017] D. Müllner. *The fastcluster package: User's manual.* 2017. (Cited on pages 125 and 127.)

[Nehrke 2009] K. Nehrke. *On the steady-state properties of actual flip angle imaging (AFI).* Magnetic Resonance in Medicine, vol. 61, no. 1, pages 84–92, January 2009. (Cited on page 65.)

[Neves 2018] A. L. Neves, L. Leroi, Z. Raolison, N. Cochinaire, T. Letertre, R. Abdeddaïm, S. Enoch, J. Wenger, J. Berthelot, A.-L. Adenot-Engelvin, N. Malléjac, F. Mauconduit, A. Vignaud and P. Sabouroux. *Compressed perovskite aqueous mixtures near their phase transitions show very high permittivities: New prospects for high-field MRI dielectric shimming.* Magnetic Resonance in Medicine, vol. 79, no. 3, pages 1753–1765, March 2018. (Cited on page 56.)

[Nickolls 2008] J. Nickolls, I. Buck, M. Garland and K. Skadron. *Scalable parallel programming with CUDA.* In ACM SIGGRAPH 2008 classes, page 16. ACM, 2008. (Cited on page 86.)

[Nistler 2007] J. Nistler, D. Diehl, W. Renz and L. Eberler. *Homogeneity improvement using a 2 port birdcage coil.* In Proceedings of the 15th Annual Meeting of ISMRM, Berlin, Germany, 2007. (Cited on page 68.)

[Nistler 2010] J. Nistler and W. Renz. *Method for controlling a magnetic resonance system*, no. US7847554 B2, December 2010. U.S. Classification 324/318, 324/322; International Classification G01V3/00; Cooperative Classification G01R33/5659, G01R33/3415, G01R33/246; European Classification G01R33/3415, G01R33/565R. (Cited on pages 68 and 95.)

[Norris 2002] D. G. Norris. *Adiabatic radiofrequency pulse forms in biomedical nuclear magnetic resonance*. Concepts in Magnetic Resonance, vol. 14, no. 2, pages 89–101, 2002. (Cited on page 56.)

[Ocali 1998] O. Ocali and E. Atalar. *Ultimate intrinsic signal-to-noise ratio in MRI*. Magnetic Resonance in Medicine, vol. 39, no. 3, pages 462–473, 1998. (Cited on page 45.)

[Ogawa 1990] S. Ogawa, T. M. Lee, A. R. Kay and D. W. Tank. *Brain magnetic resonance imaging with contrast dependent on blood oxygenation*. Proceedings of the National Academy of Sciences, vol. 87, no. 24, pages 9868–9872, December 1990. (Cited on page 47.)

[Orzada 2010] S. Orzada, S. Maderwald, B. A. Poser, A. K. Bitz, H. H. Quick and M. E. Ladd. *RF excitation using time interleaved acquisition of modes (TIAMO) to address B1 inhomogeneity in high-field MRI*. Magnetic Resonance in Medicine, vol. 64, no. 2, pages 327–333, 2010. (Cited on page 144.)

[Padormo 2016] F. Padormo, A. Beqiri, J. V. Hajnal and S. J. Malik. *Parallel transmission for ultrahigh-field imaging*. NMR in Biomedicine, vol. 29, no. 9, pages 1145–1161, September 2016. (Cited on page 59.)

[Panagiotelis 2009] I. Panagiotelis and M. Blasche. *TrueForm™ Technology*. 2009. (Cited on page 68.)

[Park 2014] D. J. Park. *B1 Mapping for Magnetic Resonance Imaging*. PhD thesis, Brigham Young University, 2014. (Cited on page 65.)

[Pauly 1989] J. Pauly, D. Nishimura and A. Macovski. *A k-space analysis of small-tip-angle excitation*. Journal of Magnetic Resonance, vol. 81, no. 1, pages 53–56, 1989. (Cited on pages 11 and 60.)

[Pedregosa 2011] F. Pedregosa, G. Varoquaux, A. Gramfort, V. Michel, B. Thirion, O. Grisel, M. Blondel, P. Prettenhofer, R. Weiss and V. Dubourg. *Scikit-learn: Machine learning in Python*. Journal of machine learning research, vol. 12, no. Oct, pages 2825–2830, 2011. (Cited on page 130.)

[Pohmann 2016] R. Pohmann, O. Speck and K. Scheffler. *Signal-to-noise ratio and MR tissue parameters in human brain imaging at 3, 7, and 9.4 tesla using current receive coil arrays*. Magnetic Resonance in Medicine, vol. 75, no. 2, pages 801–809, 2016. (Cited on pages 45 and 46.)

[Pruessmann 1999] K. P. Pruessmann, M. Weiger, M. B. Scheidegger and P. Boesiger. *SENSE: Sensitivity encoding for fast MRI.* Magnetic Resonance in Medicine, vol. 42, no. 5, pages 952–962, November 1999. (Cited on page 45.)

[Purcell 1946] E. M. Purcell, H. C. Torrey and R. V. Pound. *Resonance Absorption by Nuclear Magnetic Moments in a Solid.* Physical Review, vol. 69, no. 1-2, pages 37–38, January 1946. (Cited on page 7.)

[Rabi 1938] I. I. Rabi, J. R. Zacharias, S. Millman and P. Kusch. *A New Method of Measuring Nuclear Magnetic Moment.* Physical Review, vol. 53, no. 4, pages 318–318, February 1938. (Cited on page 7.)

[Rakow-Penner 2006] R. Rakow-Penner, B. Daniel, H. Yu, A. Sawyer-Glover and G. H. Glover. *Relaxation times of breast tissue at 1.5T and 3T measured using IDEAL.* Journal of Magnetic Resonance Imaging, vol. 23, no. 1, pages 87–91, January 2006. (Cited on pages 48 and 95.)

[Reeder 2007] S. B. Reeder, C. A. McKenzie, A. R. Pineda, H. Yu, A. Shimakawa, A. C. Brau, B. A. Hargreaves, G. E. Gold and J. H. Brittain. *Water–fat separation with IDEAL gradient-echo imaging.* Journal of Magnetic Resonance Imaging, vol. 25, no. 3, pages 644–652, 2007. (Cited on page 33.)

[Riffel 2013] P. Riffel, U. I. Attenberger, S. Kannengiesser, M. D. Nickel, C. Arndt, M. Meyer, S. O. Schoenberg and H. J. Michaely. *Highly accelerated T1-weighted abdominal imaging using 2-dimensional controlled aliasing in parallel imaging results in higher acceleration: a comparison with generalized autocalibrating partially parallel acquisitions parallel imaging.* Investigative Radiology, vol. 48, no. 7, pages 554–561, July 2013. (Cited on page 116.)

[Rohrer 2005] M. Rohrer, H. Bauer, J. Mintorovitch, M. Requardt and H.-J. Weinmann. *Comparison of magnetic properties of MRI contrast media solutions at different magnetic field strengths.* Investigative radiology, vol. 40, no. 11, pages 715–724, 2005. (Cited on page 49.)

[Saekho 2006] S. Saekho, C.-y. Yip, D. C. Noll, F. E. Boada and V. A. Stenger. *Fast-kz three-dimensional tailored radiofrequency pulse for reduced B1 inhomogeneity.* Magnetic Resonance in Medicine, vol. 55, no. 4, pages 719–724, April 2006. (Cited on page 63.)

[Saloner 1995] D. Saloner. *The AAPM/RSNA physics tutorial for residents. An introduction to MR angiography.* RadioGraphics, vol. 15, no. 2, pages 453–465, March 1995. (Cited on page 48.)

[Saïb 2018] G. Saïb, R. Tomi-Tricot, V. Gras, F. Mauconduit, N. Boulant, A. Vignaud, M. Luong, E. Giacomini, E. Chazel, D. Le Bihan, L. Le Brusquet and A. Amadon. *Z-segmentation of a transmit array head coil improves RF ramp pulse design at*

7T. In Proceedings of the 26th Annual Meeting of ISMRM, Paris, France, 2018. (Cited on page 168.)

[Schmitt 2004] M. Schmitt, T. Feiweier, W. Horger, G. Krueger, L. Schoen, R. Lazar and B. Kiefer. *Improved uniformity of RF-distribution in clinical whole body imaging at 3T by means of dielectric pads*. In Proceedings of the 12th Annual Meeting of ISMRM, Kyoto, Japan, page 954, 2004. (Cited on page 57.)

[Schmitter 2015] S. Schmitter, X. Wu, K. Uğurbil and P.-F. Van de Moortele. *Design of parallel transmission radiofrequency pulses robust against respiration in cardiac MRI at 7 Tesla: pTX RF Pulses Robust Against Respiration in Cardiac MRI*. Magnetic Resonance in Medicine, vol. 74, no. 5, pages 1291–1305, November 2015. (Cited on page 117.)

[Schneider 2013] J. T. Schneider, R. Kalayciyan, M. Haas, S. R. Herrmann, W. Ruhm, J. Hennig and P. Ullmann. *Inner-volume imaging in vivo using three-dimensional parallel spatially selective excitation*. Magnetic Resonance in Medicine, vol. 69, no. 5, pages 1367–1378, 2013. (Cited on page 62.)

[Setsompop 2008a] K. Setsompop, L. L. Wald, V. Alagappan, B. A. Gagoski and E. Adalsteinsson. *Magnitude least squares optimization for parallel radio frequency excitation design demonstrated at 7 Tesla with eight channels*. Magnetic Resonance in Medicine, vol. 59, no. 4, pages 908–915, 2008. (Cited on page 124.)

[Setsompop 2008b] K. Setsompop. *Design Algorithms for Parallel Transmission in Magnetic Resonance Imaging*. PhD thesis, Massachusetts Institute of Technology, 2008. (Cited on pages 63 and 64.)

[Setsompop 2008c] K. Setsompop, V. Alagappan, B. Gagoski, T. Witzel, J. Polimeni, A. Potthast, F. Hebrank, U. Fontius, F. Schmitt, L. L. Wald and E. Adalsteinsson. *Slice-selective RF pulses for in vivo B inhomogeneity mitigation at 7 tesla using parallel RF excitation with a 16-element coil*. Magnetic Resonance in Medicine, vol. 60, no. 6, pages 1422–1432, 2008. (Cited on page 79.)

[Siemens Healthcare 2013] Siemens Healthcare. *Brochure: TimTX, TrueForm, TrueShape*, 2013. (Cited on page 69.)

[Sodickson 1999] D. K. Sodickson, M. A. Griswold and P. M. Jakob. *SMASH imaging*. Magnetic Resonance Imaging Clinics of North America, vol. 7, no. 2, pages 237–254, vii–viii, May 1999. (Cited on page 45.)

[Soher 2007] B. J. Soher, B. M. Dale and E. M. Merkle. *A Review of MR Physics: 3T versus 1.5T*. Magnetic Resonance Imaging Clinics of North America, vol. 15, no. 3, pages 277–290, August 2007. (Cited on pages 50, 54, and 55.)

[Springer 2016] E. Springer, B. Dymerska, P. Lima Cardoso, S. D. Robinson, C. Weisstanner, R. Wiest, B. Schmitt and S. Trattnig. *Comparison of Routine Brain Imaging*

at 3 T and 7 T. Investigative radiology, vol. 51, no. 8, pages 469–482, August 2016. (Cited on page 22.)

[Stanisz 2005] G. J. Stanisz, E. E. Odrobina, J. Pun, M. Escaravage, S. J. Graham, M. J. Bronskill and R. M. Henkelman. *T1, T2 relaxation and magnetization transfer in tissue at 3T.* Magnetic Resonance in Medicine, vol. 54, no. 3, pages 507–512, September 2005. (Cited on pages 9, 16, 48, and 117.)

[Stehling 1991] M. K. Stehling, R. Turner and P. Mansfield. *Echo-planar imaging: magnetic resonance imaging in a fraction of a second.* Science, vol. 254, no. 5028, pages 43–50, October 1991. (Cited on page 50.)

[Sze 1993] G. Sze, Y. Kawamura, C. Negishi, R. T. Constable, M. Merriam, K. Oshio and F. Jolesz. *Fast spin-echo MR imaging of the cervical spine: influence of echo train length and echo spacing on image contrast and quality.* American journal of neuroradiology, vol. 14, no. 5, pages 1203–1213, 1993. (Cited on page 23.)

[Tannús 1997] A. Tannús and M. Garwood. *Adiabatic pulses.* NMR in Biomedicine, vol. 10, no. 8, pages 423–434, 1997. (Cited on page 56.)

[Teeuwisse 2012a] W. M. Teeuwisse, W. M. Brink, K. N. Haines and A. G. Webb. *Simulations of high permittivity materials for 7 T neuroimaging and evaluation of a new barium titanate-based dielectric.* Magnetic Resonance in Medicine, vol. 67, no. 4, pages 912–918, April 2012. (Cited on pages 56 and 57.)

[Teeuwisse 2012b] W. M. Teeuwisse, W. M. Brink and A. G. Webb. *Quantitative assessment of the effects of high-permittivity pads in 7 Tesla MRI of the brain.* Magnetic Resonance in Medicine, vol. 67, no. 5, pages 1285–1293, May 2012. (Cited on pages 56 and 57.)

[The National Electrical Manufacturers Association 1997] The National Electrical Manufacturers Association. *Digital Imaging and Communication in Medicine (DICOM).* NEMA PS 3 Supplement 23 Structured Reporting, 1997. (Cited on page 129.)

[Tofts 2005] P. Tofts. Quantitative MRI of the brain: measuring changes caused by disease. John Wiley & Sons, 2005. (Cited on page 48.)

[Tomi-Tricot 2016] R. Tomi-Tricot, V. Gras, N. Boulant, A. Vignaud and A. Amadon. *K_T-Points Pulse Design at 7T: Optimization of Pulse and Sub-Pulse Durations.* In Magnetic Resonance Materials in Physics, Biology and Medicine, volume 29, pages 247–400, Vienna, AT, September 2016. (Cited on pages 82, 109, and 168.)

[Tomi-Tricot 2017a] R. Tomi-Tricot, V. Gras, F. Mauconduit, N. Boulant, P. Zerbib, A. Rahmouni, A. Vignaud, A. Luciani and A. Amadon. *SAR-Constrained k_T-Points Pulse Design Applied to B1 Inhomogeneity Mitigation in the Human Abdomen at 3T.* In Proceedings of the 25th Annual Meeting of ISMRM, page 4830, Honolulu, HI, USA, 2017. (Cited on page 168.)

[Tomi-Tricot 2017b] R. Tomi-Tricot, V. Gras, F. Mauconduit, F. Legou, N. Boulant, M. Gebhardt, D. Ritter, B. Kiefer, P. Zerbib, A. Rahmouni, A. Vignaud, A. Luciani and A. Amadon. *First Clinical Assessment of k_T-Points Dynamic RF Shimming on Abdominal DCE-MRI in a Commercial 3T MRI Scanner.* In Proceedings of the 103rd Annual Meeting of the Radiological Society of North America, page SSK17:02, Chicago, IL, USA, 2017. (Cited on pages 105 and 168.)

[Tomi-Tricot 2018a] R. Tomi-Tricot, V. Gras, T. H. Dao, A. Perrot, F. Mauconduit, N. Boulant, P. Zerbib, A. Rahmouni, A. Vignaud, A. Luciani and A. Amadon. *RF-Induced Potential False-Negative Lesion in Breast T2-weighted MRI at 3T: Exploration of a Single-Channel k_T-Points Solution.* In Proceedings of the 26th Annual Meeting of ISMRM, page 4339, Paris, France, 2018. (Cited on pages 93 and 168.)

[Tomi-Tricot 2018b] R. Tomi-Tricot, V. Gras, F. Mauconduit, F. Legou, N. Boulant, M. Gebhardt, D. Ritter, B. Kiefer, P. Zerbib, A. Rahmouni, A. Vignaud, A. Luciani and A. Amadon. *B1 artifact reduction in abdominal DCE-MRI using k_T-points: First clinical assessment of dynamic RF shimming at 3T.* Journal of Magnetic Resonance Imaging, vol. 47, no. 6, pages 1562–1571, June 2018. (Cited on pages 105 and 167.)

[Tomi-Tricot 2018c] R. Tomi-Tricot, V. Gras, F. Mauconduit, F. Legou, N. Boulant, M. Gebhardt, D. Ritter, B. Kiefer, P. Zerbib, A. Rahmouni, A. Vignaud, A. Luciani and A. Amadon. *K_T-Points Pulses Reduce B1 Shading at 3T: Demonstration in Routine Abdominal DCE-MRI and Evaluation of Reliability.* In Proceedings of the 26th Annual Meeting of ISMRM, page 2689, Paris, France, 2018. (Cited on pages 105 and 167.)

[Tse 2016] D. H. Y. Tse, C. J. Wiggins, D. Ivanov, D. Brenner, J. Hoffmann, C. Mirkes, G. Shajan, K. Scheffler, K. Uludağ and B. A. Poser. *Volumetric imaging with homogenised excitation and static field at 9.4 T.* Magma (New York, N.Y.), vol. 29, no. 3, pages 333–345, June 2016. (Cited on pages 78 and 79.)

[Ullmann 2005] P. Ullmann, S. Junge, M. Wick, F. Seifert, W. Ruhm and J. Hennig. *Experimental analysis of parallel excitation using dedicated coil setups and simultaneous RF transmission on multiple channels.* Magnetic Resonance in Medicine, vol. 54, no. 4, pages 994–1001, September 2005. (Cited on page 63.)

[Van de Moortele 2007] P.-F. Van de Moortele, C. Snyder, L. DelaBarre, G. Adriany, J. T. Vaughan and K. Ugurbil. *Calibration tools for RF shim at very high field with multiple element RF coils: from ultra fast local relative phase to absolute magnitude B1+ mapping.* In Proc Intl Soc Mag Reson Med, volume 15, page 1676, 2007. (Cited on page 65.)

[Van der Meulen 1988] P. Van der Meulen, J. P. Groen, A. M. C. Tinus and G. Bruntink. *Fast Field Echo imaging: An overview and contrast calculations.* Magnetic Resonance Imaging, vol. 6, no. 4, pages 355–368, July 1988. (Cited on page 19.)

[Wang 2007] Z. Wang, J. C. Lin, W. Mao, W. Liu, M. B. Smith and C. M. Collins. *SAR and temperature: Simulations and comparison to regulatory limits for MRI.* Journal of Magnetic Resonance Imaging, vol. 26, no. 2, pages 437–441, 2007. (Cited on page 67.)

[Webb 2011] A. G. Webb. *Dielectric materials in magnetic resonance.* Concepts in Magnetic Resonance Part A, vol. 38A, no. 4, pages 148–184, July 2011. (Cited on page 56.)

[Weigel 2015] M. Weigel. *Extended phase graphs: Dephasing, RF pulses, and echoes - pure and simple: Extended Phase Graphs.* Journal of Magnetic Resonance Imaging, vol. 41, no. 2, pages 266–295, February 2015. (Cited on page 26.)

[Wiesinger 2004] F. Wiesinger, P. Boesiger and K. P. Pruessmann. *Electrodynamics and ultimate SNR in parallel MR imaging.* Magnetic Resonance in Medicine, vol. 52, no. 2, pages 376–390, 2004. (Cited on pages 45 and 46.)

[Winkler 2015] S. A. Winkler and B. K. Rutt. *Practical methods for improving B1+ homogeneity in 3 tesla breast imaging.* Journal of Magnetic Resonance Imaging, vol. 41, no. 4, pages 992–999, April 2015. (Cited on pages 94 and 99.)

[Woessner 1961] D. E. Woessner. *Effects of Diffusion in Nuclear Magnetic Resonance Spin-Echo Experiments.* The Journal of Chemical Physics, vol. 34, no. 6, pages 2057–2061, June 1961. (Cited on page 24.)

[Wu 2004] T.-F. Wu, C.-J. Lin and R. C. Weng. *Probability estimates for multi-class classification by pairwise coupling.* Journal of Machine Learning Research, vol. 5, no. Aug, pages 975–1005, 2004. (Cited on page 130.)

[Wu 2013] X. Wu, S. Schmitter, E. J. Auerbach, S. Moeller, K. Uğurbil and P.-F. V. d. Moortele. *Simultaneous multislice multiband parallel radiofrequency excitation with independent slice-specific transmit B1 homogenization.* Magnetic Resonance in Medicine, vol. 70, no. 3, pages 630–638, 2013. (Cited on page 79.)

[Wu 2014] X. Wu, S. Schmitter, E. J. Auerbach, K. Uğurbil and P.-F. Van de Moortele. *Mitigating transmit B1 inhomogeneity in the liver at 7T using multispoke parallel transmit RF pulse design.* Quantitative Imaging in Medicine and Surgery, vol. 4, no. 1, pages 4–10, February 2014. (Cited on pages 63 and 144.)

[Yan 2018] K. Yan, X. Wang, L. Lu and R. M. Summers. *DeepLesion: automated mining of large-scale lesion annotations and universal lesion detection with deep learning.* Journal of Medical Imaging, vol. 5, no. 3, page 036501, July 2018. (Cited on page 123.)

[Yanasak 2014] N. E. Yanasak and M. J. Kelly. *MR Imaging Artifacts and Parallel Imaging Techniques with Calibration Scanning: A New Twist on Old Problems.* RadioGraphics, vol. 34, no. 2, pages 532–548, March 2014. (Cited on pages 50 and 51.)

[Yang 2006] Q. X. Yang, W. Mao, J. Wang, M. B. Smith, H. Lei, X. Zhang, K. Ugurbil and W. Chen. *Manipulation of image intensity distribution at 7.0 T: Passive RF shimming and focusing with dielectric materials.* Journal of Magnetic Resonance Imaging, vol. 24, no. 1, pages 197–202, July 2006. (Cited on page 56.)

[Yarnykh 2007] V. L. Yarnykh. *Actual flip-angle imaging in the pulsed steady state: A method for rapid three-dimensional mapping of the transmitted radiofrequency field.* Magnetic Resonance in Medicine, vol. 57, no. 1, pages 192–200, January 2007. (Cited on page 65.)

[Yip 2006] C.-Y. Yip, J. A. Fessler and D. C. Noll. *Advanced three-dimensional tailored RF pulse for signal recovery in T2*-weighted functional magnetic resonance imaging.* Magnetic Resonance in Medicine, vol. 56, no. 5, pages 1050–1059, November 2006. (Cited on page 63.)

[Zhu 2004] Y. Zhu. *Parallel excitation with an array of transmit coils.* Magnetic Resonance in Medicine, vol. 51, no. 4, pages 775–784, 2004. (Cited on pages 63 and 67.)

[Zhu 2012] Y. Zhu, L. Alon, C. M. Deniz, R. Brown and D. K. Sodickson. *System and SAR characterization in parallel RF transmission.* Magnetic Resonance in Medicine, vol. 67, no. 5, pages 1367–1378, 2012. (Cited on page 52.)

[Zur 1991] Y. Zur, M. L. Wood and L. J. Neuringer. *Spoiling of transverse magnetization in steady-state sequences.* Magnetic Resonance in Medicine, vol. 21, no. 2, pages 251–263, October 1991. (Cited on page 19.)

Abbreviations and Acronyms

2D	two-dimensional
3D	three-dimensional
AFI	actual flip angle imaging
AHT	average Hamiltonian theory
BMI	body mass index
BOLD	blood-oxygenation-level dependent
bSSFP	balanced steady-state free precession
CAIPIRINHA	controlled aliasing in parallel imaging results in higher acceleration
CE	contrast enhancement
CHESS	chemical-shift-selective fat suppression
CNR	contrast-to-noise ratio
COR	coronal plane
CV	coefficient of variation
CP	circular polarisation
CPMG	Carr-Purcell-Meiboom-Gill
DCE	dynamic contrast-enhanced imaging
DSC	direct signal control
DWI	diffusion-weighted imaging
EP	elliptical polarisation
EPG	extended phase graph
EPI	echo-planar imaging
ER	enhancement ratio
ETL	echo train length
FA	flip angle
FID	free induction decay
FLAIR	fluid-attenuated inversion recovery
FLASH	fast low angle shot

fMRI	functional MRI
FNH	focal nodular hyperplasia
FOV	field of view
FS	fat saturation
FSE	fast spin-echo
FWHM	full width at half-maximum
Gd-BOPTA	gadobenate dimeglumine
Gd-DOTA	gadoterate meglumine
GPGPU	general-purpose computing on graphics processing units
GRAPPA	generalised autocalibrating partially parallel acquisition
GRASP	golden-angle radial sparse parallel MRI
GRE	gradient-recalled echo
HASTE	half-fourier acquisition single-shot turbo spin echo imaging
HBV	hepatitis B virus
HCC	hepatocellular carcinoma
HCV	hepatitis C virus
IP	in phase
IVIM	intravoxel incoherent motion
LTA	large tip angle
MP-RAGE	magnetisation-prepared rapid gradient echo
MRI	magnetic resonance imaging
NASH	non-alcoholic steatohepatitis
NMR	nuclear magnetic resonance
NRMSE	normalised root-mean-square error
OP	out of phase (complete phase opposition)
PDw	proton-density-weighted
PF	partial Fourier
ppm	parts per million
pTx	parallel transmission
RARE	rapid acquisition with refocused echoes
RF	radiofrequency
ROI	region of interest
SAG	sagittal plane
SAR	specific absorption rate
SD	sample standard deviation
SE	spin-echo
SENSE	sensitivity encoding
SNR	signal-to-noise ratio

SPACE	sampling perfection with application-optimised contrasts using different flip angle evolutions
SPAIR	spectral adiabatic inversion recovery
SPGR	spoiled GRE
SPINS	spiral non-selective RF pulse
SPIR	spectral presaturation with inversion recovery
STA	small tip angle
STEAM	stimulated echo acquisition mode
STIR	short TI inversion recovery
sTx	single-channel transmission
SVS	single-voxel spectroscopy
T_1H	T_1-hyperintensity
T_1h	T_1-hypointensity
T_1w	T_1-weighted
T_2H	T_2-hyperintensity
T_2h	T_2-hypointensity
T_2w	T_2-weighted
T_2^*w	T_2^*-weighted
TA	acquisition time
TE	echo time
TI	inversion time
TIAMO	time interleaved acquisition of modes
TNC	time normalisation constant
TOF	time-of-flight
TR	repetition time
TRA	transverse plane
TSE	turbo spin-echo
UHF	ultra-high field
UP	Universal Pulse
VIBE	volumetric interpolated breath-hold examination
VOP	virtual observation point
XD-GRASP	GRASP with reconstruction of extra motion-state dimensions

université PARIS-SACLAY
ÉCOLE DOCTORALE
Physique et ingénierie : électrons, photons, sciences du vivant (EOBE)

Titre : Applications cliniques de la méthode des points k_T pour homogénéiser l'excitation des spins en IRM à 3 teslas

Mots clés : IRM, transmission parallèle, points k_T, inhomogénéités radiofréquence, 3T, imagerie clinique

Résumé : L'imagerie par résonance magnétique (IRM) à haut champ offre un bénéfice certain en rapport signal-sur-bruit. De ce fait, les imageurs à 3T sont souvent utilisés en pratique clinique. Cependant, à haut champ, les images d'IRM sont entachées de pertes de signal et de contraste liées à la baisse de la longueur d'onde radiofréquence (RF) en deçà des dimensions de l'objet irradié. A 3T, où la longueur d'onde est de 30 cm environ dans les tissus humains, de tels artéfacts sont fréquents en imagerie abdominale, des seins ou encore des cuisses, ce qui peut expliquer la difficulté que rencontre l'IRM à haut champ à s'imposer comme référence dans les hôpitaux. Les imageurs 3T les plus récents disposent en général d'un système de transmission parallèle à deux canaux RF. Chaque canal peut en principe émettre des formes d'impulsion RF indépendantes. En pratique, sur la plupart des systèmes IRM cliniques, la méthode dite de *shim* RF statique est utilisée. Les différents canaux transmettent la même forme d'onde, en ajustant amplitude et phase de sorte à entraîner des motifs d'interférences pour contrer les inhomogénéités, mesurées au préalable sur le patient: cartes de champ RF et éventuellement de champ statique. Cette méthode fonctionne d'autant mieux qu'un grand nombre de canaux est disponible, mais montre ses limites lorsqu'il s'agit d'homogénéiser l'excitation sur un grand champ de vue. La méthode des points k_T, développée à NeuroSpin pour l'IRM cérébrale à ultra-haut champ (7T) utilise une alternance d'impulsions RF rectangulaires et de gradients de champ statique pour moduler à dessein l'aimantation des spins et ainsi homogénéiser l'excitation malgré un champ RF inhomogène. Les impulsions ainsi créées sont d'autant plus efficaces qu'elles peuvent exploiter la transmission parallèle (huit canaux à 7T). Dans cette thèse, les points k_T sont employés à 3T avec pour objectif d'en démontrer l'intérêt et l'applicabilité en routine clinique. Dans un premier temps, nous décrivons des modifications apportées à l'algorithme de conception de points k_T et à la cartographie de champ statique permettant d'adapter la technique à l'imagerie du corps – foie, seins – où la présence des poumons et de la graisse entraîne des contraintes supplémentaires par rapport au cerveau. Dans un second temps, plusieurs études cliniques sont exposées. La première concerne l'IRM du sein en pondération T_2 sur un imageur à canal d'émission unique. Elle met en évidence que le mode d'émission par défaut fonctionne correctement et n'est que peu amélioré par les points k_T. Une deuxième étude se penche sur l'imagerie dynamique du foie avec injection de produit de contraste, avec deux canaux. Des analyses quantitatives et qualitatives sont menées sur un grand nombre de patients pour comparer le *shim* RF statique avec les points k_T. Ces derniers améliorent très nettement les images obtenues chez certains patients « difficiles », permettant ainsi d'offrir une qualité d'examen et de diagnostic plus homogène sur l'ensemble de la population. Enfin, une nouvelle technique est présentée, intitulée *SmartPulse*, qui s'appuie sur le concept d'impulsions universelles, développé à NeuroSpin pour l'imagerie du cerveau, et dont le principe est de concevoir des impulsions de type points k_T qui, pour une application donnée, soient efficaces sur toute la population et permettent de se passer de calibration. En divisant la population en catégories pour lesquelles des impulsions différentes sont conçues, et en utilisant un algorithme de classification par apprentissage automatique, *SmartPulse* étend la portée des impulsions universelles au corps, et en particulier à l'abdomen, où la variabilité morphologique est importante. Par ces travaux de thèse, nous espérons donner un nouveau souffle à la gestion des inhomogénéités RF en routine clinique à 3T, et apporter des éléments permettant à terme de démocratiser l'imagerie des gros organes à ultra-haut champ.

Title: Clinical applications of the k_T-points method to homogenise spin excitation in 3T MRI

Keywords: MRI, parallel transmission, k_T-points, radiofrequency inhomogeneity, 3T, clinical imaging

Abstract: High field magnetic resonance imaging (MRI) is often used in clinical practice, for the high signal-to-noise ratio it offers. However, at high field, the radiofrequency (RF) wavelength used for imaging is shorter, which can induce loss of signal and contrast when it is close to or shorter than the dimensions of the irradiated objects. At 3T, RF wavelength is about 30 cm in human tissues, and such artefacts are frequently observed in the abdomen, as well as in the thighs or in the breasts. This is certainly one of the main reasons why high field MRI has failed to establish itself as the gold standard in hospital, where 1.5T scanners are more frequent. Recent 3T scanners usually come with a two-RF-channel parallel transmission setup: in principle, each channel can transmit completely independent waveforms. However, this technology is not exploited fully in practice, as only the static RF shimming is implemented: a single waveform is used, with adjusted amplitude and phase on each channel. This allows to create interference patterns, calculated to counteract transmission inhomogeneities measured beforehand in the patient (RF and possibly static field). This method works best when many channels are available, but shows its limits when good homogeneity is expected over a large field of view. The k_T-points method, developed at CEA-NeuroSpin for brain imaging at ultra-high field (7T) relies on a succession of short rectangular RF pulses interleaved with static gradient "blips" to modulate magnetisation at will, thus producing homogeneous excitation in spite of an imperfect RF field. Those composite pulses are even more effective as they can take advantage of parallel transmission (eight channels at 7T). In this thesis, the k_T-points technique is applied at 3T. The objective is to demonstrate its usefulness and its compatibility with a clinical routine workflow. First, several changes made to the k_T-points pulse design algorithm and to static field mapping in order to adapt them to body imaging (liver, breasts) are described. Indeed, the presence of lungs and fat add further constraints compared to the brain. Then, several clinical studies are detailed. The first one regards T_2-weighted breast MRI on a single-channel scanner. It shows that in that case the default transmit mode is satisfactory, and only slightly improved by k_T-points. A second study focuses on T_1-weighted dynamic contrast-enhanced imaging of the liver, with two transmit channels. Static RF shimming and k_T-points were compared on a large cohort. For some "difficult" patients, acquisitions were quantitatively and qualitatively better with k_T-points, which therefore offer a more uniform diagnostic quality among the population. Finally, a novel method is proposed: *SmartPulse*. It is based on the universal pulse concept, developed in NeuroSpin for brain imaging, whose principle is to design pulses (e.g. k_T-points) for a given application, that homogenise excitation in the whole population, and not only for one subject. Thus, there is no more need for cumbersome mapping and inline pulse design. *SmartPulse* extends the range of universal pulses to body imaging, by adequately clustering the population, designing different pulses for each cluster, and applying a machine learning classifier to assign the most appropriate pulse to any new subject. Proof of concept was undertaken in abdominal imaging, where inter-subject variability is considerable. We hope this thesis will give a new outlook on RF inhomogeneity handling in routine 3T MRI, and in the long run will help making body imaging more accessible at high and ultra-high field.

Université Paris-Saclay
Espace Technologique / Immeuble Discovery
Route de l'Orme aux Merisiers RD 128 / 91190 Saint-Aubin, France